INVESTIGATION OF MICROSTRUCTURAL HOMOGENEITY AND
THERMAL STABILITY OF EQUAL CHANNEL ANGULAR PRESSED
AND AGED 2024 Al ALLOY

A THESIS SUBMITTED TO
THE GRDUATE SCHOOL OF NATURAL AND APPLIED SCIENCES
OF
MIDDLE EAST TECHNICAL UNIVERSITY

BY

GUHER KOTAN

IN PARTIAL FULLFILLMENT OF THE REQUIREMENTS
FOR
THE DEGREE OF DOCTOR OF PHILOSOPHY
IN
METALLURGICAL AND MATERIALS ENGINEERING

SEPTEMBER 2014

Approval of the thesis:

INVESTIGATION OF MICROSTRUCTURAL HOMOGENEITY AND THERMAL STABILITY OF EQUAL CHANNEL ANGULAR PRESSED AND AGED 2024 Al ALLOY

Submitted by **GÜHER KOTAN** in partial fulfillment of the requirements of the degree of **Doctor of Philosophy in Metallurgical and Materials Engineering Department, Middle East Technical University** by,

Prof. Dr. Canan Özgen   _____
Dean, Graduate School of **Natural and Applied Sciences**

Prof. Dr. Cemil Hakan Gür   _____
Head of Department, **Metallurgical and Materials Eng.**

Prof. Dr. Cemil Hakan Gür   _____
Supervisor, **Metallurgical and Materials Eng. Dept., METU**

Asst. Prof. Dr. Yunus Eren Kalay   _____
Co-Supervisor, **Metallurgical and Materials Eng. Dept., METU**

Examining Committee Members:
Prof. Dr. Tayfur Öztürk   _____
Metallurgical and Materials Eng. Dept., METU

Prof. Dr. Cemil Hakan Gür   _____
Metallurgical and Materials Eng. Dept., METU

Prof. Dr. Bülent Doyum   _____
Mechanical Engineering Dept., METU

Assoc. Prof. Dr. Arcan Dericioğlu   _____
Metallurgical and Materials Eng. Dept., METU

Assist. Prof. Dr.Caner Şimşir   _____
Dept. of Manufacturing Eng., ATILIM UNIV.

Date: _____

I hereby declare that all the information in this document has been obtained and presented in accordance with academic rules and ethical conduct. I also declare that, as required by these rules and conduct, I have fully cited and referenced all material and results that are not original to this work.

Name, Last name   : Güher Kotan

Signature   :

ABSTRACT

INVESTIGATION OF MICROSTRUCTURAL HOMOGENEITY AND THERMAL STABILITY OF EQUAL CHANNEL ANGULAR PRESSED AND AGED 2024 Al ALLOY

Kotan, Güher

Ph. D., Department of Metallurgical and Materials Engineering

Supervisor: Prof. Dr. C. Hakan Gür

Co-supervisor: Asst. Prof. Dr. Y. Eren Kalay

September 2014, 203 pages

Attributed primarily to its uniqueness, simplicity and ability for effective strengthening through grain refinement without reduction in cross sectional area, equal channel angular pressing (ECAP) has been known as one of the most important metal working process. The implementation of ECAP with precipitation hardening exhibits a promising strengthening mechanism to be applied to age-hardenable metals. On the other hand, the combined effect of precipitation hardening and excessive plastic strain is quite complicated and needs detailed investigations to understand the basics of strengthening mechanisms. In this respect, the experimental work in this thesis represents a substantial step forward to understand the strengthening mechanism resulted by a combined implementation of ECAP and precipitation hardening in aluminum 2024.

In the first part of this study, various aspects of ECAP and post ECAP precipitation in comparison to solutionized and aged counterpart were investigated. Homogenization contribution of precipitation process was monitored via micro-hardness indentation and the degree of homogenization was characterized by hardness inhomogeneity index (HII). The variation of hardness, hence strain levels, observed in two different samples was also investigated considering level of back pressure, magnesium content and sample conditions.

In the second part, the response of ECAPed and post-ECAP aged samples, when subjected to long term and moderate temperatures up to 1000 hours was investigated. A limiting temperature was suggested for the safe use of an ECAPed Al 2024.

Throughout the study microstructural characterizations were performed using high resolution electron microscopy (HREM), scanning electron microscopy (SEM), electron backscatter diffraction (EBSD) and optical microscopy.

Keywords: Aluminum, Equal Channel Angular Pressing (ECAP), Aging, Homogeneity, Thermal Stability, Transmission Electron Microscopy

ÖZ

AŞIRI DEFORME EDİLMİŞ VE YAŞLANDIRILMIŞ Al 2024 ALAŞIMINDA MİKROYAPISAL HOMOJENLİK VE ISIL KARARLILIĞIN İNCELENMESİ

Kotan, Güher

Doktora, Metalurji ve Malzeme Mühendisliği Bölümü

Tez Yöneticisi: Prof. Dr. C. Hakan Gür

Ortak Tez Yöneticisi: Yrd. Doç. Dr. Y. Eren Kalay

Eylül 2014, 203 sayfa

İleri düzey malzemelerin geliştirilmesinde, eşkanallı açısal preslemenin (EKAP) benzersizliği, basitliği, kolay uygulanabilirliği ve etkin güçlendirme ve tane inceltme becerileri dolayısıyla özel bir yeri vardır. Öte yandan yaşlandırma yoluyla sertleştirme, uygulanmış ilk nanoteknoloji olarak düşünülebilecek yüz yıllık bir keşiftir. Ancak iki unsurun birleşik etkisi ve EKAPlanmış yapının ısıl kararlılığı, mekanizmaların anlaşılması için karmaşık ve ayrıntılı araştırma gerektiren zorlu konulardır.

Bu çalışmada ilk olarak, EKAP ve EKAP sonrası çöktürme, çözeltiye alınıp yaşlandırılmış emsali ile karşılaştırılarak pek çok açıdan incelenmiştir. Çöktürme prosesinin homojenleştirme katkısı mikro indentasyonla görüntülenmiş; homojenlik derecesi sertlik inhomojenlik indeksi (Sİİ) ile karakterize edilmiştir. İki farklı

numunede gözlenen sertlik, dolayısıyla gerinim, değerleri farklılıkları geri basınç farkı, magnezyum içeriği ve numune durumu açılarından araştırılmıştır.

İkinci olarak da EKAPlanmış ve EKAP sonrası yaşlandırılmış numunelerin; orta yükseklikteki sıcaklıklara 1000 saate kadar uzun süreler maruz bırakıldıklarında nasıl tepki verdikleri incelenmiştir. EKAPlanmış ve 190°C'de bir saat yaşlandıktan sonra daha stabil ve daha homojen olabilen, Al 2024 alaşımının güvenli bir şekilde, uzun süreler kullanılabileceği bir üst limit sıcaklık değeri önerilmiştir.

Bu çalışma boyunca mikroyapısal karakterizasyon yüksek çözünürlük elektron mikroskobu (HREM), taramalı elektron mikroskobu (SEM), elektron geri saçınım difraksiyonu (EBSD)ve optik mikroskopisi kullanılmıştır.

Anahtar Kelimeler: Alüminyum, Eş Kanallı Açısal Presleme (EKAP), Yaşlandırma, Homojenlik, Isıl Kararlılık, Geçirim Elektron Mikroskopisi

To my family and to the Lovely Universe

ACKNOWLEDGEMENTS

In the long years of study for my Ph.D. thesis, there have been so many precious helps that I have received from so many respectful, lovely and wise people that, it is very hard to thank all the beautiful people supported me through this journey. I am deeply thankful to my hard-working, positive, wise and creative advisor, Prof. Dr. C. Hakan Gür, for his endless support, efforts, problem solving genius ideas, his wisdom to handle any situation and support through the hard circumstances that I have went through during this journey. His attitude towards life, science, people, work and relationships free of prejudgment was the best gift that I have received and needed. I am also thankful for his patience and all the endless encouragements not only to conclude the thesis but also to take life as a whole and continue in all fields of it.

Secondly, I am very much grateful for the guidance of Assist. Prof. Dr. Y. Eren Kalay that I can't find words to define my appreciation. Until his guidance and knowledge that he shared with me, I was totally lost in the TEM images, samples and looking for a guide on how to interpret what I have seen, what else to do and how to do, literally lost in the dark. It would not be too much to say that he was the person who put the lights on and I could continue. His efforts, his love for the job, his commitment to science and never ending support in any circumstances mean so much to me that I can never appreciate enough for his valuable contributions to me, to my thesis, to my life. I wish the very best of everything for him and would not be surprised but be very happy to see him as a Nobel Prize winner one day.

Without mentioning his contribution to my life and my thesis, it would be incomplete so I want to thank from the bottom of my heart to the wisest scientist I have ever met, Prof. Dr. Şakir Bor, for his countless contributions to me as a

TABLE OF CONTENTS

LIST OF TABLES

LIST OF FIGURES

FIGURES

CHAPTER 1

INTRODUCTION

Aluminum and its alloys are the second most commonly used metallic materials followed by iron based alloys due to light weight, and lower production and shaping costs in comparison to its counterparts, i. e. Ti and Mg. They are particularly preferred in applications where reducing weight is primary concern such as transportation industry including aerospace applications. In addition to its well-known advantages, there is also a need for better mechanical properties in order to obtain higher performance. The need for improvement resulted in various developments like cold working, severe plastic deformation, precipitation hardening, Al matrix composites and new alloy designs like Al-Cu-Li for better mechanical properties along with the light weight advantage [1–5]. Another option is to use the combination of these methods with each other for further improvement in the design of advanced materials and production techniques.

The combination of severe plastic deformation (SPD) and aging is one of the candidate methods since both of them yields to better mechanical properties through different strengthening mechanisms. In severe plastic deformation the main principle is to accumulate strain in the structure using simple but effective techniques resulting in the saturation of dislocations. Among SPD techniques, equal channel angular pressing (ECAP) is very promising. It works by pressing the specimen through a die that has two channels of same size connected at an angle ideally 90°-120°. The passage causes pure shear leading to high amount of strains up to 1 at a single pass. The deformed part maintains its thickness and multiple passes without thickness reduction could be achieved.

Aging or precipitation hardening, on the other hand, results from the nano sized precipitate particles dispersed in the microstructure. The phenomenon of precipitation hardening has been discovered on Al-Cu alloys (2XXX Al alloys) in the beginning of 20th century. The existence of these nano particles, known as Guinier-Preston (GP) zones, is one of the most important discovery regarding to phase transformation phenomenon in metallurgical engineering and it has been commercialized since then. The strengthening effect due to precipitates is as high as 50% in certain alloys like Al 2024 and the complicated structure of precipitates and the precipitation sequence is still a matter of discussion [6–13]. An optimum combination of these two technqiues, i. e. ECAP and age hardening was previously investigated by our group. The kinetics of the precipitation was found to increase as much as 12 times with a considerable hardness increment.

The primary aim of the thesis is to understand the effect of single pass ECAP on precipitation of Al 2024 in terms of kinetics, precipitate morphology, size and distribution as well as the change in homogeneity of the structure without loss of mechanical properties during precipitation.

Secondly, the study aims to investigate the thermal stability of the improved Al 2024 through ECAP and aging in terms of time and temperature limits. The annealing response of ECAPed Al 2024, which is very important due to the increased kinetics, is aimed to be understood in order to determine upper limits of time and temperature for emerging application of the alloy.

Chapter 2 involes brief summary of related literature. In Chapter 3, preliminary studies on the general comparison of ECAPed and standard Al 2024 sample was discussed in terms of microstructures and aging kinetics at 190°C. The results of this part lay a foundation of Chapter 4 in which detailed investigation of hardness variations throughout the ECAPed sample during precipitation was monitored. The homogenization of the microstructure accompanied with improved hardness was mapped via micro hardness measurements which is one of the major novelties of the study. The reasoning behind increased kinetics was found to be the ease of

2

nucleation as well as diffusion via high dislocation density. The precipitate size as well as the time of peak aging was found to be 12 times lower than the standard sample. The possible causes of hardness variation in different samples were also investigated.

In Chapter 5, annealing experiments up to 1000 hours in the temperature range of 80-200°C were carried out and a thorough thermal stability measurement which was previously limited to DSC and 0.5-2 hours annealing experiments were carried out for the first time in a severely deformed metal. The annealing behavior of the complicated structure of ECAPed Al 2024 was revealed during the exposure to 150°C using transmission electron microscopy (TEM) and electron back-scatter diffraction (EBSD) techniques. 120°C was found to be a safe upper limit for ECAPed Al 2024 while 150 °C was detected as a transition temperature in terms of thermal stability. The fast reduction in hardness at 200°C showed that it is impossible to use the alloy above 190°C due to rapid recrystallization rates. The study also shows the importance of long time thermal stability experiments in the presence of severe deformation due to increased recrystallization rate.

CHAPTER 2

LITERATURE REVIEW

2.1.   ALUMINUM AND ALUMINUM ALLOYS

Aluminum is the second most abundant metallic element on earth followed by silicon yet unlike copper and iron it could not be extracted from its ore cheap enough for commercialization until 1886 when Charles Hall (Ohio) and Paul Heroult (Paris) discovered electrolytic reduction of alumina in molten cryolite (Na_3AlF_6) [1, 2]. Contrasting its late discovery, the development of aluminum industry was fairly fast. Within a few decades after Orville and Wilbur Wright invented the first successful airplane in 1903 [1], aluminum was a partner of the air force industry with engines, airframes, fuel cells, satellite components, missile bodies that are light, strong and fracture resistant [1]. Till then the growing use of aluminum has spread through modern life in kitchens, houses, cars, phones, computers and more whenever light and enduring materials are required. Today, being the second most consumed metal following iron, nearly 70% of the aluminum used is primary aluminum, directly extracted from its ore, while only 30% is recycled showing the increasing demand for long term applications [14].

It was stated that [15] aluminum has been an aerospace material for over 100 years and with the help of new innovations, it will remain to be so. Aluminum and its alloys, the backbone of aerospace industry, used in various fields of life, have such a large range of properties that it is impossible to generalize them as soft or hard, as weldable or problematic to weld. Aluminum alloys involve 7xxx series with a tensile strength of 700 MPa as well as 1xxx series of just 70 MPa both of which has its own place in the market. They have opportunities beyond limit with vast

5

possibilities of modifications through alloying and thermo-mechanical treatments. Therefore it is vital to see this range before going any further [14].

There are basically two categories of aluminum alloys wrought and cast. Wrought alloys are composed of mechanically processed products such as drawn, cold or hot rolled, forged and extruded. Cast alloys are used directly after casting [2–4, 14, 16]. In Table 2.1 the designation system according to European norms which is very similar to American norms is given. 1XXX aluminum alloys are at least 99.00% pure and further purity is expressed in the last two digits of the alloy such that 1050 indicates 99.50% pure Al alloy. Generally in Al alloys, Fe and Si are primary impurity elements which may result in cracks [1, 4, 14, 15, 17]. For all alloys the first digit shows the major alloying element or elements. Considering the subject of the study, cast alloys will be kept out of the review. In wrought alloys, the second digit of the designation may vary between 1 and 9 pointing to the special control of one or more impurity elements. For example 1140 indicates the special control of Fe and Si. For the series 2XXX to 8XXX, the last two digits do not have a special indication but the second digit represents the modifications in the original one, zero indicating the original alloy. Wrought alloys are mainly divided into two; heat treatable and non-heat treatable as shown in Table 2.1. Heat treatable alloys are precipitation hardenable alloys which include Al-Cu (2XXX), Al-Mg-Si (6XXX), Al-Zn (7XXX), Al-X (Li, etc., 8XXX) series [14].

1XXX Aluminum alloys are soft, ductile and corrosion resistant, high purity aluminum group with at least 99.00%. They are not structural alloys but since they contain some Fe and Si impurities, by the help of rolling, useful strength values for certain applications like vehicle panels may be obtained. Due to its outstanding corrosion resistance and ductility, foils for food and packaging, cans for beverages are produced from 1XXX Al. This group also includes chemical industry products [1, 3, 14, 18].

Table 2.1. Designation System for Al Alloys [14].

Aluminium Alloy Designation System (Comité Europeén de Normalisation)		Major alloying elements	Atoms in solution	Work Hardening	Precipitation Hardening	
WROUGHT ALLOYS (EN AW- European Normative Aluminium Wrought)	1XXX	None (min 99.00 %Al)	-	X	-	Non-heat treatable alloys
	3XXX	Mn	X	X	-	
	4XXX	Si	X	X	-	
	5XXX	Mg	X	X	-	
	2XXX	Cu	X	(X)	X	Heat treatable alloys
	6XXX	Mg+Si	X	(X)	X	
	7XXX	Zn	X	(X)	X	
	8XXX	Other	X	(X)	X	
CASTING ALLOYS* EN AB- EN AC- EN AM-	1XXX0	None (in 99.00% Al)				
	2XXX0	Cu				
	4XXX0	Si				
	5XXX0	Mg				
	7XXX0	Zn				
	8XXX0	Sn				
	9XXX0	Master Alloys				

* A = Aluminium
B = Ingot
C = Cast Alloy
M = Master Alloy

Owing to even 1% addition of manganese, <u>3XXX Aluminum alloys</u> have more than 10% higher strength in comparison to 1200 Al preserving the corrosion resistance. The non-heat treatable 3XXX alloys are commonly used in roofing sheet, such as 3105 and 3103 used in vehicle panel production [14].

<u>4XXX Aluminum alloys</u> has the main addition of silicon to lower the melting point of the alloy. The low melting point relative to parent alloy makes them suitable for use as welding wire and brazing filler. Although 4XXX series are not heat-treatable themselves, during welding they can dissolve some of the alloying elements of the parent and can participate to heat treatment at a limited degree [1, 3, 14, 18].

In <u>5XXX Aluminum alloys</u>, major alloying element magnesium improves strength preserving the high corrosion resistance as a result of which they are preferred in marine, sea water applications. They have good weldability but the excess Mg addition beyond 3% may lower the stress corrosion resistance if tempering was not

done properly. With their superior properties they are commonly used in the production of chemical plants, pressure vessels, bulk road and rail vehicles as well as ship structures [1, 3, 18].

The term "heat treatable" mainly means through heating and cooling procedures the strength of the alloy may be changes. The change is possible due to a second phase which can precipitate out of a super saturated solid solution where the strength of the alloy increases due to various reasons like the coherent interface between the matrix and the precipitate until the precipitates become coarse and incoherent. Solutionizing on the other hand yields to a decrease in hardness and gives opportunity to easier forming and shaping. It is possible to reheat and harden the alloys after shaping which is another advantage of these alloys over the non-heat treatable ones [1, 14]. Table 2.2 summarizes some terms and designations used for heat treatment and deformation.

Heat treatable aluminum alloys are 2XXX, 6XXX, 7XXX and 8XXX series. The last three will be explained first followed by a wider literature review on 2XXX series alloys.

6XXX Aluminum alloys have major alloying elements, Si and Mg forming $MgSi_2$ (magnesium silicide), yield to moderate strength levels. High formability and machinability combined with good weldability and corrosion resistance make them good candidate for building structures, sea and land transportation industry as well as welded structures. It is possible to form at solutionized state and then heat treat them for precipitation hardening where full T6 properties can be achieved [14].

Table 2.2. Heat treatments commercially used in Al alloys and certain designations used in Al alloys terminology [4]**.**

System for Heat Treatable Alloys	
T1	Cooled from an elevated temperature shaping process and naturally aged to a substantially stable condition (not cold-worked after an elevated temperature shaping)
T2	Cooled from an elevated temperature shaping process + cold worked+naturally aged to a substantially stable condition
T3	Solution heat treated+cold worked+ naturally aged to a stable condition
T4	Solution heat treated+naturally aged to a stable condition
T5	Cooled from an elevated temperature shaping process + artificially aged (also products that are not cold worked after elevated temperature shaping process such as casting or extrusion)
T6	Solution heat treated + artificially aged (for products that are not cold worked after heat treatment)
T7	Solution heat treatment + overaged stabilized (Precipitation heat treatment beyond max strength to provide some special properties like enhanced resistance to stress-corrosion cracking or exfoliation corrosion)
T8	Solution heat treated+cold worked+ artificially aged
T9	Solution heat treated+ artificially aged+ cold worked
T10	Cooled from an elevated temperature shaping process + cold worked+ artificially aged

Heat Treatment Designation	
F	as fabricated
O	Annealed
H	Strain hardened
W	Solution Heat treated (Unstable temper)
T	Stable temper

H (Strain Hardened) Temper Designations			
HXY	X: secondary treatment Y:degree of deformation	HX2	¼ Hard
H1	Strain hardened only	HX4	½ Hard
H2	Strain hardened and partially annealed	HX6	¾ Hard
H3	Strain hardened and stabilized by low T treatment	HX8	Fully Hard (75% higher YS)
		HX9	Extra Hard

7XXX Aluminum alloys are aluminium-zinc-magnesium alloys with or without some copper addition. They show the highest strength among Al alloys. One of the typical and common 7XXX series alloy is designated as 7075 with 5.0-6.0% Zn, 2.0-3.0%Mg and 1.0-2.0% Cu with a tensile strength of 580 MPa and ~150HB (~184 HV) of hardness. Although they have the best mechanical properties and are

used mainly in military applications, their fabrication is difficult and requires high technology. They are more expensive than other heat treatable alloys besides they may have low stress corrosion resistance [14].

Actually <u>8XXX Aluminum alloys</u> consists of all alloys other than (1-7)XXX alloys. For special applications some alloys of Al with different alloying elements like Li are produced. These special productions are categorized under the designation of 8XXX [14]. Li is one of the four elements that is highly soluble (more than 10 at. wt%) in Al, the other three being Zn, Ag and Mg. To summarize 8XXX designation is used to identify some new alloys designed especially to lower weight and increase specific strength [19].

<u>2XXX Series Al Alloys</u>

2XXX series Al alloys with considerable amount of Cu and Cu-Mg alloys are the second strongest among all Al alloys following 7XXX series. They are heat treatable and the oldest series of all age hardenable alloys. Actually the phenomenon of age hardening was discovered in 1906 by a researcher, Alfred Wilm, in 1906. This was the beginning of precipitation hardening phenomenon and the alloy named as Duralumin, or 2017, with a composition, 4% copper, 1% magnesium and 0.5-1% manganese. It is still a popular age hardenable alloy used in aircraft, machine construction, military equipment and rivets. This very first age-hardenable alloy opened the doors for further improvements yielding to 2X24 alloys which have higher strength compared to 2014, 2017 and 2030 [14], [20]. The main application fields of 2xxx series Al alloys are aircraft and truck body components due to good damage tolerance, high toughness and strength. Some of these applications are fuselage skin, lower wing surfaces (aircraft structures), skin sheet; truck wheels, screw machine products [4, 5, 17]. 2X24, where X represents a modification or special control of Si and Fe, is an easy to produce alloy when compared to 7XXX alloy. The general compositions and properties of Al 2x24 are tabulated in Table X. Generally they are not easy to cold deform and weld, usually used with anodic

protection. They have good fatigue properties and when the Si and Fe amount is controlled they have good fracture toughness [1].

Table 2.3. Temper designations and corresponding mechanical properties of Al 2024 [15, 17]**.**

Temper	Form	Yield (0.2) (MPa)	UTS (MPa)	Shear (MPa)	Elongation (A50) %	Hardness HB	Hardness HV
O	Sheet	75	185	125	20	55	60
T3	Unspecif.	340	475	290	18	120	125
T4	Extr. Tube	330	460	285	20	120	125
T8	Unspecif.	450	485	300	6	130	140

Table 2.4. Standard Compositions of 2X24 Alloys [1]

Alloy Desig.	Si (%)	Fe (%)	Cu (%)	Mn (%)	Mg (%)	Cr (%)	Zn (%)	Ti (%)	Unspec Each (%)	Unspec. Total (%)
2024	**0.50**	**0.50**	3.8-4.9	0.30-0.9	1.2-1.8	0.10	0.25	0.15	0.05	0.15
2124	**0.20**	**0.30**	3.8-4.9	0.30-0.9	1.2-1.8	0.10	0.25	0.15	0.05	0.15
2224	**0.12**	**0.15**	3.8-4.4	0.30-0.9	1.2-1.8	-	-	--	-	-

2.1.1. Effect of Alloying Elements

2.1.1.1. Effect of Copper

Addition of Cu to aluminum results in a binary phase diagram as shown in Figure 2.1. The high solubility at high temperatures and the low solubility at room temperature as well as the presence of the Al_2Cu phase in the diagram yields to the age-hardenability of the alloy. However, Al-Cu alloys, though their nature has been

studied by many researchers [21–27], are not commonly used commercial alloys in the binary form. The maximum strengthening effect of Cu on Al is observed when it is in the range of 4-6 wt% depending on the accompanying alloying elements, constituents. The aging leads to strengthening however it causes loss of elongation, too [28].
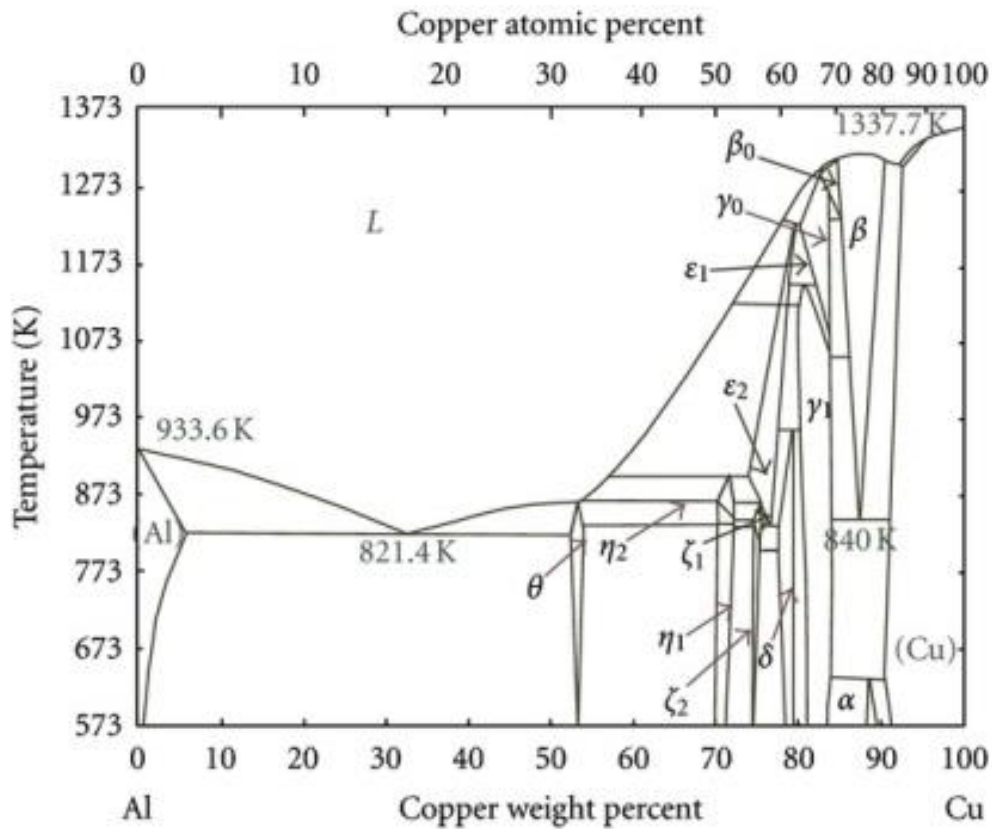
Figure 2.1 Al-Cu phase diagram [1].

2.1.1.2. Effect of Magnesium

The major effect of Mg addition to particularly Al and Al-Cu alloys is the increase in the strengthening in the as-quenched condition. Age hardening at room temperature further increases the strength of the alloy while ductility is preserved.

Artificial aging enhances yield strength one step further at the expense of a lower tensile elongation. Maximum strengthening with Mg addition can be obtained by artificial aging after cold deformation. In naturally aged alloys the reverse is applicable, i.e. the benefit of Mg may decrease. The effect on corrosive behavior depends on the heat treatment and product type [28].

2.1.1.3. Copper-Magnesium and Manganese

The Al-Cu-Mg-Mn alloys are commercial high strength aluminum alloys because Mg and Mn addition results in an increase in tensile strength. Up to 0.5% Mn, the yield strength also increases but leads to a loss in ductility. As a result, commercial alloys do not contain more than 1% Mn in their constitution [4, 17, 28].

2.1.1.4. Copper-Magnesium and Iron

While in cast aluminum alloys the iron content is beneficial for dimensional stability, in wrought alloys it has the potential to decrease tensile strength in heat treated condition even with concentrations of 0.5%. There is also a connection between Si and Fe for property control because Si has the ability to tie up excess Fe in the form of αFeSi constituent. The low Si accompanied by high Fe may otherwise be detrimental because the excess iron forms Cu_2FeAl_7 leading to a reduction in Cu content needed for precipitation of $AlCu_2Mg$ or $AlCu_2$ [4, 17, 28].

Silicon, after tying up excess iron, may itself form Mg_2Si precipitates contributing to the precipitation hardening process. As a result it may be concluded that iron content should be either controlled by Si or should be low enough. On the other hand there is a connection between fracture toughness and Fe+Si content as mentioned in Wang et. al [5] which is represented in Figure 2.2 showing that K_{IC} decreases with increasing (Fe+Si) content.
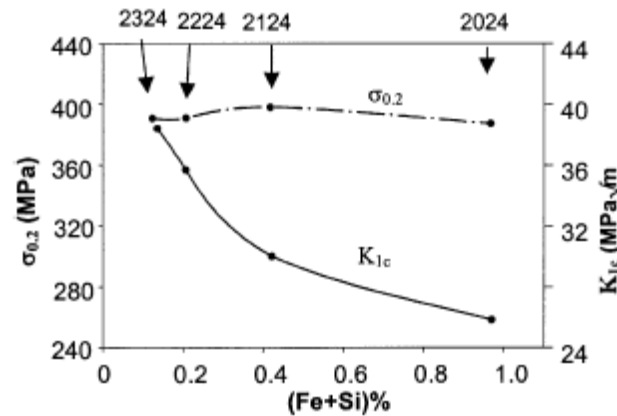
Figure 2.2. Effect of (Fe+Si) impurity on fracture toughness and strength in 2X24 alloys [5]**.**

2.1.1.5. Effect of Zinc/ Titanium/Chromium

Zinc is a strength increasing alloying element especially in presence of other alloying elements. Generally it does not have a negative effect. Titanium helps refinement of the cast alloys and also improves weldability of the alloy. Cr is commonly added to some Al-Mg, Al-Mg-Si and Al-Mg-Zn alloys up to 0.35 %. Excess Cr may result in highly coarse constituents when combined with Mn, Fe and Ti [1, 4, 17].

2.1.2. Al 2x24 Alloys

In 2x24 series Al alloys, T3, T4, T6, T8 heat treatments are commonly used. The main application fields of 2xxx series Al alloys are aircraft and truck body components due to good damage tolerance, high toughness and strength. Some of these applications are fuselage skin, lower wing surfaces (aircraft structures), skin sheet; truck wheels, screw machine products [4, 5, 17].

The exact microstructural constituents in Al 2024 could not yet be clarified because the precipitation sequence of Al 2024 still has mysteries in it. There are various ideas about the phases and phase transitions during precipitation hardening [5, 16,

14

29–40]. As a result it will be most convenient to consider, as much as possible, every possible phase mentioned in literature as a probable candidate to be observed in the current study. Starting from the most obvious to the least clear ones, the features that have been identified in Al 2024 will be discussed.

One of the well-known groups working on Al-Cu-Mg alloys is Starink et. al. with numerous studies [5, 16, 31, 32, 40]. In one of their work, they categorized the secondary phases under three captions; constituent particles, dispersoids and precipitates depending on their functions and temperature ranges for formation [5].

2.1.2.1. *Constituent Particles*

The phases formed upon solidification by eutectic reaction are referred to as constituent particles. They may transform by further heat treatments into dispersoids or disappear during homogenization. It is possible for them to be significantly coarse particles up to several tens of micrometers. Faster solidification and deformation with or without heat treatment decrease the size of particles but as Fe and Si impurity content increases the particle size increases too. Constituent particles are classified as soluble and insoluble by heat treatment [3, 5] The insoluble phases like $Al_{12}Fe_3Si$ and Al_7Cu_2Fe are results of Fe/Si impurities and they are mentioned to be detrimental to the structure acting as crack initiation sources. Both corrosion resistance and crack growth rate are affected by them negatively. The soluble phases like Mg_2Si, $CuAl_2$, Al_2CuMg, are solidification products with no harmful effects. Al_2CuMg and $Cu Al2$ are S and θ phases, respectively, that may form as precipitates into the matrix after proper solutionizing and quenching. In Table 2.5 various phases that have been reported in literature are listed with their corresponding crystal structures and lattice parameters [5].

Table 2.5. Constituent Phases in Al 2024 [5]

Phase	Structure	Lattice Parameter, nm
$Al_{12}(Fe,Mn)_3Si$ $Al_{12}Fe_3Si$	$Im\overline{3}$	a = 1.23
Al_7Cu_2Fe $Al_6(Cu, Fe)$	P3/mnc	a = 0.6336, c = 1.487
Mg_2Si (β)	$Fm\overline{3}m$	a = 0.6351
Al_2Cu (θ)	I4/mcm	a = 0.6066, c = 0.4874
Al_2CuMg (S)	Cmcm	a = 0.401, b = 0.923, c = 0.714

2.1.2.2. Dispersoid Particles

They are the products of long term heat treatment which is specified as homogenization. Dispersoids are the phases formed when Al combines with the transition metals, Cr, Mn, Zr to form intermetallics with little or no solubility in the Al matrix due to their slow diffusivity. They form very small precipitates which are less than 1 micron during either solidification or ingot preheating. They delay or even prevent static recrystallization during processing of the alloy like thermomechanical treatments at relatively high temperatures [41]. Especially in structural applications, during ingot homogenization, phases that contain Zr, Mn, Cr, Sc are intentionally allowed to be formed [5].

Dispersoids are not always advantageous because microviods may nucleate due to decohesion at the interface between the dispersoid and the matrix which may further grow into void sheets. Their size, coherency as well as the spacing between each other are important parameters. Closely spaced intermetallics are more effective to retard recrystallization and as expected coherent precipitates such as Al_3Zr are more effective than incoherent ones like $Al_{20}Mn_3Cr_2$, $Al_{12}Mg_2Cr$ [5].

They are said to form during long term heat treatments by solid-solid reaction, as an aid to control grain size and recrystallization with a size range of 0.2-0.5 microns.

By the diffusion of elements such as Mn into the constituent phases such as $Al_{12}Fe_3Si$, dispersoids like $Al_{12}(Fe,Mn)_3Si$ may form [41].

In Al 2024, the main dispersoid is $Al_{20}Cu_2Mn_3$ which is usually named as T-phase dispersoid with a growth direction of <010> in Al. The XRD investigations have shown that they hav an orthorhombic structure with lattice parameters of a=2.42nm, b=1.25nm, c=0.775nm. Howeer, the space group of T-phase dispersoid is not clear and possibilities are Bbmm, Bbm2 or Bb2mb. Dispersoids may contain twins [5].

2.1.2.3. S Precipitates

S precipitate, Al_2CuMg (orthorhombic) is one of the stable second phase particles the others being, $Al_7Cu_3Mg_6$ (cubic, Q), $(Al_xCu_{(1-x)})_{49}Mg_{32}$ (0.76 < x < 0.91) (cubic, T), and $Al_5Cu_6Mg_2$ (Mg_2Zn_{11}-type cubic, V) in Al-Cu-Mg alloys [34].

The addition of Mg to the alloy leads to the formation of S phase rather than or accompanied to the Ɵ which is commonly known precipitate of Al-Cu alloys. Unlike Ɵ, S phase can be considered as a newly investigated precipitate since the debates on its structure as well as the precipitation sequence still continues [5, 6, 13, 16, 30, 42–46].

Basically there are four suggested structures for S phase [5, 42, 47, 48] three of which is summarized in Figure 2.3. Although the proposed models are relatively old the discussion is reconsidered in a recent study in 2011 [6] claiming the Perlitz & Westgren (PW) model as the most appropriate one when first principle calculations were also included. PW model suggests that Al_2CuMg is an orthorhombic structure with Cmcm space group and lattice parameters as 0.400, 0.923 and 0.714 nm for a, b and c, respectively. Mondolfo model was proposed as a modified PW model with P1 space group and shifted Cu-Mg atomic layers. In the Radmilovic Kilaos (RK) model, the difference is the switched atom positions of Cu and Mg. This model was rejected because depending on the first principle calculations by Wolverton [49]. The formation enthalpy of RK model was found as 16.4 kJ $mol^{-1}atom^{-1}$ while the

value of PW model was calculated as -19.4 kJ mol^{-1}atom^{-1}. On the other hand when PW and Mondolfo were considered, both of the PW and Mondolfo were reported to be supported by XRD experiments [42].
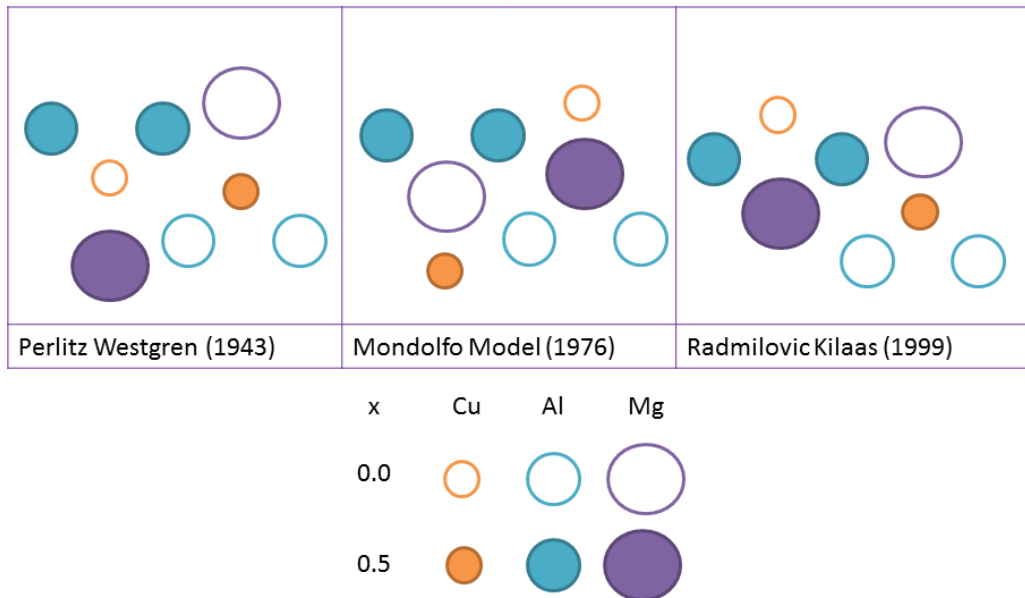
Figure 2.3. The proposed structures of S phase. [42]

Various arguments were considered in the study [42] regarding the probable misinterpretations of the S phase structure. On the subject of diffraction patterns and XRD, weak diffraction of the precipitate when compared to the strong matrix was regarded to be the cause of difficulties in differentiating the overlapped peaks and spots. In HRTEM results, image simulations were regarded to be a necessity for accuracy. The first principle calculations of the precipitates in Al matrix that include the strain and interfacial energy considerations were stated to be important for the accurate results. Results of the study [42] confirm the PW model to be the only possible one.

In the study by Wang and Starink, 2005, [5] three models for S phase were also mentioned but the third being Jin model proposed in 1990 rather than RK because it was considered as a modified version of PW which was rejected as in the case of RK model due to first principle calculations. This study on the variants of S phase also indicates that PW model is correct [5, 6].

The S phase was said to be unshearable and its strengthening effect was attributed to the Orowon bowing mechanism working on small S precipitates so there are no sliced precipitates to observe in a structure including S precipitates [6]. However, the size of the precipitate was reported to be important for strengthening. Same study mentions that the type of nucleation whether homogeneous or heterogeneous had a major effect on the strengthening behavior of these particles.

2.1.2.4. GPB Zones structure

As many arguments as the S phase has been done on the existence, hardening effect and the nature of GPB zones [6, 29, 30, 46, 50–53]. The detection of GPB zones could not have been possible in diffraction patterns in the form of strikes as it was for GP zones until recently [6] as seen in Figure 2.4 because they could only be observed in the DSC data that gives a peak near the short range order zone as well as dissolution effect was observed in DSC results indicating a metastable phase formation. However, there is a disagreement on the time of appearance in the literature also. Some relatively older studies claim the initial rapid hardening to be due to GPB zones while new studies attribute this rapid increment to the co-clusters.
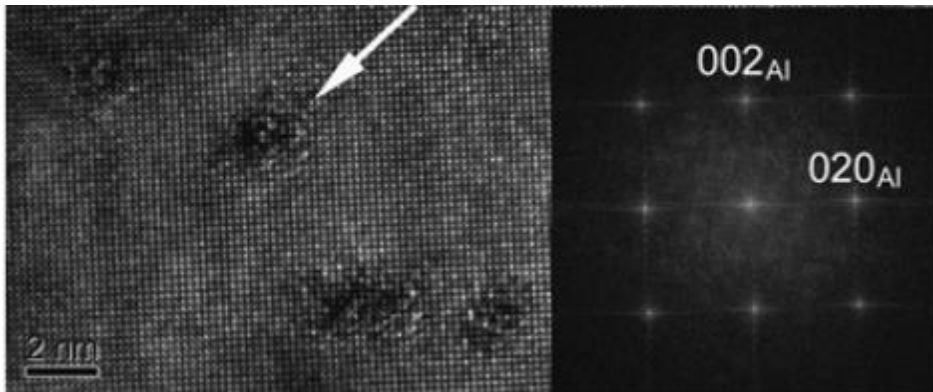
Figure 2.4. Al-Cu-Mg alloy after aging at 195C for 9 hours. GPB zones were detected through FFT of HRTEM. Adopted from [6]**.**

2.2.   STRENGTHENING MECHANISMS

Strength is the response of a material to external loads in terms of internal forces and deformation [54]. When tension test is considered, the resistance to permanent deformation may be attributed to yield strength and the load limit above which a material fails may be regarded as ultimate tensile strength. Hardness is another term which is defined as the measure of ease with which a solid body plastically deforms [55]. When strength is considered, regardless of the term to be used, perfect crystals free of defects have the highest potential for high strength but thermodynamically and practically it is not possible to use perfect crystals in daily life. Crystalline materials include defects of various forms such as vacancies, dislocations and surface. These imperfections yet are very helpful since they make it possible to have properties such as ductility, formability, toughness and hardenability. Even ductile failure, rather than brittle, of a metal after certain plastic deformation is due to movement of line defects, i. e. dislocations. Likewise, strengthening of an alloy or metal is possible only when the motion of dislocations is hindered. There are various ways to immobilize dislocations and hence strengthen metals and alloys but the key to all strengthening phenomenon remains the same; stopping dislocation motion. Basically strengthening can be cultivated in five major ways. If an analogy

20

is to be made, dislocations moving through the material are just like cars travelling. There are five major ways to slow down or even to stop the cars:

- Fencing as smaller regions as possible (Grain boundary strengthening)
- Introducing curves, bends and even some roughness on the road (Solute solution hardening)
- Increasing the number of cars and causing traffic jam (Work or strain hardening)
- Modifing the road by introducing small stones into the road (Precipitation hardening)
- Introducing big rocks on the road (Dispersion hardening)

2.2.1. Solid Solution Strengthening

Solid solution is the dissolution of one element into another in solid state. The solute atoms may be located in between atoms, at interstitial sites, or may replace solvent atoms, at substitution sites. The sizes of atoms and crystal structure of the solvent are the most critical parameters. Small atoms like C, N may easily occupy interstitial sites of an FCC Fe easily while it is harder if not impossible for them to dissolve in a bcc Fe. The same thing applies to substitution of small atoms by large atoms. There needs to be a correlation of atomic sizes for proper dissolution. The solubility limit of an element in another is mainly determined by the difference in atomic sizes and stable crystal structures. As in the case of Cu and Ni which are fully soluble in one another, the atom sizes only differ 3% and they both exist in the FCC structure [56–58]

The atoms of the alloying element located at various atomic positions of the alloy cause strain fields around themselves. These fields interact with the fields of dislocations. The interaction may result in hindering or slowing down the dislocation. The type of dislocation as well as the symmetry of the stress field of the

solute atom is very important on determining the degree of hindrance. The misfit is proportional to da/dc where a is lattice parameter and c is solute concentration [14].

Edge dislocations have two components in their fields both hydrostatic (volume change) and deviatoric stress fields (distortional, shape change, shear). On the other hand screw dislocations have only distortional component. When the defects are symmetrical the interaction of solute and dislocation is limited to edge dislocation's hydrostatic component. In the case of asymmetry both screw and edge dislocations are affected by the stress field of the [54, 57] a result the effect of asymmetric solute dissolution is higher than the symmetric. The Table 2.6 shows the various types of alloys and solute atom combinations with their corresponding contribution to hardness. In Table 2.6, the types of defects in various materials with their corresponding hardening contribution are given.

Table 2.6. Type of solutes and their contribution to the hardening of the material [57]**.**

Material	Defect	Hardening Effect $d\tau/dc$ as $f(G)$
Symmetrical Defects		
Al	Substitutional atom	G/10
Cu	Substitutional atom	G/20
Fe	Substitutional atom	G/16
Ni	Interstitial carbon	G/10
Nb	Substitutional atom	G/10
NaCl	Monovalent substitutional ion	G/100
Nonsymmetrical Defects		
Al	Vacancy Disk (quenched)	2G
Cu	Interstitial Cu (irradiation)	9G
Fe	Interstitial carbon	5G
LiF	Inters. fluorine(irradiation)	5G
NaCl	Divalent substitutional ion	2G

Another effect of the alloying element is the change in the local elastic modulus as a function of solute content. It is also important to note that the interactions may

sometimes be temperature dependent and an alloying element may result in an increase in strength at low temperatures while a decrease can be observed at high temperatures.

2.2.2. Dispersion Hardening

Al alloys may also be enhanced by means of insoluble fine particles which act as a barrier to dislocation motion. There are two common possibilities to obtain dispersoids. One is by alloying additions that form stable, insoluble dispersoids as in the case of T-phase dispersoids. They usually form by a solid state reaction during long term heat treatment to be used as grain size and recrystallization controller. They also increase thermal stability during thermo-mechanical heat treatments. Especially in structural applications phases containing Zr, Cr, Mn, and Sc are intentionally allowed to be formed during ingot homogenization. Second option is using oxide, carbide powders with high strength like Al_2O_3 and mixing them with matrix alloy forming a compact to be sintered [56–58].

2.2.3. Work Hardening

It is one of the oldest methods of strengthening metals dating back to Bronze Age [57]. When work is applied to a metal; it strengthens owing to the increase in number of dislocations. It can be applied to any metal with a reasonable ductility. It has the advantage of shaping as well as strengthening by a single process while producing wires or sheets for example. In the fabrication of Al products, processes applied such as extruding, drawing, rolling, bending, etc. exerts force on the system, doing work on the system. When the temperature is above T_{rec} ($T_m/2$) hot work is done and there is no strengthening effect [14]. In the case of "cold work" when the process is carried out below T_{rec}, the dense dislocations causes traffic jam and further dislocation movement is hindered [14]. For pure Al and non-heat treatable Al-Mg alloys work hardening is the only way to strengthen as it is for all non-heat treatable wrought alloys. For heat treatable alloys, before or after heat treatment, cold work leads to further strengthening [56].

Figure 2.5.a shows the variation of strength with dislocation density. It is interesting that when dislocation density is very low and very high the strength is highest while moderate dislocation density yields to the lowest strength.
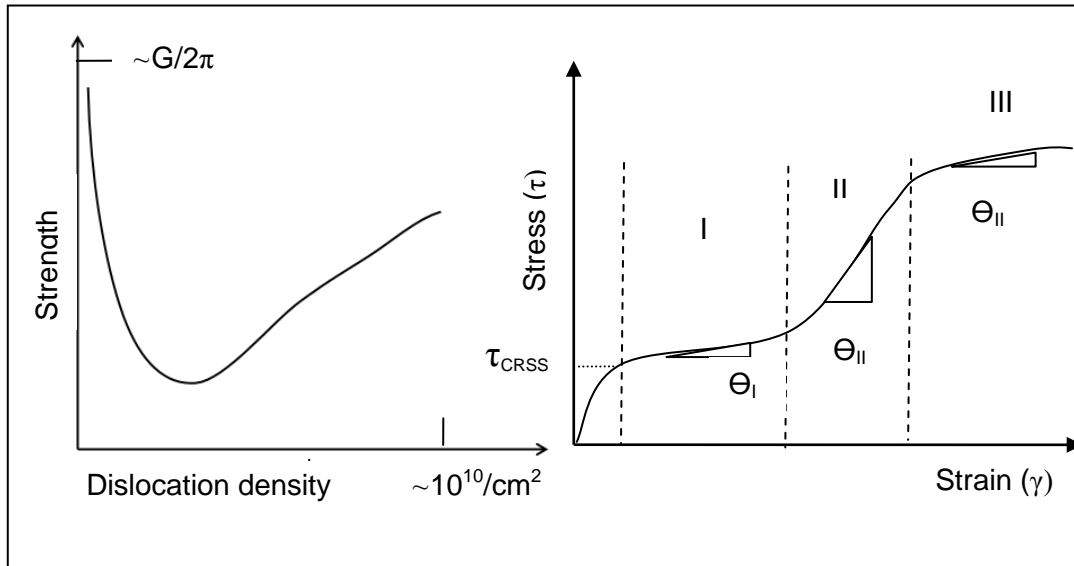
Figure 2.5. (a) The variation of strength in relation to dislocation density and (b) Stress strain curve for a single crystal during work hardening [57]**.**

In understanding the strain hardening phenomenon, the best approach is to investigate single crystals for simplicity. In Figure 2.5.b stress strain variation for a single crystal is shown. Apart from the initial elastic region there are three stages commonly observed in all single crystals during deformation. The initial stage is easy glide region where the dislocations are not interacting with each other but heterogeneously distributed as stain rate is low. The second stage initiates when there are enough dislocations to be distributed homogeneously throughout the crystal. The second stage involves the cell structure formation surrounded by dislocation clusters with low dislocation density inside. The behavior of the material was stated to be dependent on the stacking fault energy (SFE). When SFE is high, the dissociation of dislocations into partials, which are sessile dislocations, is hard

and hence they can glide and gather around the cells as it is seen for Al. Whereas for low SFE alloys, the substructure is formed as planar dislocation arrays rather than cells as it is for Cu-7%Al alloy. Both of these structures were found to increase the strain rate [57].

For further deformation there is a certain amount of τ stress required to activate a Frank-Read source in relation to the mean free dislocation length l where τ is proportional to Gb/l, dislocation density $\rho=1/l^2$ leading to an incremental shear stress of $\Delta\tau$ to overcome dislocation barrier where $\Delta\tau$ is proportional to Gb$\sqrt{\rho}$ [56].

Kuhlmann-Wilsdorf suggests that an increase in flow stress due to decreasing cell size results in the linear hardening during the second stage. Although the characteristic of the structure remains the scale varies. Further deformation leads the diminishing of the number of free dislocations within the cells. When the movement of glide dislocations begin to be relatively easy from one wall to another interactions between dislocations subside. A saturation point for the cell size decrease was said to be reached stabilizing the cell size with further deformation. The structure reaches to the third stage at this point and strain hardening rate drops. For high SFE metals stage three could be reached at a lower stress. There are different theories on the mechanism both leading to the same conclusion that high SFE lowers the shear stress in stage three, τ_{III} [54, 56, 57]

It is also important to relate the single crystal theory and polycrystalline behavior but since in poly crystals multi-slip mechanisms operate simultaneously it is difficult. It is stated that third stage is commonly observed in polycrystals while the correlation was made by the following equation:

$$\frac{d\sigma}{d\epsilon} = \overline{M}^2 * \frac{d\tau}{d\gamma}\pi r^2 \qquad\qquad 2.1$$

where $\overline{M}$ is an orientation factor that is reciprocal of Schmid factor as a result of which for polycrystalline FCC metals, strain hardening rate is 9.5 times higher than that of a single crystal [56].

2.2.3.1. Cold Working of Aluminum

Al 2024 is a high-strength, age-hardenable Al-Cu-Mg alloy, and it is widely used in the aerospace and transport industries [1, 59]. Age-hardening is one of the well-known techniques used to improve the mechanical properties of this alloy by providing a nearly 50% hardness increment [60]. On the other hand, a relatively new approach is to combine cold working with age-hardening to attain further strengthening and homogenization of the structure [56]. The main disadvantage of cold working is the unwanted change in the size and shape of the material, which often causes stress related cracking. For example, in both sheet and rod production there is a deformation limit to preserve crack-free structures; as a result, multiple passes are obligatory to achieve remarkable strength [56].

2.2.3.2. Severe Plastic Deformation (SPD)

Severe plastic deformation is considered to be an effective grain refinement method to produce ultra-fine grained (UFG) structure which means in the range of 100-1000nm, ideally 100-200 nm. The basic requirements or the aims of the process of an effective SPD can be summarized as (i) UFG structure with high angle grain boundaries (HAGB), (ii) uniform nanostructure throughout the whole structure, (iii) crack and damage free samples [61]. SPD is a tool first suggested by Segal in 1981 for polycrystalline metals in order to improve mechanical properties. Its principle is introducing high amount of strain, and hence dislocations into the system so that a refinement of grains could be driven. Severe plastic deformation is also used to produce nanocrystals out of amorphous alloys as studied by Aronin et. al [62].

Apart from other cold working methods, the difference of severe deformation such as ECAP and HPT (represented in Figure 2.6) was stated to be due to non-monotony in deformation. Non-monotony, which is introduced by Smirnov-Aljajev in 1978, is a result of the presence of rate component of deformation tensor with a variation in sign. Simple shear was regarded to be strongly non-monotonic as well as ECAP and SPD processes. The strain was said to be linearly correlated to the degree of non-

monotony (DNM). DNM was regarded as a parameter to determine the degree of grain refinement, hence effectivity of deformation in regards to mechanical property increment. So to compare cold working with ECAP or any other SPD method, it is stated that due to the higher DNM, the evolution of UFG structure was sooner than monotonic deformations [63]. So a distinction between cold work and SPD can be made with this perspective even though the final induced strain values are the same.

Different SPD techniques were developed in order to increase the strain induced at a single passage as in a study by Nakashima et. al. in 2000. However, a highly complicated die did not yield to better strain and hardness than a regular ECAP die [64].
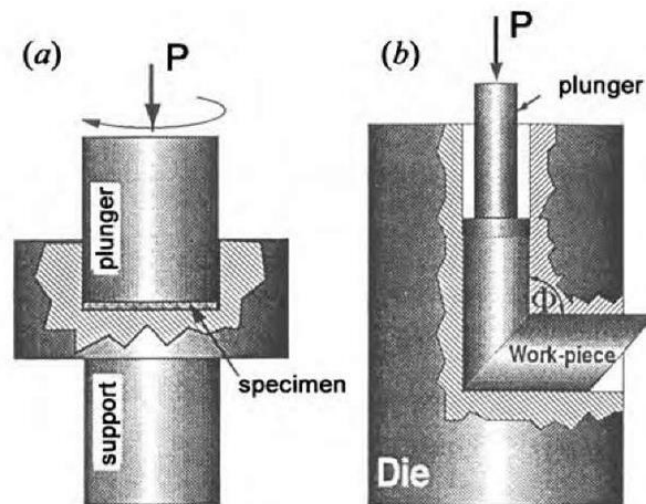
Figure 2.6. High pressure torsion and equal channel angular pressing schemes.
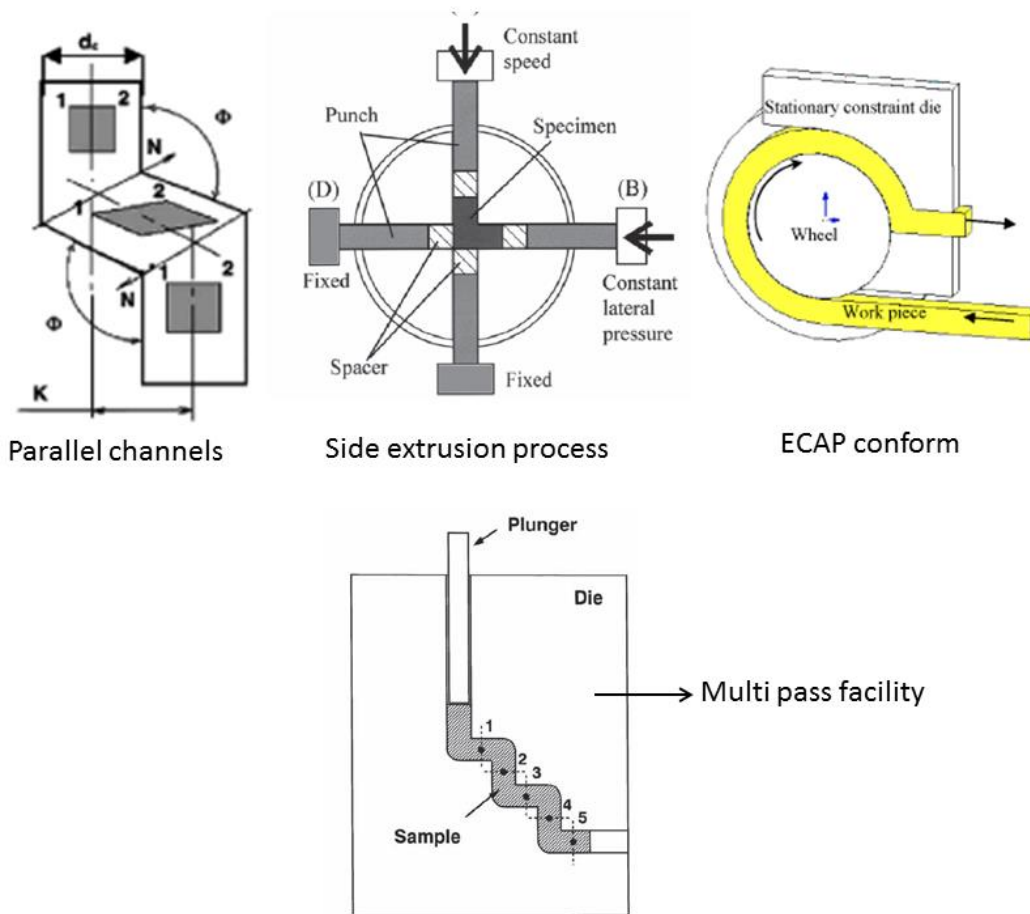
Figure 2.7. Different ECAP and SPD processes suggested. [64–66]

In general a certain limit on the refinement of a certain system at a specified temperature was pronounced. In HPT, this limit was mentioned to be 200 nm at room temperature for Ni, in the study by Bachmaier et. al [67]. However methods to overcome this limit was also considered as repeated HPT combined with cold rolling as well as using HPT applied powders to increase the strain and bypassing the limit of refinement in the same study on Ni.

The largest sample sizes reported using HPT is as high as 30x10 mm [67]. SPD is regarded as a nanotechnology production method likely to be commercialized more and more each year [68]. For commercialization of SPD, methods of continuous

ECAP and ECAP with parallel channel were proposed and experimented on CP Ti and Cu [65].

2.2.3.3. Equal Channel Angular Pressing

ECAP is defined to be a procedure to produce UFG structures through repetitive pressing by means of accumulated strains [69] and is regarded as the most well developed processing technique among SPDs [70]. The invention of equal channel angular extrusion goes back to 1972 but until the early 90's, when ultra-fine and nano-structured materials became highly popular, the method was not given enough attention. Though the concentration was on the grain refinement of the process, the main importance of the technique was stated as the attainment of simple shear [71].

The system is shown in Figure 2.8, the main principles are represented in Figure 2.9 in which different die corners were represented as well as the shearing behavior of a square section.
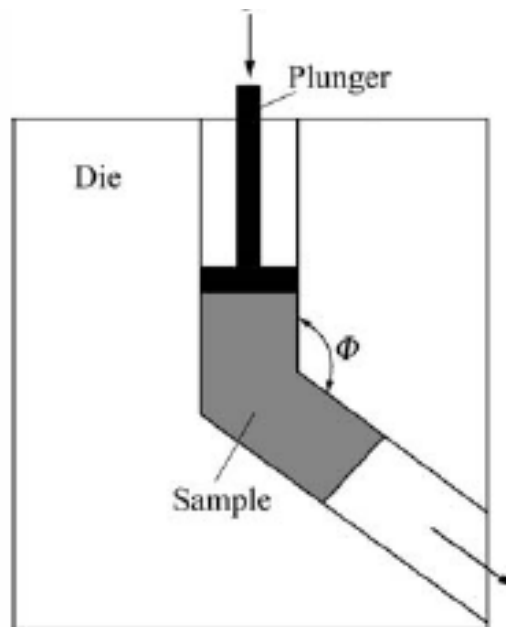
Figure 2.8. Representative ECAP process [72]
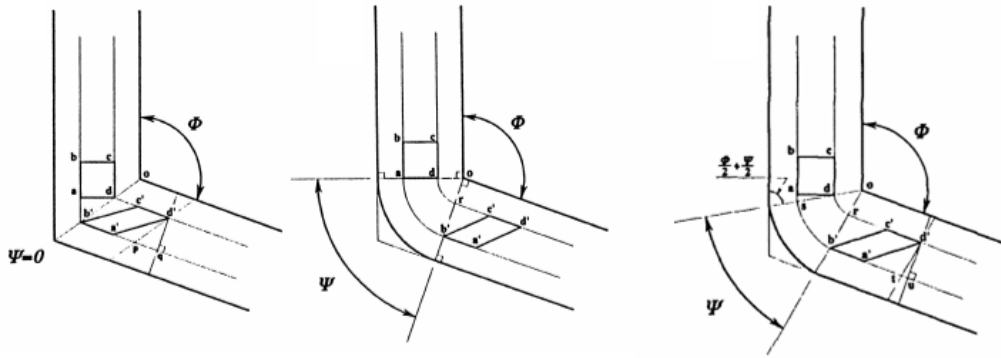
Figure 2.9. Principles of ECAP with different die corners [61]

The strain induced by ECAP is generally calculated by the equation 2.2,

$$\Delta \epsilon = \frac{2}{\sqrt{3}} \cot\left(\frac{\varphi}{2}\right) \qquad \qquad \textbf{2.2}$$

For φ=120° the strain is calculated as about 0.67 which is an average value. When engineering strain is to be calculated the equation 2.3 (ε is true stain and e is engineering strain) is used and the strain (e) is found as ~0.97. It can be concluded that the strain induced during ECAP through a 120° die corresponds to ~97% cold work. More accurate strain distributions are obtained through finite element analysis and calculations.

$$\epsilon = \ln(1 + e) \qquad \qquad \textbf{2.3}$$

ECAP is a process applied to various metals and alloys including magnesium, steel, zinc, titanium and aluminum with a variety of paths and temperature ranges [73, 74]. In a study carried out using Mg alloy, ZK60, two different temperatures were used during ECAP for homogeneous grain refinement down to 0.8 microns. The initial two passes was performed at 513 K while the following two passes at 453K [74]. Grain refinement of Mg was succeeded using multi-pass ECAP process, initially a bimodal grain size distribution was achieved but with further passes a homogeneous structure was achieved [75]. Another study of continuous processing

to produce steel sheets was performed by Saray et. al. By ECA extrusion of 1.2 mm thick and 200 mm wide steel sheets up to 8 passes with an improvement of 2.6 times of the original sample with high losses of ductility [76]. One of the advantages of ECAP process was stated to be the extremely high elongations and hence tensile ductility achieved resulting in the probability of superplastic forming. It was stated that superplastic sheets may be produced using ECAP prior to rolling [77].

In studies of ECAPed Al-Mg alloys, the fatigue properties were found to either improve or remain the same as cold rolled counterparts depending on initial structure and test conditions. Fatigue life of UFG titanium was found to increase considerably compared to the coarse grained counterparts. ECAP technology was stated to have further perspectives in fatigue performance enhancement [78].

Deformation mechanism of ECAP, a physical model of different colored tiny sand particles are observed during the flow through a transparent ECAP die. The flow lines were investigated and it was stated that a difference in the flow lines of inner and outer corner of the die existed. This difference was also stated to be the cause of the variation in the magnitude of shear strain imposed throughout the sample diameter [79].

The lowering of the friction and angles close to 90 degrees were pronounced as the ways of attaining homogeneity avoiding the free surface zone at the corner of the die. While multi-passes were considered to be essential for high strains, strain inhomogeneity was mentioned as well as material softening at further passes. Higher deformation temperatures and lower processing speeds were suggested for the inhomogeneity of the products [71].

In a study carried out on Zr, the first pass was found to be the stage of the most evident grain refinement while subsequent passes were stated to be insignificant. However, a transformation of low angle boundaries to high angle grain boundaries was observed. The yield strength was found to be in agreement with the Hall-Petch equation. Hardness of the Zr through a single pass was found to increase by 25 %

whereas subsequent passes up to 8 yielded an increase of 38% due to refinement of grains of 270 nm with high angle grain boundaries. It was stated that average spacing between GNBs was improved from 0.5 microns to 0.25 microns. The main difference besides the distance was stated to be the level of misorientation [80]. Evolution of low angle grain boundaries into high angle grain boundaries with further passes was observed in CP Ti, too [81].

When age-hardenable Al alloys were considered, multi-pass ECAP was found to be ineffective due to over-aging induced by dislocation density or even precipitate coarsening during ECAP. The common observation was hardness drop after a few passes. An optimization of aging and ECAP combination was achieved through post ECAP aging [82].

2.2.4. Grain Boundary Strengthening

Grain boundaries are surfaces separating two or more different oriented grains from each other forming a barrier. The orientation difference may be large as it is in high angle grain boundaries or low as it is in low angle grain boundaries, tilt boundaries. The energy of the boundary is related to both the orientation misfit and coherency of the boundary. Low angle grain boundaries, as well as coherent boundaries, have low energy which makes them thermodynamically stable. High angle grain boundaries and/or incoherent boundaries have high energies and they may act as unstable, high energy regions throughout the material. Grain boundaries serving as barriers to glide dislocation movement are effective strengthening factors. The very well-known Hall-Petch equation explains the degree of hardening [54, 56–58]:

$$\sigma_{ys} = \sigma_i + k_y * (\frac{1}{\sqrt{d}}) \qquad\qquad 2.4$$

Where σ_{ys} is yield strength, σ_i is overall resistance of lattice to dislocation motion, k_y is the "locking parameter" which is the relative hardening contribution of grain boundaries and d is the grain diameter.

The equation was derived from the assumption that n dislocations may exist at a certain length L (between source of dislocation and boundary) and the lead dislocation, closest to grain boundary, will experience a total stress of $n\tau_s$ where τ_s is the average resolved shear stress in the slip plane. The longer the distance L, the higher will be the stress so that a critical value τ_c required for the dislocation to pass through the grain boundary may be reached more easily. As a result the fine grain size distributes the overall stress and τ_c cannot be reached easily.

σ_i was suggested to be divided into two components such that [56][57]:

σ_{ST} : structure sensitive including the parameters such as precipitate-dislocation, dislocation-dislocation and dislocation-solute interactions excluding temperature effect.

σ_S : Temperature sensitive and related to Peierl's stress

$$\boldsymbol{\sigma_{ys} = \sigma_S + \sigma_{ST} + k_y * \left(\frac{1}{\sqrt{d}}\right)} \qquad \textbf{2.5}$$

The formula includes short range order effects (Peierl's stress <10Å), long range order effects such as dislocations (100-1000Å) and very long range order effect (>10000Å). It is important to note that below a certain size, the $k_y * \left(\frac{1}{\sqrt{d}}\right)$ part of the equation cannot be valid [57].

2.2.5. Precipitation Hardening

Since the scope of the current study is mainly concerned with precipitation behavior, the theory of precipitation will be discussed in four main parts. The first part will be on the basics of precipitation and how it is possible for an alloy to be precipitation hardened. The second part will be on the strengthening mechanisms which are possible in relation to precipitates. Thirdly precipitation hardening will be discussed as a phase transformation and the precipitation behavior of 2x24 alloys will be concisely stated.

2.2.5.1. The Basics of Precipitation Hardening

When Alfred Wilm invented the 2017 alloy, which was patented by him in the name of Duralumin in 1908, he was probably not aware of the fact that his invention would have been one of the most popular research topics in material science and the alloy would have conserved its popularity even after a hundred years [20]. The discovery resulted in not only the improvement of Al alloys but also various age hardenable alloys of copper, nickel and even steel were discovered following decades. Precipitation phenomenon was regarded as the most interesting discovery of metallurgy [20] since then.

It might be interesting to remind that discovery, as a scientific tale on how science is up to ordinary efforts in daily life. The reasoning behind the research was to produce a better Al alloy that would be used in military applications in the upcoming First World War. Alfred Wilm was working on an Al-Cu-Mn alloy and decided to add 0.5% Mg before shaping it into a sheet and heating in a salt bath at 520°C followed by quenching on a Saturday morning. Just before leaving for sailing on the Havel River he and his assistant, Jablonski, had taken some hardness measurements. On Monday morning they were to finish their measurements of hardness but were shocked to see that hardness numbers were significantly higher than it was recorded a few days ago. As would do any scientist, they checked the calibration of the hardness machine and repeated the experiment noticing that after four days at room temperature the hardness had increased and preserved that value. The patent of the alloy, with 3.5-5.5%Cu, plus less than 1% Mg and Mn, was obtained and interestingly Alfred Wilm abandoned metallurgy after publishing his works and moved back to his farm. In 1937, he died not knowing that he invented the first nanotechnology as noted by Hornbogen [20].

Years of research have continued on aluminum alloys and precipitation phenomenon yet some of its mysteries still remains unknown [3]. The very conditions required for an alloy to be precipitation hardenable are among the major conclusions driven from these studies that are generally accepted [3, 4, 14, 17, 19,

28, 41]. The main requirement is the relatively high solubility of one element in the other at high enough temperatures denoted as C_{max} in Figure 2.10 on a representative phase diagram. The second crucial condition is the sharp decrease in solubility limit upon cooling (C_{max} to C_{min}). The alloy composition (C_0) is needed to be in between C_{max} and C_{min}. The fourth and last requirement is proper heat treatment of the alloy starting with proper solutionizing followed by quenching and artificial aging at an optimum temperature for a certain time period or natural aging at room temperature depending on the alloy composition and application [83]. The principle is that super saturated solid solution is obtained by quenching the alloy after solutionizing because otherwise the second phase particles may nucleate and grow at grain boundaries. The super saturated solid solution (SSSS) of α needs to precipitate out as A_xB_y phase for thermodynamic stability. The possible temperature range for precipitation reaction can be regarded as below the maximum solubility limit to room temperature. But when the kinetics is taken into account, at low temperatures, atomic movement is slower although driving force is very high while at high temperature the driving force is too low for a phase transformation in spite of high mobility of solute atoms. As a consequence of the kinetics of the reaction a schematic TTT can be drawn where optimum aging temperature lies at the intermediate temperature range as seen in Figure 2.11. It should be stated that the difference from the equilibrium phase mixture of α+A_xB_y is the homogeneous distribution of intermediate phases called clusters and GP/B zones followed by a semicoherent Θ′ or S′. A sequence of phase transformations occurs before the stable A_xB_y formation. The sequence usually includes clusters, GP/B zones and coherent/semicoherent Θ′/S′ phases. Only after their formation, homogeneous distribution of fine A_xB_y particles is possible. Very small particles of transitional phases and A_xB_y formed by this heat treatment lead to considerable hardening of the alloy. The mechanisms of hardening will be discussed next.
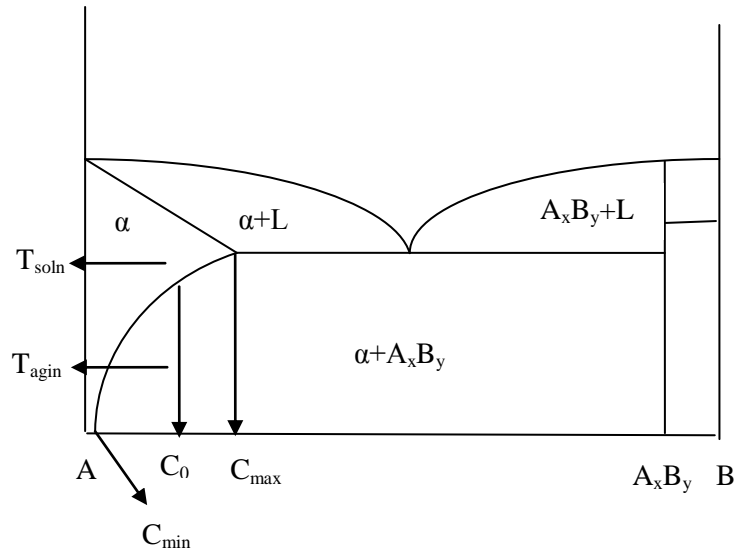
Figure 2.10. A schematical, hypothetical phase diagram showing thermodynamic age-hardenable requirements
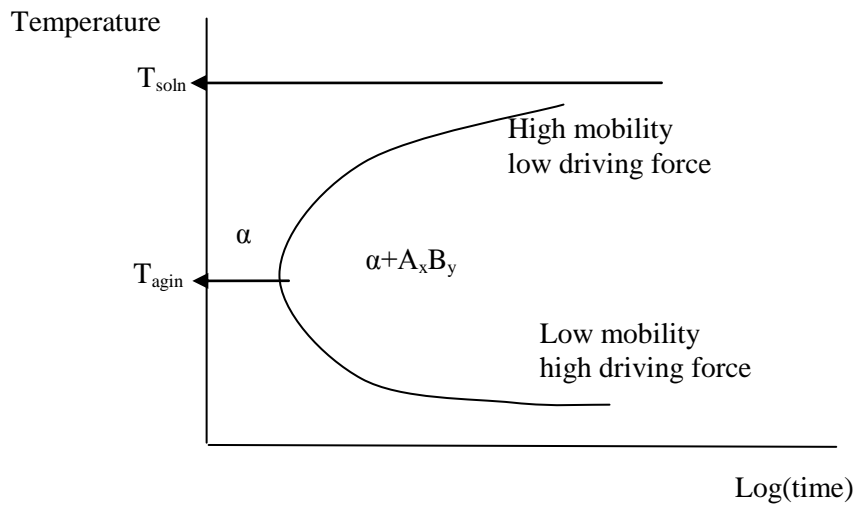
Figure 2.11. A representative TTT curve for precipitation transformation [57]**.**

2.2.5.2. Strengthening Possibilities in Relation to Precipitates

Before explaining the mechanisms underlying the hardening of super saturated solid solutions, a representative hardening curve may be looked upon as seen in Figure 2.12. Since the simplest and most widely investigated precipitation hardening alloy is Al with 4-5% Cu, its aging curve at an arbitrary aging temperature can be investigated. The initial peak belonging to the formation of Guiner-Preston (GP) zones due to very small clusters of solute atoms, only a few atomic distance thick and a few nanometers long, may not be always present as a different peak but may exist as the initial part of the main peak, shown in the figure as dotted curve. The hardening continues at the under-aged condition until a peak point referred to as peak aging is reached followed by decreasing hardness as a consequence of precipitate coarsening which is regarded as over aging [1, 56, 57, 83, 84].
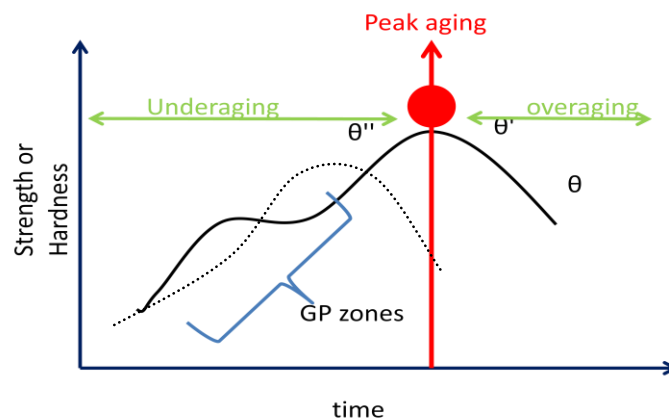
Figure 2.12. A schematical age-hardening curve for Al alloys [83]**.**

The possible mechanisms that may lead to the hardening behavior described above are categorized by Dieter and others as follows:

- Coherency strain
- Stacking fault energy

- Ordered structure
- Modulus effect
- Interfacial energy and morphology
- Lattice friction stress

All of which are dependent on certain properties of the individual phases and their relation to each other [56].

Coherency strain is a result of mismatch between the matrix and the precipitate in terms of lattice parameter. The degree of strain increases with increasing amount of lattice parameter difference. It is also common to have a directional coherency leading to rod, needle or disk like precipitates rather than cubes or spheres. The higher the degree of misfit and hence the strain field the harder the dislocation motion through the matrix. A rough relationship was suggested to describe the increase due to coherency [56, 57]:

$$\Delta\sigma = 2G\epsilon f \qquad\qquad 2.6$$

When ϵ is the misfit strain field proportional to lattice parameters of the two phases, f is the volume fraction of precipitates and G is the elastic modulus of the matrix.

A more detailed equation was suggested as:

$$\Delta\sigma \sim 6G(\frac{r}{b})^2 f^{1/2} \epsilon^{3/2} \qquad\qquad 2.7$$

R is particle radius and b is the Burgers vector. It is stated that in general most of the strengthening is due to strain fields [56, 57].

Significant stacking fault energy (SFE) differences between the two phases may also result in a hardening effect. Different SFEs lead to variation of fault width which may dominate dislocation-particle interaction when glide dislocations enter the precipitates. Important parameters are SFEs, partial dislocation separation force and distance, SF width and particle size [56, 57].

Particle cutting by dislocations is a common phenomenon in precipitation hardening. The dislocations may cut through or bow a particle depending on the size and spacing of the precipitates as well as the modulus.

Ordered structures like Al_2Cu, if attempted to be cut, the interaction of dislocation and precipitate causes generation of anti-phase domain boundary due to distorted order. The energy of an anti-phase domain boundary (AFDB) is nearly ten times of an ordinary phase boundary as a result strengthening occurs. Strengthening due to ordered structures also brings about high temperature strength [56, 57].

If the particle to be cut by dislocation is coherent with low misfit strain, it would also create new surfaces but would not increase the energy and lead to strengthening that much. The creation of additional surface area by cutting through the precipitate is another strengthening effect depending on the energy of the newly formed surface. The strengthening due to surface energy is given by:

$$\Delta\sigma = \frac{2\sqrt{6}}{\pi}\gamma_s\frac{f}{r} \qquad\qquad 2.8$$

γ_s is the particle-matrix surface energy. When the surface energy to volume ratio is high as in the case of plate or needle shaped particles, the strengthening affect increases [56, 57].

The local elastic modulus variations due to different G values of particle and matrix may increase or decrease the energy of a moving dislocation causing a strengthening. Practically however, the difference is not enough for hardening while increased voids have effective contribution to the strengthening.

Lastly the strengthening due to Peierl's stress as defined in the equation below where σ_p and σ_m are the strength of particle and matrix, respectively [56, 57].

$$\Delta\sigma \sim \frac{5.2f^{\frac{1}{3}}r^{\frac{1}{2}}}{G^{\frac{1}{2}}b^2}(\sigma_p - \sigma_m) \qquad\qquad 2.9$$

Although above mentioned possibilities are predicted, the combinational effect could not be predicted easily. The summation of the mechanisms causes an increase in hardness up to a critical point which is denoted as peak aging in Figure 2.12. When the cutting of particles is no longer possible the bowing movement of dislocations around precipitates starts. This phenomenon of moving around the particles was defined by Orowan back in 1947. The shear stress needed to bow between particles, when λ is the separation of two obstacles, defined as

$$\tau_0 = Gb/\lambda \qquad\qquad 2.10$$

The equation is updated in 1968, considering the interaction in both sides of the particle [56, 57].

$$\Delta\sigma = \frac{0.13Gb}{\lambda} * \ln\frac{r}{b} \qquad\qquad 2.11$$

Lastly, the shape of the precipitate which is usually needle, rod or plate rather than sphere or cube has an astounding effect on hardening, in some cases twice of the hardening that occurs with a cube or sphere. The bowing around the particles leaves loops as well as creating dislocation cell structures on them.

2.2.5.3. *Precipitation Hardening as a Phase Transformation*

Phase Transformations

The basis of phase transformations depends on thermodynamic stability of certain phases according to the phase diagrams. The most stable phase has the lowest free energy and hence it is very likely to form. Thermodynamic stability though cannot be the only consideration since kinetics of phase transitions has a powerful impact upon the microstructure of an alloy. Some thermodynamically favorable phases do not have a chance to grow for many years due to very slow kinetics of the transformation in process. As a result, two aspects are to be considered cooperatively, thermodynamics and kinetics. Both will be further discussed to remind and combine some important details of phase transformations to the current study. There are basically two methods of classification of phase transformations.

One depends on the active mechanism for transformation which is either diffusional (civilian) (pearlite formation or precipitation) or diffusionless (military) (martensitic) and the other depends on the steps of process which are nucleation growth like martensitic and precipitation transformations or nucleation-free like recovery. The stepwise manner will be more meaningful in describing the precipitation phenomenon because nucleation is the most important step affecting the kinetics of a certain transformation like precipitation. There are two possibilities of nucleation which will be discussed in detail emphasizing the kinetics and thermodynamics that will remind valuable information in understanding and discussing the results of this chapter [56, 58, 84–86].

✓ *Homogeneous Nucleation*

Homogeneous nucleation is a term to define the critical size nuclei formation of a new phase in the bulk of metastable phase rather than at defects [[56, 58, 84–86]. It also serves as a guide to more easily understand transformation because it excludes the effect of defects in the structure over the process. As stated in [86] there are three thermodynamically important parameters to be considered. Before explaining them, it would be best to assume a precipitation reaction as follows at a temperature T_2: A schematic phase diagram with its corresponding free energy curves for clarifying the terms to be discussed is given in Figure 2.13.

$$\alpha' \text{ (sss)} \rightarrow \alpha + S$$
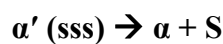
In which α' is a metastable super saturated solid solution of aluminum with a composition X_0, which is to be transformed into a more stable composition of α phase and a new phase rich in Cu and Mg solute atoms, S precipitate, in the current study which is Al_2CuMg. It should be noted that the transformation requires long range diffusion. The total driving force for phase transformation is shown in figure as ΔG_0; ΔG_n is the driving force for nucleation which is higher than ΔG_0 because of the high chemical potential of solute atoms denoted as $\mu^{\alpha}_{Cu,Mg}$.

The three energetic contributions of phase transformation are:

- Energy decrease due to formation of a thermodynamically more stable phase S with a volume V denoted as ΔGv.V where

$$\Delta G_v = \Delta G_n / V_m \qquad \textbf{2.12}$$

- Vm is the molar volume of S phase.
- The free energy increase due to the formation of a new surface is Aγα/S, A is the area, γα/S is the surface energy of the newly formed phase boundary of α and S phases.
- The strain energy related to the density difference of the new phase to be formed out of super saturated solid solution, α'(sss). The new phase may have a higher density leading to a smaller volume and a tensile misfit strain energy or lower density and higher volume leading to a compressive misfit strain energy both of which will be denoted as ΔGst.

The total energy change is:

$$\Delta G = -V\Delta G_v + \sum A\gamma + V\Delta G_{st} \qquad \textbf{2.13}$$

For an incoherent spherical precipitate of radius r, it is;

$$\Delta G = \frac{4}{3}\pi r^3 (\Delta G_{st} - \Delta G_v) + 4\pi r^2 \gamma \qquad \textbf{2.14}$$

The derivative of the equation gives the critical radius r^*, activation energy barrier ΔG^*, concentration of critical sized nuclei C^*, as follows [86]

$$r^* = \frac{2\gamma}{(\Delta G_v - \Delta G_{st})} \qquad \textbf{2.15}$$

$$\Delta G^* = \frac{16\pi\gamma^3}{3(\Delta G_v - \Delta G_s)^2} \qquad \textbf{2.16}$$

$$C^* = C_0 \exp(-\frac{\Delta G^*}{kT}) \qquad \textbf{2.17}$$

Where C_0 is the number of atoms per unit volume in the phase, the nucleation rate is

$$N_{\text{hom}} = \omega C_0 \exp\left(-\frac{\Delta G_m}{kT}\right) \exp\left(-\frac{\Delta G^*}{kT}\right) \qquad \textbf{2.18}$$

Where ω includes vibration frequency of the atoms and the area of critical nucleus, ΔG_m is the activation energy for atomic migration per atom, k is the Boltzmann constant and T is the temperature of transformation.

The important variable is ΔG^* which is dependent on both three energy terms, surface energy of phase boundary, the misfit strain energy and the driving force. Among them, surface energy is the most dominant. The equation gives certain clues about various conditions valuable to the current study. For example when the precipitate is incoherent, the energy of the formed surface is significantly high and it is nearly impossible to observe homogeneous nucleation. On the contrary, a formation of a coherent precipitate becomes feasible by homogeneous nucleation because the energy of the coherent surface is negligibly low. In the case of transformation into S and alpha phases, coherency is not possible but the system has an alternative solution to the problem. Transition metastable phases like GPB zones (Guiner-Preston-Bagaryatsky) which have the coherency relationship are likely to form first. Following GPB zones one or more intermediate S phases (S" and S') form most probably nucleating on the GPB zones. The transformation towards stable and incoherent S phase occurs through the dissolution of transition S (S') and formation of stable S nucleating heterogeneously at usually defects like grain boundaries[56, 58, 84–86]. Heterogeneous nucleation will be discussed on the next heading. The transformation of α' into α phase of intermediate composition between α' and stable α and GPB zones is actually formation of solute clusters with the same crystal structure as the matrix. In Figure 2.14, they are connected by a dashed line which represents their crystallographic relationship. Although this type of transformations are usually attributed as homogeneous in many transformations a combination of both homogeneous and heterogeneous nucleation are observed depending on the available nucleation sites.
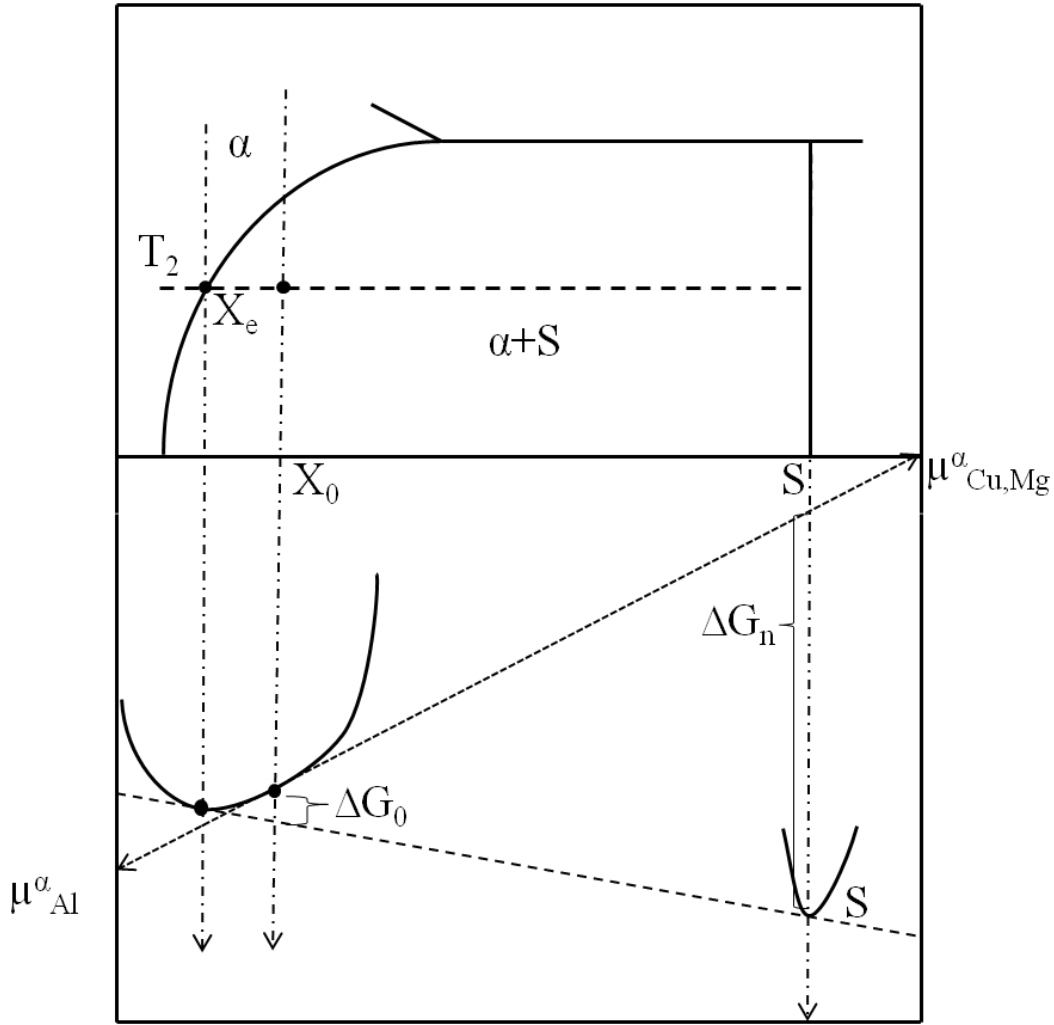
Figure 2.13. Schematic phase diagram and corresponding free energy curves for a precipitation reaction [86]**.**
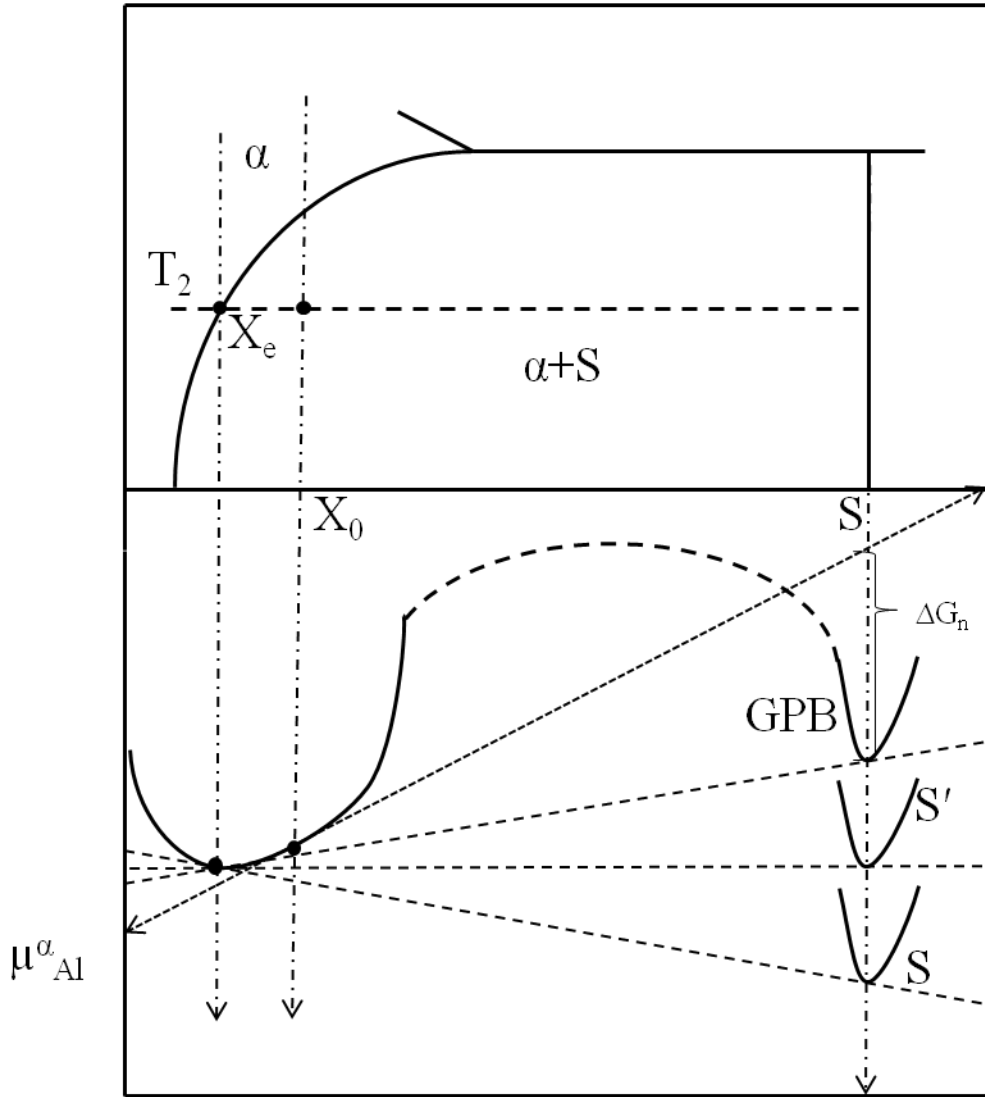
Figure 2.14. Metastable coherent phases are shown in Gibbs free energy diagram [86]

✓ *Heterogeneous Nucleation*

The main criterion for heterogeneous nucleation is that defects like excess vacancies, dislocations, boundaries, etc. act as nucleation sites. Energy of already present defects is lowered when a new phase forms. As a result, the energy barrier for nucleation is lowered by means of the decrease in defect energy. The energy equation then becomes;

45

$$\Delta G_{het} = -V(\Delta G_v - \Delta G_{st}) + \sum A\gamma - \Delta G_d \qquad\qquad 2.19$$

ΔG_d term is the reduction of free energy in the defect during transformation. Another important difference is stated by [86] that incoherent phase boundary results in a very small misfit strain energy. Both of these aspects are reasons for heterogeneous nucleation to be more common when compared to homogeneous nucleation. Depending on the defect type, only heterogeneous nucleation will be discussed at dislocations because ECAP process increases dislocation density very significantly. Although there are claims that the deformation leads to excess vacancies just after ECAP, since controversies exist, it will not be further discussed separately but will be included in Al-Cu-Mg precipitation section [61].

✓ *Heterogeneous Nucleation at Dislocations*

The energy equation for heterogeneous nucleation shows that the energy is lowered by decrease in defect energy. Incoherency was mentioned to be preferable for it lowers the strain energy but it also increases the surface energy very much. When the defect in consideration is a dislocation, an important condition is present. Porter and Easterling [86] state that the distortion around the dislocation can assist nucleation in many ways. If a coherent nucleus with a negative misfit is to be formed, it will prefer to do so above the edge, at the compressive strain region and will reduce the strain energy. If the misfit is positive it will form below the dislocation. It is important that coherent precipitation can be assisted by dislocations. Another way of assisting is by solute segregation at the dislocations so that a composition close to the precipitate composition will already be present. It has also been stated that dislocation can act as a diffusion pipe during the evolving of nucleus into a critical size [9].

Defects are more likely to act as nucleation sites, if they have higher energy. However regarding the current study, small but denser defects like dislocations and excess vacancies have higher priority because the probability of nucleation at a densely present defect will be more than a dilute defect like high angle grain

46

boundary. For example, it has been stated that defects like excess vacancies might assist nucleation either by relieving misfit strain energy or by increasing substitutional diffusion rates [56, 58, 84–86].
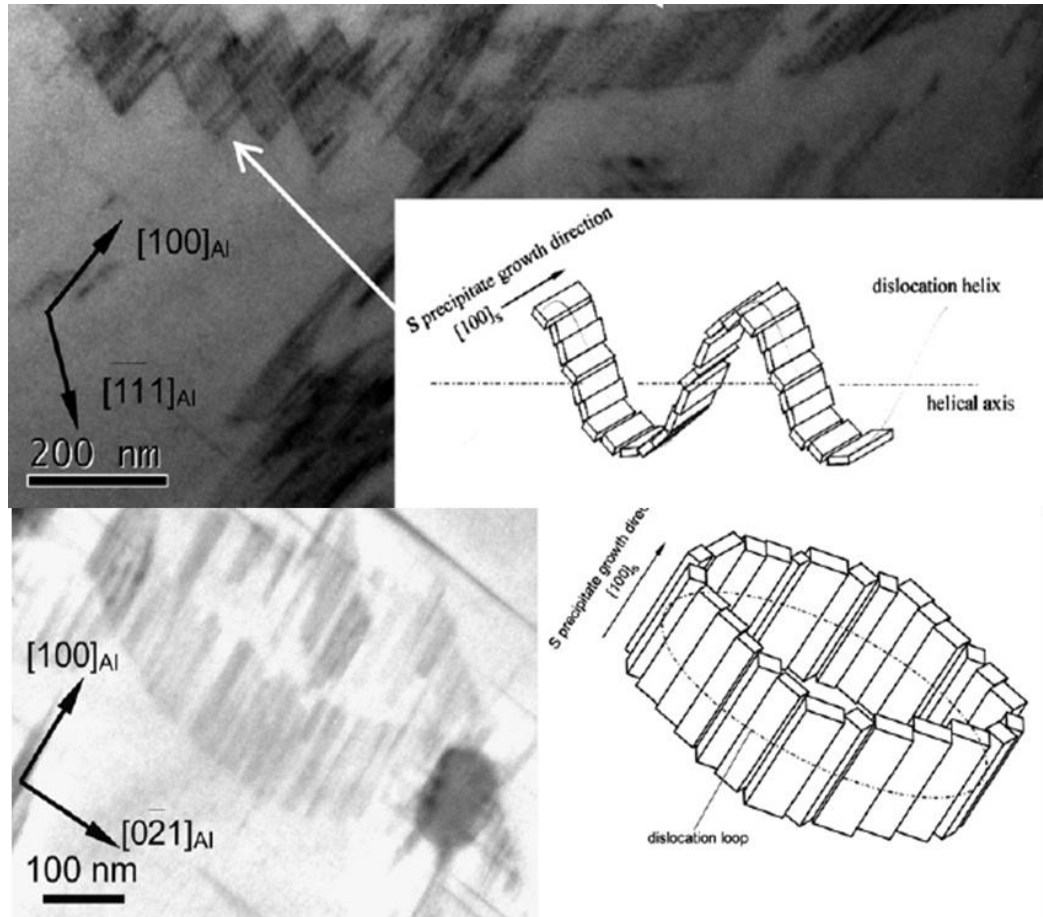
Figure 2.15. The heterogeneous nucleation of S precipitates on dislocation helix and loop in Al-Cu-Mg alloy adopted from [6]**.**

An important recent study on the heterogeneous nucleation of S precipitates on dislocation line, helix and loop has shown that there is a tendency of formation of type II S precipitates lying parallel or nearly parallel to the original dislocation path. It is considered that either the dislocation line direction is in the habit plane of the precipitate or there is a variant selection of the precipitate during nucleation. As a

result of this tendency, it has been stated that since the forms of helix, line or loop are composed of pure edge dislocations one after the other, there are separate formations of S precipitates in each one of these. As a consequence of this the Figure 2.15 type of formations are observed throughout the solutionized and aged Al-Cu-Mg alloys also observed in the current study [6].

2.2.5.4. *Precipitation in Al-Cu-Mg Alloy*

The precipitation behavior of Al-Cu-Mg alloys have been a great deal of discussion [5–13, 16, 29, 30, 33–35, 37, 38, 40, 42–46, 50, 51, 60, 87–92] especially in the last two decades and improvement on high resolution microscopy and atom probe tomography has recently led to the understanding of the hardening phenomenon behind the precipitation in Al-Cu-Mg alloys especially in 2011 [6, 8, 23, 42, 50, 51].

Bagaryatsky proposed the first precipitation sequence of Al-Cu-Mg in early 1943 as Super saturated solid solution (α) ➔ GPB (Gunier-Preston-Bagaryatsky) zones ➔ S″➔S′➔S(AlCuMg$_2$). This proposal was updated by many studies and refined into the following sequence:

SSSS(α) ➔ Solute Clusters (Mg-Cu)➔ GPB zones+S ➔ S which is accepted in recent studies [44, 50, 51] for the ease of understanding and avoid confusion.

Even the crystal structure of S phase itself has been accepted to be PW model [6] very recently and there is no consensus on the precipitation sequence either. There are numerous ideas on the sequence and Table 2.7 summarizes some of them [5]. Among these structures it is obvious in Table 2.7 that S′ phase was stated to be different from S phase by slight deviations of the lattice parameters which was pointed out as the result of the variations in the degree of coherency [48]. On the other hand numerous studies confirmed that S″ was only a different variant of the equilibrium S phase by some authors [11, 46, 48] while there are authors suggesting [12, 30] the existence of GPB2 zones as well as S″

SSSS(α) ➔ Solute Clusters (Mg-Cu)➔ GPB2 zones/S″ ➔ S.

48

It has been stated that while S phase was responsible for the peak hardening. GPB2 as well as S″ had little contribution to this hardening. It is important to mention that both the co-clustering and co-existance of GPB zones and S phase or some form of it are commonly accepted.

Table 2.7. Proposed structures for different phases in Al-Cu-Mg alloys [5]

Phase	Composition	Structure	a (nm)	b (nm)	c (nm)
α	Al (2024)	Cubic	0.404	-	-
S phase	Al_2CuMg	Orthorhombic	0.400	0.923	0.714
S′ (coherent)	Al_2CuMg	Orthorhombic	0.405	0.906	0.724
S′ (semi-coherent)	Al_2CuMg	Orthorhombic	0.404	0.925	0.718
S″ (coherent)	$Al_{10}Cu_3Mg_3$		0.404	1.212	0.404
S″ (coherent)	$Al_5Cu_5Mg_2$	Cubic	0.827	-	-
S″ (coherent)	$AlCuMg_2$	Orthorhombic	0.405	0.405	0.810
S″ (coherent)	$AlCuMg_2$	Prim. Monoclinic, β=91.7°	0.320	0.405	0.254
GPB2	Cu-Mg	Tetragonal	0.58	-	0.81
GPB2	Al_2CuMg	Tetragonal	0.41	-	0.81

In the current study, most recent researches carried out using atom probe tomography and HRTEM were taken into account and for the sake of simplicity of it the following sequence will be preferred [6, 50, 51].

SSSS(α) ➔ Solute Clusters (Mg-Cu)➔ GPB zones+S ➔ S.

The ternary phase diagram for Al-Cu-Mg is given in Figure 2.16. The phase diagram is very important in relation to the current study since the composition range of Al 2024 in the current study with Mg content of 1.73-1.95 lies on the phase transition but it should be reminded that the effect of Mn, Si and Fe also have direct influence on the phase diagram and the Mn content of Al 2024 is considerably high

to take the ternary as a strict map however it still has the value to guide on the possibilities.

In Al-Cu-Mg alloys there are two main strengthening regions observed as seen in Figure 2.17, there is a rapid hardening region denoted as I though it cannot be observed in high Cu-Mg alloy due to the very early hardening even in a few minutes.
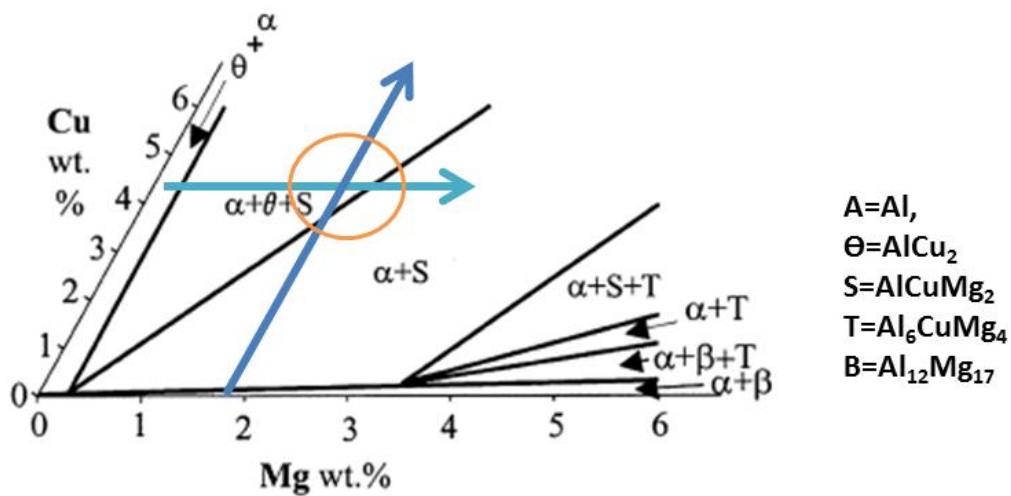
Figure 2.16. Isothermal section of ternary phase diagram of Al-Cu-Mg at 200°C [5]**.**
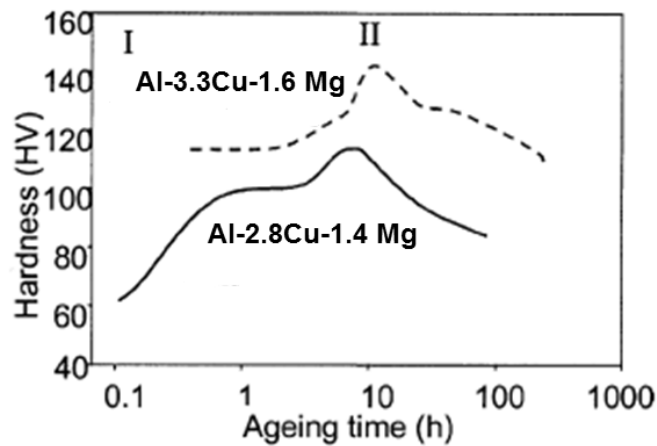
Figure 2.17. The hardening response of Al-Cu-Mg alloys at 190°C adopted from [5]**.**

The rapid hardening of the aging of 2XXX alloys at the very beginning of aging, as short as 1 minute at 150°C, had led to the idea of formation of a coherent zone. In fact the initial hardening effect was reported to be the 60% of the overall hardening effect of total aging. On the rapid hardening (RH) the ratio of Cu/Mg as well as the region of phases were stated to be very important. In the region of (α+Θ) and when the Cu/Mg ratio is high, the RH behavior was not observed as well as in the binary alloys of Al. But in (α+S) region when a small amount of silver was present RH was also observed [51]. When Cu/Mg ratio is high, the RH behavior lowers and the increase of Mg increases the rapid hardening. Though there are various suggestions on how the rapid hardening occurs at this initial stage, the common point is the co-clusters of Mg and Cu and their interaction with dislocations rather than grain boundaries. Another important point is that, RH is not observed to be effective in natural aging but requires a certain temperature increment after quenching even for a few minutes [30, 51].

The second stage of hardening was attributed to GPB zones and coherent S precipitation in many studies while in some it was directly attributed to be a result of S precipitates. All of them may have a point because it is probable that they only use different terminology. It is important to know that uniform, fine distribution as well the coherency of GPB zones and S precipitates are the factors that affect the hardening. S precipitates are indicated to form in a certain relationship with the matrix such that $[100]_{Al}//[100]_S$; $[0-21]_{Al}//[010]_{S \text{ and}}$ $[012]_{Al}//[001]_S$ forming 12 variants of the S phase. The precipitation of S phase was observed as homogeneous or preferred along the Burger's vector of the dislocations which is called as heterogeneous S precipitates. There are various studies on the coexistence of GPB and S phase after long aging hours such as 80 hours at 170°C in literature while the hardness is still preserved at high levels [50]. However in 114 hours, after over-aging, no sign of GPB zones were observed which may indicate that the hardening behavior was related to GPB zones as well as small S precipitates [50]. Another important issue on S precipitates that precipitate heterogeneously on dislocations is that they can form precipitate groups depending on the dislocation distribution of

the matrix before aging. These precipitate groups were considered to act as a single particle hence the size of the precipitate groups was stated to be very effective on the degree of hardening. Depending on the energy calculations, critical sizes of 425 and 212 were calculated [6]. It was stated that unlike GPB zones (up to 100 atoms) and co-clusters (3-20 atoms), S precipitates (larger than 2 nm) were resistant to shear and Orowan bowing was required for dislocation motion. In deformed Al-Cu-Mg, due to the more uniform distribution of dislocations, a lower S precipitate group size and hence higher thermal stability was expected [6]. The alloying elements such as Si, Ti, Zn were also stated to be observed in the GPB zones and S precipitates using atom probe tomography [50]. In the over aged state, general observation is the large S precipitate groups as well as large, interacting, individual S precipitates as well as the absence of GPB zones.

CHAPTER 3

PRELIMINARY STUDY: EFFECT OF ECAP ON AGE HARDENING OF Al 2024

3.1.   EXPERIMENTAL PROCEDURE

The current study involves the investigation of ECAPed commercial Al 2024 alloy parts prepared by E. Saraloğlu et. al. [93]. Before going any further, it is vital to state the method of production although the production method is beyond the scope of the current study. The composition of the sample was reported as in Table 3.1. Al 2024 alloys in rods and rectangular shape were used. All of the samples were heat treated at 495°C for 1 hour in a muffle furnace to solutionize and homogenize the microstructure followed by quenching into ice-salt-water mixture at 0°C. While the rod shaped samples of ~18 mm diameter and ~50 mm length were pressed through equal channel angular press, the rectangular samples were directly subjected to aging at 190±1°C in an oil bath right after quenching [93].

Table 3.1. As-received composition for Al 2024 alloy [93]

Cu	Mg	Mn	Zn	Si	Fe	Ni	Cr	Al
4.900	1.240	0.595	0.156	0.106	0.1	<0.1	<0.1	Bal.

ECAP system is shown in Figure 3.1. The die was made of H13 tool steel and the angle between two channels is 120°. The need for back pressure was maintained through feeding cupper blocks of 60 mm in front of the aluminum samples to avoid

crack formation and maintain balance between feeding and exit parts of the system. Each sample was placed after a Cu insert so the first sample was subjected to a lower back pressure in comparison to the samples placed afterwards. In this way low and high back pressure could be maintained. Between each sample and Cu block 5 mm long MoS_2 pellets were introduced for lubrication. ECAPed samples were kept in a cooler at -18°C. ECAPed samples were cut in perpendicular and shear directions for hardness measurements and TEM sample preparation. Preliminary studies were carried out to see the general points that may lead the study towards a more meaningful direction. For this purpose the aging behaviors of supersaturated solid solutionized Al 2024 with and without ECAP were investigated. One of the high back pressure samples were cut into pellets with corresponding thin sections next to them for TEM observation as shown in Figure 3.2 and macro-hardness tests were carried out.

Figure 3.1. ECAP system composed of pressing unit, 120° angle die and 18 mm diameter punch.
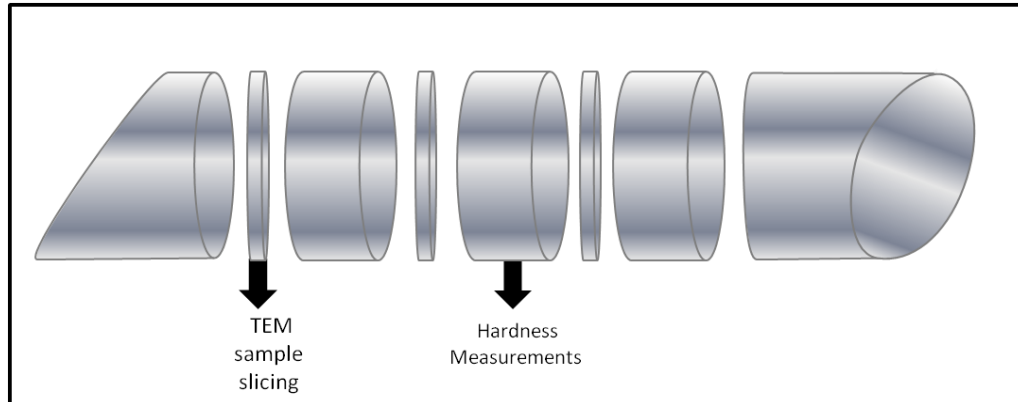
Figure 3.2. The precision cutting procedure of the sample perpendicular to the pressing direction for macro-hardness measurements and TEM sampling.

TEM samples were punched into 3 mm diameter discs and grinded using 2000 SiC grinding paper down to 100 µm occasionally measuring by means of a micrometer. The samples were then dimpled down to a total of <10µm thickness from both surfaces leading to a concave appearance at both facets. Fischione model 200 dimpling grinder was used for dimpling. The final thinning was carried out at Fischione model 110 twin jet electropolisher by electropolishing in an acid solution of 25 % nitric acid with 75 % methanol. The electropolishing was performed at subzero temperature range of - (25-30°C) at a voltage of ~10V for about 10-15 seconds.

3.2. RESULTS AND DISCUSSION

3.2.1. Macro-hardness and Optical Micrographs

The randomly collected macro-hardness measurements of ECAPed sample cut perpendicular to the longitudinal direction showed that there is inhomogeneity throughout the sample. In Figure 3.3, Brinell hardness results are shown. One of the sections had porosity observable through eye inspection. It might be resulted from the deformation or remnants of casting porosity. The defected part, as expected, was observed to have more inhomogeneity and in general upper part (close to the inner

corner of the die) of the sample was found to have higher hardness than the lower part.
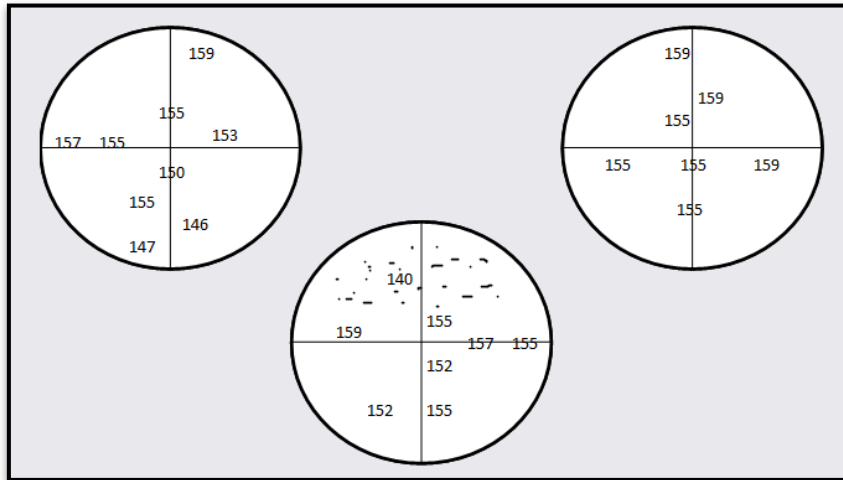
Figure 3.3 Brinell macrohardness results of ECAPed sample.

The optical micrographs of the sample cut parallel to shear plane are shown in Figure 3.4. It is not possible to observe the cell structure but deformation of the sample can be noticed from the columns of grains throughout the whole sample. The increased dark spots at the bottom are also interesting features that can be detected in the structure which may be porosities produced during ECAP process. The density increase at the bottom of the sample may be related to the corner gap effect during ECAP.

The time intervals of the preliminary experiments did not yield to a good match of states for an accurate comparison of ECAPed and solutionized samples. Yet the microstructures of the two samples at any time interval of the precipitation sequence show such a huge variation that a general comparison of the two would be meaningful regardless of small time differences.

In this aspect two conditions can be compared, the microstructures around the peak and the microstructures of overaged state.
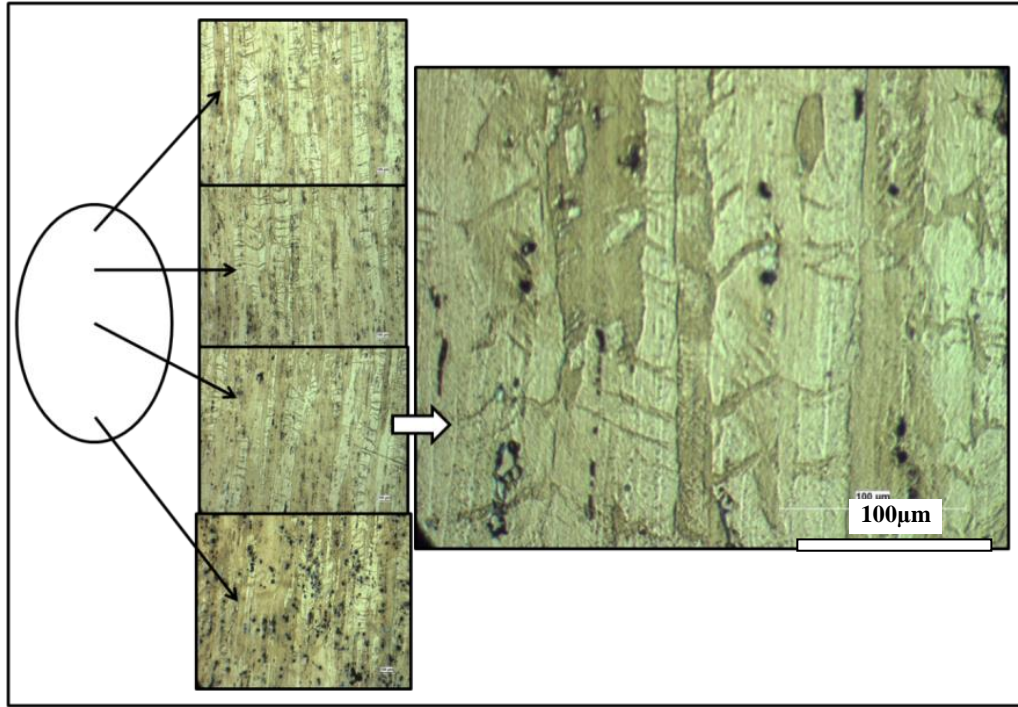
Figure 3.4. Optical images of ECAPed sample. The cell structure can not be observed by optical microscopy whereas the deformation direction is visible.

The preliminary results on aging of solutionized Al 2024 has yielded to the curve in Figure 3.5 where the data points are limited with near peak aged, slightly overaged and overaged states. Peak-age time of solutionized Al 2024 was found to be around 11-12 hours consistent with the literature [28] TEM investigation was carried on the near peak aged and overaged Al 2024.

The ECAP processed sample showed nearly 12 times faster aging when compared to solutionized counterpart, the data points are also limited as presented in Figure 3.5. The peak aging time was in the range of 0.9-1.2 hours but could not be determined exactly because of the missing data points. On the other hand the

inhomogeneity of the sample combined with the limited number of data, five macro-hardness indents, yielded an incomplete and exaggerated aging curve. One hour (near peak aged) and 80 minutes (overaged) aged ECAPed samples were compared to 11 (near peak aged) and 24 hours (overaged) aged standard sample, respectively.
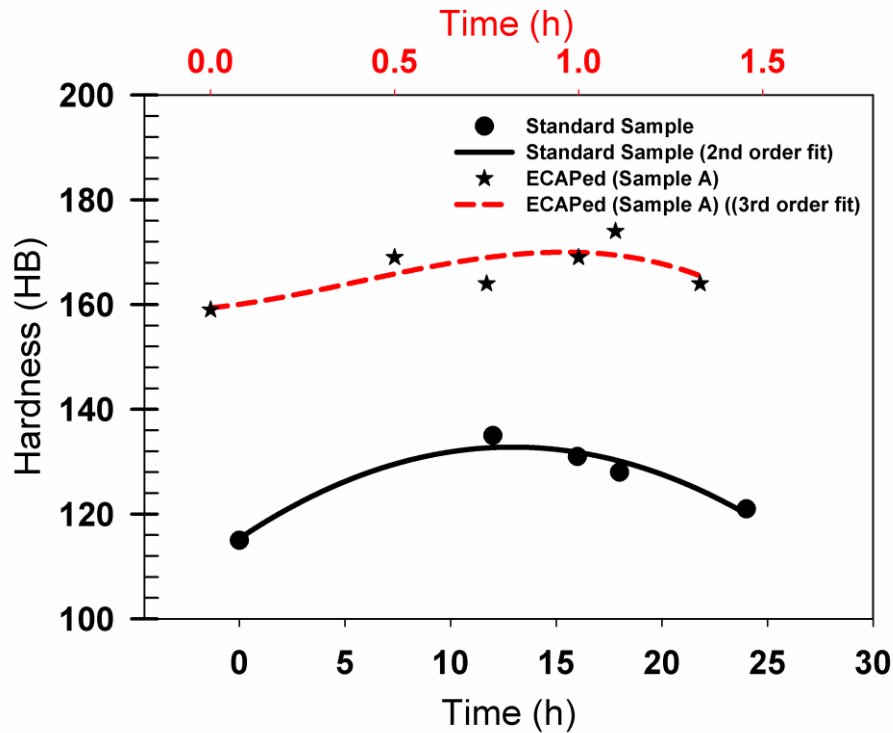
Figure 3.5. Variation of hardness with aging time at 190°C for ECAPed and standard Al 2024.

3.2.2. TEM Study

3.2.2.1. ECAPed State

Representative TEM images of the ECAPed samples given in Figure 3.6 show the accumulated dislocations which are referred to as "dislocation forests", the dark regions of the images. These structures were in the form of bands at a certain angle

whereas through tilting the specimen they disappeared and reappeared at different locations as expected [94]. In Figure 3.6a, dense dislocation rich regions are observed but when the specimen was tilted by a few degrees, they disappeared as in Figure 3.6b and Figure 3.6c, tilted images of the same region. Even at those regions where there seemed to be no dislocations, there is a good chance of having considerable amount of dislocations visible at another angle when b is not perpendicular to g. According to the invisibility criterion for dislocations, $\vec{g}.\vec{b} = 0$ where $\vec{g}$ is the diffraction vector and $\vec{b}$ is the Burger's vector of the dislocation, when the condition is satisfied the dislocation becomes invisible because the contrast is very weak [95]. Higher magnification image, Figure 3.6d, indicates that due to high dislocation density other features become hard to identify, especially the grain or cell boundaries. In the image, Figure 3.6d, T phase dispersoids are seen among the dislocation forest and in spite of their large sizes the boundaries of even these particles cannot be distinguished from the matrix. This indicates the level of difficulty to observe much smaller phases such as GPB zones and S phases, which are usually coherent with the matrix, in a severely deformed region.

3.2.2.2. *Peak Aged State*

In standard Al 2024 after 11 hours aging, microstructure involves precipitates in the shape of needles as presented in Figure 3.7consistent with the literature. The distribution of precipitates seems to be randomly oriented relative to the grain but they are either parallel or crossing one another at a certain angle. At this stage, when hardness is high, the coherency of precipitates is expected to create strain fields around themselves such as the ones encircled in Figure 3.7b while at certain angles precipitates are observed as clear needles which may indicate partial coherency of the precipitates along the interphase boundary or a low mismatch of lattice parameters between precipitates and the matrix. In the third image, Figure 3.7.c, a triple junction is observed. It is definitely a thicker boundary than normal probably due to heterogeneous nucleation and growth of S precipitates along the junction through the boundary. Although the size of the precipitates seems to vary between

200nm and 500nm, the strain field around the precipitates avoids distinguishing between individual precipitates. This necessitates the imaging in dark field where the diffraction spot is chosen for individual group of precipitates.
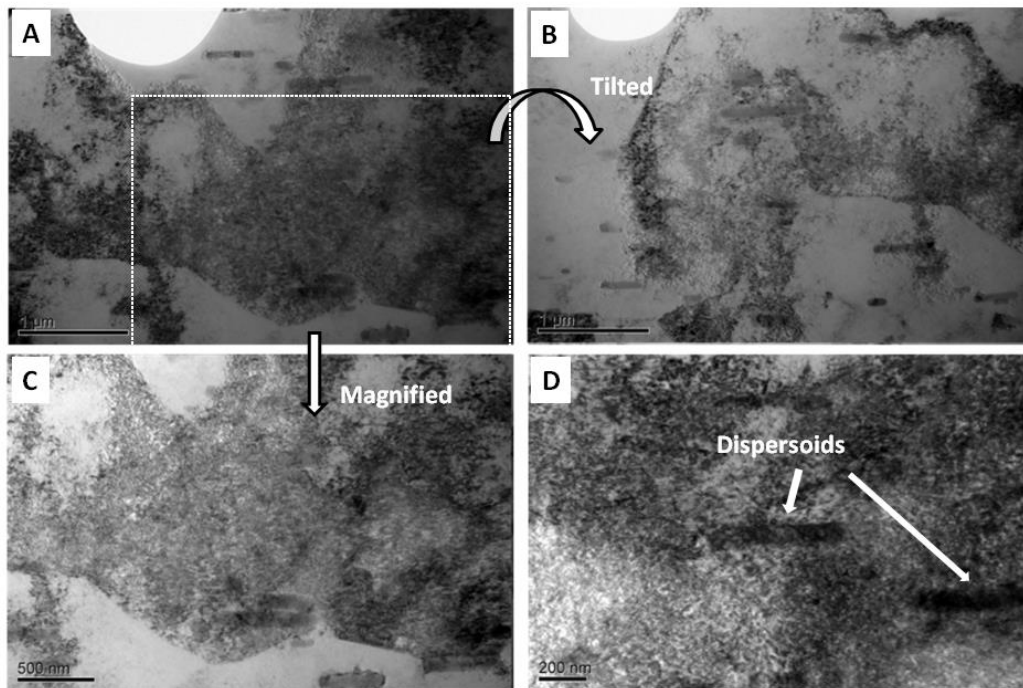
Figure 3.6. TEM images of the ECAPed structure of Al 2024 (a), (b), (c) belong to the same region but at various tilts; (d) is closer view of a dislocation forest.)
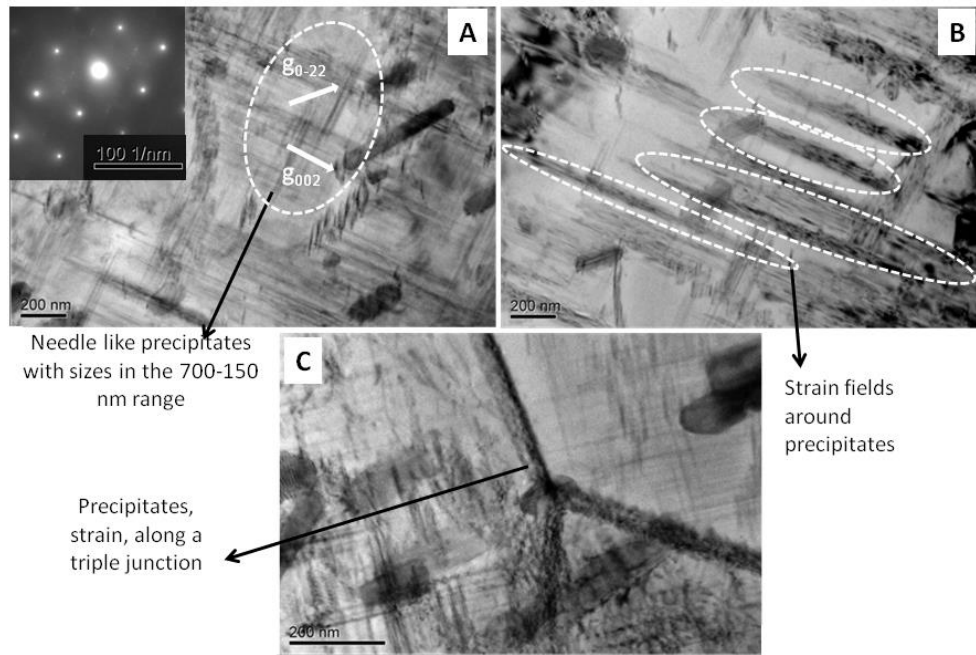
Figure 3.7. TEM images of solutionized and aged Al 2024 for 11 hours.

A common feature of Al 2024 microstructure is the T-phase dispersoid as mentioned in theory. They serve as obstacles for grain growth and are often associated with some strain around them which may be due to the pinned dislocations or nucleation of S precipitates around them. The orientation relation of the T-phase dispersoid with the matrix may also have a connection to the observed strain. Twin formation inside the dispersoids is reported in a study which indicates low stacking fault energy and a high mismatch of SFE's between the dispersoid and the matrix which is an element increasing the strengthening effect of the dispersoid.
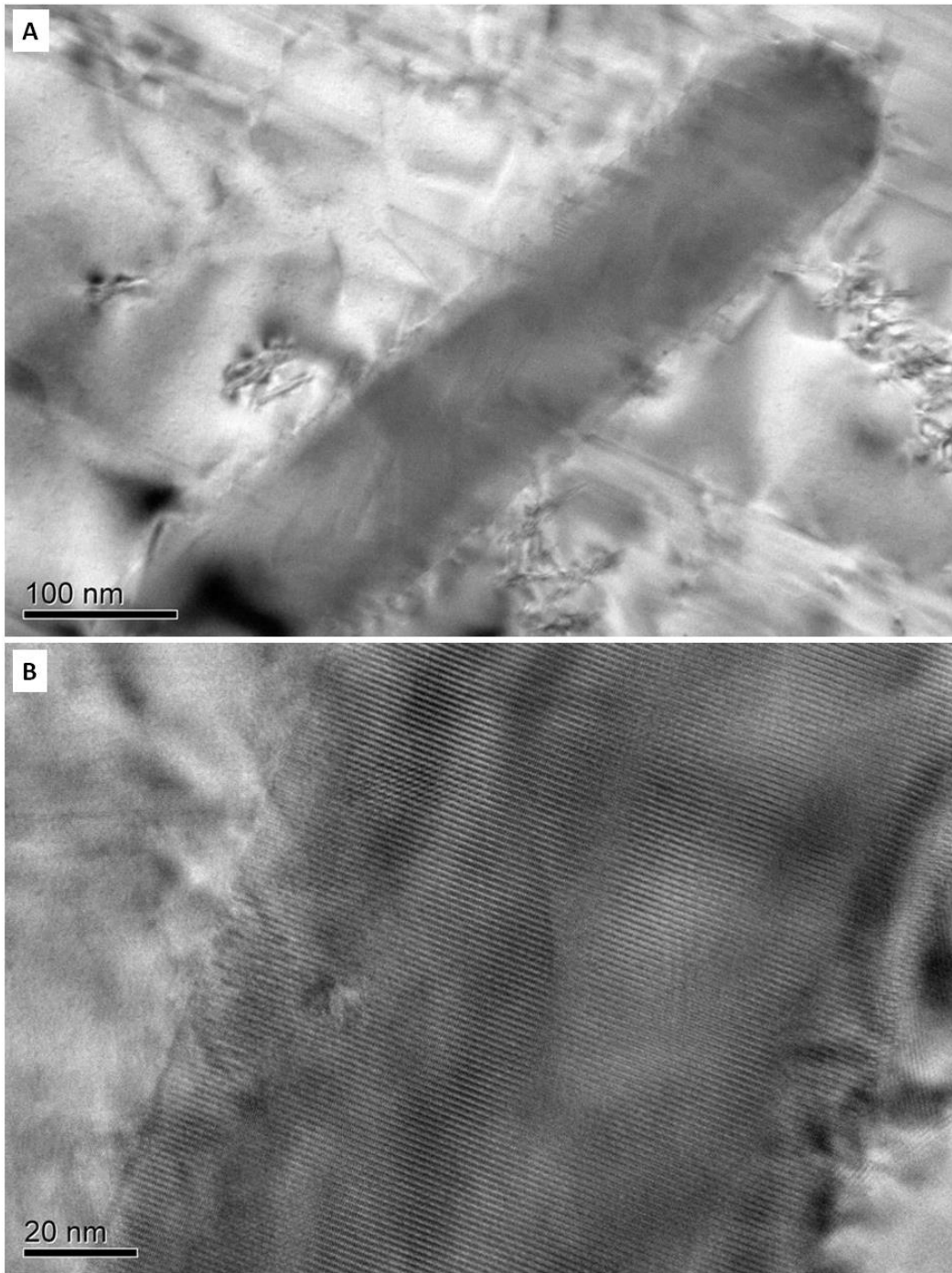
Figure 3.8. T-phase dispersoid in solutionized Al 2024.

In ECAPed and an hour aged sample, the precipitate size was found to be obviously smaller compared to the solutionized and aged sample. On the other hand due to the already present strain fields resulting from high dislocation density, the size of the precipitates cannot be determined with accuracy. At certain tilts (angles) however, it becomes possible to observe precipitation structure in the form of small needles dispersed throughout the grain. It is possible that the needle like appearance may be the strain field of each precipitate rather than the actual precipitates so DF imaging is required for adequate investigation of precipitate size and morphology. The various precipitates are imaged in Figure 3.9 at suitable angles for proper observation so precipitate structure in the form of small needles dispersed throughout the grain is visible. Yet they are hard to distinguish due to the dislocations and deformed structure.
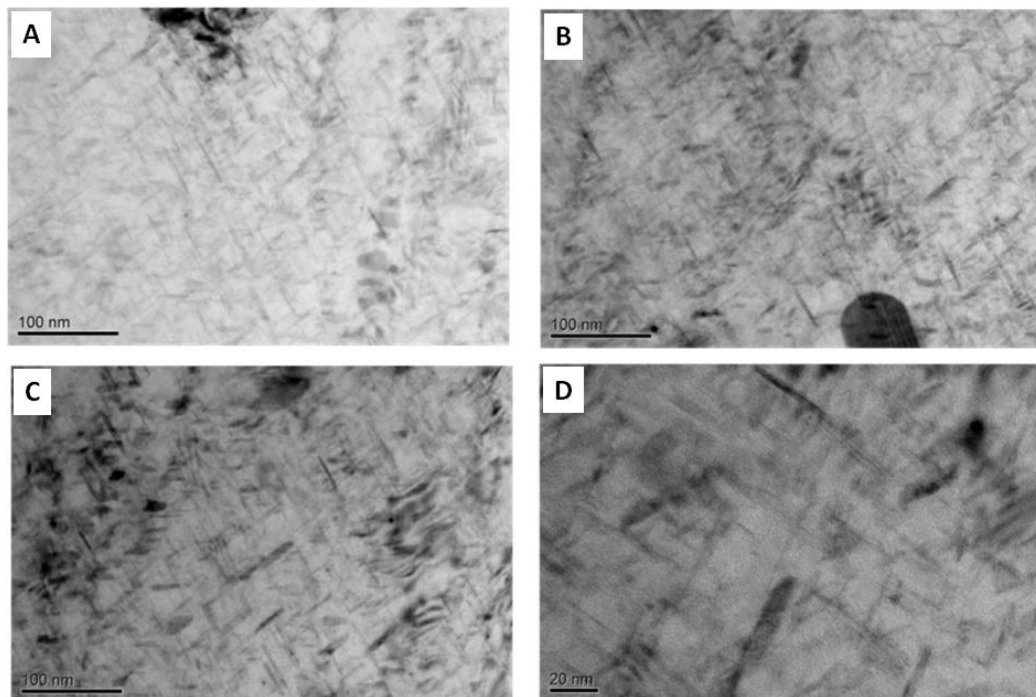
Figure 3.9. Near peak aged (at 190°C, 1 hour) Al 2024 microstructures at various regions and two different magnifications.

The precipitation at 190°C for an hour was found to be effective in some regions on the rearrangement of dislocations into cells as presented in Figure 3.10a and b. The cell sizes were found to be about 300 nm which is large enough to be considered as subgrains. Although it was difficult to observe the precipitates in regions of high deformation, a few images of precipitates dispersed into the dislocation forests can be seen in Figure 3.10c and d. HREM images on the other hand could not be attained due to the strain fields around the precipitates that may easily interfere with the precipitates. It is necessary to remember that GPB zones are usually observed in the form of strain fields hence the differentiation between coherent S/S′ precipitates with GPB zones cannot be possible at sizes of a few nm thickness. The higher magnification images in Figure 3.10 d, e show two different forms of precipitates. On the left among the dislocations small white, shorter precipitates are observed whereas on the right the strikes of either precipitates or GPB2 zones are observed.
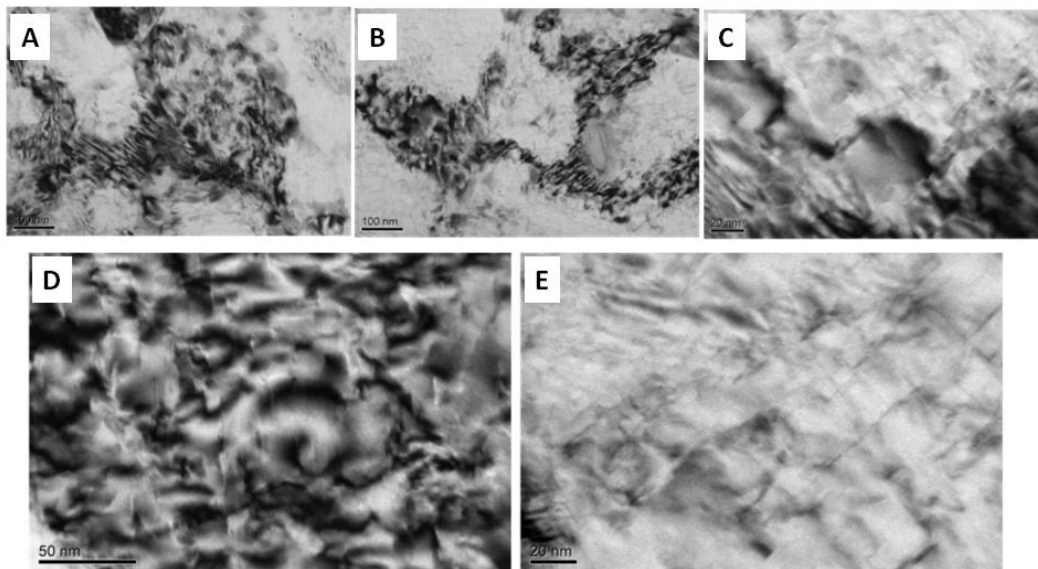
Figure 3.10. TEM micrographs of the ECAPed and pre-peak aged Al 2024, (a, b and c) rearranged dislocations form cells of a few 100 nm and (d and e) precipitates.

3.2.2.3. Over-Aged State

Solutionized and quenched into a supersaturated solid state, Al 2024 alloy initially dissociated into GPB zones and a less supersaturated alpha Al followed by formation of coherent S/S′ phase. The final stage is the formation of stable and incoherent S precipitates of Al_2CuMg as in the case of 24 hours of aging at 190°C. The structure has now become nearly homogeneous in the sense that precipitates are all around the structure with a nearly constant density. Growth of precipitates into longer needles is obviously noticed in addition to the improved network between the precipitates in Figure 3.11.

The hardness of ECAPed and over-aged samples dropped from 174 HB to 164 HB after aging 20 more minutes than near peak aging time of 1 hour. Unlike in over-aged standard sample, the precipitate density was found to be similar to the near peak aged sample, hard to detect an obvious change throughout the sample regarding the precipitates. In Figure 3.12, two types of precipitate regions are given. The first column of images (a, c) belong to cell like interconnected precipitates and the second column (b, d) is composed of parallel array of precipitates aligned together with no or little perpendicular precipitates. This may be an indication of different structures co-existing in the same sample or observation of the same structure at varying orientations. No significant difference from the near peak aged sample in size, distribution or observation of the precipitates can be noticed in over aged ECAPed sample. However in Figure 3.13, sign of recrystallization can be seen. The arrow marks an obvious new ellipsoid grain formed along the deformation direction. It should be noted that the newly formed grain includes either precipitates or some strain due to precipitates.
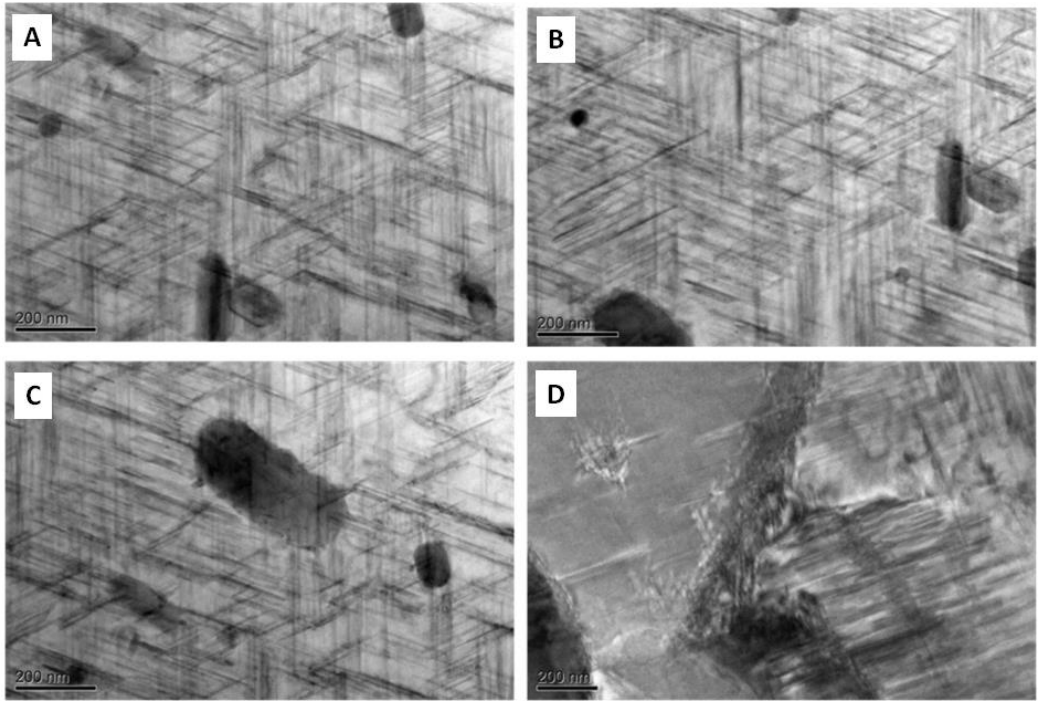
Figure 3.11. TEM micrographs of the solutionized and over-aged Al-2024 alloy (190°C/24 h.)
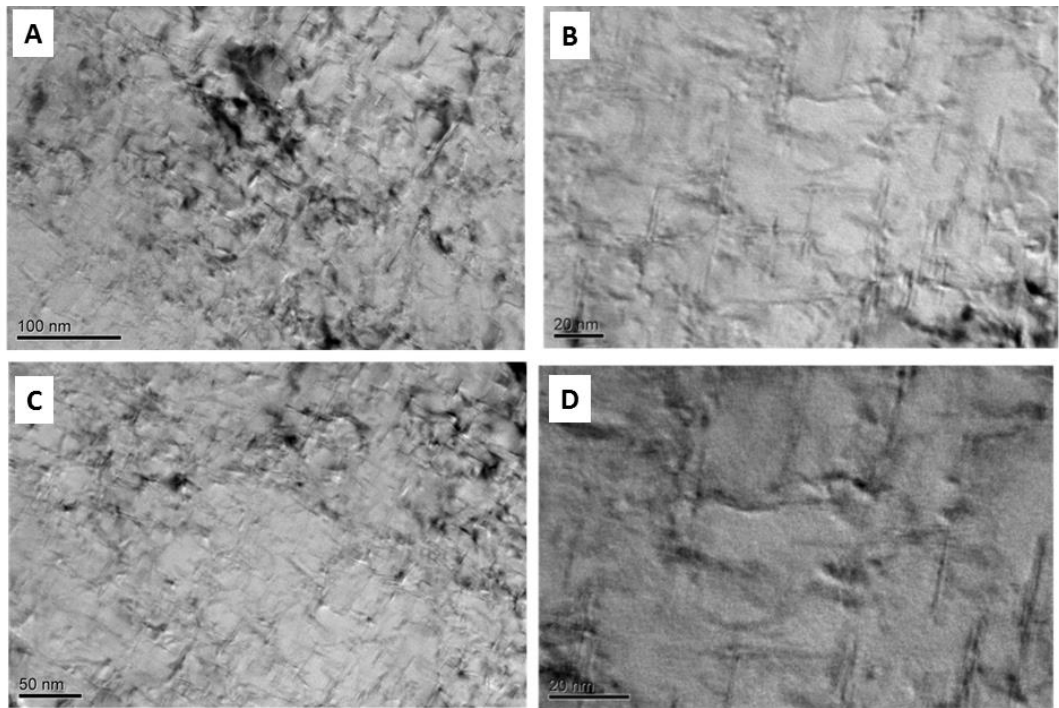
Figure 3.12. TEM micrographs of the ECAPed and over aged Al 2024,(a and b) precipitates in two directions (c and d) precipitates in single direction (190°C/ 80 min.)

Figure 3.13. TEM images of the ECAPed and over aged Al 2024 (190°C/ 80 min.)

The initiation of recrystallization may partially be considered as the cause of hardness drop of 10 HB accompanied to over aging. The HREM images of ECAPed and over-aged structure could be seen in Figure 3.14. HREM images of precipitates were obtained, most probably due to the lack of strain fields around the precipitates. In near peak aged sample, high resolution images were not possible to focus due to the strain present around the precipitates whereas in over-aged sample they could be focused. The lack of strain may be either due to the loss of coherency of precipitates or loss of dense dislocation structure through recrystallization. The ease of observation may be a sign of recrystallization progressed preserving the deformation orientation due to the presence of homogeneously distributed precipitates throughout the sample. On the other hand, the reason behind ease of observation could possibly be the incoherency of over-aged precipitates. This may lead to a rough conclusion that although a visual difference could not be detected, either recrystallization or over-aging or their combined effect caused the hardness drop.
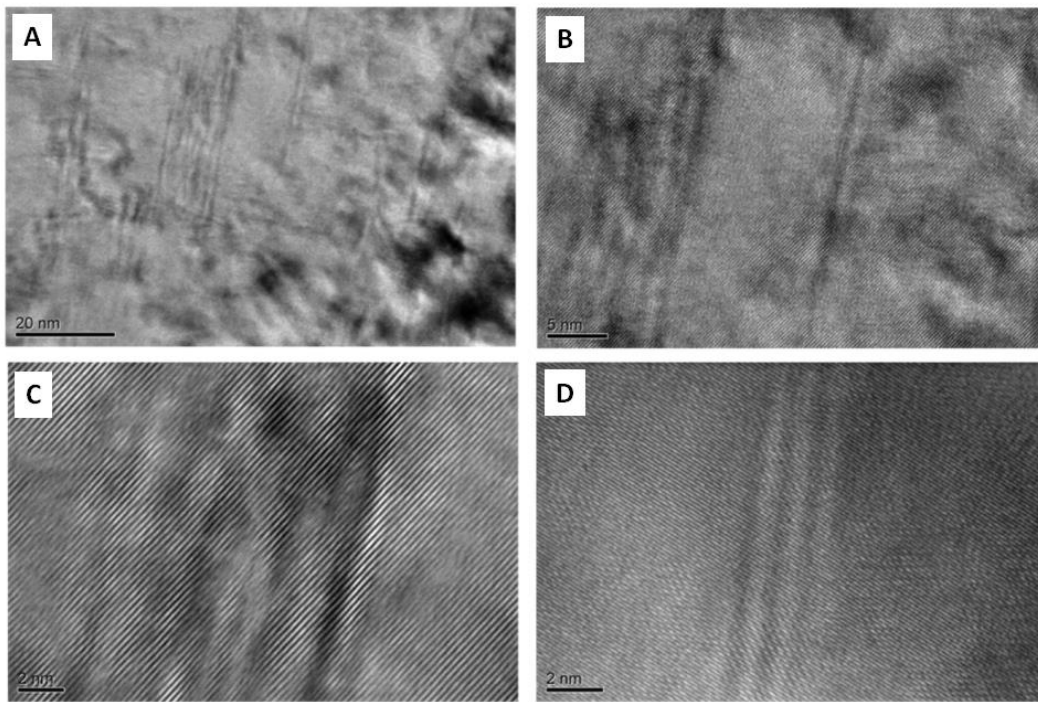
Figure 3.14. HREM images of precipitates in ECAPed and overaged Al 2024

CHAPTER 4

INVESTIGATIONS ON THE INHOMOGENEITY OF ECAPED Al 2024

Production always involves errors, deviations and inhomogeneity throughout a certain sample or a certain batch regarding composition, defects, mechanical properties, etc. New production techniques, as in the case of severe plastic deformation (SPD), may initially encounter these problems but as they evolve, these issues are eliminated leading to a commercially applicable system. During this evolution, the investigation of inhomogeneity in a single pass ECAPed Al 2024 is important because in the case of age hardenable alloys, single pass ECAP leads to best hardening effect but due to the absence of homogenization gained through multiple passes, inhomogeneity is a major disadvantage. As a consequence, to investigate the inhomogeneity and the effect of aging on the final microstructure is absolutely necessary by means of thorough investigation before, during and after aging.

In this chapter of the study, main emphasize will be on the two inhomogeneity issues related to ECAP process and Al 2024. It should be noted before going any further, that in a direct analysis of ECAP system through conducting experiments in different conditions was not possible in this study. The samples were produced in the previous study [93] and further work on the production method or the production parameters are beyond the scope of the study. However, huge variations in hardness among different samples were detected. To understand the possible cause or causes of this variation, the differences in composition and production parameters were detected as Mg content and back pressure, respectively. Using the data obtained from the already available samples, the effect of backpressure and Mg content on

the hardness variation among different samples was briefly discussed as parameters that may or may not have an effect on the standardization of ECAP products. To summarize, the first part of this chapter presents the results and discussion on the variation of hardness in samples processed through the same ECAP die. In the second part, an individual sample was investigated regarding the inhomogeneity in terms of micro-hardness variation and the response to precipitation at 190°C was analyzed for the possibility of elimination of the inhomogeneity.

4.1. LITERATURE REVIEW

4.1.1. Homogeneity of ECAP

Severe plastic deformation (SPD), an alternative technique to classical deformation hardening methods, aims to obtain ultra-fine grain structure, lower than 1 μm, with high angle grain boundaries uniformly distributed throughout the volume, free from the cracks or damage [61]. Among the SPD techniques, equal channel angular pressing (ECAP) and high pressure torsion (HPT) are the most promising ones. ECAP is comparatively simple and easy to perform on various alloys and composites. It is applicable to large billets and it is said to provide complete homogeneity in the final product when multiple passes are applied [96]. ECAP can be used for samples as large as 4 cm in diameter and 10 cm in length [77]. In contrast, using HPT, an exceedingly ductile Al sample 8.57 mm in height and 10 mm in diameter could be hardly produced due to the sample size limitation being so dominant [97]. In the case of the Al 2024 alloy, when the production was limited to 1.5 mm in thickness and 14 mm in diameter, a hardness value of 275 HV was attainable [98].

In practice, however, the final structure after the ECAP process may not be as homogeneous as desired. Finite element analyses in ECAP have shown that the lower part of the sample has less strain [99, 100], which results in inhomogeneity in both the microstructure and mechanical properties of the sample. There are several studies on the elimination of this inhomogeneity through annealing such as Qiao et.

al. (2009) [32] or further ECAP processing [101]. Usually homogenization in ECAP is achieved by increasing the number of passes, but even this treatment does not always result in total elimination of inhomogeneity. For instance, ECAP processing of age-hardenable Al alloys of 2024 and 6061 has resulted in a minimum hardness deviation ($\Delta H = H_{maximum} - H_{minimum}$) of 15 HV after 6 passes. In fact, a difference as high as 30HV was observed in some regions of these samples [101]. There also exist a study that led to a very low ΔHV of 4 HV for pure Al after four passes when the ECAP was carried out inside a copper tube [102]. These varied results of the previous studies indicate that there still is no agreement on the degree of homogeneity after ECAP and further studies are necessary to reveal this relationship more clearly.

4.1.2. Hardness Inhomogeneity Index

To investigate the inhomogeneity during deformation, one of the major tools is the finite element method and FEM analysis studies define the inhomogeneity using a parameter called strain inhomogeneity index that is shown by:

$$\varepsilon_i = \frac{(\varepsilon_{max} - \varepsilon_{min})}{\varepsilon_{avg}}$$

4.1

where ε_{max}, ε_{min}, and ε_{avg} are maximum, minimum, and average magnitudes of effective strain [102, 103]. With a similar approach, a hardness inhomogeneity index can be defined as:

$$H_i = \frac{(H_{max} - H_{min})}{H_{avg}}$$

4.2

where H_{max}, H_{min} and H_{avg} represent maximum, minimum, and average hardness values, respectively. In this manner, both average values and hardness variations are included in the data analysis. The range of deviation is an important index as it calls attention to the weaker regions that may act as fracture initiation sites.

The deformation inhomogeneity manifested in the first pass may diminish to a certain extent by consecutive ECAP passes. Ultra-fine grain structure can only be achieved through a certain amount of passes, but the minimum grain size achievable is said to be dependent mainly on the amount of strain induced after the first pass. The first ECAP pass has the most significant impact on mechanical properties and final grain size [61, 96]. On the other hand, subsequent passes are regarded as a means to attain homogeneously-distributed grains of high angle grain boundaries [77]. Multi-pass ECAP process is essential if the strengthening mechanism depends solely on grain refinement through deformation [66]. However, in the case of age-hardenable alloys, ECAP and age-hardening should be considered together. Different approaches are proposed for the optimization of these two strengthening mechanisms, (i.e. grain-size reduction by deformation and precipitation hardening by aging). Pre-ECAP aging, dynamic aging and post-ECAP aging are examples of alternative choices that are carried out in combination with multi-pass or single pass ECAP [12, 82, 93, 104–106].

Previous studies considering the pre-ECAP aging, showed that over-aged 2024 Al alloy subjected to multi-pass ECAP holds a maximum hardness of 187 HV after 3 passes at 150°C, and further ECAP process results in a hardness drop [105]. The magnitude of the observed ΔH values may be a result of overaging and dynamic recrystallization. Dynamic precipitation shows better results in terms of hardness enhancement than dynamic recrystallization. A study by Kim et. al. [107] on Al 6061 showed a remarkable increase in strength after four ECAP passes at 100 °C, but a minimum ΔH of 15 was obtained.

When multi-pass ECAP is considered, post-ECAP aging becomes less effective for both homogenization and strengthening. This is because ECAP stimulates precipitation due to the high quantity of nucleation sites on which precipitation becomes energetically favorable. Post-ECAP aging after a single pass has led to a hardness of 205 HV after 30 hours of aging at 100 °C, but homogeneity-correlated properties are not clear [82]. Post-ECAP aging is promising for homogenization,

which is an outcome of the fine distribution of precipitates nucleated at defects resulting from deformation [12, 32]. Several theories [66, 82, 98, 105, 106, 108–113] have been proposed to correlate strengthening in age-hardenable ECAPed alloys through grain size refinement by deformation and precipitation hardening by aging; yet, there is no commonly accepted explanation for the exact mechanism.

4.2.   EXPERIMENTAL PROCEDURE

Throughout the study, three ECAPed Al 2024 samples, with varied hardness values, were investigated. The samples were 18 mm wide and 45 mm long cylinders and all were quenched into 0°C ice-salt-water mixture after solutionizing at 495 °C for an hour. The same 120° die was used to ECAP them once. The back pressure was controlled by a number of Cu blocks that were sent through the ECAP channel prior to sending the Al samples. This allowed formation of different back pressures which will be mentioned as high (HBP) and low back pressure (LBP) throughout the study. The first sample (Sample A) was used for preliminary studies as discussed in Chapter 3. Porosities were observed in the sample and the information regarding back pressure was not available. The second sample (Sample B), produced applying high back pressure (HBP), was used for the inhomogeneity investigation that is discussed in the second issue of the current chapter. The third sample (Sample C), produced applying low back pressure (LBP), was used for thermal stability analysis that is discussed in the proceeding chapter. All of these samples were tested for their hardness values in the as ECAPed state as well as throughout aging. Sample A, cut perpendicular to the pressing direction, was subjected to Brinell Hardness test using 500kgf weight and 10 mm diameter ball. Brinell hardness numbers (BHN) obtained was converted to Vickers using conversion table. Sample B and C were cut at an angle of 46° parallel to the shear direction. The hardness measurements were carried out at a constant load of 4.9N and 10s of dwell time using a Shimadzu Micro Hardness Indenter. To be able to compare the results, Al 2024 samples in rectangular cross-sectioned bulk shape were also solutionized at 495 °C for 1 hour and quenched into 0°C ice-salt-water mixture prior to aging. Interrupted aging

experiments were conducted for all samples at 190°C. The aging kinetics of Sample B and Sample C, as well as the solutionized and quenched sample, were compared.

4.2.1. Precision Cutting and Map Design

HBP sample (Sample A) was chosen to be used for observation of inhomogeneity due to its higher hardness value. The sample was marked according to its orientation during ECAP as "TOP" and "BOTTOM". An illustration is shown in Figure 4.1. Cutting was performed at an angle of 46° considering the shear plane in order to observe deformation bands in pure shear condition. Two 0.5 mm thickness disks were cut adjacent to the surface of a 1 cm thick hardness sample from which the microhardness data was collected. Figure 4.1 shows the sample cutting process schematically. A thin section was also cut from the Al 2024 block which was not ECAPed after solutionizing and quenching for control purposes.
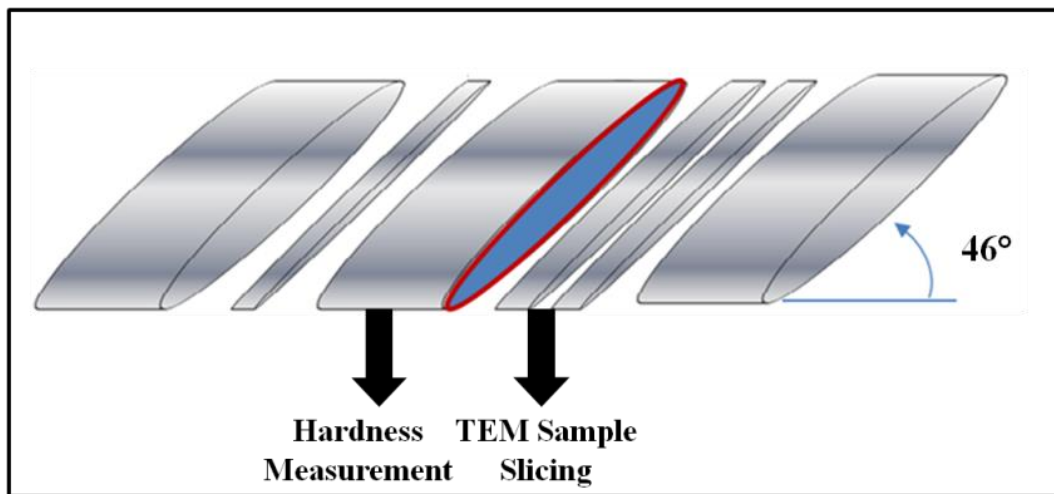
Figure 4.1. ECAP sample precision cutting for hardness measurements and TEM sample.

Prior to the aging process, all the surfaces of the samples were polished and the surface of HBP-ECAPed sample was subdivided into 16 regions of interest close to

the central part as shown in Figure 4.2. The central point was assigned as the origin (0,0) of an (x,y) coordinate system, and each hardness indentation was recorded with its relevant coordinate. The penetration of hardness indentations were about 60–70 μm in size, therefore a minimum 500 μm interval between each hardness mark (x,y) was kept to maintain data reliability. For each aging time 16 indentations were executed under a constant load of 4.9N and 10s of dwell time. The variation in hardness values throughout the cross sectional area was represented using color-coded contour maps. A similar approach was carried out for standard sample with 12 regions for each aging time whereas mapping was not executed.
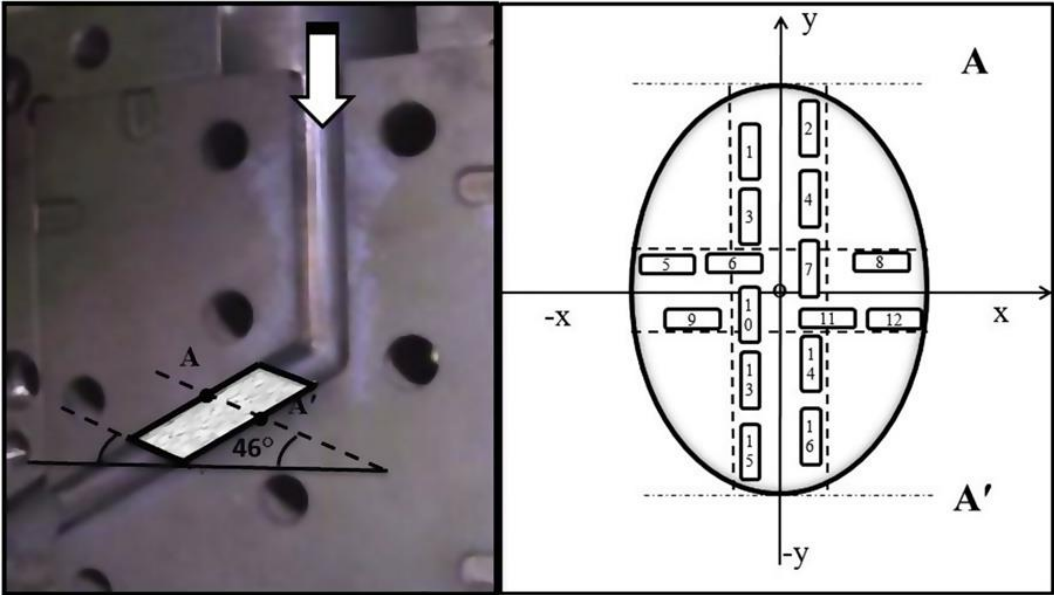
Figure 4.2. (a) The120° ECAP die with a representative sample passing through at a shear angle of 46°. The characterization studies were carried out along the AA' section shown (left).(b)The sample was separated into 16 regions by locating multiple guidelines as shown, two of which are passing through the center, represented as (x,y) coordinate system (right).

4.2.2. Sample Preparation for Electron Back Scattered Diffraction (EBSD) Analysis

EBSD is a technique which has the capability of presenting different information about a particular sample. The grain boundary misorientation angle, sub-cell structure, size distribution, grain orientation, strain, texture and many other properties may be detected using EBSD detector of a field emission scanning electron microscope (FESEM). The sample size and the area of investigation are also advantageous especially when compared to TEM. The only disadvantage is the difficulty in producing a smooth enough surface for proper data collection. As a result, sample preparation is more tedious than a conventional metallographic specimen.

All samples were grinded using the 600-2000 range SiC grinding papers and polished using 1μm diamond polisher. The electro-polishing was carried out using two systems. Initially Streurs, Lecropol-5 was used. To obtain a surface adequate for data collection with EBSD, various etchants and other variables were tested to polish Al alloys. After each trial, EBSD monitoring was performed since the shiny sample surfaces did not always guarantee the EBSD data collection. The parameters used could be seen in Table 4.1. The optimum etchant was found to be 5% (volume) perchloric acid in ethanol. Optimum process parameters were 20 volts as voltage, 20 l/s as flow rate, 15 seconds of polishing time at 22 ˚C. The optimization could be performed for standard samples but for ECAPed samples, due to deformed structure, the quality of the polished surface obtained was below average hence a new polishing option was needed.

Table 4.1. The optimization of electro-polishing parameters for EBSD sample preparation.

Etchant	Voltage (V)	Flow rate (l/s)	Time (sec)	Temp. (°C)	Result
60%Ethanol 20%Water 15%Buthy. 5 Perchloric Acid	25	10	15, 30, 45	22	poor
60%Ethanol 20%Water 15%Buthy 5 Perchloric Acid	40	10	15	22	poor
60%Ethanol 20%Water 15%Buthy 5%Perchloric Acid	20	20	15	7, 3, RT	RT average poor
5 %perchloric ethanol	20	20	15	22	Good for Soln, average for ECAPed
5 %perchloric ethanol	20	20	5, 10, 20, 25	22	poor
5 %perchloric Ethanol	17	20	15	22	Average for ECAP

The ECAPed samples in the form of thin plates were punched into 3 mm discs to be polished using •Fischione model 110 twin jet electro-polisher, which was originally designed for TEM sample preparation. The punched discs were then electro-polished without any dimpling and thinning. The results were better compared to Buehler polisher. It was also possible to exactly locate the place of the sample. Both shear and transverse directions of the ECAPed sample were investigated at three locations, top, middle and bottom, according to the ECAP die as represented in Figure 4.2.

4.2.3. Interrupted Aging

Both solutionized and ECAPed bulk samples for microhardness measurement and thin slices for TEM sampling were aged at 190±1°C in a silicon oil bath in pairs at different baskets. After a certain time period they were water quenched and cleaned using detergent, water and ethanol. Two TEM specimens were punched for each time period at specified locations and microhardness measurements were immediately performed at predefined locations. The experiments continued until over-aging.

Time periods varied between 2 minutes to 10 minutes for each interruption during the aging of ECAPed samples, Sample B (HBP) and Sample C (LBP) while for solutionized and quenched samples, these periods were as long as 1 to 3 hours.

4.2.4. TEM Sample Preparation

TEM specimens were punched from the thin slices of samples and were thinned down to 100μm using 2000 SiC grinding paper. Dimpling was performed at •Fischione model 200 dimpling grinder and minimum 45μm deep dimples were created at both sides of the samples so that a maximum 10μm thickness remained. The samples were then electropolished at -30°C in a 10% nitric acid solution at about 10 V for 10-15 seconds until perforation.

4.3.   RESULTS AND DISCUSSION

4.3.1. Hardness Variation in Different Samples

Studies on the reproducibility of SPD products, one of which is stated in the review by Valiev and Langdon, are very rare [66]. The deviation in the properties of nearly identical samples did not get enough attention. However, for commercialization, reproducibility is one of the lead factors effective on economic efficiency accompanied with service life both of which are discussed further in the current study as well as service temperature.

The reasoning behind the variation in hardness of similar products cannot be easily determined referring to the current literature, as mentioned above, but probable causes considering small but important details will be discussed. The properties which may cause the hardness differences of the three ECAPed samples are summarized in Table 4.2. An interesting outcome is that the sample including porosity has the highest hardness. The coexistence of pores and high average hardness value may indicate a heavier strain, enough to cause defects observed in the form of pores. Sample A could not be identified according to the applied back pressure so it is not possible to relate the high hardness to back pressure for this particular sample. On the other hand, the porosity observed may have been already present in the sample before ECAP as a low quality mill product. Besides sample defect there are two parameters worth to investigate; back pressure and Mg content which are small but major differences detected between Sample B and C.

Table 4.2. Various properties of the samples

	Observations	Hardness (HV)	Hardness Deviation	Back Pressure	Mg content	Cu/Mg
Sample A	Porosity	188	6.3	NA	1.95	2.32
Sample B	No defect	180.2	3.5	High	1.94	2.34
Sample C	No defect	164.6	4.1	Low	1.72	2.56

4.3.1.1. Effect of Back Pressure

In literature, back pressure is stated to be effective on crack-free production using ECAP as well as to obtain a more homogeneous structure. Another benefit of back pressure on Cu, in the presence of 400 MPa back pressure, was found to be a grain refinement improvement from 0.24 microns to 0.18 microns. Since the final grain size is understood to be determined at the first pass of ECAP, the most dominant

effect of back pressure could be expected in the first pass [96]. The easiest way to impose back pressure is to increase the level of friction. As a means to increase the friction, especially at the exit, a viscous/ductile medium was proposed to be inserted at this region.

Actually there are no studies on what will happen in a system of multiple samples with ductile medium as Cu blocks at the exit and in between. For this purpose, finite element analysis using various analysis programs, Simufact, Deform and Marc were initiated by Dr. Şimşir's group, experienced on the subject [114] yet, probably due to the multiple deformable-deformable contacts, the simulations could not continue after a certain point. The images regarding the simulation trials are presented in Figure 4.3. The order and relative sizes of Cu block (c1) and Al (a1) were implemented in the system; in either of the simulations a strain of about 0.8 was reached at the inner corner of the Cu block while the outer corner remained at values of 0.5-0.6. The simulations were interrupted by the program when the contact surface of two different Cu blocks (c2-c3) entered the deformation zone. The contact surface of Cu and Al (a1-c1) is also shown in the upper simulation. When it was clarified that the simulations in the presence of deformable-deformable contacts could not be finalized, to see the effect of feeding order in the case of a long whole billet simulations were carried out. The results are presented in Figure 4.4.

Calculated strain distributions are seen as half sections in the image and the strain towards the exit of the die (first part to pass through the die) shows the least amount of strain. The homogeneity of the strain distribution is best at the center and the highest strain values accompanied with high inhomogeneity are achieved at the portion last to enter the die. The lowest strain distribution is found to be 0.2-0.55 while the highest is 0.3-0.9 corresponding to 22-73% and 35-145 % cold work, respectively. The middle region, which shows the most homogeneous distribution with the strain range 0.55-0.80, is equal to a cold work of 73-122%.
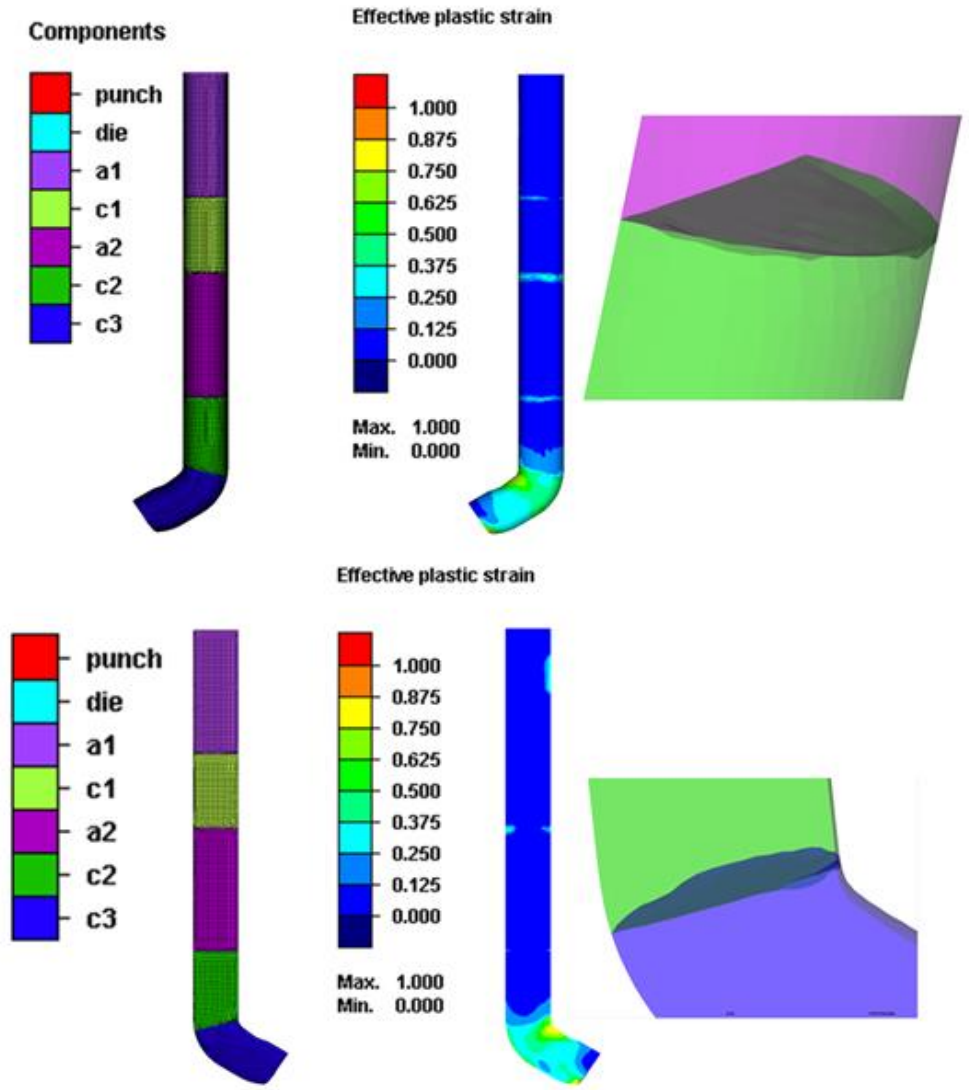
Figure 4.3. The simulation trial results of the ECAP system used in the study.
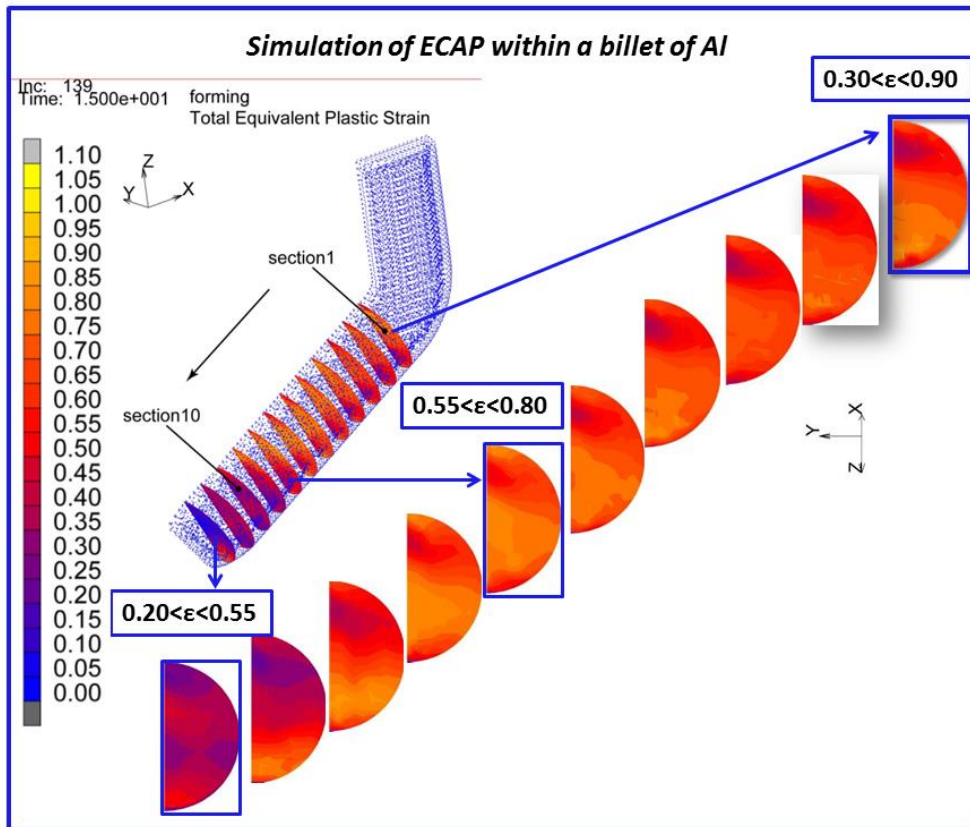
Figure 4.4. The simulation of an Al billet through 120° die.

The hardening behavior of Al 2024 with cold working is shown in Figure 4.5 which is adopted from Zhao et. al. [115]. A linear relationship is easily noticed hence the line is extended towards higher cold working ranges. Regarding the hardness values in hand, Sample C corresponds to ~60% cold work, equivalent to 0.47 in terms of strain, while for Sample B, the values are ~92 % and 0.65 for cold work and strain, respectively. In the light of the strain maps produced through simulation, it is probable to have Sample B at the middle regions and Sample C close to the end which is not far from the actual case. Although the order of Sample A is not well known, regarding the positions it may belong to the last loadings. The results of the simulation supports the idea that the order of the samples, hence applied back pressure, is a major influence on the hardness inhomogeneity among the samples, yet the values mentioned above may be different from the actual values. It is also

possible that the strain caused by ECAP may have a slightly different resultant hardness than cold working.
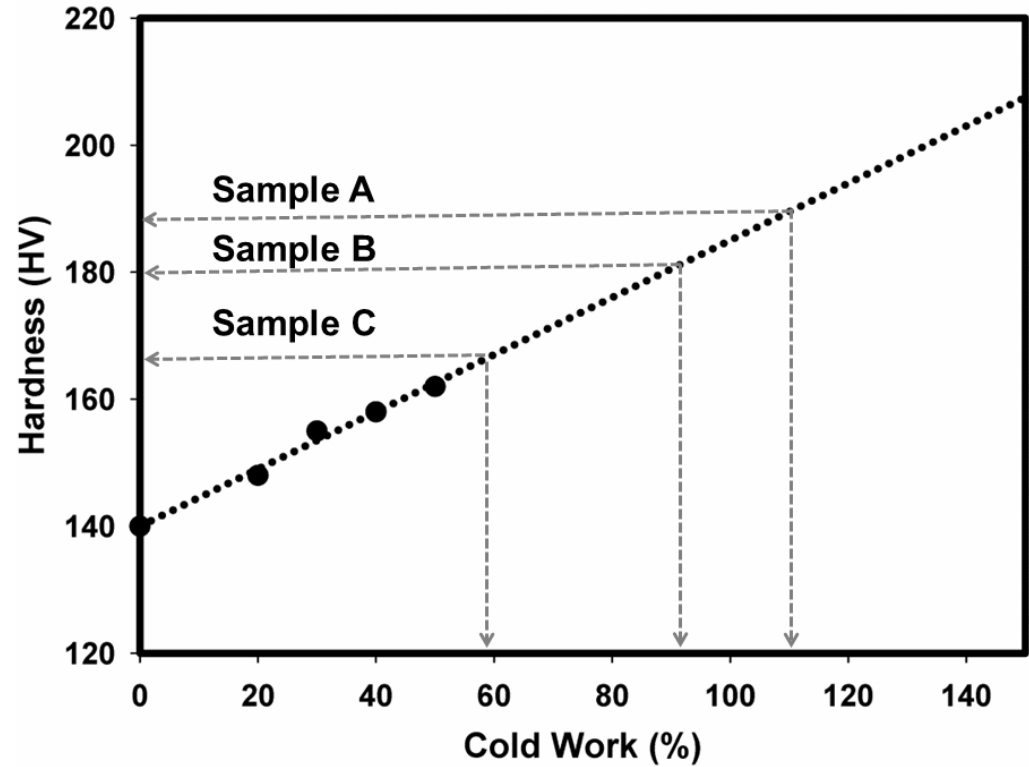
Figure 4.5. Hardening of Al 2024 by cold work amount, adopted from [115]**.**

4.3.1.2. Effect of Magnesium Content

The samples used in the experiments were commercial products so the chemical compositions were checked using EDS analysis equipment of FESEM at a magnification of 250X and a working distance of 10 mm with a death time of about 39 to be as accurate as possible. In case of any variations due to optimization, the data were collected at the same session one after another. 15 data from each sample, for a time span of 90 seconds, were collected. The chemical compositions are found

presented in Table 4.3. The major significant variations are observed in Mg and Si content.

The high Si content (which is in the range of specifications) have effect on solidification temperature range of the alloy hence may be the cause of casting porosity observed in Sample A. Other than porosity, there is no direct relationship with Si and work hardenability and it is solely high in the first sample.

The second difference is in Mg content. There are two important facts to be pointed out regarding the liability of EDS on Mg content and the possible effect of Mg in Al alloys. First of all, since Mg is a low Z element, the standard deviation of EDS for Mg was calculated as 0.09-1.14 which is very close to the difference in Mg content 0.23. On the other hand, high Mg content in Al alloys was indicated to increase the precipitation hardening effect after cold working. It is also stated that being an effective solute atom, Mg may increase the stored energy, strain and hardness, in Al alloys during cold deformation [1]. In the review of Langdon and Valiev [96], it has been stated that Mg has an effect on the temperature rise during deformation as well as the final strength. The comparison was carried out between Al-1Mg and Al-3Mg. 2% Mg increment was found to increase the strength from 100 MPa to 170 MPa. With a very rough approximation 0.2% Mg could cause 7 MPa of UTS increase but to be able to obtain 15 HV hardness increment, at least 45 MPa raise in UTS would be required. As a result the variations as small as 0.1-0.2% in Mg content cannot be responsible for hardness deviation of 15 HV after ECAP process by itself but may play a role to some extent. To conclude, low Mg content could be one of the factors leading to the deviation in hardness after deformation but it cannot be the major cause of the inhomogeneity among samples. On the other hand, it would be a valuable contribution to investigate the effect of Mg content on strain levels of Al 2024 (rather than pure Al) during ECAP.

4.3.1.3. Combined Effect of Back Pressure and Mg Content

The hardness variation among samples may be a result of both Mg content and back pressure; hence passing order of the samples through ECAP die. During the passage due to high friction and deformation most of the work is converted to heat. Heating due to the friction during ECAP may cause rapid hardening which is easier in the presence of higher Mg. Mg is also effective on increasing the temperature increment during ECAP. It might be possible that the sample entered into the die last with a higher Mg content may have experienced a rapid hardening at relatively higher temperatures during deformation more than the other/s. It is stated that the increased Mg content increases the rapid hardening amount [51] and a temperature raise of a few minutes or even 60 seconds were enough to observe rapid hardening. It might be possible that sample C which has the lowest Mg content experienced none or very little rapid hardening while Sample A and B, with higher Mg content, experienced a more effective rapid hardening. The differences in Cu/Mg ratio represented in Table 4.2 shows that Sample C has highest Cu/Mg ratio which is a factor lowering the effect of rapid hardening during precipitation.

Table 4.3. EDS Analysis of Sample A, B and C.

	Al	Cu	Mg	Mn	Si	Fe	Zn	Ti	Cr
Sample A	92.09	4.53	1.95	0.59	0.40	0.24	0.11	0.07	0.03
STD Dev	0.20	0.10	0.14	0.03	0.06	0.03	0.06	0.02	0.02
Sample B	92.36	4.54	1.94	0.59	0.11	0.24	0.10	0.08	0.05
STD Dev	0.16	0.09	0.12	0.05	0.03	0.05	0.07	0.02	0.03
Sample C	92.62	4.41	1.72	0.59	0.12	0.24	0.14	0.07	0.05
STD Dev	0.18	0.08	0.09	0.03	0.06	.0,.03	0.07	0.02	0.02

To conclude, the most probable reason of hardness inhomogeneity among samples is the order of the samples which may be considered as back pressure as well as ECAP temperature variation. Secondly Mg content may promote the work hardening amount in the Al 2024 samples. A minor probability is the dynamic rapid hardening during ECAP.

4.3.2. EBSD Results

In the EBSD images of the ECAPed sample, two directions were investigated. The sample was cut through the shear direction at an angle of 46° and EBSD images of top, middle and bottom parts were collected. The 0.5 cm thick sample cut at the shear angle was divided into two from the transverse direction and again the top, middle and bottom regions were inspected.

In Figure 4.6 A, B and C (transverse direction), there is no significant difference other than the small grains of the middle part (B). At this direction no clear sign of difference regarding EBSD images could be noticed. However when the shear direction is inspected, the bottom part of the sample was clearly observed to have lower strain in comparison to top and middle regions. This may be indicative of the dead zone at the corner of the die mentioned in the literature [96]. This result is also in agreement with the hardness results. However, at the transverse direction the dead zone or corner gap effect could not be identified by EBSD.
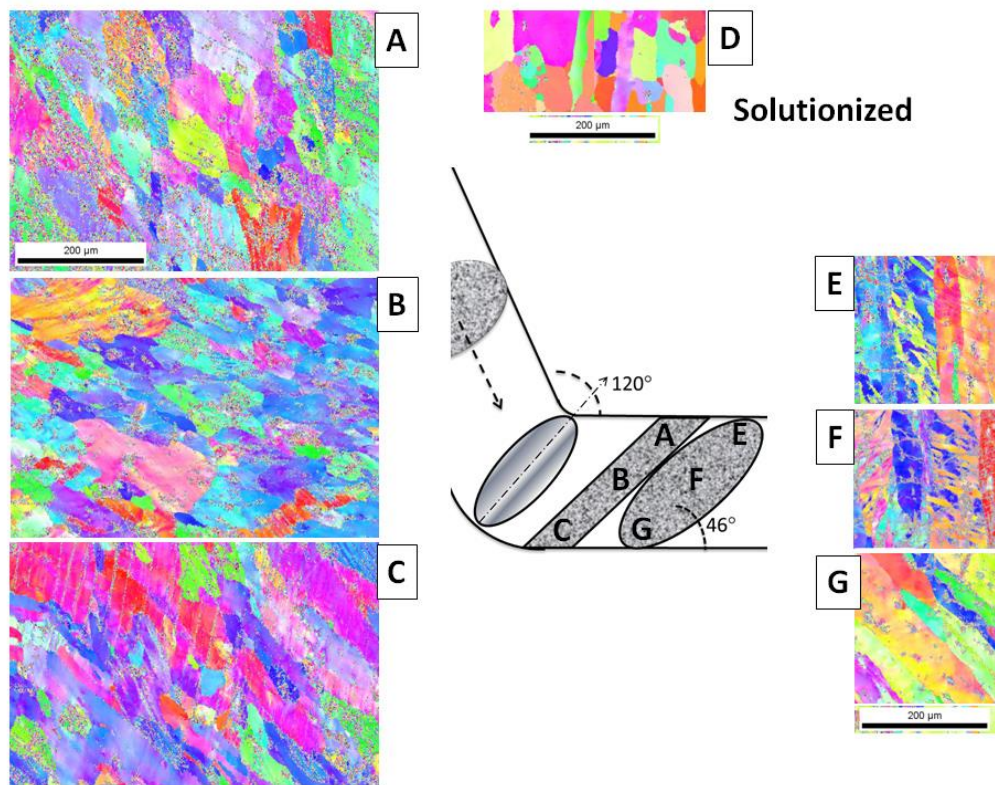
Figure 4.6. EBSD images of ECAPed sample in transverse direction (a), (b), (c) and shear directions (e), (f), (g), at top, middle and bottom of the sample, respectively accompanied with (d) Standard sample and schematic representation of the sample

4.3.3. Microhardness Data and Aging Behavior

The microhardness variation through aging can be observed in Figure 4.7 and Figure 4.8 for the standard and the ECAPed samples, respectively. There are certain differences between two figures:

- Time of process: The peak aging time is as low as 1 hour for Sample B (HBP ECAPed) and nearly 80 minutes for Sample C (LBP ECAPed) while for standard sample it is ~11.5 hours. Precipitation of ECAPed Al 2024 is 12 times faster than the standard sample.

- The peak aged HBP ECAPed sample (Sample B) had~50% higher hardness than peak aged standard sample.

87

- Total hardness increment: In ECAPed samples, the total hardness increment during precipitation was found to be lower than the standard sample. However when the ECAPed samples are compared there is no significant difference.

- Rapid hardening: The initial steep hardness increase which is commonly observed in Al 2024 at the beginning of aging could not be observed in ECAPed samples.
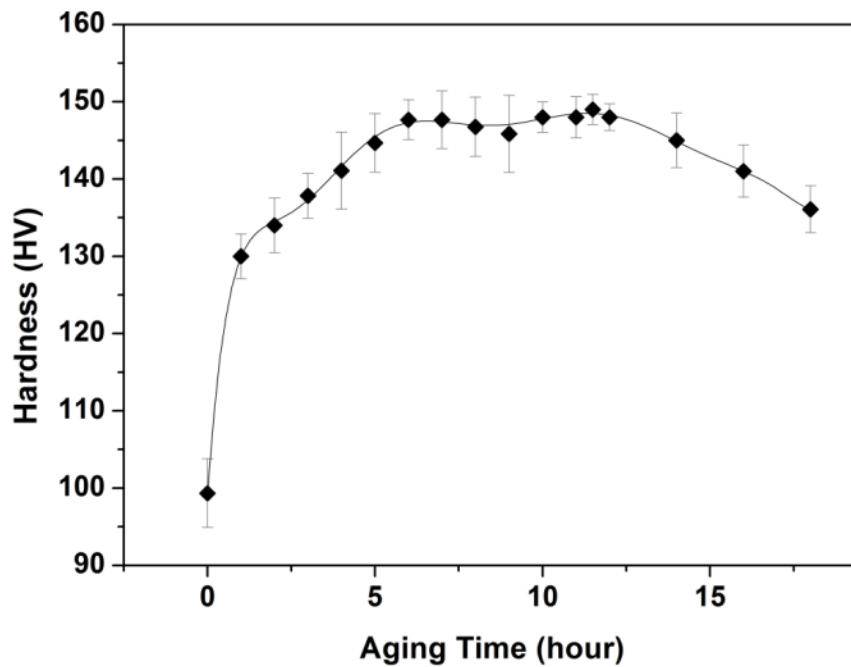
Figure 4.7. Variation of hardness with interrupted aging of standard Al 2024.
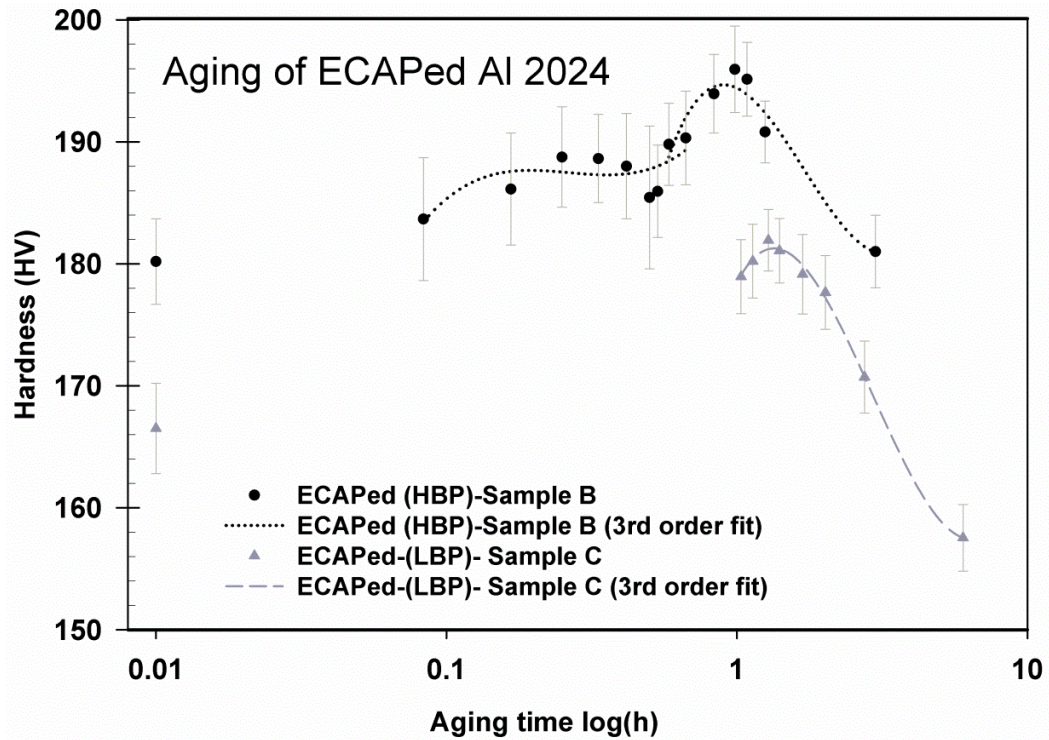
Figure 4.8. Variation of hardness with interrupted aging of low back pressure (LBP) (Sample C) and high back pressure (HBP) (Sample B) ECAPed Al 2024.

In literature, there is no consensus on precipitation sequence and hardening mechanisms in Al-Cu-Mg alloys during precipitation. It is more difficult when possible processes occurring as a consequence of severe deformation are included. To be able to detect every possible variation and to ease the understanding of the processes, the hardness plots are divided into three regions of interest although last two regions may be regarded as a single peak due to the small drop in the initial peak. Figure 4.9 shows the comparison of standard sample and ECAPed HBP Sample. Last two steps are common in both samples while the rapid hardening in standard Al 2024 is not observed in ECAPed samples. All three steps will be explained and discussed in detail.
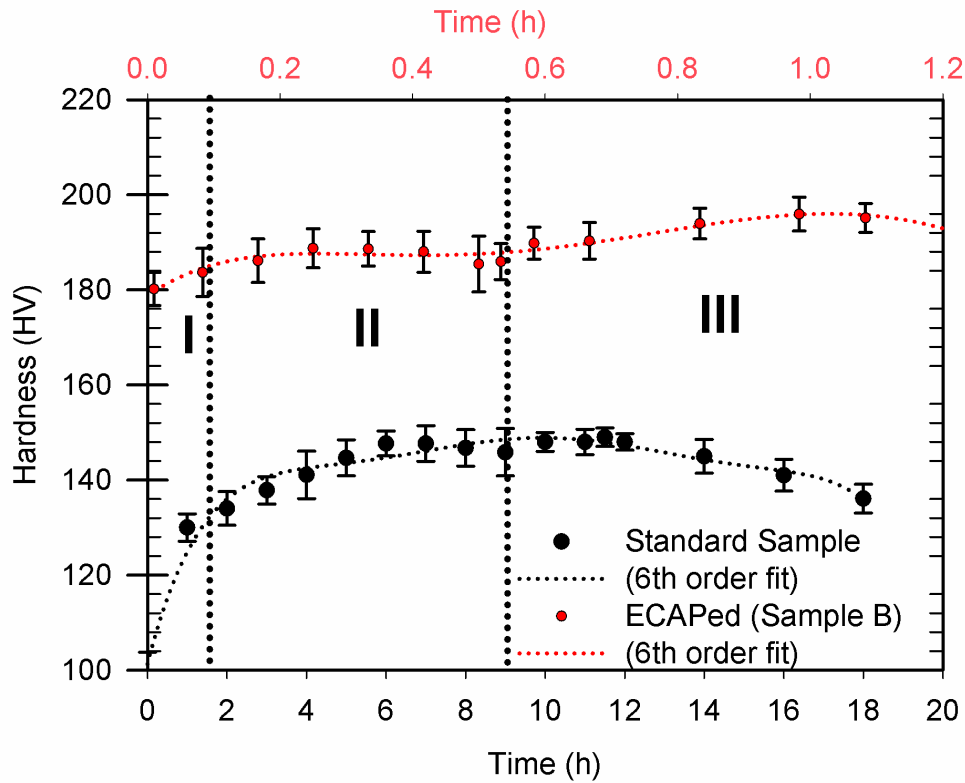
Figure 4.9. Comparison of 190°C aging behaviors of standard and ECAPed Al 2024 samples.

4.3.3.1. First Stage of Hardening

Table 4.4 summarizes the investigated stages. The hardening of standard sample during the first stage is 33.5 HV in one hour but for ECAPed samples this initial hardening is only 4-7 HV. After ECAP the hardness was 180 and 167 for HBP and LBP samples, respectively. The total hardness values would be 213.5 and 200.5 HV after the initial stage but they are calculated as 184 HV for HBP and 170 HV for LBP Samples. The loss in hardening is interesting. There are two possible causes of the drop; either the rapid hardening has occurred during ECAP or it shares the same hardening mechanism with ECAP (dislocation density increase) and the coinciding strengthening mechanisms do not operate together. To be able to decide it is important to understand the basis of rapid hardening in the standard sample.

The sudden increase of hardness, in a few minutes, at a high aging temperature is a general observation during aging of Al-Cu-Mg alloys. This behavior was tried to be explained in different studies considering different theories. Basically two recent theories are worth to mention. A common theory is that clusters of Cu and Mg are formed by the help of quenched in vacancies and these clustering lead to the formation of loop dislocations. In this theory the clusters are said to be the cause of hardening, the phenomenon mentioned as cluster hardening. But in a study by Hono [44] it was shown by HRTEM and APFIM that at the very initial stage there was no homogeneous cluster formation of Cu or Mg. However the more recent study by the same group using a more advanced Atom Probe Tomography indicated the existence of co-clusters. In another theory it is suggested that the main hardening is due to the formation of a sessile dislocation network resulted from the interaction of dislocations and solute atoms or clusters rather than directly cluster based hardening. In both of these theories and others, a relationship between solute atoms and dislocations were accepted and most recent studies have proven the existence of co-clusters of Cu-Mg and even Si [51].

There are two requirements of rapid hardening; defects, to ease diffusion, and temperature, to increase mobility. In the case of ECAP, temperature rise during deformation which may last for a few minutes is possible and a huge amount of defect is created. As a result both of the two requirements of rapid hardening may be satisfied. In an ECAP die, the possible temperature rise may lead to rapid hardening in a few minutes. This early rapid hardening may be the reason of not being able to observe the initial hardening during post ECAP aging. Another possibility is that the deformation may have decreased the temperature required for co-cluster formation as well as the time since apparently the kinetics has been speeded up due to deformation. Thirdly, if rapid hardening is a mechanism depending on density of dislocations, formation of a sessile dislocation network, since ECAP itself is a dislocation density based hardening method; the coexisting of both could yield to less hardening than expected.

4.3.3.2. Second Stage of Hardening

The second stage of age hardening is observed for all samples with different process times. For ease of measurement, peak hardness values and times corresponding to complete the peak for each sample are tabulated in Table 4.4. Time of process is calculated from the end of the previous stage to the end of the transition at the lowest hardness point. In this stage, formation of GPB zones and possible coherent or semi-coherent S phases are expected.

The hardness increments are 14.5 HV, 6 HV and 5 HV for standard, LBP ECAPed and HBP ECAPed samples, respectively. The hardening amounts are lower in ECAPed samples. This may indicate that softening mechanisms, such as recovery and recrystallization, are co-working during aging. The kinetics of transformation is found to vary a lot. For the harder ECAP sample, the time of transformation is faster. While it is about 450 minutes for standard sample, for ECAPed samples the time of transformation was in the 30-60 minutes range for LBP ECAPed sample and 30 minutes for HBP ECAPed sample. The transformation of HBP-ECAPed sample was found to be 15 times faster compared to the standard counterpart.

This increase may result from higher diffusion rates and heterogeneous nucleation of GPB zones on dislocations. Although GPB zones generally nucleate homogeneously, the aging temperature is too high and time is too short for such a nucleation. Considering the literature on the GPB zones, a heterogeneously nucleating transformation is more feasible as a consequence of high aging temperature and high density of dislocations which act as nucleation sites for GPB zones. For the case of solutionized sample, 6 hours is a long enough time for homogeneous nucleation accompanied by heterogeneous nucleation.

Table 4.4. The samples representing different stages of hardening.

	SAMPLE CODE	HARDNESS (Hv)	Δ TIME (min)	PROCESS	Possible Hardening Mechanism	Possible Softening Mechanism
STAGE 1	Standard	$HV_i = 99$ $HV_f = 132.5$ $\Delta H_v = 33.5$	90	Quenched Ageing at 190°C	Co-cluster formation	-
	ECAPed LBP (Sample C)	$HVi = 99$ $HV_{ECAP} = 167$ $\Delta HV_{stageI} = 4\text{-}6$ $\Delta HV = 72\text{-}76$	5-10	ECAPed	Work hardening + co-cluster formation	Dynamic Recovery (Dislocation tangles and cells)
	ECAPed HBP (Sample B)	$HVi = 99$ $HV_{ECAP} = 180$ $\Delta HV_{stageI} = 4$ $\Delta Hv = 85$	5	ECAPed	Work hardening + co-cluster formation	Dynamic Recovery (Dislocation tangles and cells)
STAGE 2	Standard	$HV_i = 132.5$ $HV_f = 147$ $\Delta HV = 14.5$	453	Ageing at 190°C	GPB+S	No softening expected
	ECAPed LBP (Sample C)	$HV_i = 172$ $HV_f = 178$ $\Delta HV = 6$	30-60	Ageing at 190°C	GPB+S	Recovery Recrystallization
	ECAPed HBP (Sample B)	$HV_i = 184$ $HV_f = 189$ $\Delta HV = 5$	0.25	Ageing at 190°C	GPB+S	Recovery Recrystallization
STAGE 3	Standard	$HV_i = 147$ $HV_f = 148$ $\Delta HV = 1$	147	Ageing at 190°C	GPB+S	Coherency loss and precipitate growth
	ECAPed LBP (Sample C)	$HV_i = 178$ $HV_f = 182$ $\Delta HV = 4$	30-60	Ageing at 190°C	GPB+S	Recovery Recrystallization
	ECAPed HBP (Sample B)	$HV_i = 189$ $HV_f = 196$ $\Delta HV = 7$	30	Ageing at 190°C	GPB+S	Recovery Recrystallization

4.3.3.3. Third Stage of Hardening

The third and final stage of hardening is observed in all three samples with variations in kinetics rather less than the second stage. Unlike the first two stages,

time of process in Table 4.4 is determined at the peak points because there is no exact time of completion of over-aging. In the last stage precipitation of S phase is expected while GPB zones may still coexist with the S phase. The size, distribution and coherency as well as the interaction of precipitates are important factors to determine the hardness of the system.

Hardness increments are 1 HV, 4 Hv and 7 Hv for standard, LBP ECAPed and HBP ECAPed samples respectively. Again the hardening amounts are pretty close to each other but this time they seem to be directly proportional to the degree of hardening during ECAP. Higher dislocation density leads to higher strengthening during the formation of S precipitates. It is possible that S precipitate formation is more homogeneous and easier in the presence of dislocations. The standard deviation is observed to diminish for all samples.

When the kinetics of transformation is considered the variation between samples is lower. The longest process time still belongs to the standard sample, about 150 minutes, whereas for HBP-ECAPed sample (B), it is 30 minutes which is 5 times faster than standard sample. It could be possible that the precipitates formed at the second step acted as nucleation sites and time of process is actually for the growth of these nuclei. For LBP-ECAPed sample (C) it is about 45 minutes as expected. The variations in the precipitate phase formed will be discussed in more detail in TEM data analysis part.

The final hardness reached (196 HV) is a significant improvement for Al 2024 alloy. In fact it was shown that further ECAP passes do not result in further hardness improvement but mostly help on the grain refinement of the structure [66]. In our case another advantage was the lowered time of precipitation hardening process approximately 1/12th of the commercial one.

According to the literature [57] the combination of strengthening mechanisms are added to each other. In this case the hardness values can be added to or for recovery and recrystallization, can be subtracted from to formulate the hardening behavior.

To calculate let's assume that precipitation and deformation are totally independent mechanisms. The total hardening of solutionized sample during the last two stages is 49 HV, while it is only 16 in ECAPed HBP sample. The loss of 33 H hardness may be a result of recovery and recrystallization and dynamic rapid hardening during ECAP. In the case of dynamic rapid hardening, there is no loss of hardening but the strain during ECAP becomes inefficient.

4.3.4. Micro-Hardness Maps

The micro-hardness maps obtained during aging of ECAPed sample are meaningful in three ways. First of all they show roughly the hardness distribution throughout the sample. Secondly, they indicate that the time differences during aging can be observed locally at low and high strain regions. Similar kinetic differences detected between Sample B, C and standard sample are noticed indicating the effect of dislocation density variations on kinetics in the local, much smaller scale too. Thirdly they prove that the age hardening process somehow acts as a homogenization process throughout the sample. All these three will be explained further.

4.3.4.1. Peak 1 (Stage 2)

Figure 4.10 shows the variations in hardness throughout the sample up to 30 minutes. The sample initially showed high hardness at the center and low hardness especially at the bottom. As aging continued, at 10 min, the hardness began to spread towards the sides while a rapid hardening was observed at the center. This indicates that the hardest region began age hardening first; however in15 minutes a drop began at the center and hardening continued at the sides. The hardness variations gradually increased until 30 minutes. It is not possible to explain every variation on the maps during the aging because the hardness data of the same point could not be repeated at the next time interval but a close point was measured. However the maps showed that the structure was experiencing kinetic variations throughout the sample as if multiple samples were in the structure. The variation of

kinetics have now become much more complicated than it was for individual samples because the driving force for transformation continuously changed as the transformation progressed. When the maps are reconsidered, at 30 min map the decrease at the center dominated such that the finishing time for the whole sample was determined for the first peak. It is also very remarkable that the hardness inhomogeneity became so obvious that the range of hardness extended to 176 to 200 HV range.
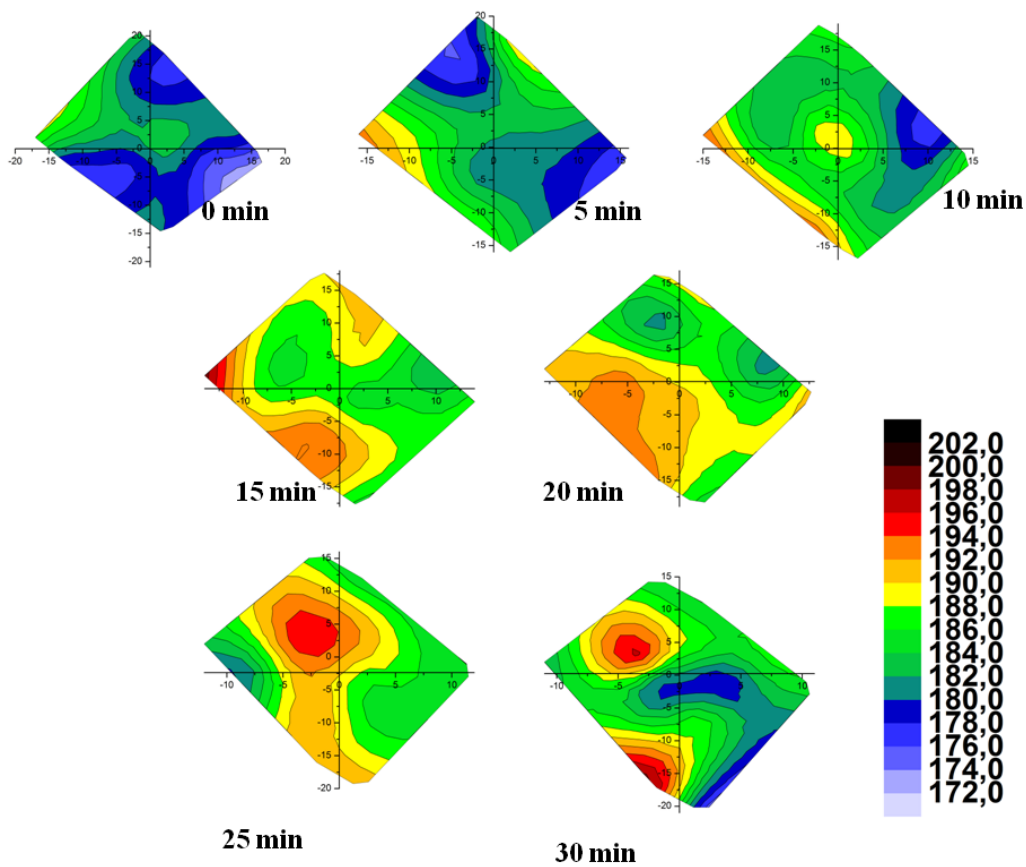
Figure 4.10. Micro hardness maps of HBP-ECAPed sample during interrupted age hardening at 190°C (0 to 30 minutes).

4.3.4.2. Peak 2 (Stage 3)

The micro hardness maps in the time range 35-180 can be seen in Figure 4.11. The inhomogeneity immediately started to drop at 35 minutes; since the improvement was high a one minute interval map was taken at 36 minutes. After 40 minutes of aging, a hardening at the top middle started and extended throughout the sample in 10 more minutes. At 60 minutes, peak aging was observed especially at the bottom which was previously least hard region. Although 60 minutes aging led to the highest hardness when homogeneity is considered the optimized microstructure belongs to 65 minutes of aging. The degree of hardening is higher for previously low hardness regions. This might indicate the absence of recrystallization at these regions. In highly deformed regions, the driving force for recrystallization is high so softening first starts at those regions.

In Figure 4.11, it is also seen that further aging above a certain time resulted in an increase in the inhomogeneity of the structure. The 180 minutes aging especially may indicate that recrystallization is progressing accompanied with over-aging. The top region might have recrystallized and over-aged while the bottom part just started to experience these processes.

The dislocation density and strain differences throughout the sample resulted in varieties in the timing of aging and recrystallization. The over-aging and recrystallization of high dislocation regions might have retard over-aging of low dislocation regions.
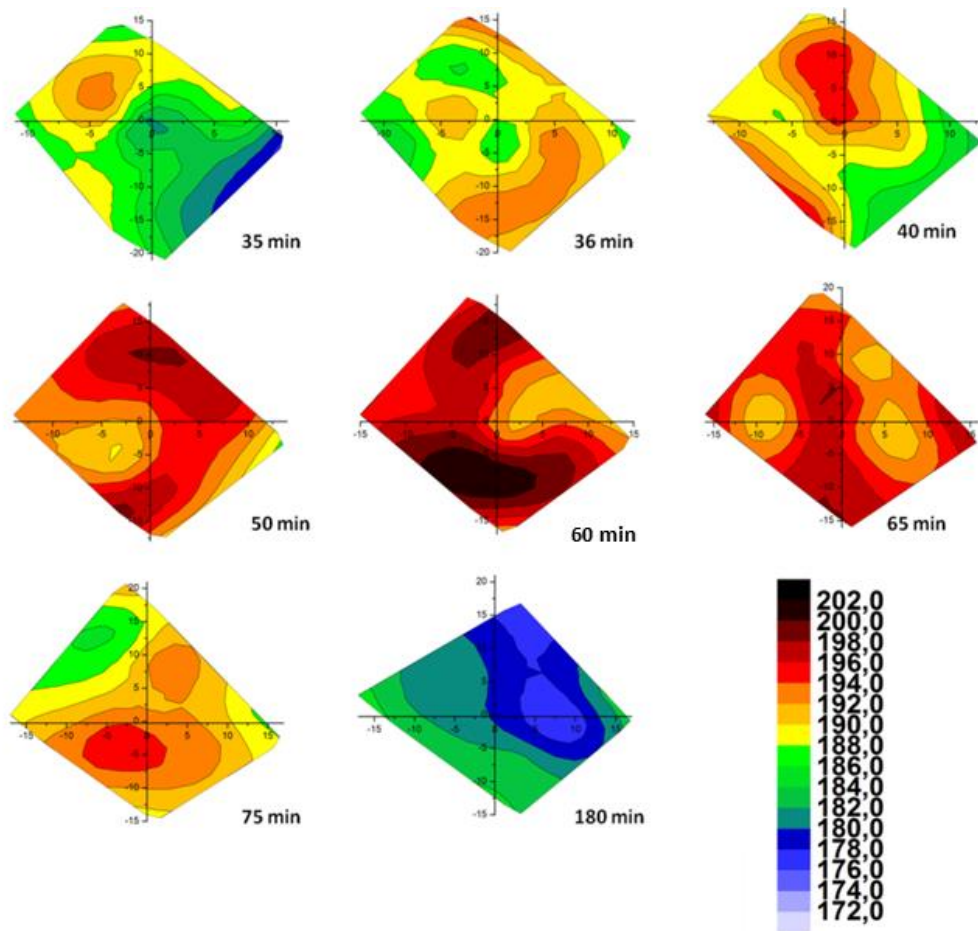
Figure 4.11. Micro hardness maps of ECAPed HBP sample during interrupted age hardening at 190°C (35 to 180 minutes).

4.3.4.3. *Variation of the Hardness Inhomegeneity Index (HII)*

As previously discussed in theory, the variation in hardness can be quantified in a more scientific way if defined using more parameters. The standard deviation only considers the change in a certain property however the relative meaning of this variation remains out of the equation. The integration of standard deviation with the average value would be more meaningful especially in engineering science. Using the index helps to know whether a value is practically small or large. For example a

1 HV deviation is very small for a sample with an average hardness of 200 HV while for a 50 HV hardness sample, it is relatively larger.
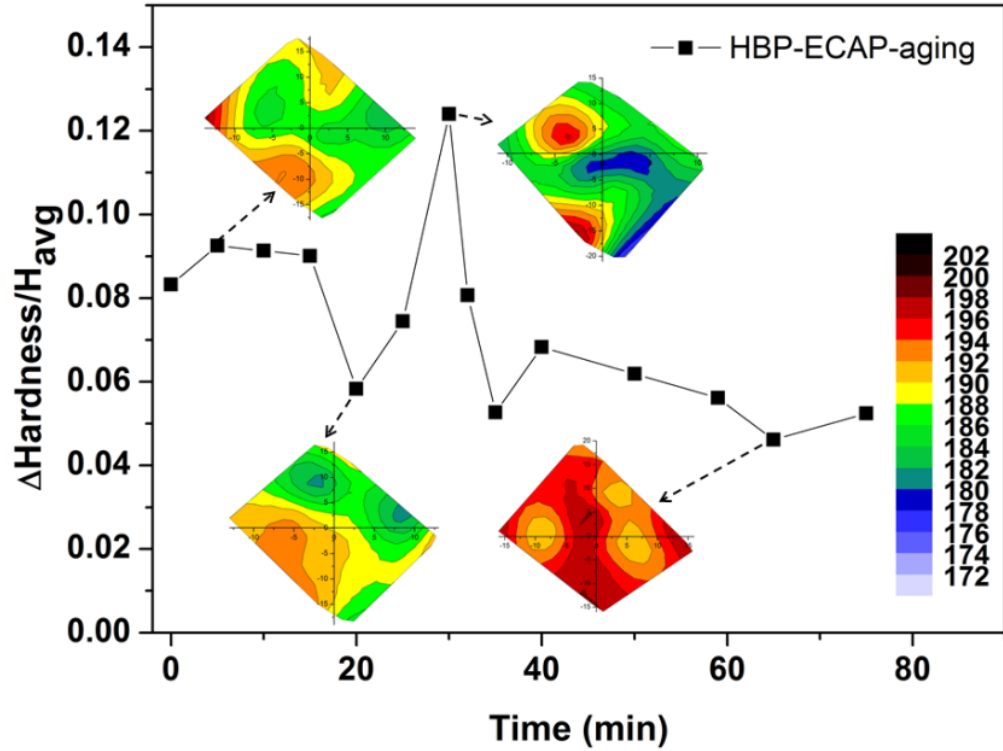
Figure 4.12. Variation of the hardness inhomogeneity index of the ECAPed sample during precipitation hardening with corresponding micro-hardness maps.

The hardness inhomogeneity index is $\Delta H_{stdev}/H_{average}$. The values calculated for the precipitation sequence is represented in Figure 4.12. As can be seen from the graph initial inhomogeneity was about 0.08. Local maximum and minimum values were present throughout the process. Especially the peak at 30 minutes made a maximum of all with a HII of 0.125. On the other hand the sudden homogenization was noticed right after the inhomogeneity peak. The lowest value was observed at 65 minutes with less than 0.05. Nearly 50 % reduction in inhomogeneity could be attained. The homogenization after single pass ECAP with a hardness increase of

~15 HV in only 65 minutes of precipitation could be regarded as a very good achievement when compared to the standard and peak aged counterpart. The whole process increased the hardness from 150 HV to 196 HV and the inhomogeneity problem was also eliminated.

Hardness inhomogeneity index of sample C was also calculated and compared with Sample B in Figure 4.13. Although there are missing data between 0-60 minutes, the lowest HII was achieved about 80 minutes close to the peak aged condition as also observed for sample B. The two lowest points follow one another in the graph. The data points of sample C completes the missing ones of sample B and vice versa showing that throughout the whole aging process there are variations of HII with a general trend of decrease in time.
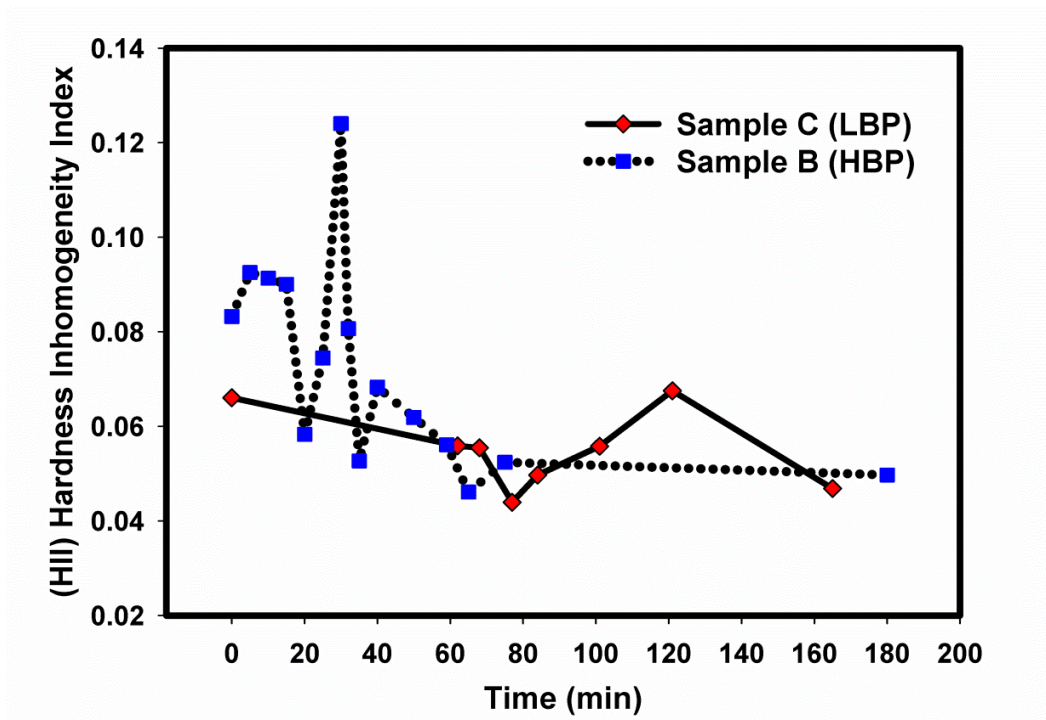
Figure 4.13. HII variation during agin of ECAPed samples; B and C.

4.3.5. TEM Results

In chapter two, a comparison between standard and ECAPed samples was roughly discussed. The current section will be a more detailed investigation of both under the light of micro-hardness data analysis. The proofs on the previously mentioned stages and claims will be presented. The differences between the two groups of samples will be shown especially considering the precipitate sizes. For the inhomogeneity discussion, two samples belonging to the same time and different regions will be investigated in accordance with the hardness variation. Unfortunately it was not possible to produce TEM samples of all regions and all times but only a representative pair regarding inhomogeneity studies.

4.3.5.1. Aging of Al 2024 without ECAP

TEM results of standard Al 2024 will be considered in two stages of aging. It would not be practical to explain through every stage so two stages were chosen; 9 hour aged sample and peak-aged sample.

The 9 hour aged samples were found to possess S precipitates of different sizes, the longest being smaller than 400 nm but mostly less than 200 nm, denoted by circles in Figure 4.14a. The distribution of precipitates may be considered as relatively homogeneous. On the left side of Figure 4.14a, a dislocation rich region can be observed shown by arrows. Figure 4.14b shows the precipitates in a closer objective. The precipitates are in the form of needles parallel to each other or at a certain angle, nearly vertical to one another. This may indicate a relationship between the matrix and the precipitate growth direction.

The actual sizes of precipitates were not easy to determine because as can be seen in Figure 4.15 although they look like individual precipitates in bright field image, in dark field they are observed as a group of very closely arranged precipitates, named as S precipitate groups.
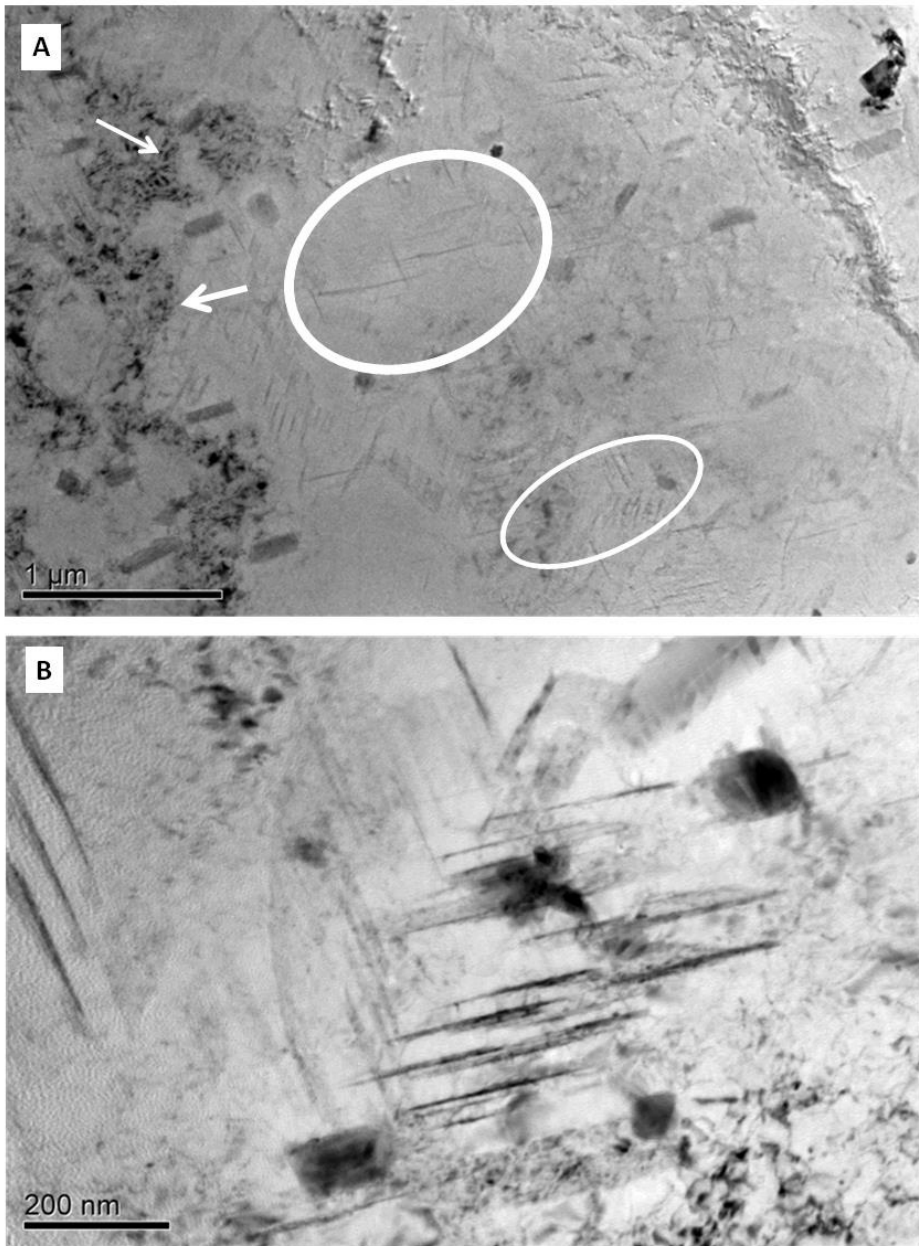
Figure 4.14. TEM micrographs of the solutionized, quenched and aged sample (190°C/9h)
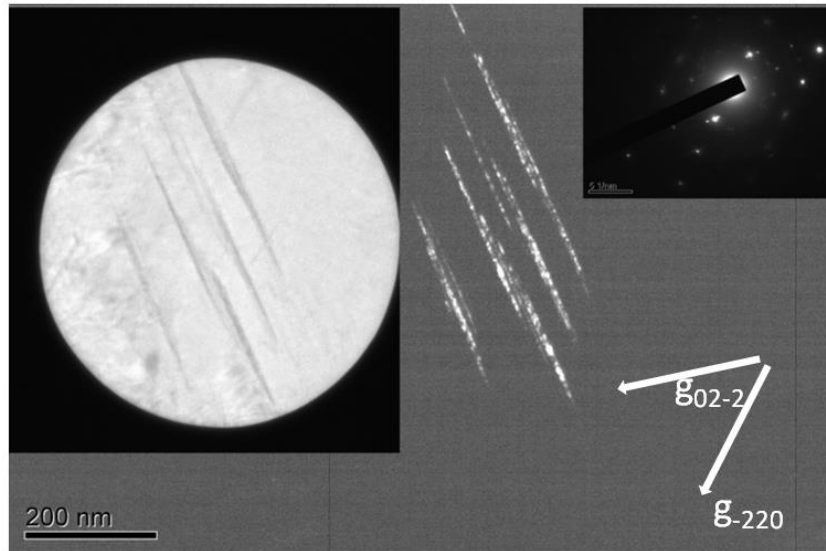
Figure 4.15. Bright field and dark field images of a group of precipitates in the solutionized, quenched and aged sample (190°C/9h).

Regarding the hardening sequence of standard Al 2024, the rapid hardening stage at the beginning was stated to be a result of the interaction between dislocations and solute clusters. Formation of a sessile dislocation network at early stages of precipitation was suggested and the hardening was attributed to this sessile dislocation network formed around clusters of solute atoms. TEM images would be helpful on the clarification of this stage because the dislocation network should be observed throughout the sample if there is hardening related to dislocation formation. When solutionized and rapid quenched samples were investigated, occasional dislocation network regions were observed. They were much less than the ones in the ECAPed samples as expected but high enough to prove that a hardening due to dislocations may be meaningful. In Figure 4.16, the dislocation rich networks are clearly seen. These may be indicative of the first hardening step of solutionized and rapid quenched sample. It might be thought that this may be formed during TEM sample preparation but having observed various Al samples

before, the dislocations usually observed in a regular TEM sample are far less from this density and especially this much spreading around cannot be seen.

A general look in the peak aged samples (190°C for 11.5 h) is shown in Figure 4.17. Well distributed precipitate rich regions, not totally interconnected, as it is usually seen in over-aged samples, but with local connections at certain parts are seen. In the general view, a grain rich in dislocations can be observed. The closer view in Figure 4.17b showed that the dislocations are rather less dense compared to the 9 hour samples.

The peak aged structure was found to contain various precipitates arranged in different manners in Figure 4.18 two of which are presented. Both images show that precipitates prefer to align either closely and parallel to each other or at a certain route. They are located on the previously existing dislocation lines and this alignment shows that S precipitates were formed by heterogeneous nucleation at the dislocations, a probable dislocation path is shown in Figure 4.18.

In Figure 4.18, the image contains a series of parallel precipitates. It is interesting that when certain tilts were applied, some of them were observed as if they were a single precipitate at a certain plane and direction when perceived with bright field imaging.

The high resolution images in Figure 4.19 shows the coherent interface between the precipitate and the matrix. Higher magnification images showed that in either side of the precipitate the coherency was maintained as it is shown in the same figure.
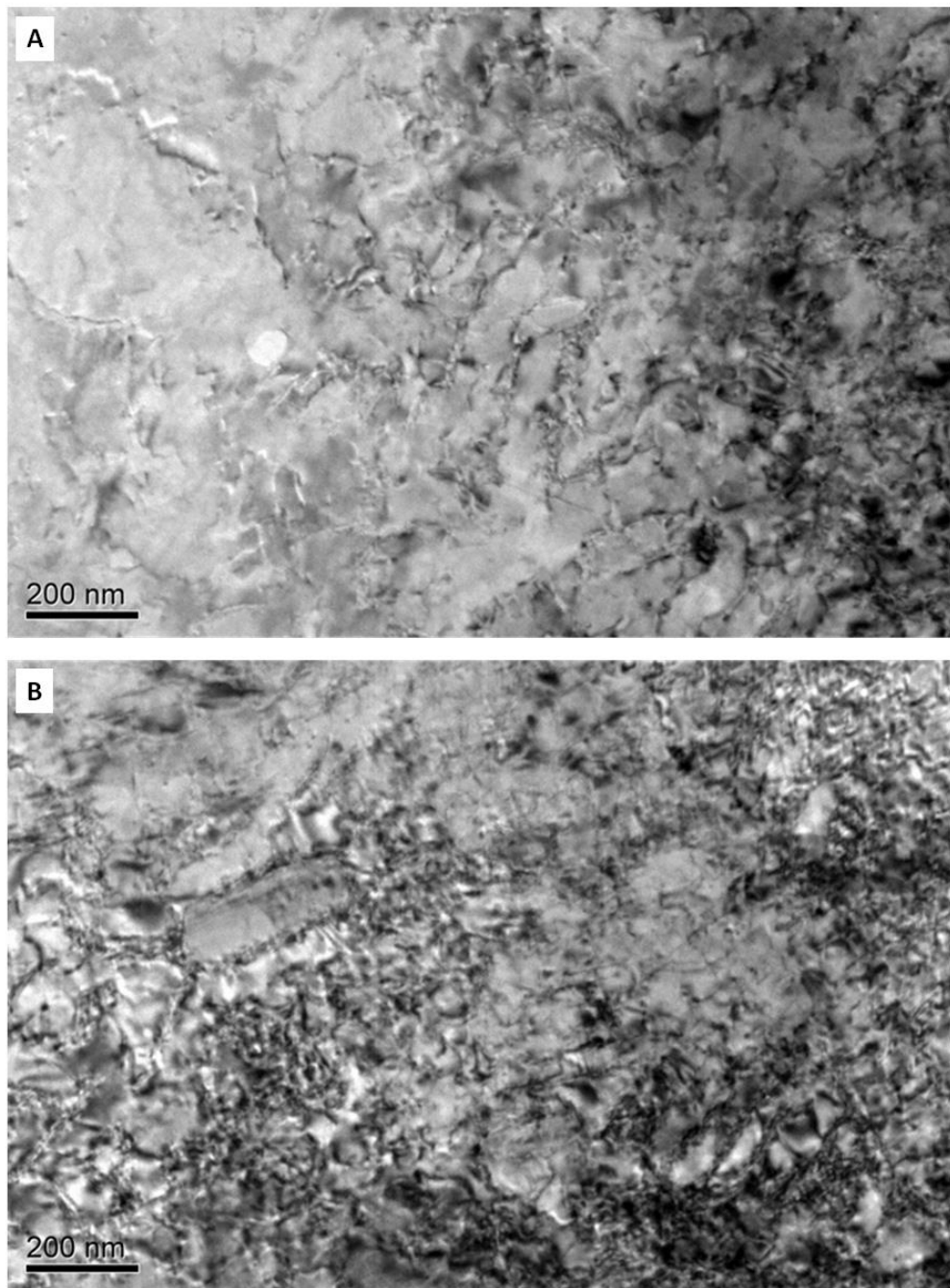
Figure 4.16. Dislocation rich regions and dislocation network in the solutionized, quenched and aged sample (190°C/9h)
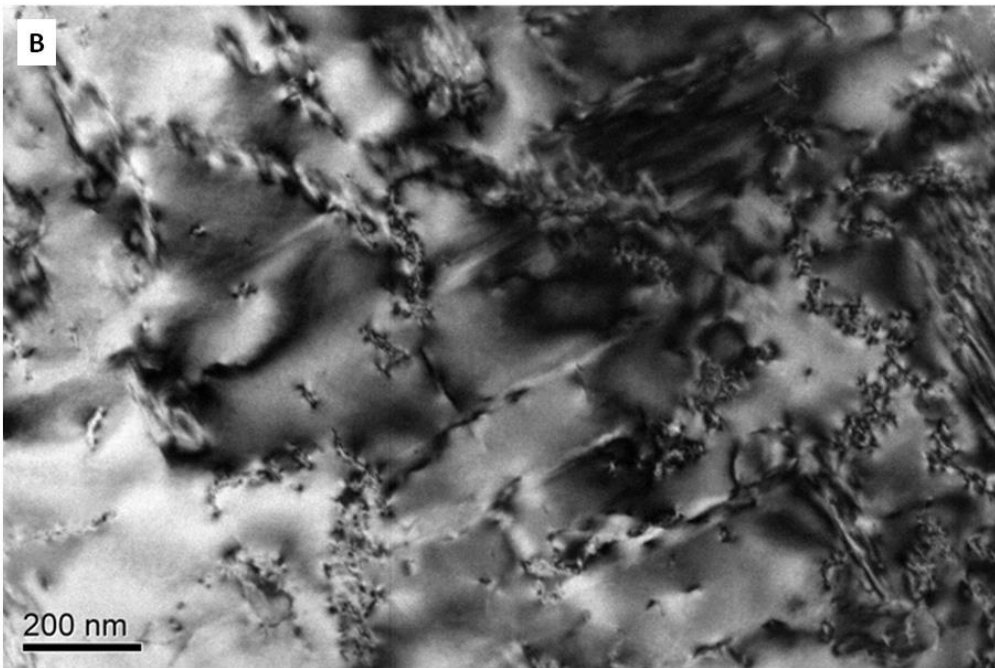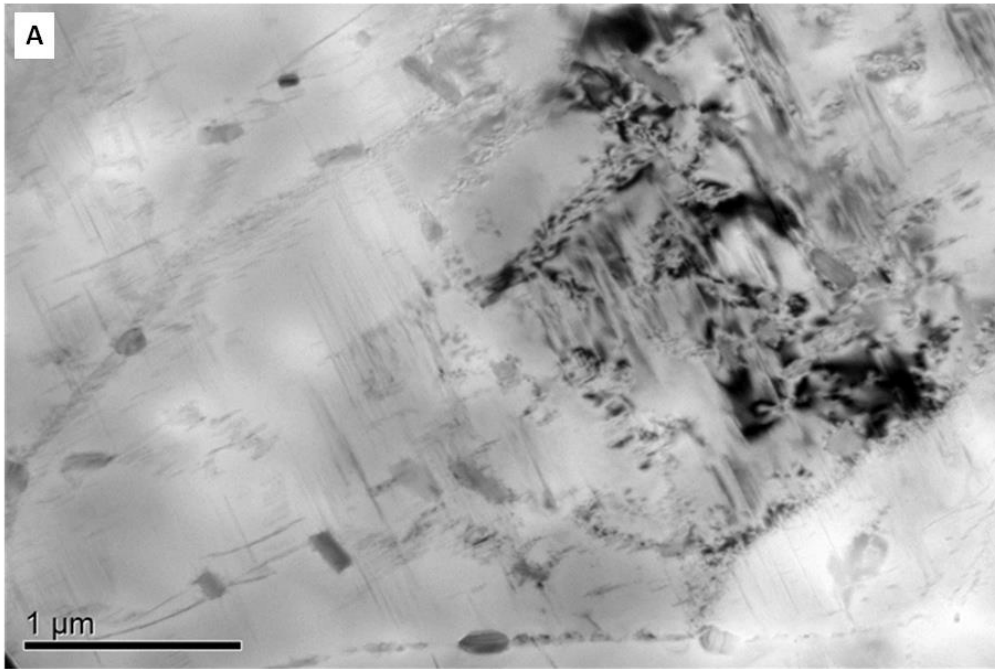
Figure 4.17. Peak aged Al 2024 (190°C without ECAP). a) general view, b) a dislocation rich region.
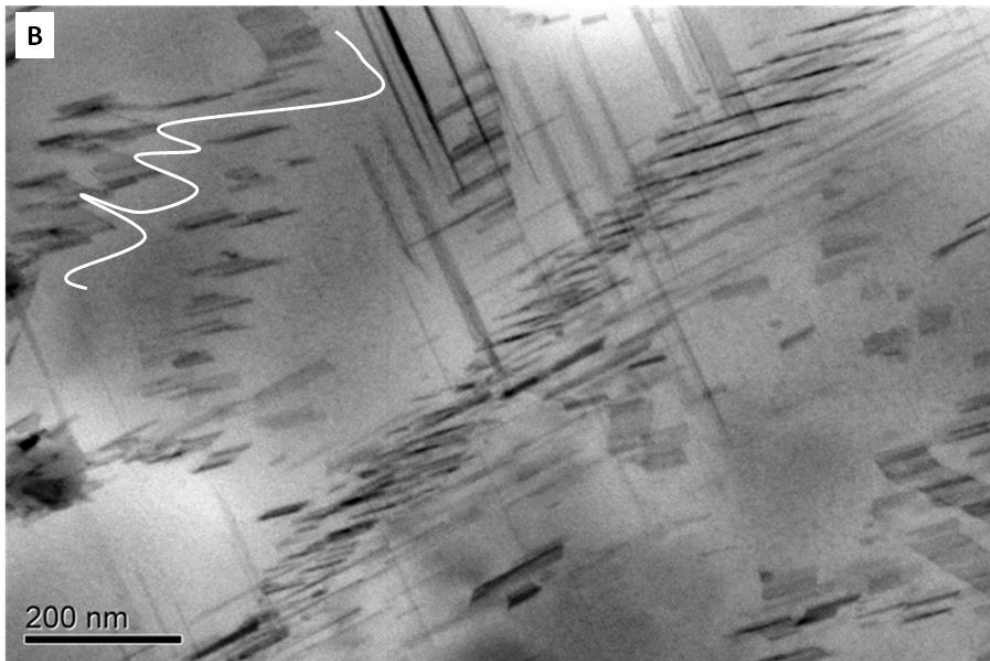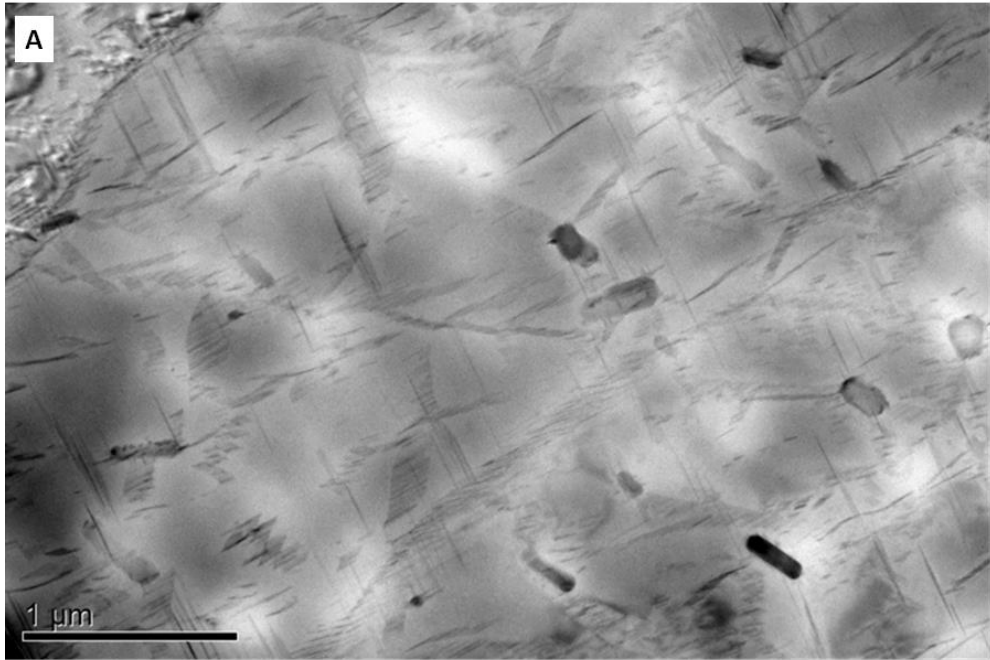
Figure 4.18. General view of precipitate distribution in the peak aged Al 2024 (190°C, without ECAP).
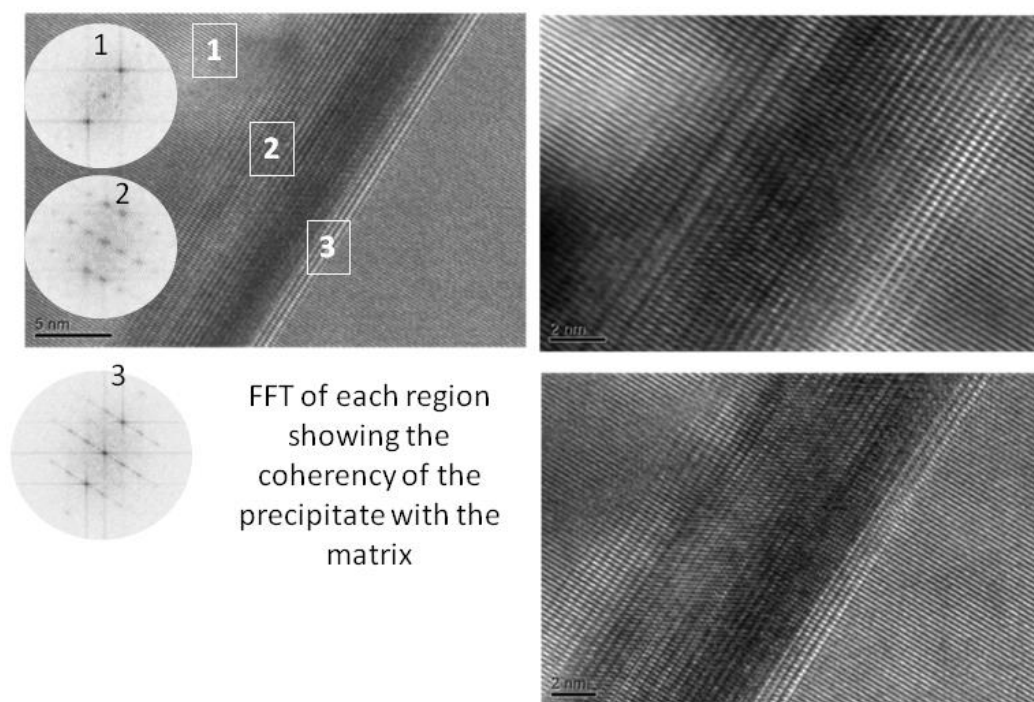
Figure 4.19. HREM images of precipitates in the peak aged Al 2024 (190°C; without ECAP).

4.3.5.2. *Results of ECAPed (High Back Pressure) Al 2024*

TEM results of ECAPed and aged samples were investigated for two stages of aging: 50 min aged, and peak-aged. Besides, images of a couple of samples punched off from certain locations after 35 minute aging with their corresponding micro-hardness variation graphs were presented. The differences in the microstructures, especially GPB zones and precipitates were investigated.

35 Minutes Aged Al 2024 at Two Different Locations

During age hardening of ECAPed (HBP) sample, various TEM samples were collected at various times in order to obtain any meaningful relationship between hardness and TEM images. One of the most meaningful couple of samples was collected at a significantly important time, at 35 minutes. A slight drop in hardness

was detected and the inhomogeneity was nearly at its highest. It was most probable to get any TEM samples that would lead to an explanation to the inhomogeneity increase. In Figure 4.20 variations of hardness in the max and min hardness regions as a function of aging-time were given. At region 9 the hardness has started to increase and at region 13 it has already begun to drop. This means that the GPB zone formation has been completed in region 13 and it has been progressing in region 9. The TEM samples of those regions were investigated.
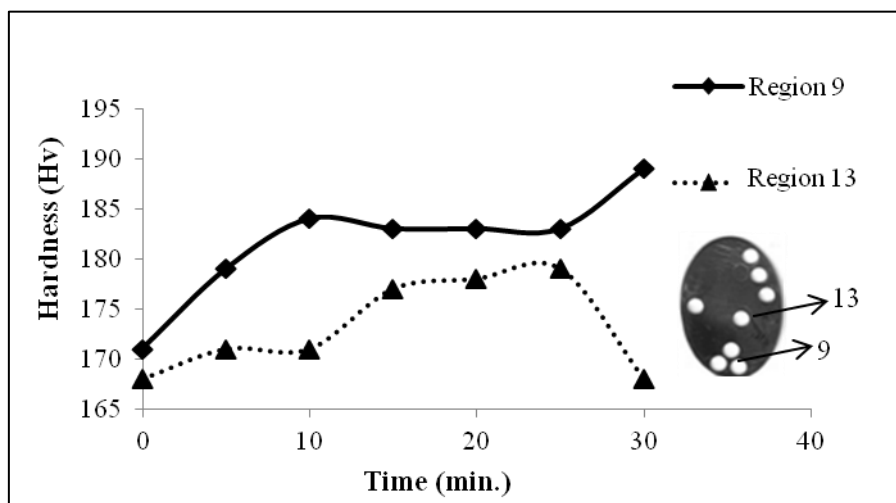
Figure 4.20. Hardness variations of two regions; 9 and 13 with corresponding sample locations.

In the corresponding figures of 35 minutes aged ECAPed Al 2024 (Figure 4.21, Figure 4.22, Figure 4.23) the strikes on the images are the GPB zones. They are, in fact, a few atomic planes thick needles creating strain fields around them which would be observed in the form of coffee beans if they were spherical. The strain they create results in the observed strikes cut at the center. In Figure 4.21, the general view of regions 9 and 13 were observed respectively. In Figure 4.21a, a dislocation rich region is observed with a white region including some GPB zones. It might be best to remember that region 9 is at the middle stage of hardening due to

GPB zones; hence they are hardly visible. However, in Figure 4.21b, the strikes are denser and easy to observe. These are representative images of the GPB zones throughout the samples.

In Figure 4.22.a and Figure 4.22.b, the GPB zones in region 9 and 13 are seen respectively, the latter being overaged in terms of GPB zones. It might be concluded that the precipitates or zones are easier to notice and more interconnected in region 12 which supports a more overaged state.

Lastly, high resolution images of the GPB zones are shown for both regions in Figure 4.23. Though some differences may be seen, it is not possible to make a certain claim on these images other than a relative clarity of GPB zones might be noticed in Figure 4.23.b when compared to Figure 4.23.a.

It would be appropriate to say that these are not statistically valid results but the images are representative of the samples. Although the differences are not easy to notice at first sight, they are not unnoticeable at all.
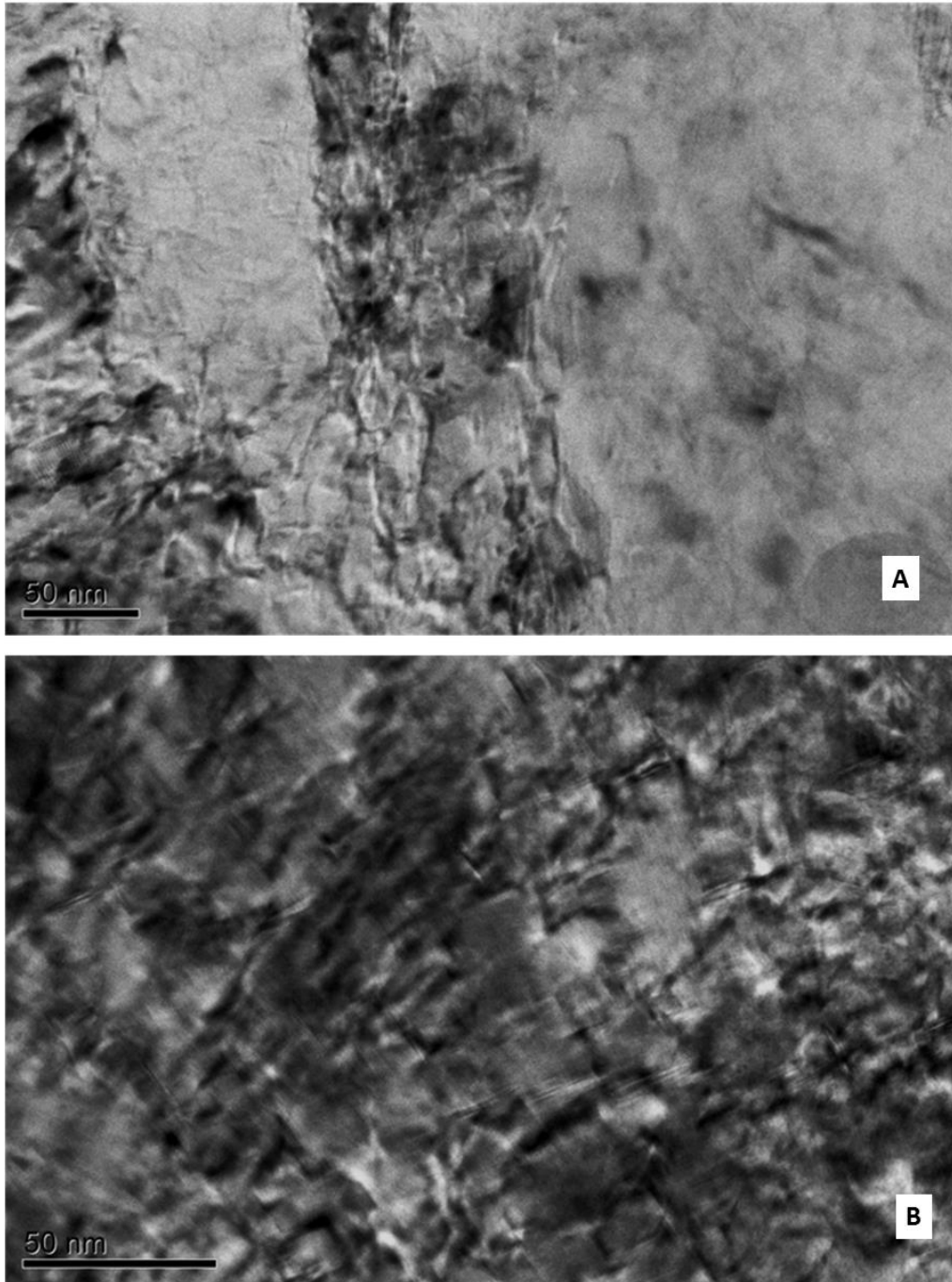
Figure 4.21. (a) Region 9 (bottom), continuing the hardening due to GPB zones. (b) Region 13 (middle) the peak due to GPB zone has been completed and hardness has dropped. (ECAPed; 190°C/ 35 min.)
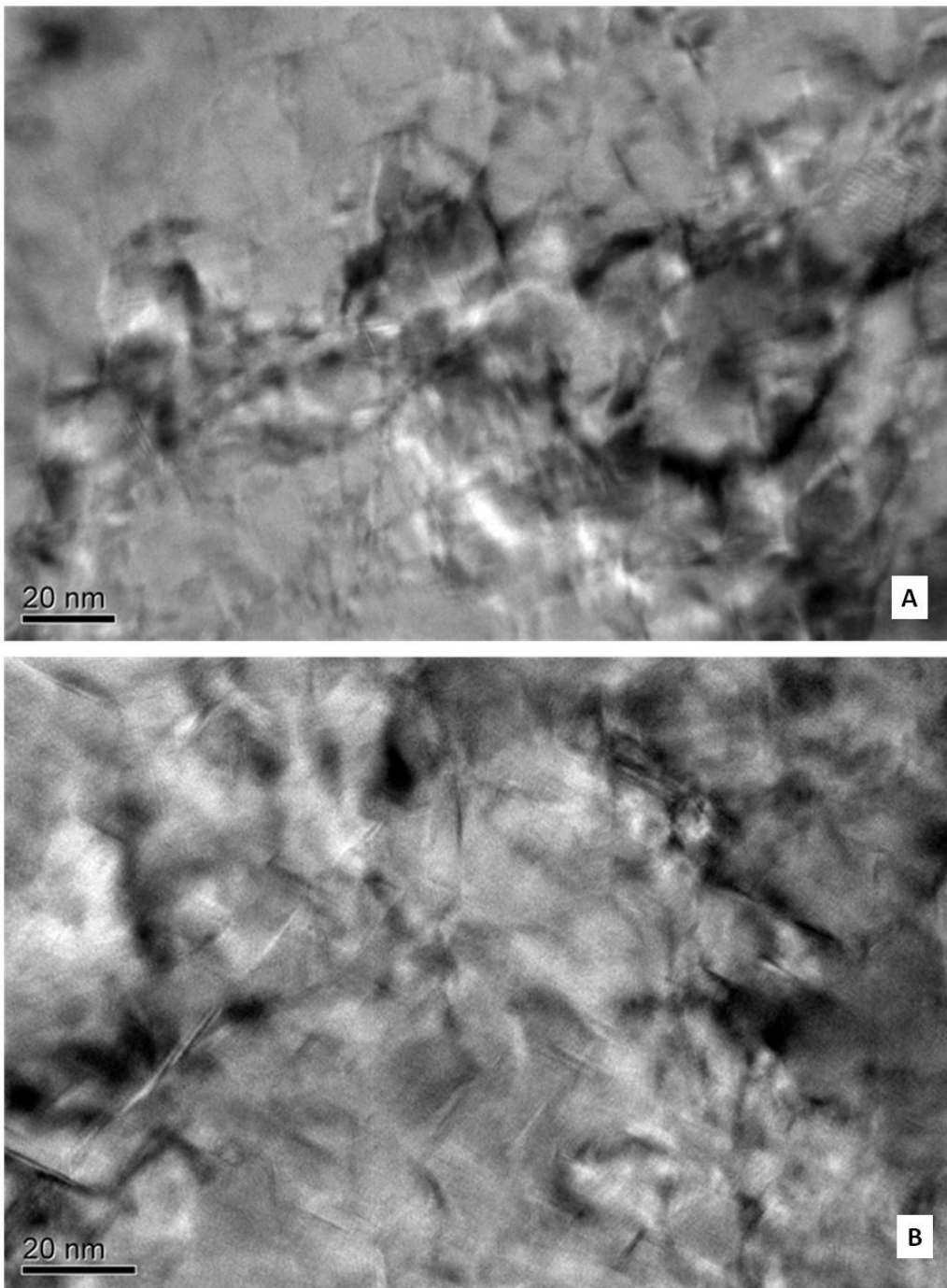
Figure 4.22. (a) Region 9 (bottom), continuing the hardening due to GPB zones. (b) Region 13 (middle) already the peak due to GPB zone has been completed and hardness has dropped. (ECAPed; 190°C/ 35 min.)
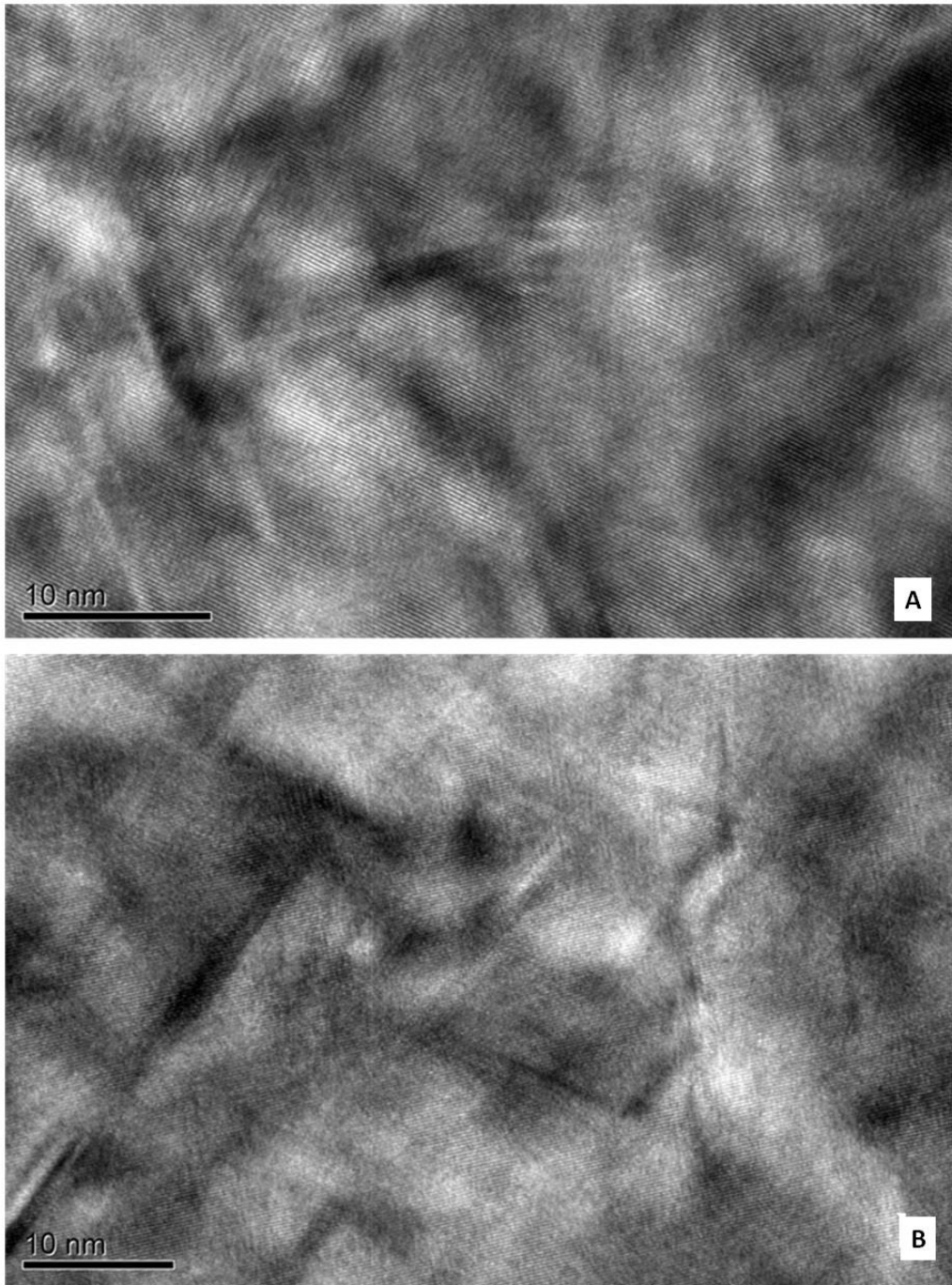
Figure 4.23. (a) Region 9 (bottom), continuing the hardening due to GPB zones. (b) Region 13 (middle) already the peak due to GPB zone has been completed and hardness has dropped. (ECAPed; 190°C/ 35 min.)

In Figure 4.24, an example of occasional subgrain or new crystal formation, free of dislocations, is encircled in the ECAPed sample after 50 minutes of aging at 190°C. These new crystals were observed throughout the sample which may indicate recrystallization and the dislocations were found to rearrange indicative of recovery. In Figure 4.25, the dislocations form cell walls around the GPB rich regions. It could not be observed whether the dislocations themselves also contain GPB zones or not. The GPB zones in between the dislocations were not easy to recognize in bright field mode so dark field imaging was performed. Unlike the inner parts of the cells, newly formed precipitates were observed at these parts. In Figure 4.26 dark field images of precipitates formed among the dislocation network are presented. The sizes of precipitates are not more than 15 nm whereas they were loosely distributed. Only about 5-6 precipitates are observed at each diffraction spot which is much less than the ones in peak aged samples.
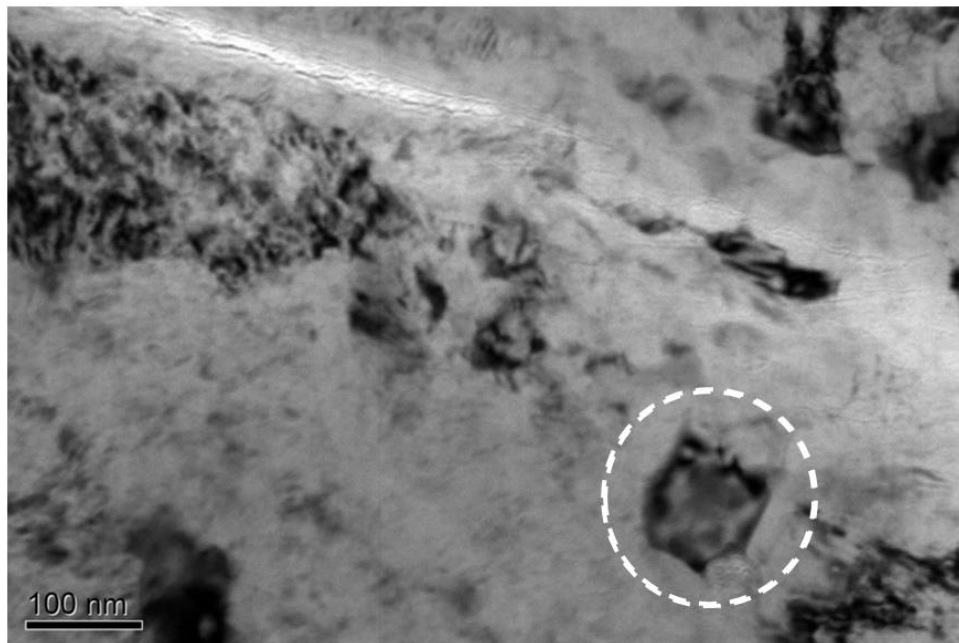
Figure 4.24. Subgrain or new crystal formation (about 100 nm size) in the ECAPed and 50 minute-aged Al 2024 sample.

It might be concluded that at this stage GPB zones and small precipitates of coherent S phase coexist although coherency detection was not possible due to their size range and locations. But due to the size/surface area considerations, only coherent precipitates could be formed energetically. Otherwise the surface energy relative to precipitate volume would remain too high for the transformation.
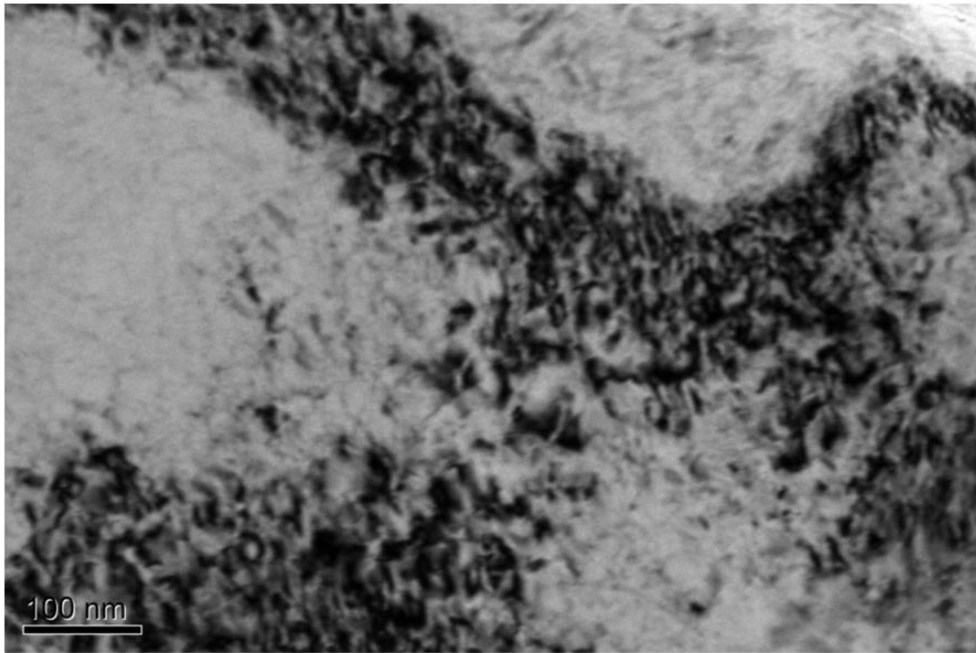
Figure 4.25. Cells around the GPB zone rich regions in the ECAPed and 50 minute-aged Al 2024 sample.
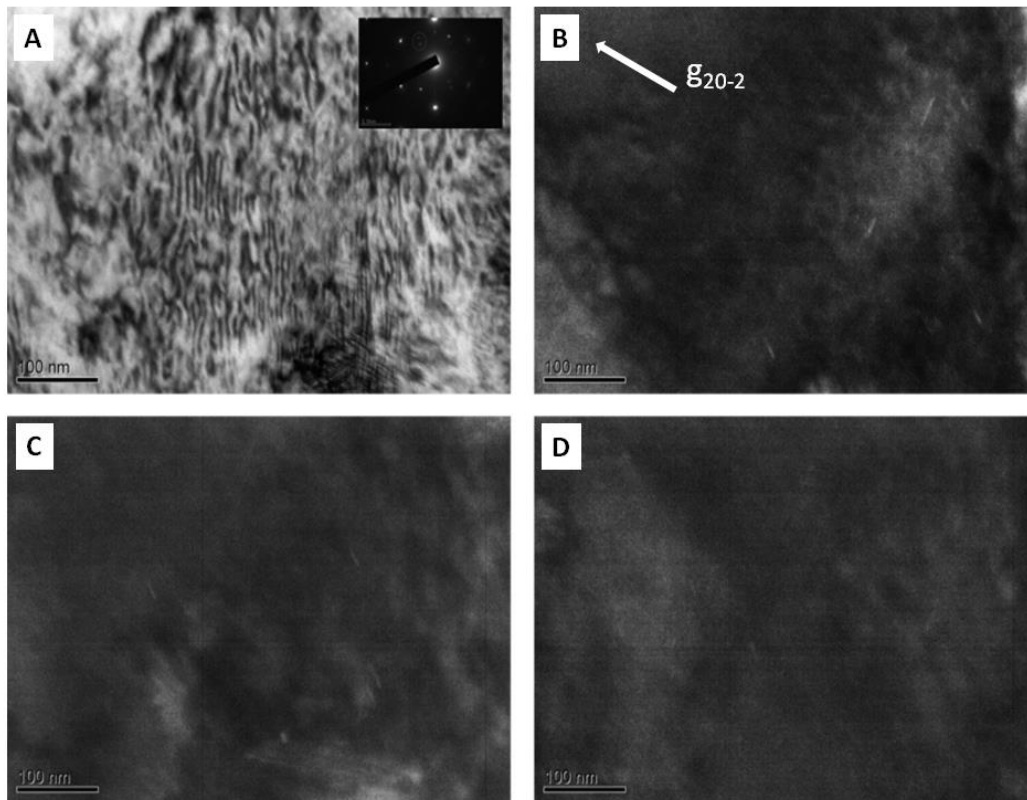
Figure 4.26. Newly formed precipitates at dislocation network regions imaged by dark-field electron microscopy (a) Bright field image; (b),(c),(d) Dark field images at different diffraction spots.

ECAPed and Peak Aged (60 minutes) Al 2024

The general view of the peak aged sample in Figure 4.27.a showed that dislocation rich regions have been modified into more local areas. They looked more organized probably due to the precipitates formed upon them and accompanied recovery and even recrystallization processes. Peak aged samples are further investigated in terms of precipitate size and distribution. Figure 4.27.b shows a region with some traces of precipitates in the form of slight strikes. The coherency of the precipitates is probably less than GPB zones so they are harder to observe without dark field imaging.

116
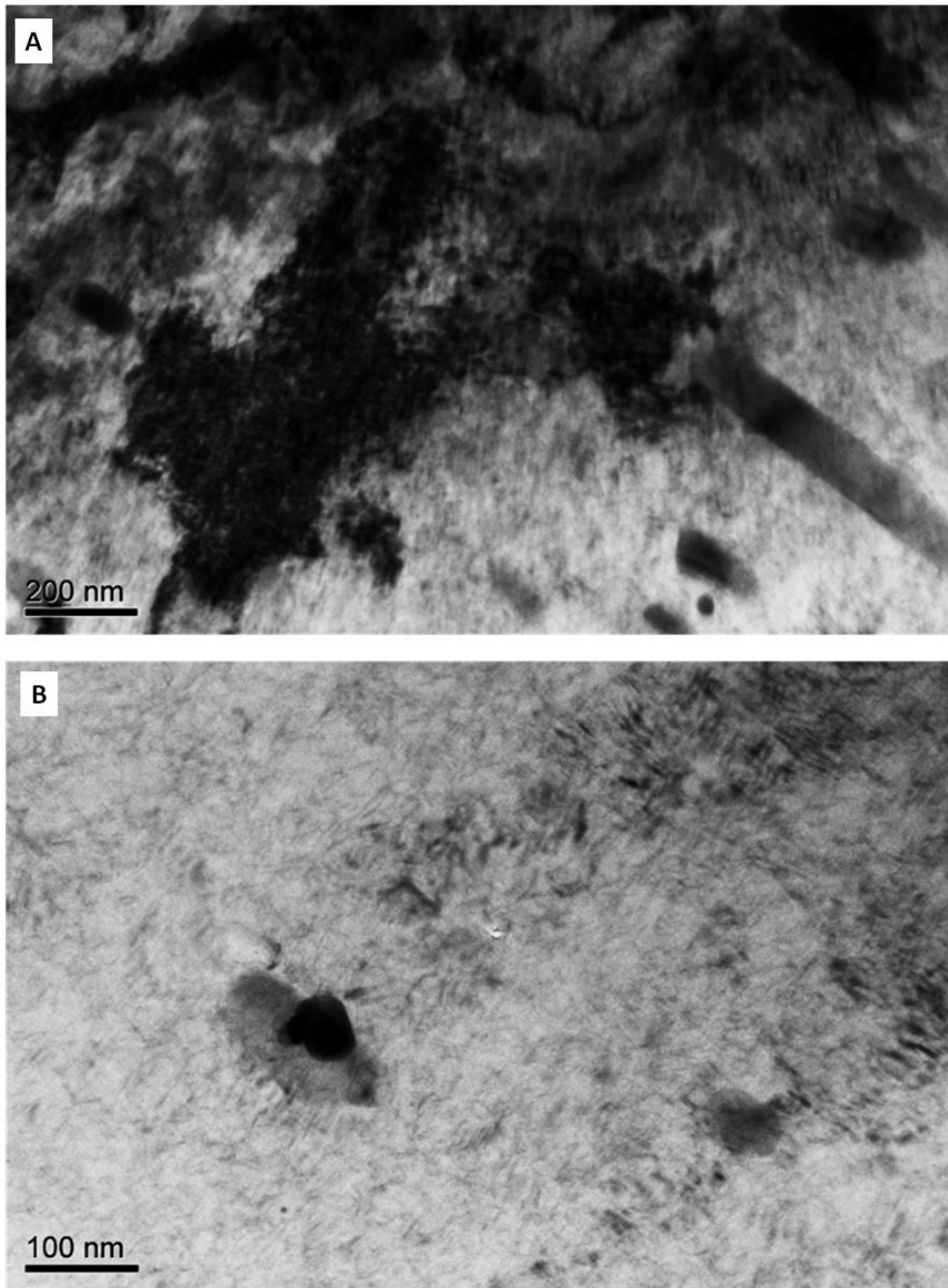
Figure 4.27. ECAPed and peak aged sample with (a) dislocation rich region, and (b) traces of precipitates.
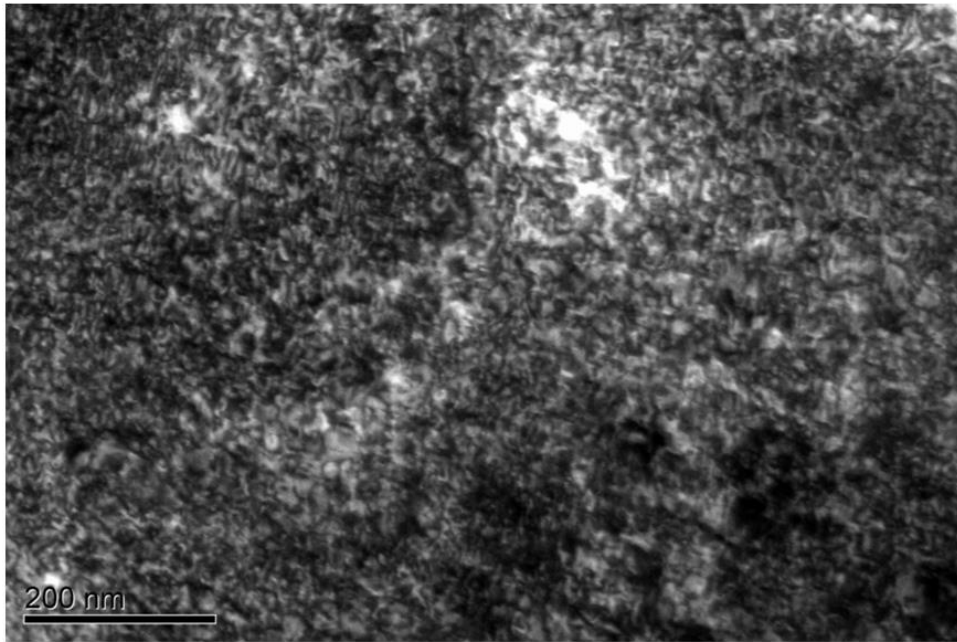
Figure 4.28. The more organized dislocation region due to precipitates in ECAPed and peak aged Al 2024.

4.3.5.3. *Comparison of Standard and ECAPed Peak Aged Al 2024 with Respect to Deformation*

The comparison of the precipitates in Al 2024 samples with and without severe deformation is one of the key points of the current study. It is not only important for the understanding of the kinetics but also valuable to see the variations in general.

When the images in Figure 4.29 and Figure 4.30 are observed, the distribution of the precipitates in ECAPed sample is found to be more homogeneous. Though they are still parallel to one another, the distance between them is more distinct. Obviously in ECAPed sample shorter precipitates are seen and they seem to have a more rounded shape rather than being in the form of needles. This might be an indication of the coherency differences of the two precipitates.

The size distributions of precipitates were investigated using Image J quantitative analysis and the lengths of the precipitates were measured. Although bright field images of standard samples were satisfactory for appropriate measurements, it was impossible for the ECAPed samples even to see an individual precipitate without dark field imaging hence the images in Figure 4.29 (a and b) and Figure 4.30 (c and d) were used for calculation. Minimum 200 counts were carried out for standard sample and all visible precipitates were counted in ECAPed sample.
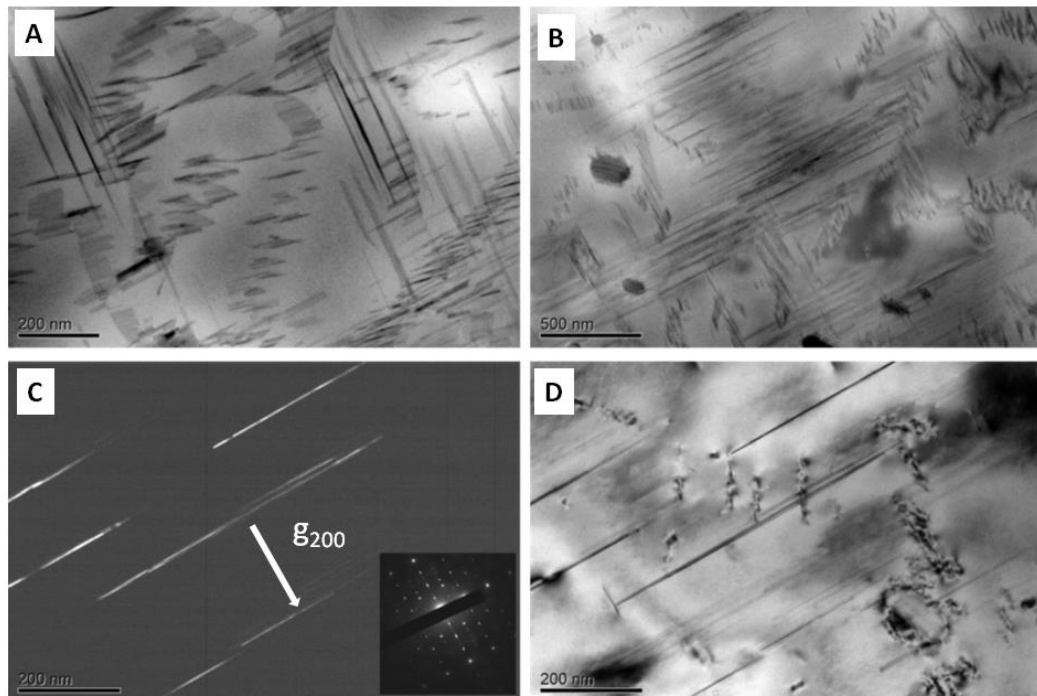
Figure 4.29. Peak aged precipitates of solutionized and quenched Al 2024.
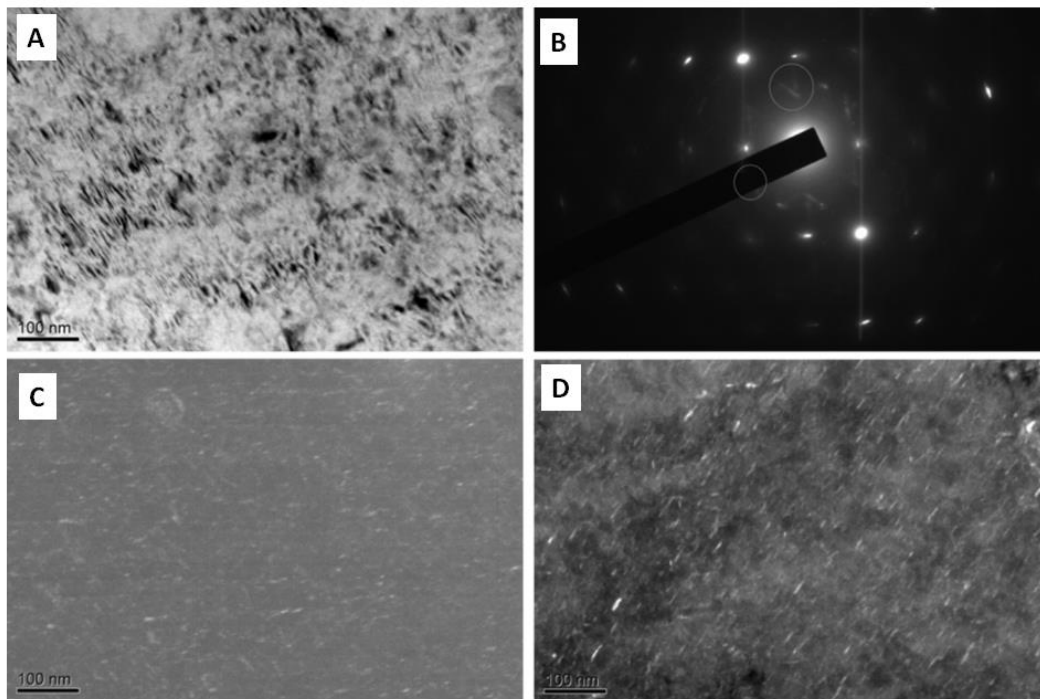
Figure 4.30. Precipitates observed in the ECAPed and peak aged sample using dark field imaging.

The precipitate distributions of standard and ECAPed Al 2024 are shown in Figure 4.31 and Figure 4.32. In standard peak aged samples, precipitates were found to be close to 100 nm and few precipitates of large sizes were measured. The small precipitates were found to dominate however in ECAPed and peak aged sample, Figure 4.32, a more homogeneous distribution is observed. The size distribution curve tremendously changes and the average sized precipitates dominate rather than very fine and very large precipitates.

While this was the case for individual data, the comparison of these two groups would be more meaningful to compare the precipitate size differences between ECAPed and standard Al 2024. The average size of precipitates in ECAPed samples was found to be 11.6 nm whereas for standard sample it was calculated as 137.3 nm.

The size of the precipitates has become about 12 times smaller than it was for standard sample after ECAP which is in agreement with the time of their formation.

The average precipitate size of ECAPed sample, which is 12 times smaller than standard, indicates that heterogeneous nucleation of precipitates at the densely distributed dislocations is the main reason of fast aging observed in ECAPed samples. The time needed for diffusion of atoms in order to grow the precipitates from 1 to 12 units was not required in the case of ECAPed samples because there were 12 times more nucleation sites to precipitate on, in the deformed structure.
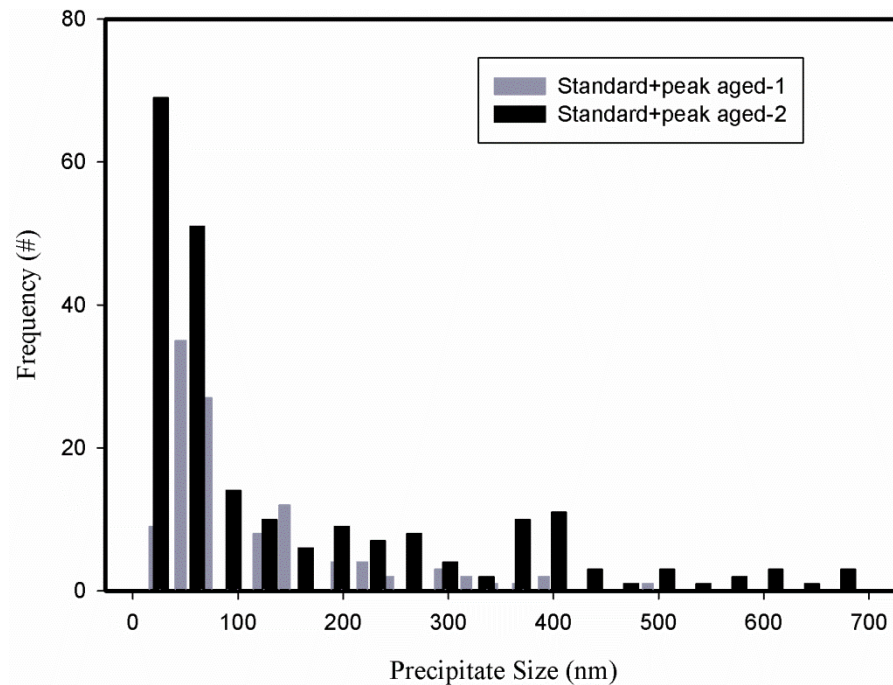
Figure 4.31. Size distributions of precipitates in standard sample for two images in Figure 4.29a and b
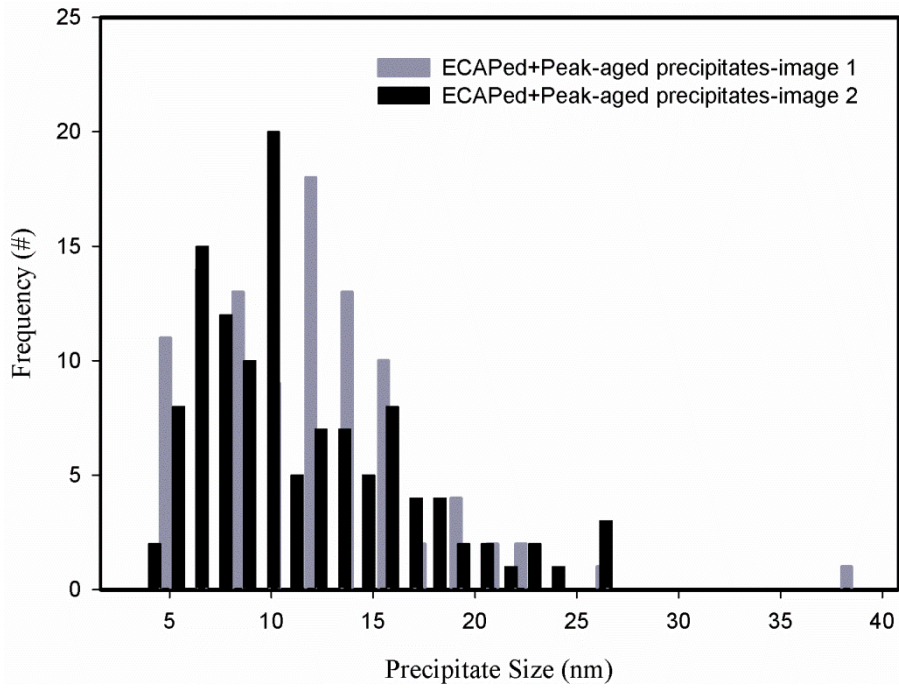
Figure 4.32. Size distributions of precipitates in ECAPed sample for the images in Figure 4.30c and d.
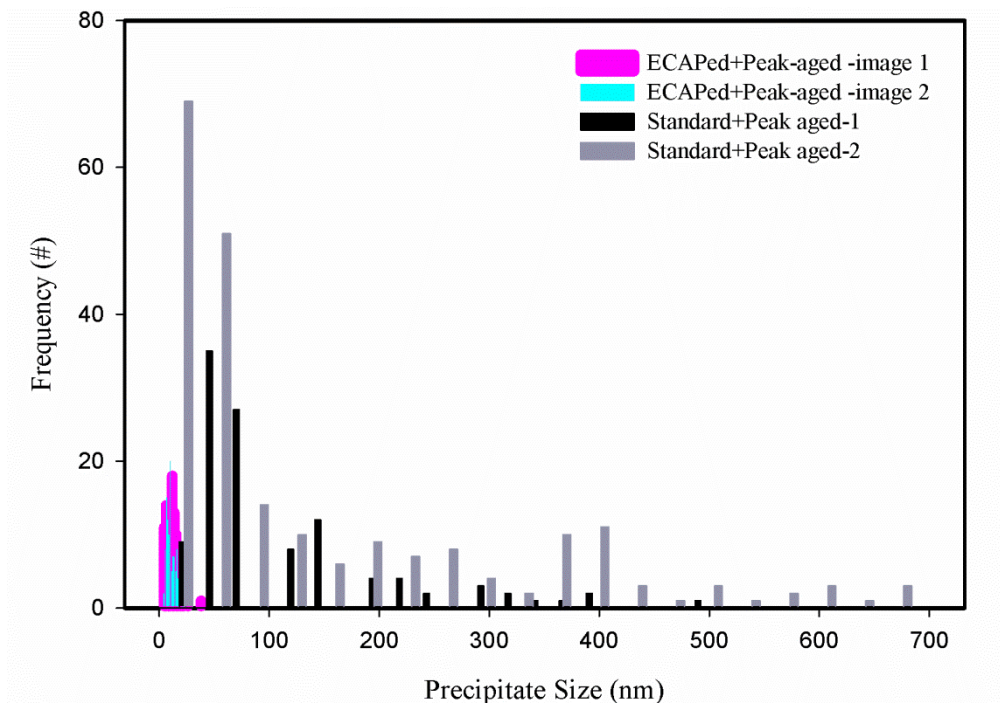
Figure 4.33 The comparison of size distribution of precipitates in the ECAPed and standard Al 2024.

122

CHAPTER 5

INVESTIGATIONS ON THE THERMAL STABILITY OF ECAPED Al 2024 ALLOY

5.1.   INTRODUCTION

Severe plastic deformation, especially ECAP, leads to an improvement in mechanical properties like hardness and tensile strength [61, 116]. Hall-Petch equation states that at low temperatures, grain refinement leads to mechanical property enhancement. hence the stability of both the microstructure and the enhanced mechanical properties, when subjected to relatively high/moderate temperatures, becomes very critical due to the involvement of the high energy microstructure. However, the temperature increase combined with the fine grained structure may result in an increase in the flow of the material. As a result, the thermal stability of refined structures is regarded to be highly important [116]

2xxx and 7xxx alloys are stated to be the most stable Al alloys after ECAP in regards to temperature variations owing to their precipitation hardenability and hence the precipitate and dispersoid content [117]. Stepwise testing, by short (a few hours at most) exposures to certain temperatures, are encountered often in literature for SPD processed products [117–127]. Another common method is differential scanning calorimeter (DSC) but its resolution at high heating rates such as 10K/min may lead to not so well defined, distinguished results while low heating rates, not commonly used, may be a better option. These methods mentioned above may provide a more accurate idea on thermal stability of non-heat treatable alloys, however, when severe deformation and super saturation is taking place simultaneously, the outcome of exposure to certain temperatures for a long time is

not so easy to predict. When a commercial application is considered, it is not only beneficial but also essential to know the safest temperature and safest lifetime of a certain product, especially if it is to be used in aerospace and transport industry. This study aims to answer these questions not through estimations but through experimental results suggesting a safe temperature limit and service time in accordance to the minimum mechanical property requirements. It also provides insights on the effects of post-ECAP aging on the thermal stability. The major focus of this part of the study is to investigate the stability of ECAP processed Al 2024 when subjected to moderate temperatures for long time periods and investigating the responses in terms of microstructural differences.

Throughout the study 1000 hours of annealing heat treatments at 80°C, 120°C, 150°C and 200°C and interrupted hardness measurements were conducted. However, critical samples and critical time periods were chosen for meaningful explanations of the results since investigating all the microstructures using TEM and EBSD would not have been a feasible option.

5.2. LITERATURE REVIEW

5.2.1. Thermal Stability

Thermal stability is defined in the literature as the preservation of the properties when a sample is subjected to different temperatures. Besides the mechanical properties, various other engineering properties such as electrical conductivity/resistivity, corrosion resistance, thermal conductivity, and optical properties may vary with temperature. Although thermal stability is a result of the microstructural stability, it is not so easy to determine accurately which microstructural character affects which property. On the other hand, it is also possible to observe a change in a property without a significant variation in the microstructure, such as the transition of precipitates from coherency to semi-coherency.

Thermal stability may also be regarded as a resistance to change. It is advantageous in some cases when change is detrimental to the property required for a certain application while, in some cases, it may be undesirable for a specific application, like thermal sensors that require immediate reaction to temperature variations.

All structural changes are based on thermodynamics and kinetics involved. Although thermodynamics mainly discuss macro systems [127], all changes result from the need for thermodynamic equilibrium hence the microstructural changes are rooted in this requirement. Very similar to any change in life, the driving force for the transition may run into a barrier such as the time required for the process to be completed. There are certain cases in which a detectable transformation can never proceed at a certain time interval and a metastable phase, i. e. martensite, practically becomes an equilibrium structure. In other cases time needed for a certain process decreases due to increased kinetics, and another more probable process may be surpassed. The barrier to the transition is an advantage for improved thermal stability. At this point distinguishing the difference between theory and practice is crucial. All transitions from one state to another need time and in complicated microstructures, where parallel processes are likely to occur, it is difficult to determine the duration of change or in other words, the level of stability. The current case can be regarded as one of such systems where both precipitation sequence and annealing, including recovery and recrystallization, coexist.

5.2.2. Recovery and Recrystallization

Plastic deformation of any kind has the effect of increasing the free energy of a crystalline material immediately. When the temperature is high enough for atomic movements, this increased energy can spontaneously disappear but at low homologous temperatures, the kinetics is slow and the unstable structure is preserved until a higher mobility state is thermally activated through a heating process namely, annealing. The defects, hence the increased free energy, may be eliminated or rearranged to low energy configurations during annealing [128].

In general, two types of defects, dislocations and vacancies, are increased during plastic deformation. It is highly important to underline that vacancies are annealed out at low temperatures and has very little effect on the microstructure as a hardening aid although it is possible for the excess vacancies to affect the precipitation sequence as a mobility increasing factor instead of temperature, especially in severe deformation cases. On the other hand, elimination of vacancies might also be considered as a type of recovery process at low temperatures but cannot be defined as a phase transformation [84]. In addition, in the case of annealing stimulated recovery and recrystallization, vacancies are not determined as a major parameter.

Defining recovery as "the processes taking place while the original grain structure is preserved"[84], leads to confusion since using today's technology a significant change may be observed in the original grain structure whereas an optical microscope shows no difference at all. In this study recovery will be referred as "the annihilation and rearrangement of dislocations" in order to provide a more accurate definition. On the other side of the coin lies the recrystallization which is usually attributed to newly formed equiaxed grains [58] but recent studies have shown that recrystallized grains are not necessarily equiaxed [128]. Another consideration is that the borderlines between various annealing phenomena are not as clear as they were formerly defined in literature, since new technology and more developed deformation techniques provide opportunities for observations that were not available, yet they constitute a profound base for understanding many of the variations. Taking practical concerns rather than phenomenological categorization, the three major mechanisms of annealing is categorized according to Humphreys et. al. in Table 5.1 [128]. The dynamic recovery and recrystallization are left out but static annealing phenomena have been included.

Table 5.1. Static annealing examples [[128]

	Recovery	**Recrystallization**	**Grain growth**
Continuous "Uniformly occurring throughout the material"	Subgrain growth	Continuous recrystallization	Normal Grain growth
Discontinuous "Heterogeneously occurring throughout the material"	Discontinuous subgrain growth	Primary recrystallization	Abnormal Grain Growth

As discussed earlier, cold deformation and SPD are means of increasing dislocation density. For the mechanical property enhancement, the most important parameters are regarded as structure of the metal or alloy and the dislocation density. It has been stated that up to 5-6 times higher strengths could be achieved through deformation. As previously discussed the very high dislocation densities, such as $\sim 10^{16} m^{-2}$, as well as the very low ones, lead to the highest strength values while moderate dislocation densities, annealed state $\sim 10^{11} m^{-2}$, result in the lowest strength values. When a metal, with an excessive dislocation density, is heated to $\sim T_m/3$ the annealing process initiates with loss of dislocations and rearrangements leading to the loss of mechanical strength as well [128].

5.2.2.1. *Recovery*

Recovery can be defined as restoration of the properties of a deformed structure to its undeformed state to a certain degree, prior to recrystallization. Recovery is known to be mainly a result of variations in the dislocation structure, mechanisms that are summarized in Figure 5.1. The processes mentioned theoretically take place in the represented order but they may coexist or some of the mechanisms may not take place in some systems. Another possibility is that some of the mechanisms might have already taken place during deformation which is a dynamic recovery process [58, 128].

It is important to note that recovery and recrystallization are competing processes in the sense that there is no possibility for recovery after recrystallization. In a study on pure Al deformed at -170°C, the DSC data showed that vacancy annihilation took place at -70°C and recrystallization took place at -20°C without any sign of recovery [128]. This particular case is a good example of the competition between recrystallization and recovery. On the other hand recovery may use up the stored energy that is the driving force for both recovery and recrystallization, resulting in affecting the kinetics and the nature of recrystallization.

The degree of recovery depends on various parameters and conditions. The main factors can be listed as the amount of strain, nature of the metal, especially stacking fault energy and annealing temperature as well as deformation temperature [84][128].

At a constant temperature, during annealing, higher strain increases the degree of recovery unless the combined effect of strain amount and annealing temperature correspond to an early recrystallization. Likewise, increasing the temperature leads to a more complete recovery.

The nature of the metal such as purity, alloying elements and especially stacking fault energy are key parameters to the recovery process. When the stacking fault energy, γ_{SFE}, is high, the recovery tools such as dislocation climb and cross slip are easy, so recovery is promoted by the metal as in the case of Al alloys. Solute atoms may affect the dislocation motion in various ways such as pinning the dislocations, affecting vacancy concentration and mobility or even by varying the γ_{SFE}. An interesting fact about the solute effect is that dislocation pinning avoids dynamic recovery but since the amount of stored energy increases, the static recovery is encouraged by the presence of the solute atom. Magnesium, for example, has such an effect in aluminum. Solute Mg atoms pin the dislocations and avoid dynamic recovery which raises the stored energy as well as the static recovery.

In addition to thermal analysis, recovery may be measured by the variation of properties which are sensitive to microstructure, such as density and electrical resistivity since numerical determination of the stage and overall state of a system is not easy even with TEM analysis. Hardness variation may be attributed to recovery to a small extend and high hardness drops are usually accepted as a specific sign of recrystallization. Although the kinetics of recovery for simple systems can be estimated through the variation of these properties, not only because different processes may involve but also because recovery itself does not consist of a single step, it may be misleading to interpret the variations as a direct indicates of recovery process. Yet there are two types of common, isothermal, empirical kinetic relationship of recovery with a certain property. Type I is applicable to poly crystals which is defined as

$$\frac{dX_R}{dt} = -\frac{C_1}{t} \qquad\qquad \textbf{5.1}$$

X_R is the change of parameter from the annealed condition, C_1 is a constant. When integrated the equation becomes,

$$\frac{dX_R}{dt} = -\frac{C_1}{t} \qquad\qquad \textbf{5.2}$$

In Figure 5.1 five stages of recovery are shown but basically there are two important dislocation mechanisms involved: dislocation migration or rearrangement (into a lower energy state) and annihilation. The basic mechanism of dislocation tangle and cell formation is dislocation rearrangement while dislocation annihilation in cells, subgrain formation and subgrain growth more dominantly occur as a result of dislocation annihilation.
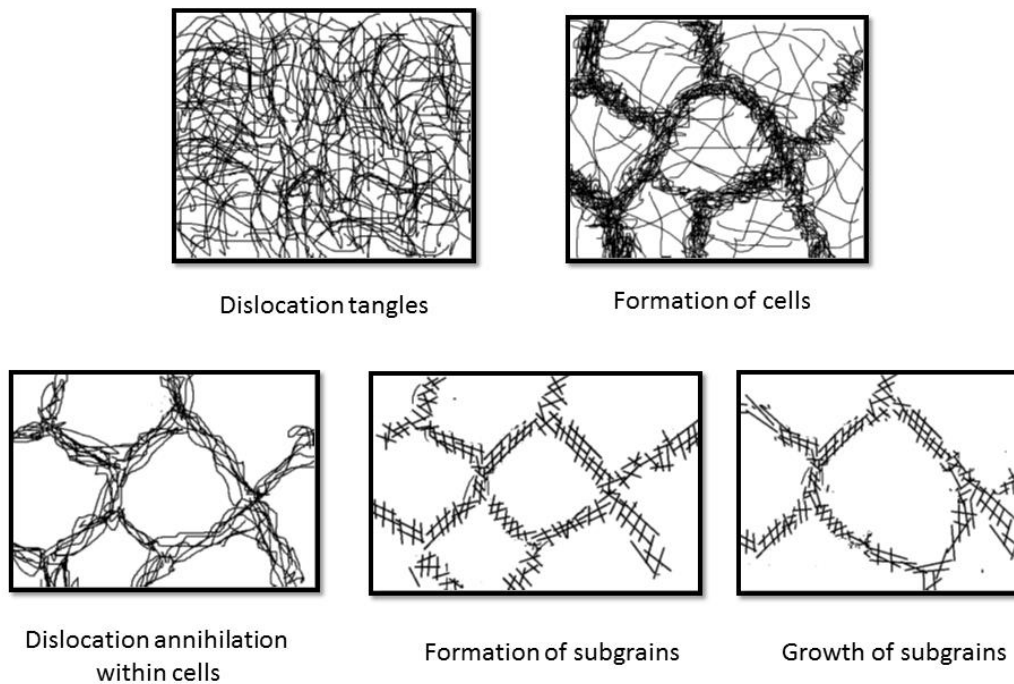
Figure 5.1. The five possible recovery states. Sketches adopted and reproduced from Ref [128]**.**

Rearrangement of dislocations into more stable arrays may be achieved by polygonization. Polygonization is the formation of low angle grain boundaries created by the excess dislocations occurring after annihilation that are usually recognized in single slip systems and single crystals. Another more common method is sub-grain formation as a result of large strains applied to polycrystalline metals where the mechanisms are much more complex due to variety of Burgers vectors of dislocations involved. They react forming a 2-D network and high stacking fault energy leads to formation of 3-D cells with walls of complex dislocation tangles. The cell size depends on the alloy and the strain as well as the strain distribution throughout the material [128]. Cells differ from sub-grains in some ways. First of all cell boundaries include dislocations spreading towards the cell interiors and contain certain amount of dislocations within, while sub-grains have clearer boundaries with no dislocation inside. However both have low angle boundaries and have slight variations in their orientations.

Dislocation annihilation may occur in many ways but the most common one is by means of dipole edge dislocations which lie at the same glide plane with opposite directions. In this case, they can easily anneal out each other and this process may take place even at low homologous temperatures. On the other hand, when dipole edge dislocations are at different glide planes, dislocation climb is necessary which also necessitates higher temperatures though in the case of high stacking fault energy metals, such as Al, dislocation climb may also be observed at low homologous temperatures. Dislocation annihilation leads to the formation of subgrains and the movement of the subgrain boundaries result in the growth of these subgrains.

In the case of complex dislocations, bulk/core diffusion and thermally activated glide/cross-slip are examples of possible mechanisms. Thermally activated glide or climb controlled recovery rate is formulated as below:

$$\frac{d\sigma}{dt} = -c_1 \exp\left(-\frac{Q(\sigma)}{kT}\right) \qquad \textbf{5.3}$$

Where activation energy (Q) is a function of internal stress (σ) c_1 is constant, K is Boltzmann constant, t is time and T is temperature. It is important to note that increase in the dislocation density results in a decrease of the activation energy (during cold work) while annealing with applied temperature increases the activation energy [128].

It is possible to observe cells and even sub-grains in a deformed alloy right after deformation due to dynamic recovery but in some cases sub-grain formation may not be visible due to a prior recrystallization. The parameters that support the sub-grain formation are high stacking fault energy, low solute content, large strains and high deformation temperature. In the case of ECAPed Al 2024, stacking fault energy and strain are high but deformation temperature is relatively low, except a hard to control temperature rise that may have occurred and solute content is high. It

is not possible to predict which of these parameters would dominate or what their combined effect could be.

The last stage that could be observed in recovery is the coarsening of sub-grains, the driving force of which is the stored energy at the boundaries. The energy of the system after sub-grain formation is still high due to total area of low angle boundaries and the coarsening can lower the free energy. Usually sub-grain growth is attributed to occur in materials in which recrystallization is not possible. The following equation was derived for the kinetics,

$$D^n - D_0^n = c_1 t \qquad\qquad 5.4$$

In which D_0 is the subgrain size at t=0 and c_1 is temperature dependent rate constant and n is the exponent when close to 2 resulting in grain growth kinetics after recrystallization but it may vary up to 4. It should be stated that the amount of sub-grain growth is rarely greater than 2 for the ratio of D/D_0 because it is often bypassed by recrystallization [58, 84, 128].

Subgrain Growth Controlled By Particle Coarsening

Small, unstable particles such as precipitates may start to grow or transform after obtaining a stabilized sub-grain structure during sub-grain growth. The growth/transformation rate of particles directly affects or even controls the rate of sub-grain growth. To describe the process, extended recovery term is used since previously stabilized structure restarts the recovery process. The structure that formed as a result of extended recovery varies with the degree of coarsening. It may be similar to continuous recrystallization process but the main difference is that it provides no significant change observable on the distribution of grain/subgrain misorientation.

5.2.2.2. Recrystallization of Two Phase Alloys

Recrystallization is a renewal process of a deformed metal involving the formation of new, strain free grains in the structure. Its driving pressure is the amount of strain

imposed and high enough strains may cause a decrease in the recrystallization temperature due to high stored energy and hence high driving pressures. Even if the alloy consists of the same particles, the recrystallization temperature may vary according to the strain amount. Recrystallization is a very broad subject to be discussed thoroughly so in this part of the review the discussion will be limited to the recrystallization of two phase alloys particularly the relationship between recrystallization and precipitation.

Second-phase particles, either in the form of dispersoids already present in the alloy or in the form of precipitates to be formed, have significant influence on the recrystallization behavior of the alloy. In a two phase alloy there are two basic options; already present particles and particles that are precipitating in the process of annealing. Both of these cases are present in an as quenched and ECAPed Al 2024 alloy due to the present dispersoids in the structure and super saturated state ready to precipitate.

If the strength of the particle is low and particles deform they lower the recrystallization tendency while harder particles have a diverse effect. Individual effects of particles are not easy to determine but there are two general processes that might be observed; particle stimulated nucleation (PSN) and boundary pinning.

It is important to pay attention to the particles that are already present in an alloy prior to deformation since they may influence the overall density of dislocations, homogeneity and the deformation behavior around the particles which will determine the possibility of PSN afterwards. These particles are also likely to increase the stored energy during deformation as well as the driving pressure for recrystallization. Relatively large particles may induce the nucleation of new crystals which is termed as particle stimulated nucleation (PSN). On the other hand particles that are small and closely spaced may utilize a noteworthy pinning effect on grain boundaries which may be high or low [84, 128]. The effect of particles varies according to the particles' size, shape, spacing and volume fraction.

The combined effect of size and spacing of thermally stable particles may lead to a strong pinning effect that prevents recrystallization of deformed or recovered structure up to the melting temperature. Usually this could be the case when metal matrix composites are considered. However, particles that are larger than 1 micron was found to accelerate new crystal formation in the same alloy [128].

PSN is a commonly observed phenomenon in commercial alloys such as copper, aluminum, nickel and iron when the particle size is above or close to 1 micron since many alloys include large particles. It may be controlled by particle distribution and may be used as an aid for homogeneous small grained microstructures. The possible outcome of PSN may be a textured recrystallization depending on the orientation of the particles. A low deformation temperature as well as high strain are some of the factors that may stimulate PSN [128]. In the ECAPed Al 2024, both low deformation temperature and high strain are present as well as dispersoids of various sizes. PSN might be the possible mechanism observed in the samples annealed at 190°C and 200°C.

To conclude, in general three major effects of particles in an alloy can be observed two of which promote recrystallization while the other may inhibit. First of all, the particles present make the process of deformation harder hence increase both the stored energy and the driving pressure for recrystallization. When the particles are large, they may act as nucleation sites for recrystallization which is the second promoting effect of particles present in the structure. Contrary to large particles, if the spacing between the particles is small, they may well apply a considerable pinning to not only low angle grain boundaries but also to the high angle grain boundaries. This hindering effect may be highly observed if the precipitation occurs before recrystallization. It can be concluded that size, distribution and the volume fraction of the second phase are the most important parameters to be considered. Both the recrystallization kinetics and the final grain size depend strongly on the inter particle spacing as well as the size of the particles [128].

It is stated that when compared to a single phase alloy, the retardation and even complete inhibition of recrystallization are frequently observed in the two phase alloys. Especially in systems when there are small particles, it is important to remember that the recrystallized grains do not need to be or even cannot be equiaxed but they are shaped in ragged forms due to the pinned grain boundaries.

When the deformed alloy in consideration is also a super saturated solid solution which is about to precipitate then the relation of precipitation to recrystallization is very important. The situation becomes highly complicated not only because the precipitation nature and kinetics are likely to be affected by the deformed structure but also the recovery and recrystallization might be interfered by the presence of precipitates. This is the case of supersaturated and ECAPed Al 2024 in the current study. Although it is impossible to construct an exact match of time temperature transformation diagram for Al 2024, a schematic figure represented in Figure 5.2 adopted from Humphreys et. al. [128, 129] for a cold-rolled super saturated Al alloy of minor alloying element is represented as a starting point for a more clear discussion.

There are three basic regions divided by two critical temperatures (T_A and T_B) in the diagram showing the coexistence of three possibilities of precipitation and recrystallization. In this case recovery may be regarded as a former process that has already started during deformation.

Region I (T>T_A): is the only temperature range in which recrystallization is not affected by precipitation reaction. It proceeds and is finalized before any precipitation and subsequent precipitation may be observed depending on the super saturation and duration of annealing.
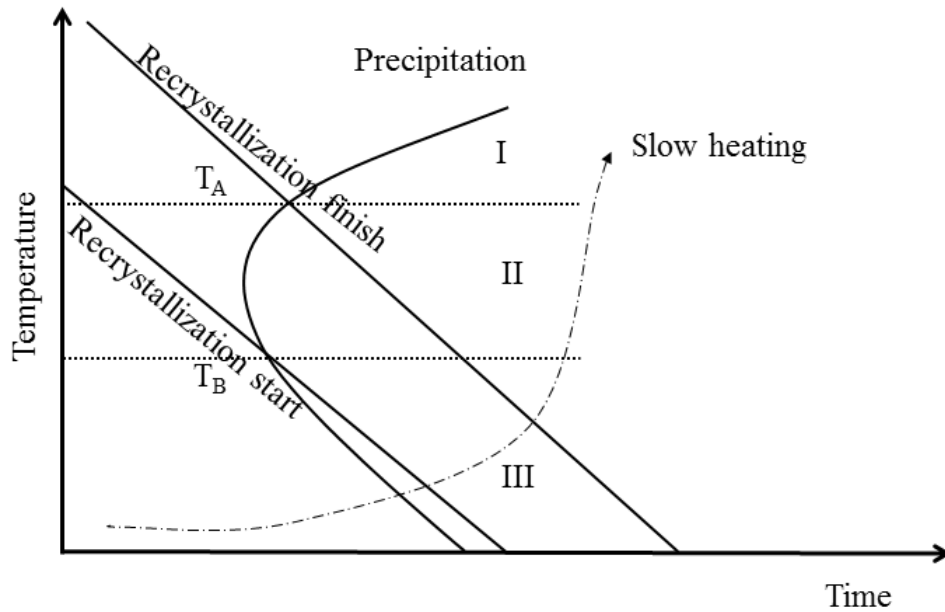
Figure 5.2. Schematical TTT diagram of a cold-rolled supersaturated aluminum alloyadopted from [128, 129]**.**

Region II ($T_B<T<T_A$): is the temperature range where recrystallization is observed prior to precipitation. It is likely that the precipitation may inhibit the completion of the recrystallization process.

Region III ($T<T_B$): Lastly the third region, which is the most relevant to the current study, is the temperature range which is relatively low compared to others. In this range, priority is of precipitation and hence retardation of recrystallization is very likely. The recrystallization lines drawn belong to a dilute Al alloy in the absence of precipitates. It is very likely that at the lower parts of the TTT an expected retardation for recrystallization will occur.

A three step process is expected in this region. The first step is the precipitation and recovery in which a pinning due to the presence of precipitates may be observed, inhibiting the recrystallization. In the second step, coarsening of the precipitates or transformation of them into incoherent stable phases is to be expected. The sub-grain growth is expected as a result of precipitate growth or transformation. This

phenomenon is stated as "recovery" through particle controlled sub-grain growth. The last step of the region is recrystallization which can only occur at sufficiently long times and high enough temperatures originating at high angle grain boundaries, large second phase particles or heterogeneities [128].

Heating rate is stated as another important factor, because at low heating rates precipitation occurs prior to recrystallization and formation of new crystals is retarded whereas high heating rates surpasses the precipitation zone in the TTT diagram.

5.2.3. Thermal Stability of Aluminum Alloys

Thermal stability of all engineering materials is important due to a probable exposure to relatively high temperatures. In the case of low melting temperature Al alloys, it is crucial to determine the property variations with temperature. While the term, thermal stability, may include extreme conditions like very low temperatures, in the case of aluminum, low temperatures enhance mechanical properties by nearly 25% [1]. When aluminum with a melting temperature of 660.37°C is alloyed with Cu, Mg, Mn, Zr, Fe and Si to form 2024 alloy, melting temperature drops to 638°C with the solidus and incipient melting temperatures of 502°C and linear thermal expansion coefficient [1]. When annealing temperature range is calculated according to the equation, $1/3T_m$, it gives the beginning temperature of the annealing as -15 to +31°C (258-304 °K) which is very low. From this standpoint, even room temperature deformation may be considered as hot deformation for Al 2024. With this in mind the temperature ranges selected in the current study (80-200°C) for thermal stability can be considered as high temperatures. If the initial annealing temperature is taken as the recrystallization temperature, which is generally stated as ½ T_m (114-182°C) to $2/3T_m$ (244-334°C), then the temperature range selected for ECAPed Al 2024 in this study covers the lower part of that region. It should be noted that the temperature and kinetics of annealing may vary depending on so many factors that it is not possible to predetermine the response of the ECAPed Al 2024. However, regarding Al 2XXX alloys and S precipitates, in 2011, the strength

and thermal stability was suggested to be improved by maintaining the precipitates below a certain size and increasing their density [6]. The current study can easily be regarded as a response to the suggestion.

The most common method to detect mechanical response to temperature in long time intervals is creep testing. There are also long term thermal property tests reporting the tensile test behavior after exposure to various temperatures for durations of 100, 1000, 10000 hours [1, 130]. Data for Al 2024 in relation to these tests could not be obtained, however a sample data for 2124-T851 was represented in Table 5.1 [1]. The difference in chemical composition between Al 2024 and Al2124 is also given. T851 states that the sample was stress relieved by stretching, compressing or a combination of both after solution heat treatment, cold working, and artificial aging. As can be seen, the only variation is the upper limit of Si and Fe percentages. The alloy composition in the current study can also be found in the table.

Table 5.1. Thermal stability data for Al 2124 T851 and compositions

Temp. °C	T Time of Exposure to Temp. (h)	At Indicated T				At RT after heating		
		Tensile Strength (MPa)	Yield Strength (MPa)	Elongation (%)	Elastic Modulus (GPa)	Tensile Strength (MPa)	Yield Strength (MPa)	Elongation (%)
-80	-	525	490	8	76	-	-	-
24	-	485	450	8	72	485	450	8
100	0.1-10000	455	420	9	71	485	450	8
150	1000	400	380	11	68	475	435	8
175	100	360	340	12	66	470	420	8
175	1000	330	305	14	66	455	400	8
175	10000	295	250	16	66	405	305	10
205	100	305	270	15	63	435	370	8
205	1000	260	220	19	63	395	305	9
205	10000	185	140	28	63	290	165	12
Compositional Differences in Al Alloy								
Alloy Designation	Si (%)	Fe (%)	Cu (%)	Mn (%)	Mg (%)	Cr (%)	Zn (%)	Ti (%)	Unspecified Each (%)	Unspecified Total (%)
2024	0.50	0.50	3.8-4.9	0.30-0.9	1.2-1.8	0.10	0.25	0.15	0.05	0.15
2124	0.20	0.30	3.8-4.9	0.30-0.9	1.2-1.8	0.10	0.25	0.15	0.05	0.15
Alloy Comp	0.24	0.40	4.41	0.72	1.97	0.21	0.26	0.23	-	-
Std dev(±)	0.04	0.05	0.14	0.05	0.10	0.03	0.07	0.03	-	-

5.2.4. Thermal Stability of Severely Deformed Materials

The thermal stability of severely deformed materials is investigated in various studies [117–126, 131–137]. The main concern of these studies was to investigate the variations in grain size, grain boundary type and mechanical properties. The stability of ultra-fine grain size was measured through TEM and EBSD. The mechanical testing was performed either by tensile or modified tensile test in substandard size or by hardness measurement. Differential scanning calorimetry was also considered as a tool to investigate structural variations. Another less common investigation was X-ray diffraction to measure the difference in lattice parameter and strain [117–127, 131–137].

The kinetics of microstructural and mechanical variations was measured by DSC and by isothermal or isochronal heating curves. The duration of temperature exposure was limited to 2 hours. In Table 5.2, some of the recent studies carried out are summarized. It should be noted that the longest annealing period in these studies was 672 hours and carried out only in the cold rolled Al alloy [135]. Especially for ECAPed or HPT processed samples there are no significant studies on how long time annealing would affect the properties and microstructure. An investigation of long term thermal stability of severely deformed structures in accordance to the standards have not been found during literature search whereas quick and incomparable tests were easy to come by[117–127, 131–137].

At temperatures above 150°C, the response of SPD processed Al alloys is quicker and meaningful data could be produced even for few annealing hours. A study by Ning et. al. on highly cold deformed Al 2024, it was stated that recovery of the deformed structure starts at the beginning of 190°C aging . But since the formation of GP zones (they are not observed) increases strength the level of decrease in strength is eliminated [111].

Table 5.2. Some recent, thermal stability studies on severely deformed alloys.

Year	Alloy	Deformation Process	Thermal Stability Temp	Time of Exposure	Mechanical Property Results
Horita et. al. 2000 [117]	Al 1100	ECAP (90°) 6 passes	100°C, 150°C, 200°C 250°C, 300°C, 350°C	1 hour	Tension test
	Al 3004	ECAP (90°) 6 passes	100°C, 150°C, 200°C 250°C, 300°C, 350°C	1 hour	Tension Test
	Al 2024	**ECAP (90°) 6 passes**	**100°C, 200°C, 300°C**	**1 hour**	**Grain size measurement**
	Al 6061		100°C, 200°C, 300°C	1 hour	Grain size measurement
	Al 5083		100°C, 200°C, 300°C	1 hour	Grain size measurement
	Al 7075		100°C, 200°C, 300°C	1 hour	Grain size measurement
Mao et. al. 2005 [134]	Al 2024 (over aged)	ECAP (90°) 8 passes	100°C, 200°C, 300°C	1 hour	**Grain size measurement**
	Al 2024 (peak aged)	ECAP (90°) 4 passes	100°C, 200°C, 300°C	1 hour	**Grain size measurement**
Cabbibo et. al. 2004[11 9]	**Al 1200**	**ECAP (90°)**	**130°C, 240°C, 330°C**	**1 hour**	**Hardness measurement**
	Al3103	**ECAP (90°)**	100°C, 200°C, 300°C	1 hour	**Hardness measurement**
Hansen et. al. 2008 [135]	Al 1200	Cold Rolled (Strain =2.3)	RT to 400°C	2 hour	**Hardness measurement**
	Al 1200	Cold Rolled (Strain =4.6)	RT to 400°C	2 hour	**Hardness measurement**
	Al 1200	Cold Rolled (Strain =4.6)	200°C, 210°C, 230°C	672 hour	**Hardness measurement**
M. Lewandowska 2005 [122]	Al 2017	hydrostatic extrusion	100-400 °C	1 hour	**Grain size measurement Microhardness (sudden drop after 150°C)**
Rebhi et. al. 2011 [124]	99.1 % Al	ECAP (90°) 1 pass	50-400 °C	1 hour	**Hardness measurement XRD analysis**
Kuzel, 2013 [137]	Cu Cu-Zr	ECAP	100°C, 140°C, 160°C, 180°C, 200°C	30 minutes	**In situ XRD**
Islamgaliev 2011 [133]	Al-Cu-Mg-Si alloy	HPT	20-250 °C	30 minutes	**Hardness measurement XRD Analysis**

5.3.   EXPERIMENTAL PROCEDURE

Homogenization of ECAP processed Al was investigated previously. It was shown that through precipitation the inhomogeneity due to severe deformation could be eliminated. On the other hand, increased aging kinetics may be detrimental to service time especially when the relatively high temperatures are considered. While Al 2024 alloy was known to be stable up to 150 °C, the thermal stability of ECAPed Al 2024 was only investigated in short terms by isochronal or isothermal investigations. For long term thermal stability investigation, the single pass ECA pressed aluminum 2024 alloy, with a chemical composition given in Table 5.1, was divided into various pieces as shown in Figure 5.3. The temperatures were selected according to the reported lowest aging temperature, 80 °C, as the lower limit and just above the optimum aging temperature, 200°C, as the upper limit. The intermediate temperature 150°C was reported as a critical limit, and 120°C was chosen as a candidate limit temperature for severely deformed Al 2024.

The ECAPed sample was cut through the shear angle and each part was used for a specified temperature with its TEM sample adjacent to the surface where micro hardness measurements were taken. The elliptical pieces, except for the 190°C piece, were cut into two pieces one of which was slightly larger in order to distinguish easily. The larger parts were aged at 190°C for one hour prior to thermal exposure.

The Vickers microhardness measurements were carried out according to a map designed for homogeneous data collection from 15 regions of each sample which was shown in Figure 5.3. The time intervals of exposure to annealing temperatures were increased in time. Initially 6, 12, 24, 48, 168, hours were selected to be able to see the precipitation and general behavior. Further time intervals were chosen as long as possible for practicality and short enough to obtain required data hence the experiments were continued with various interruptions until 1000 hours. The samples were quenched into water after annealing at each interruption before micro hardness and XRD measurements and TEM sampling.

XRD measurements were conducted using a 0.15 slit with a rate of 1°/min, rotating the sample in the range of 20-90° degrees.
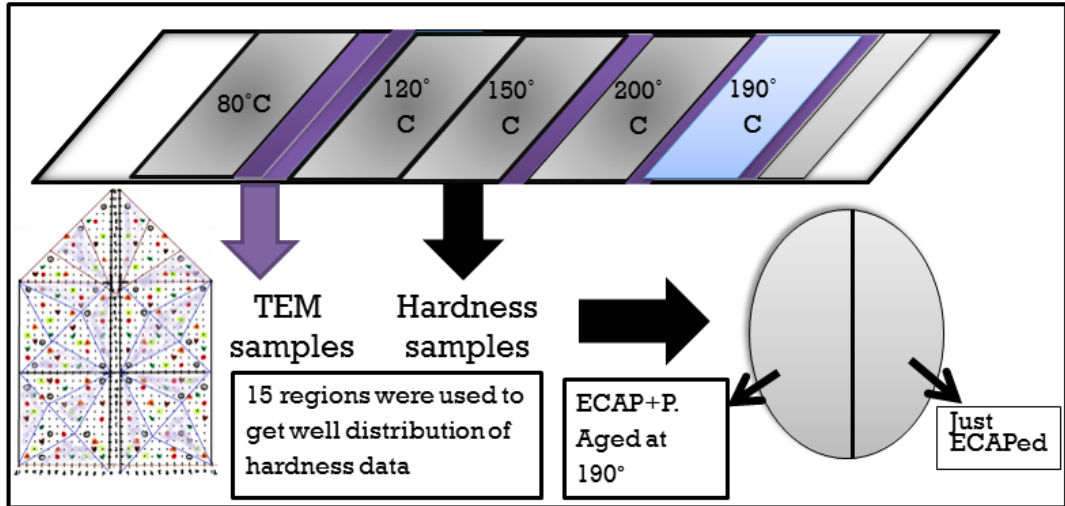
Figure 5.3. The sample sectioning and hardness measurement map.

The corresponding TEM samples were collected for critical micro hardness variations from all the samples.

The DSC measurements for ECAP processed and ECAP processed and peak aged samples were carried out in central lab. The heating rate was 10°C/min from -2°C to 500°C.

XRD measurements were performed using a slit of 0.15 between 20-90° with a scan rate of 1° per minute rotating the sample. The data for long term thermal stability of commercial Al 2024 alloy was also not available in the literature for Al 2024 alloy but could be found for 2124 alloy though the micro hardness data could not be directly obtained.

This part of the study will include the thermal stability at different temperatures as well as the effect of post-ECAP precipitation on thermal stability. The temperatures

of interest will start with 150°C since it is an important limit temperature and continue with higher temperatures such as 190 and 200°C. Lastly the behavior of the ECAPed samples at 120°C and 80°C will be discussed. The data is mainly of the hardness variations but some of the samples are further investigated using TEM or EBSD to ease the understanding of the different behaviors in hardness plots.

5.4.   RESULTS AND DISCUSSION

The DSC data obtained from Sample B and C did not give any meaningful results and hence they are not presented in the results of this study. Likewise, XRD data was found to have too low resolution in order to distinguish the complicated phases such as precipitates and dispersoids from the Al matrix and each other. Thus, the results of the study are composed of EBSD and TEM investigations with their corresponding micro-hardness measurements. The data will be presented as a blend of the three to ease the understanding of the variations.

Figure 5.4 and Figure 5.5 show the microhardness variation during annealing at 80°C, 120°C, 150°C and 200°C of ECAPed and ECAPed+peak aged samples, respectively.

Above 150°C, peak aging after ECAP could be regarded as ineffective except the homogeneity of the structures. Below 150°C, on the other hand, the peak aging after ECAP seemed to be effective on a homogeneous structure with stability and improvement in mechanical properties.

A secondary peak after 500 hours of annealing emerged in samples tested at and below 150°C. Sudden drop of hardness, indicating recrystallization, was seen in samples at and above 150°C. Hence it is possible to say that 150°C is a limiting temperature for ECAPed samples in terms of thermal stability. Both recrystallization and a secondary peak are observed at this temperature.
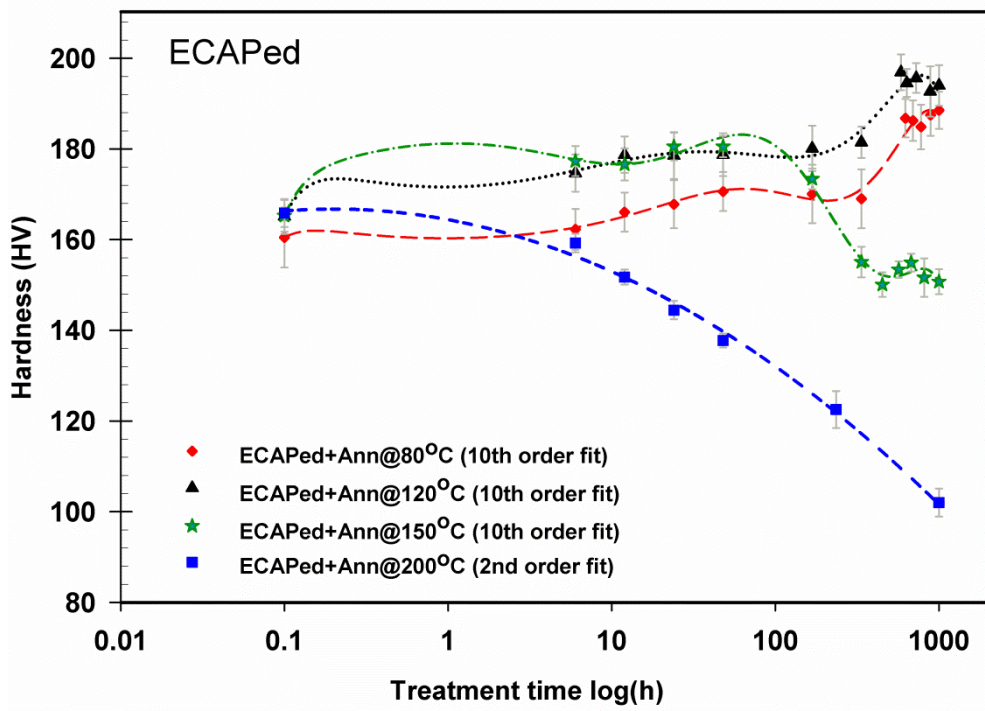
Figure 5.4. Variations of the micro-hardness of the ECAPed samples at different annealing temperatures.
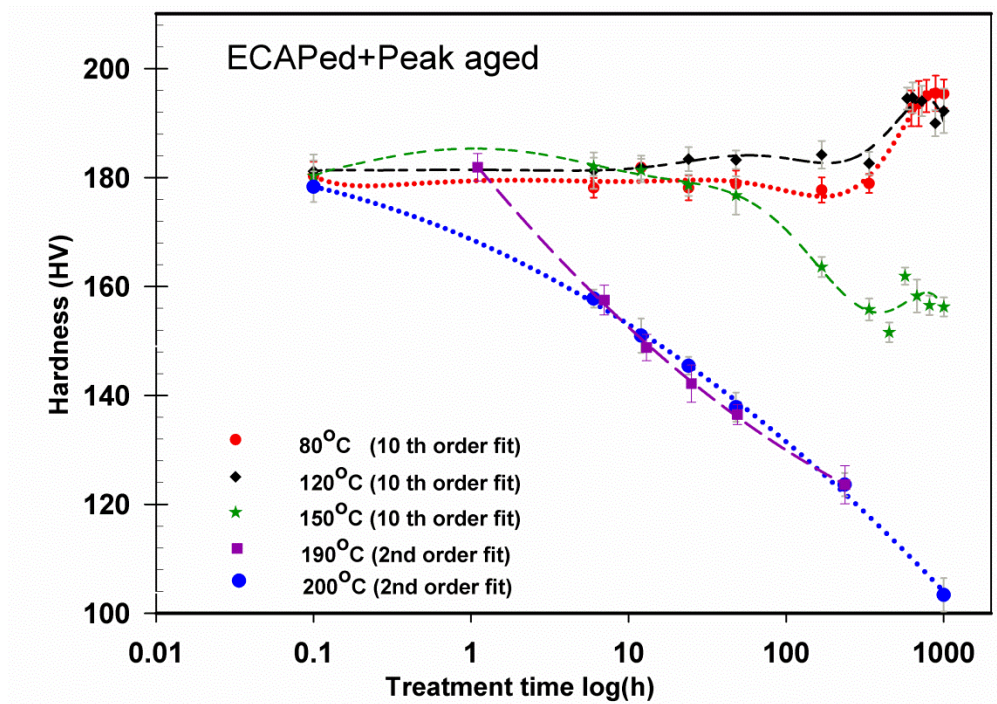
Figure 5.5. Variations of the micro-hardness of the ECAPed and peak aged samples at different annealing temperatures.

The comparison of ECAPed samples with 2124-T851 is presented in Figure 5.6. It should be noted that the conversions from tensile strength of 2124-T851 to Vickers hardness were carried out using a conversion table generally used for steels. This may be regarded as inappropriate; however it provides an opportunity for comparison.
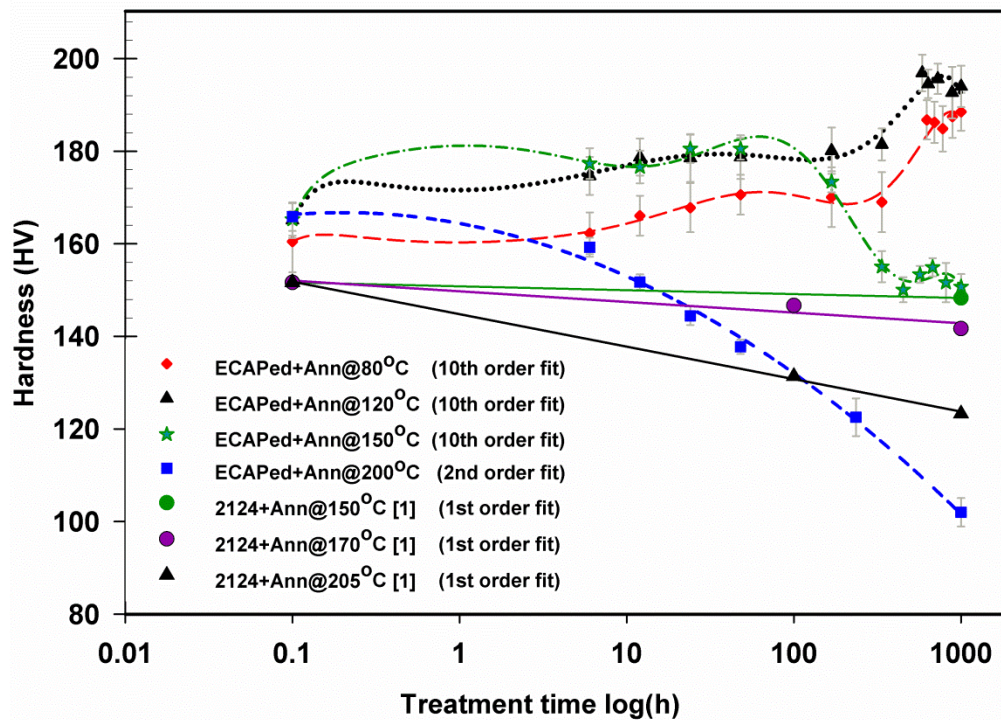
Figure 5.6. Thermal stability of ECAPed Al 2024 and cold deformed Al 2124 alloys.

When the hardness values of ECAPed Al 2024 is compared with cold worked Al 2124, the hardness of ECAPed Al 2024 is found to be lower than that of cold worked 2124 alloy after 1000 hours of annealing at 200°C. Although conversion errors from UTS to HV at lower strengths can cause the unexpected result, it is suspected that an abnormal grain growth controlled by particle coarsening might be the reason of the decrease of hardness in ECAPed Al 2024. This result shows how important long term thermal stability characterization is prior to commercialization.

146

Due to the unknown nature and unpredictable behavior of SPD materials; tedious characterization is a must.

The ECAPed and post ECAP aged Al 2024 samples are found to preserve and even improve their mechanical properties during annealing at 80°C and 120°C. 150°C was detected to be a limiting temperature for applications involving long term exposures to high temperatures. In addition, it seems to be a key transition temperature that shows both high and low temperature behaviors at different stages. It includes the sudden drop that is observed in samples annealed at 200°C and the secondary peak emerged in samples annealed at 80°C and 120°C. As an intermediate temperature, detailed investigation on annealing of ECAPed Al 2024 at 150°C may enlighten the underlying mechanisms during annealing of ECAPed Al 2024. Consequently, the variations of ECAPed sample at 150°C is thoroughly investigated and presented whereas other temperatures are briefly explained in the following sections.

5.4.1. Stability of ECAPed Structure at 150°C

When heated to 150°C, ECAPed sample experienced a typical precipitation process as a function of time (Figure 5.7). A similar precipitation behavior observed in 190°C was noticed. A two-step aging with a slight decrease in between, a deviation is recognized. Yet it is hard to decide in either case whether it is an actual separation or only a deviation. For ease of understanding however, the stepwise process may be helpful. The initial hardening (stage 2) at 150°C has developed in nearly 10 hours with about 13 HV increment, slightly higher than 190°C. The second hardening (stage 3) showed an increase of 4 HV, similar to 190°C, in about 36 hours. After 500 hours of annealing at 150°C, a third hardening peak appeared. It is an interesting behavior of the alloy, probably due to another precipitate formation.
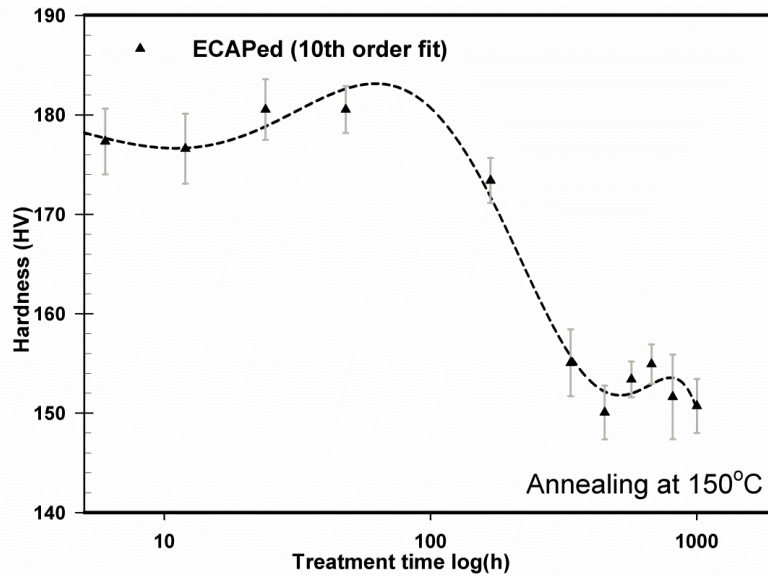
Figure 5.7 Hardness variation of ECAPed Al 2024 at 150°C as a function of treatment time.

5.4.1.1. After 6h at 150°C

The data presented in Figure 5.8 shows the deformed structure of ECAPed sample after 6 hours of annealing at 150°C. The various colors in EBSD data represent different crystal orientations as denoted by the color coded map given below the EBSD image. EBSD image with color variations throughout the elongated grains shows that deformed structure was preserved. The crystal orientation differences inside the grains can be attributed to the deformed structure recovered in the form of cells which are also imaged in TEM. The TEM images represent cell formation surrounded by high density dislocation regions, so called dislocation forests. The dislocations at the interiors of the cells were preserved. This indicates that cell formation stage of recovery had been activated but annihilation of dislocations inside the cells had not occurred yet.

The size, distribution and shape of cells vary with grain orientation as it is also visible in EBSD image. For example, the pink and purple grain enclosed by the big circle in Figure 5.8a show higher orientation difference while in the green grain,

148

small circle, variations are less. It should also be noted that less or more, in all grains color variations exist and there are no grains of single, uniform color. In each data a representative hardness plot is attached for the ease of following the data.

In Figure 5.8, a few cell walls shown by arrows (c) are seen accompanied with the corresponding diffraction pattern (d) of the image. The cell wall sizes are about 400 nm in width. The diffraction pattern forms an interrupted ring pattern which is a sign of misorientation differences, hence polycrystallinity. This indicates that the cell walls shown in Figure 5.8-c are separating regions of varying orientations such as subgrains in a coarser grain.

Figure 5.8-e and f include the bright field and dark field images of a T-phase dispersoid immersed in the deformed structure. In Figure 5.8-g, the circled spot belongs to the dispersoid lying parallel to the (-220) plane of the matrix and the dislocation rich region is observed around it. The observation of precipitates was not possible in the diffraction pattern.

At this point, it is important to understand how cells, formed during recovery, can be observed using TEM. Cell walls are nothing but densely arranged dislocation tangles around a less dense dislocation rich region. The observation of dislocations in TEM can only be possible when diffraction vector g and Burger's vector b are not perpendicular to each other. Whenever an image is observed in TEM some of the dislocations cannot be observed due to this dislocation invisibility criterion. When we observe a cell at an angle there is a certain amount of invisible dislocations throughout the cell interiors as well as along the cell walls. When the sample is tilted, the invisible ones become visible and previously visible dislocations fade in the image. This variation may not be homogeneous and strongly dependent of the sample and beam direction as well as the b of dislocations. The following suggestion may not be valid for some of the cells but may apply for others.
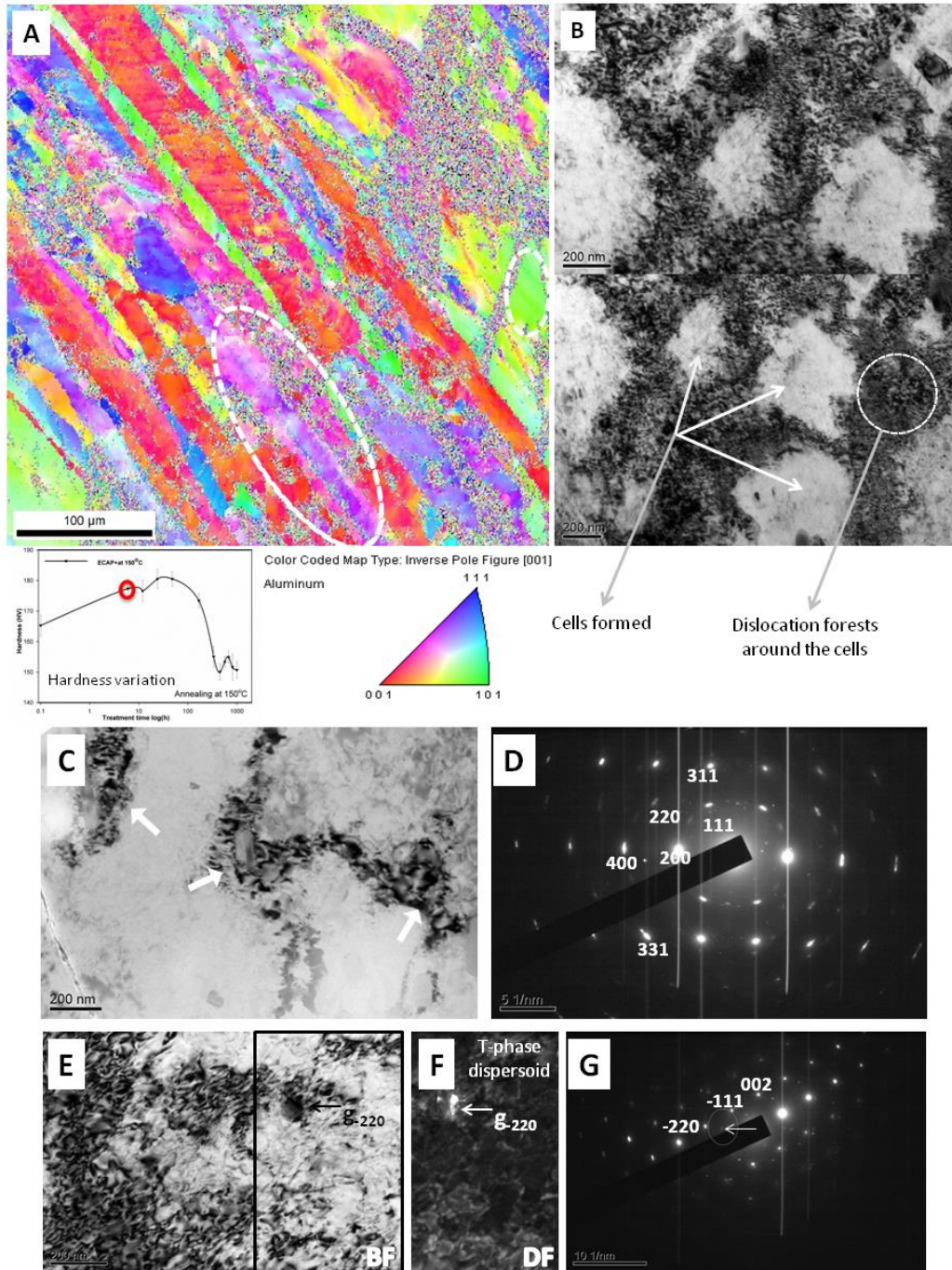
Figure 5.8. ECAPed and heated (150°C / 6h) sample: (a) EBSD image, (b) TEM image accompanied with the hardness variation plot and color coded map. (c) Cell walls formed and (d) its diffraction pattern. (e) A bright field image, (f) its dark field counterpart, (g) diffraction pattern of a dislocation rich region with a dispersoid.

Cell sizes, amount of deformation as well as the distribution of dislocations throughout the sample vary in ECAPed structures due to inhomogeneity, as indicated in Chapter 4. The generally easy to notice structure of cells shown in Figure 5.8 b may not always be observed directly. Depending on the orientation of the viewed grain/grains; cells and especially cell walls may be observed as if they were individual grains. This may be due to the partial observation of cell walls at a certain perspective as represented in Figure 5.9; schematic explanation of how the observation may vary with respect to the grain orientation. This is best supported by spread diffraction spots viewed as if to form a circle as in Figure 5.10 b. It should also be reminded that the thickness of the sample definitely alters the resultant image. For relatively thin regions of the sample, at the edges, dislocation density may seem to be low because only the projection of a depth of 10-20 nm thickness is observed. When the thickness increases, away from the edges, the observed image becomes much more complicated. Even the edge thickness varies from one region to another; hence it may not be meaningful to drive a conclusion on dislocation density depending on various TEM images. Yet, the precipitate size variations and relations of precipitates to the matrix, dark field images, the recrystallized grains or dislocation free subgrains, are more countable observations in TEM.
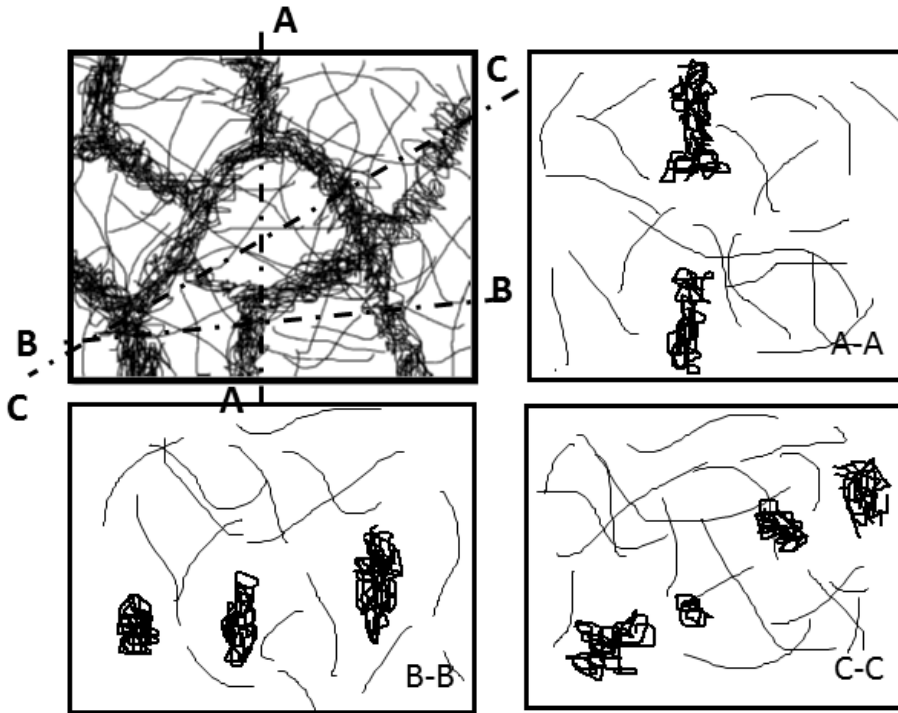
Figure 5.9. Possible observations of cells formed and cell walls using TEM.

Another image of the general view of 6 hour annealed ECAPed sample at 150°C is shown in the Figure 5.10-a with its corresponding diffraction pattern (b). Due to the grain orientation, walls of various cells denoted with red arrows are observed. T-phase dispersoids are marked by blue arrows and the combined image of dispersoids and cell walls are encircled. The diffraction pattern is circular which represents polycrystalline nature in general and in particular multiple cells in this image. All aluminum peaks are not observed in the diffraction pattern which may indicate texture, and there are undefined spots which, most probably, belong to the dispersoids. In the lower part of the Figure 5.10-c, a cell with dislocations inside is visible. This gives the idea that the sample is on recovery of the deformed structure and at its initial stages. The precipitation may be a more dominant process since grain interiors as well as dislocation rich cell walls may contain tiny precipitates, either GPB zones or S″/S′ phases. The traces of precipitates are visible in Figure 5.10-d in the form of small white particles of about a few nanometers. Due to very

small sizes, deformed structure as well as high coherency of the precipitates, the diffraction patterns do not show any sign of GPB zones or precipitates. However, observations on the over aged and peak aged structures and the increased hardness led to the conclusion that these white regions are signs of early stages of precipitation.
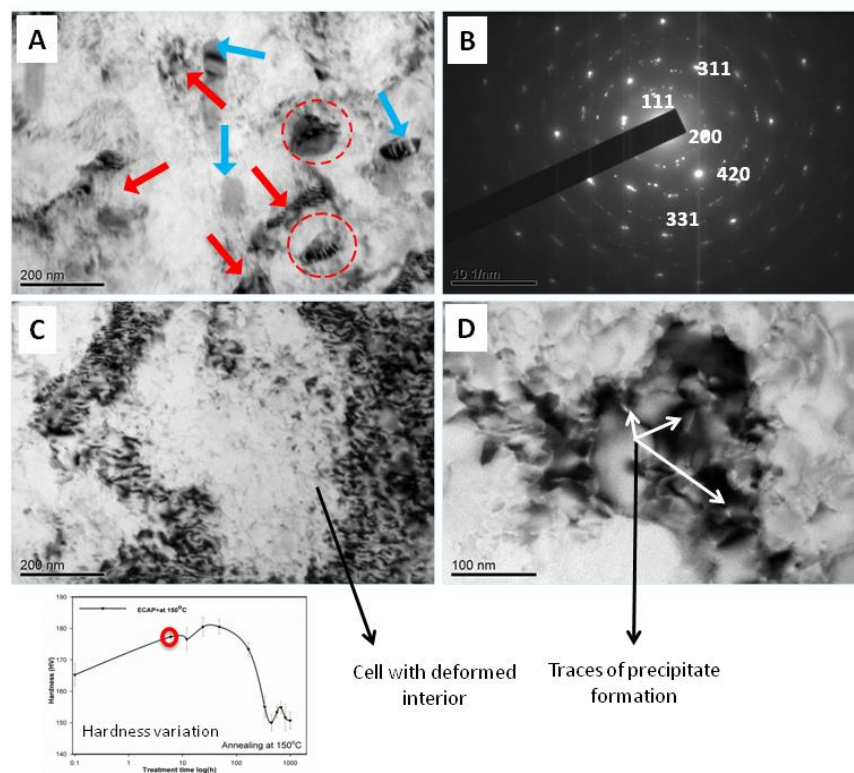
Figure 5.10. ECAPed and heated (150°C / 6h) sample: (a) Dispersoids and cells formed, (b) DP, (c) A cell with dislocation inside, (d) Traces of precipitates accompanied with the hardness variation plot.

To conclude, the observed microstructures and diffraction patterns show that recovery has started in the sample. The precipitates are too small to observe, but hardness increment indicates precipitation. Small hardness drops resulting from recovery is surpassed by precipitation and there is an overall increase of hardness rather than a small drop or preservation of hardness. The hardness increment could only be attributed to precipitation. This gain and loss balance may also be the reason for the lack of rapid hardening stage in ECAPed Al 2024 system.

5.4.1.2. After 24h at 150°C

After 24 h of annealing at 150°C, the second part of precipitation which leads to peak hardness is observed. Figure 5.11 shows the EBSD data where the deformation bands as well as the blend of colors are compatible with the TEM image shown in (b). In Figure 5.11-c, red arrows indicate the cell walls while blue ones denote the T phase dispersoids all of which are reflected in the diffraction pattern in Figure 5.11-d. The corresponding hardness value is circled in red in the hardness variation plot.

Since the hardness of the sample is close to the peak value, though the image of precipitates was not clear, the traces of them in the form of strains or small white regions were expected. Regarding the hardness improvement, the presence of coherent, very small S precipitates or GPB zones or both is probable. In Figure 5.11-e, strikes and white small bands are seen which may be the sign of precipitation. The precipitates themselves still cannot be observed clearly because they are supposed to be coherent with the matrix and the dislocations they have nucleated on hinder the ease of observation. Yet the traces of precipitates can be noticed in Figure 5.11-f.
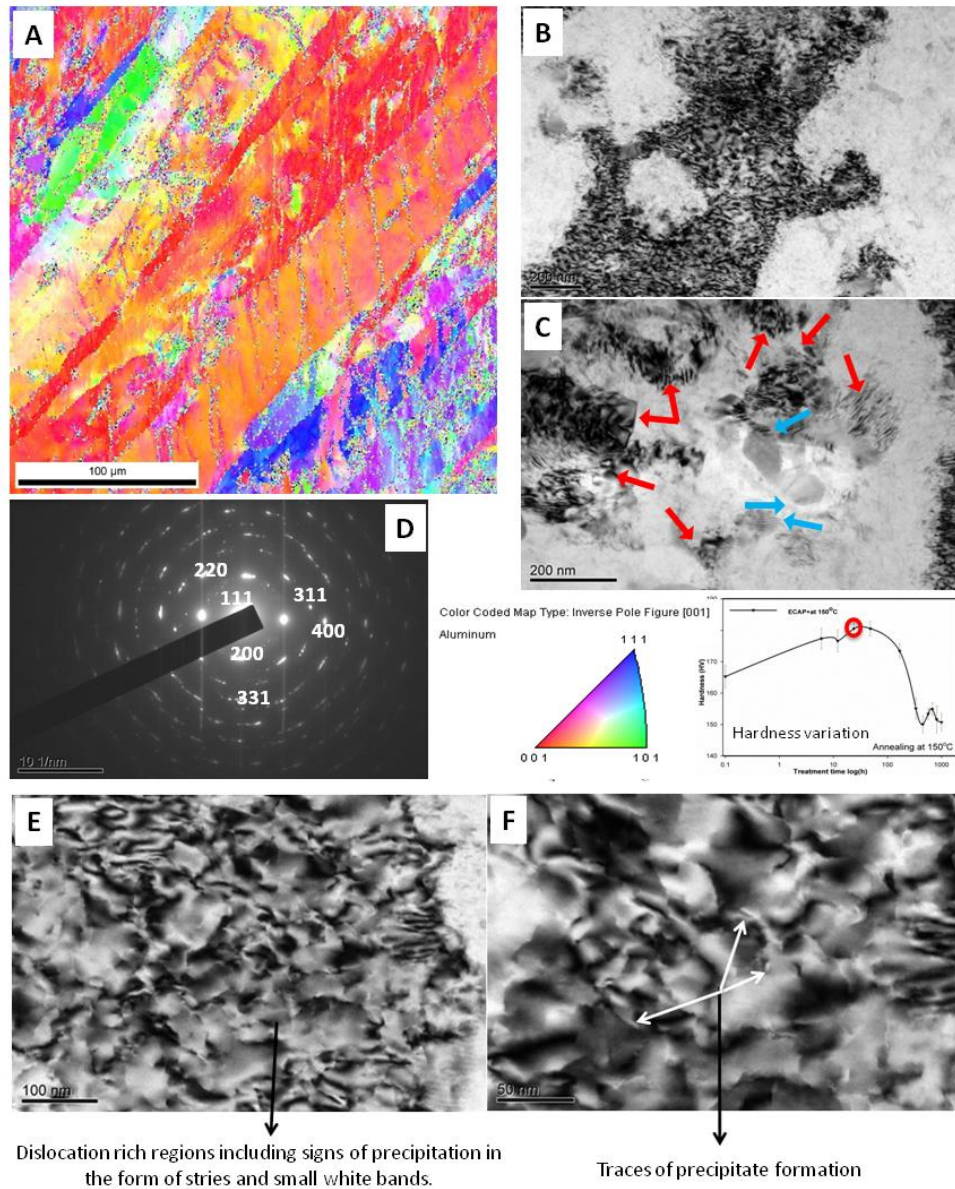
Figure 5.11. ECAPed and heated (150°C / 24h) sample: (a) EBSD image (b) cell formation, (c) cell walls and dispersoids, (d) Diffraction pattern of "c" accompanied with the hardness variation plot and color coded map. TEM images of (e) dislocation rich regions (f) traces of precipitates.

The increase in hardness can be attributed to the precipitates formed throughout the structure, especially at dislocations, in coherent or at least semi-coherent form. It is

nearly impossible to define the structure, shape or composition of the precipitates at this stage. Progress in recovery cannot be differentiated in the TEM micrographs and EBSD data and there is no sign of recrystallization at this stage of annealing

5.4.1.3. After 48h at 150°C

48 hours of annealing at 150°C resulted in over aging of ECAPed Al 2024 and the expected observation was to be able to see precipitates clearly in bright field imaging if not in diffraction mode. In Figure 5.12-a, the general view shows large dispersoids in the dislocation rich region and the deformed structure was found to be preserved throughout the sample. In Figure 5.12.b and c, two types of precipitates are seen; the encircled region in Figure 5.12-b shows long needles of precipitates which may be strain fields of GPB zones and arrows in Figure 5.12.c point to small but thicker precipitates which could not be detected in diffraction patterns. The loss in coherency of precipitates led to the relaxation of strain fields around them. As a result clearer observation of precipitates through TEM could be possible. Yet they preserve the coherency enough to prevent the observation in diffraction mode and dark field imaging.

Though not with a good accuracy, the precipitate size can be roughly measured. Both the hardness variation and TEM images supports the initiation of over aging stage of S precipitates. No signs of recovery and recrystallization could be detected at this stage hence the drop of hardness can be attributed to over aging while hardness loss due to recovery and recrystallization processes may still be present
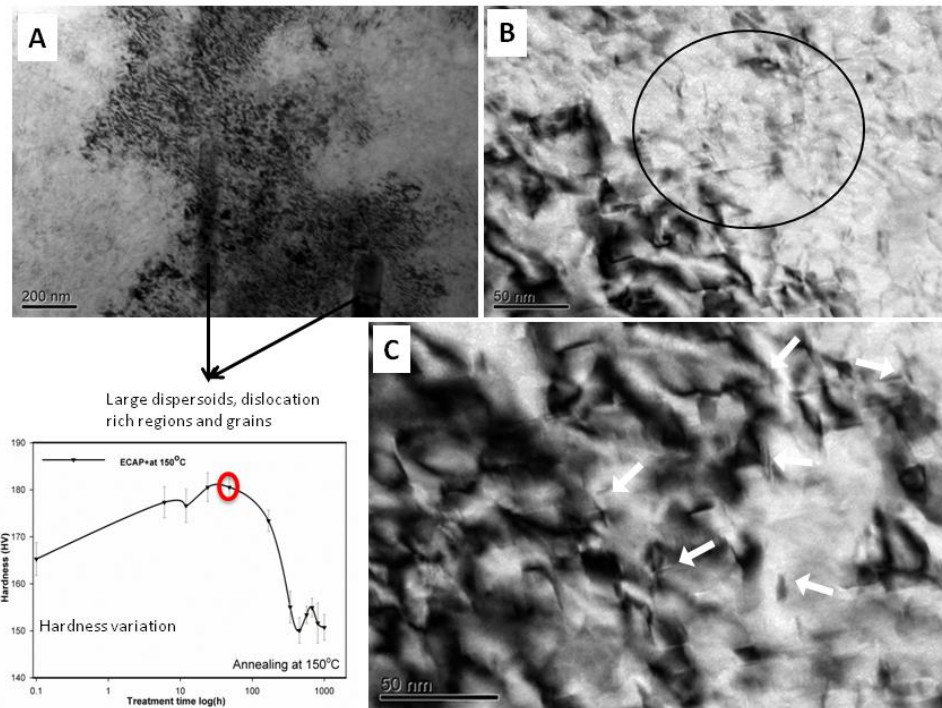
Figure 5.12. ECAPed and heated (150°C / 48h) sample: TEM images of (a) General view with dislocations rich regions and large dispersoids (b,c) precipitates accompanied with the hardness variation plot.

5.4.1.4. After 168h at 150°C

A large hardness drop is observed as a result of 168 hours exposure to 150°C. This stage is the beginning of sudden hardness drop so it is highly important to understand the microstructural changes which are keys in understanding the annealing behavior.

In Figure 5.13-a, when EBSD image of the sample is investigated, changes like enlarged orange color in the grain marked with big circle as well as the small cyan and pink grains marked with small circle are observed. These observations may indicate further recovery (subgrain formation and subgrain growth) and even recrystallization of the structure, respectively. In Figure 5.13.b, interconnected

precipitate network which indicates further over aging is pointed out by ellipsoids. The cell wall in between is preserved.

In Figure 5.13.c, grains or subgrains free of dislocations are observed and indicated by white arrows while in a large portion of the sample the deformed structure was preserved. It should be reminded that in TEM, it is possible to miss a feature present in the structure due to small sample sizes but if it can be observed in TEM, the feature is most probably present in the structure. This may be regarded as a clear indication of the beginning of the recrystallization which will progress yielding to the sudden hardness drop
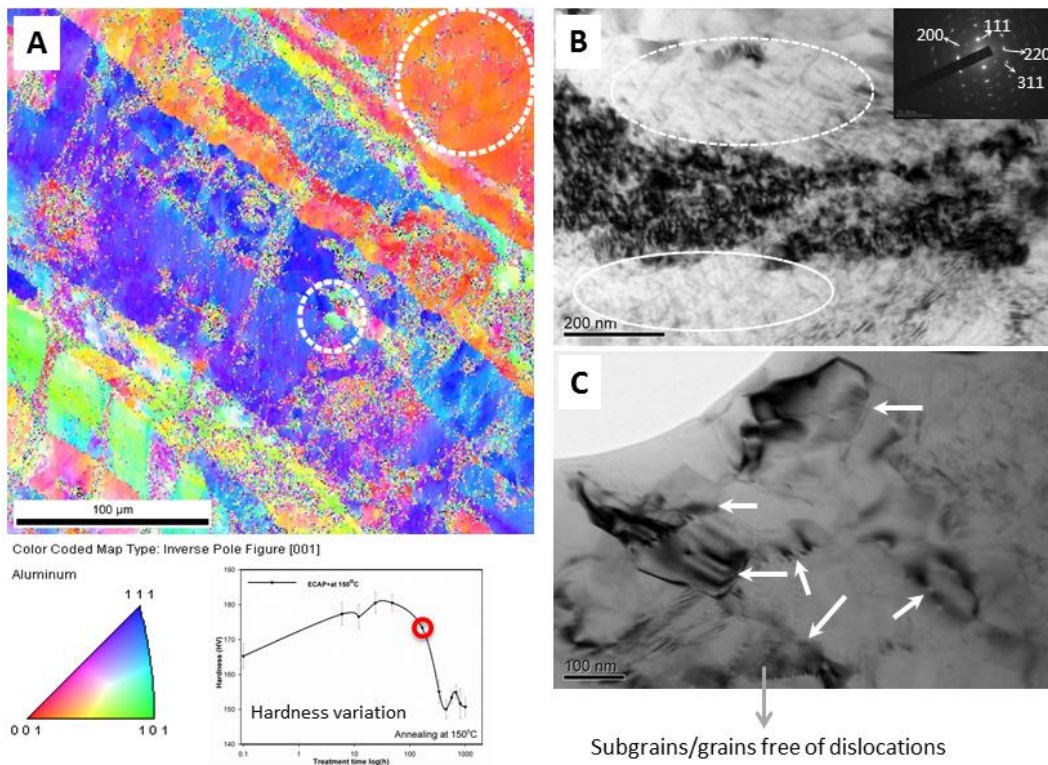
Figure 5.13. ECAPed and heated (150°C / 168h) sample: (a) EBSD image (b) cells including precipitates, (c) new grains formed accompanied with the hardness variation plot and color coded map.

In Figure 5.14 a, and b, precipitates are observed in bright and dark field images with corresponding diffraction pattern. The precipitates are in the over aged state and semi-coherent if not incoherent. The size (about 50 nm) and distribution of precipitates as well as ease of observation support the hardness drop observed. In Figure 5.14a, the dark and light regions could be interpreted as newly formed grains at first glance but when the diffraction pattern of the image was examined, the spots were found to be slightly elongated than a single spot. As a result, the various forms observed are more likely to be subgrains rather than recrystallized grains.

The TEM image in Figure 5.14.c shows a general view of precipitates while (d) and (e) are high resolution images of commonly observed precipitate types. Figure 5.14d shows an example of long needle shaped precipitate with sharp edges in either side whereas Figure 5.14.e shows an interconnected bunch of precipitates crossing each other at an angle of 80°/100°. The angles were measured out of curiosity, but a further TEM study on the relationship between the angles and properties may be carried out, when all the images are collected at the same zone axis. It is very likely that during the heterogeneous nucleation of precipitates at dislocations which already have a certain relationship with the matrix, the relationship is preserved.

The high resolution image of S precipitates in Figure 5.14.f shows the semi-coherency of the precipitates. The thickness of the precipitates is a few atomic distances. According to the FFT of the region marked as a yellow square, at the lower left, slight rotations of individual precipitates with respect to the matrix are observed. This type of precipitation, by heterogeneous nucleation, could be possible at a dislocation line formed by pure edges according to the theory of heterogeneous precipitation of S explained by Feng et. al. [6]. It is also meaningful to observe these precipitates, which are stated to have few or no effect on hardening hence heterogeneous nucleation of S precipitates at the dislocation lines support the hardness drop. It should be noted that the precipitates are smaller in size when compared to standard Al 2024 yet the hardness drop continues..
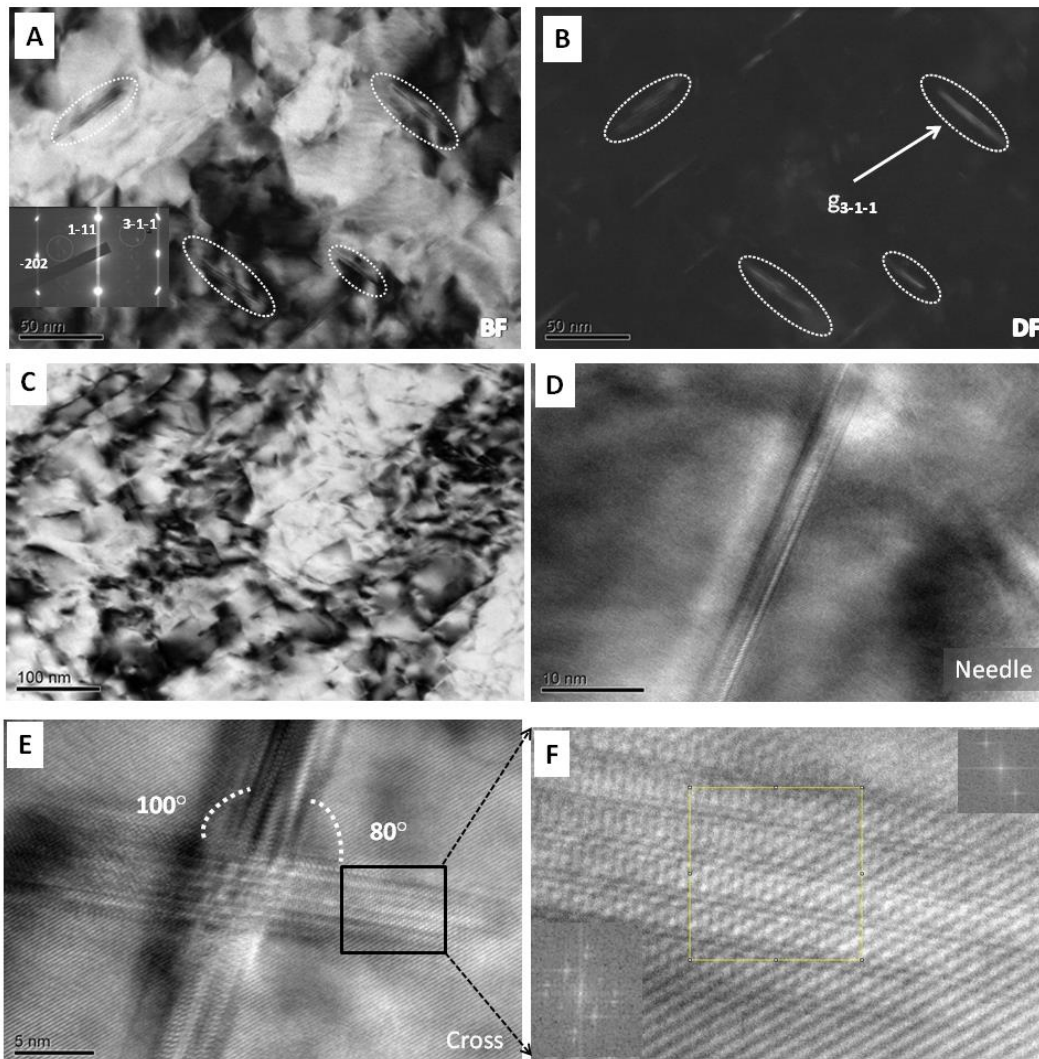
Figure 5.14. ECAPed and heated (150°C / 168h) sample: (a) Bright field image (b) dark field image. (c) Partially annealed dislocations, (d) needle like precipitates, (e) precipitates crossing each other, (f) HREM analysis of the precipitates in (e).

To conclude, 168 hours of annealing of ECAPed Al 2024 at 150°C was found to be critical. Observations on the microstructural evolution involve new formed recrystallized grains, subgrain formation and growth (EBSD), over aging in the form of heterogeneously nucleated S precipitate groups and coherency loss of precipitates. All of these observations not only support the hardness drop but also points to an emerging hardness drop.

160

5.4.1.5. After 336h at 150°C

The end point of the deep hardness drop observed in the hardness plot also gives enlightening information on the causes of the drop. First of all, when ECAPed sample after 336 hours of exposure to 150°C was observed, it was seen that loss of hardness was accompanied by recrystallization of the deformed structure as can be seen in Figure 5.15-a. The EBSD image is marked with arrows showing possible recrystallized small grains and the circle represents a large grain of nearly homogeneous dark blue with slight light regions in the middle indicating complete recrystallization. Throughout the sample a sharper view of grains are easy to notice. It should be reminded that in the presence of very small precipitates recrystallization cannot proceed in equiaxed form or a total elimination of strain is not possible. The tiny precipitates distributed nearly homogeneously into the structure help the preservation of the deformed view of TEM images shown in Figure 5.15b. Very thin cell walls accompanied with high precipitate density are seen in Figure 5.15b. The interiors are found to be filled with interacting precipitates (Figure 5.15-c) indicating over aging of the S phase or precipitation of heterogeneous S phase. The region in Figure 5.15-d shows the general view of precipitates. By means of dark field imaging, the precipitates are clearly observed in Figure 5.15-e and g. They are very dense and their size has increased up to 100 nm. A precipitate size measurement analysis was carried out using the dark field images.

.
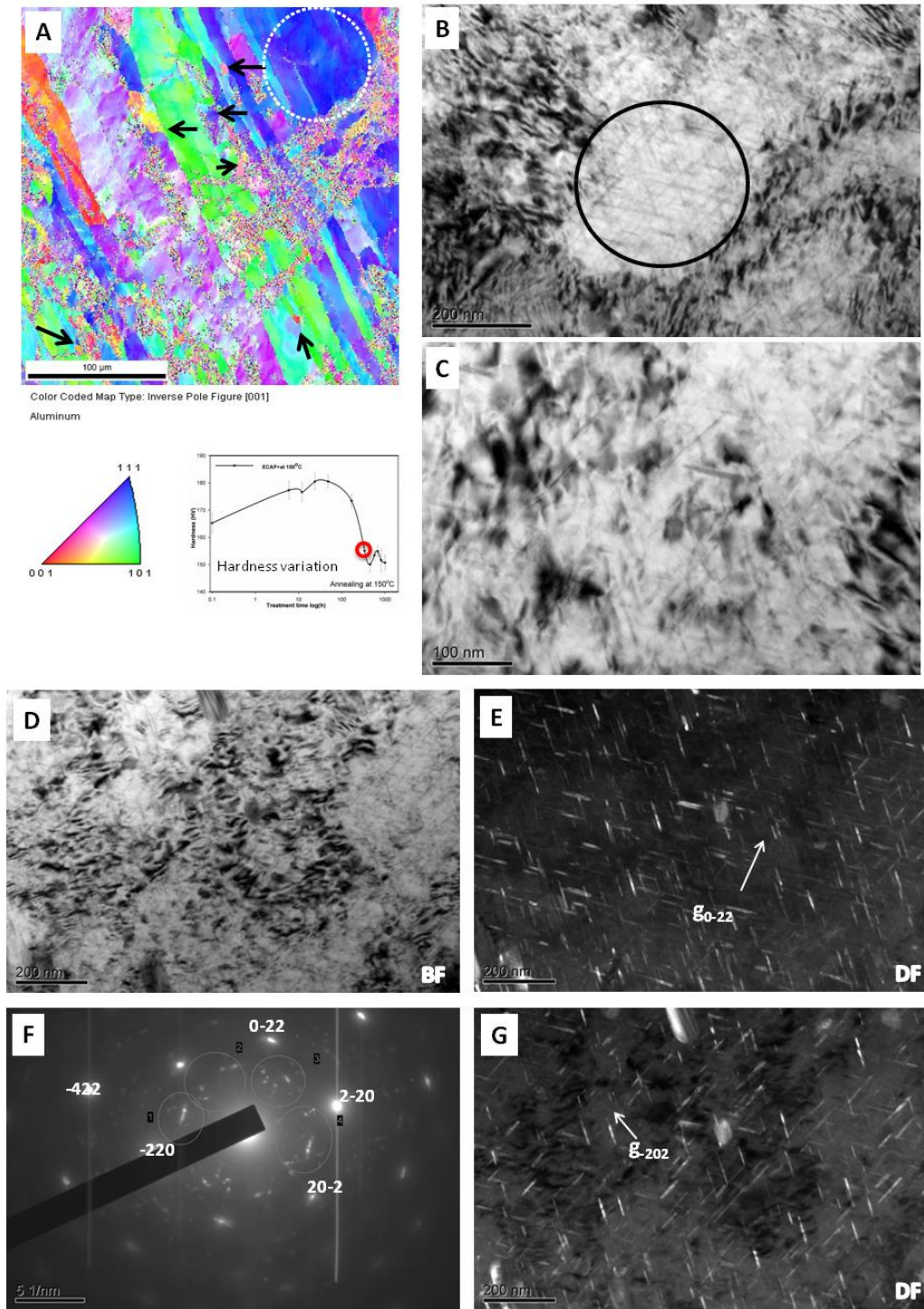
Figure 5.15. ECAPed and heated (150°C / 336h) sample: (a) EBSD image, TEM images of (b) cells including precipitates, (c) precipitates accompanied with the hardness variation plot and color coded map. Another TEM micrographs (d) BF image, (e, g) DF, (f) Diffraction pattern of precipitate rich region.

The closer investigation of precipitates (Figure 5.16) showed that they are mostly interconnected to each other and the angle between interacting precipitates have shifted from 100°/80° to 120°/60° which may or may not be indicative of incoherency level but worth further investigation. The precipitates are easily observed in bright field imaging.

To conclude, at this stage of microstructural evolution, all three possibilities for hardness loss coexist: Recovery of the general structure, recrystallization and over aging, semi-coherent or incoherent precipitates interacting with each other. However, they did not lead to a further drop of hardness and an increase in the hardness plot was observed.
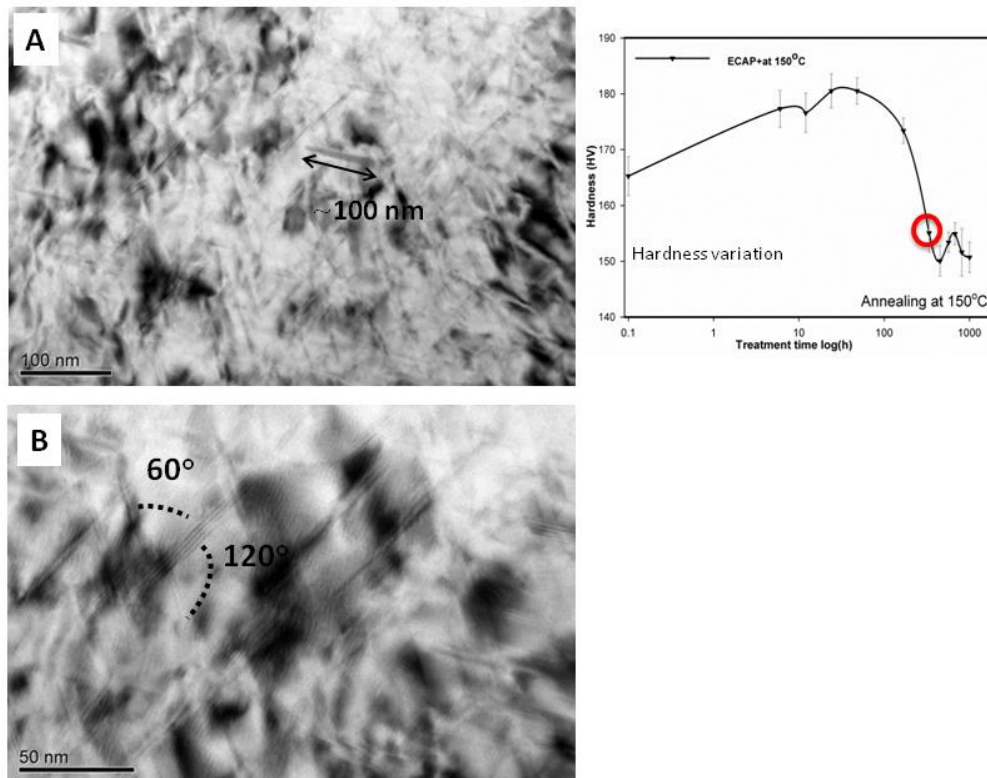
Figure 5.16. ECAPed and heated (150°C / 336h) sample: TEM micrographs (a) precipitates (b) High resolution image of crossed precipitates.

5.4.1.6. After 568h at 150°C

The structure of ECAPed sample after 568 hours could be investigated only through EBSD and the investigation of the peak was left for the peak aged counterpart of the 150°C sample.

When Figure 5.17-a and b, the EBSD images of ECAPed and 568 hours annealed sample at 150°C, were investigated the deformed structure is still easy to notice while more uniform grains are observed especially for some colors for example dark blue (111) and yellow ~(103). Image in Figure 5.17.b was collected to observe if there is any possibility of recrystallization. In the grain circled, which is a blend of pink, yellow and purple, a reorientation of grains similar to recrystallization is observable. When compared to previous EBSD images including the same colors, no such observation was possible so the figure is likely to be a sign of recrystallization. Although a progress in recrystallization is noticed, hardness increase rather than a sharp drop is detected. Actually a partial increase from 150 HV to 157 HV is obvious. This hardness increase can be attributed to a secondary precipitation (most probably omega phase) but the study will not go through those details due to limited time. The investigation of these precipitates will be left for the future works.

164
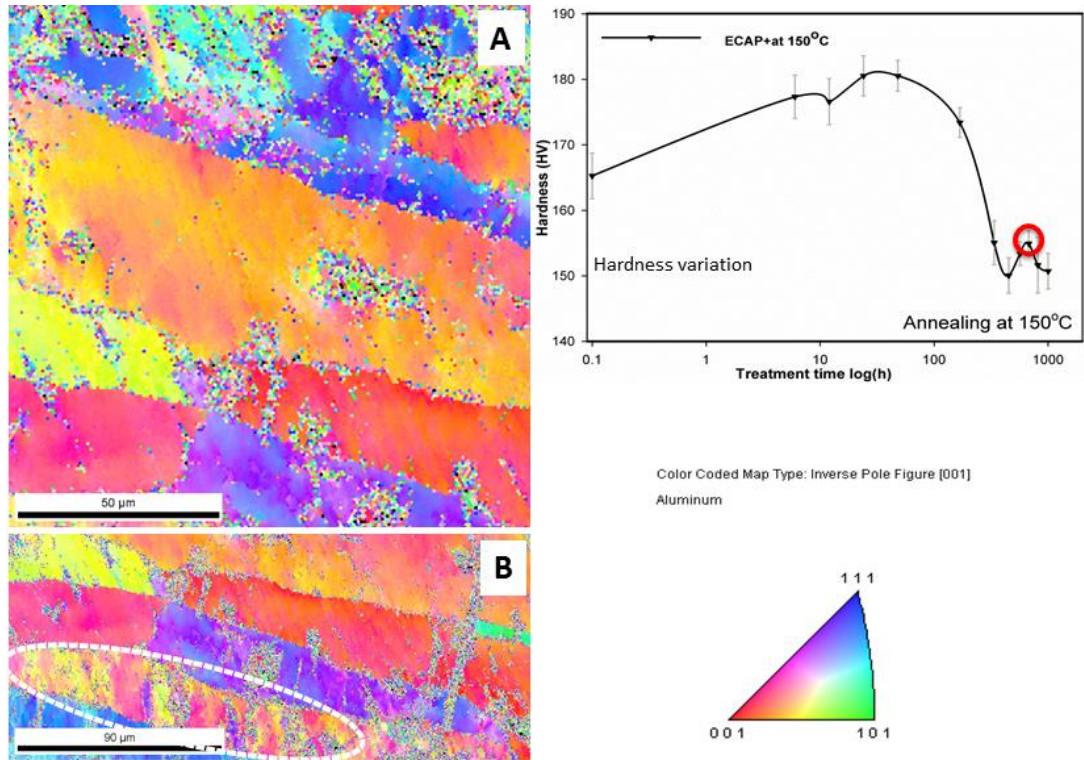
Figure 5.17. ECAPed and heated (150°C / 568h) sample: (a), (b) EBSD images of recovered grains accompanied with hardness variation plot.

As a general summary of the results, Figure 5.18 can be helpful. The initial and final structures are not too far from each other whereas the hard to notice differences result in major property variations. The initial structures were deformed and precipitate free. Time leads to the formation of precipitates as well as the proceeding of recovery and recrystallization. Until the 168 hours no sign of recrystallization was observed which is consistent with the hardness data. The hardness variation can be said to be a result of combined effect of precipitation, recovery and recrystallization.

During annealing at 150°C, the lead mechanism was precipitation until over aging (168 hours). After over aging, main mechanism became recrystallization which was

modified due to the presence of homogeneously distributed fine precipitates. Recrystallization yielded to a drastic hardness drop accompanied with over aging until a new precipitate emerged.

Figure 5.19 summarizes the variations in precipitate size and distribution.. The precipitates after 48 hours were found to be in a narrow size region of 5-20 nm indicated as pink colored distribution. This specifies that similar precipitates are formed rather than continuous nucleation and growth of precipitates hence the hardness is high. When time evolves, after 168 hours, the narrow distribution was observed to extend which were signs of heterogeneously nucleating S precipitates as well as coarsening of already present precipitates. The final precipitate size and distribution, as well as lack of precipitates in the 5-15 nm range, showed that precipitates were not nucleating any further but coarsening. The coarsening of particles may lead an increase in recrystallization rate and rapid hardness drop although there is no significant, or best to say easy to notice, change in EBSD images..
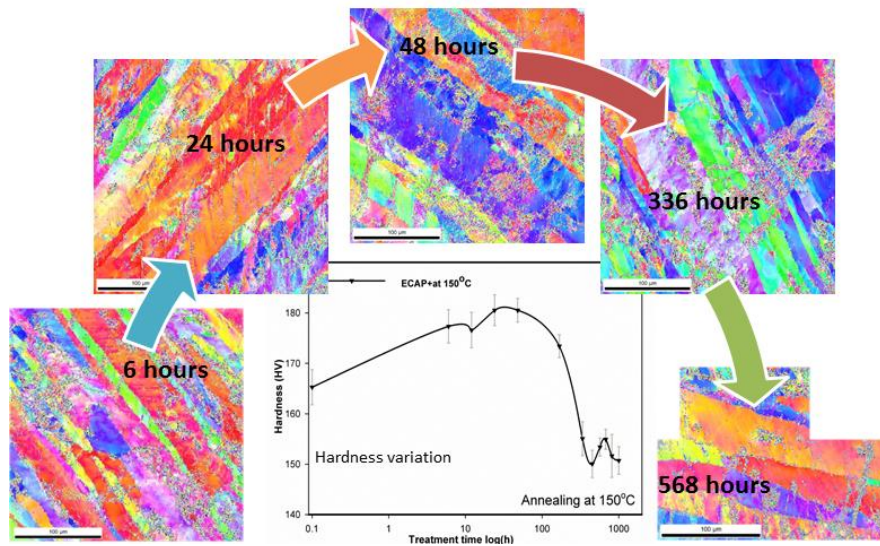
Figure 5.18. Variation of ECAPed Al 2024 structure by annealing at 150°C.

166

It should also be noted that due to dislocation rich microstructure not only the kinetics but also the distribution and final sizes of precipitates have shown huge variations. When the effect of temperature was considered in relation to190°C, the process is much slower at 150°C but the peak hardness values are the same.
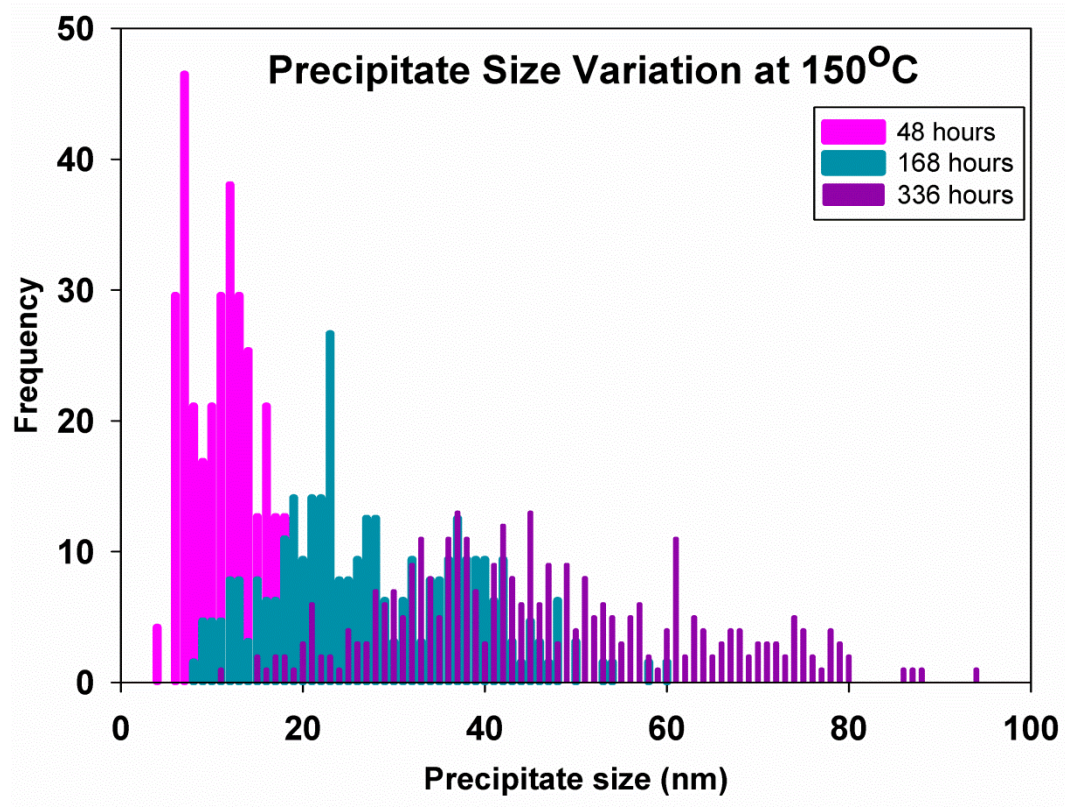
Figure 5.19. Precipitate size distribution during annealing of ECAPed Al 2024 at 150°C.

5.4.2. Effect of Peak Aging at 190°C on Thermal Stability

Figure 5.20 shows the hardness variation of ECAPed and post-ECAP aged samples. The upper graph is represented in log scale and the lower one is linear so that the stabilization after secondary peak could be recognized. It was observed that peak aging at 190°C have some minor effects on thermal stability at 150°C. In peak aged

ECAPed sample, the drop of hardness after 48 hours is steeper than solely ECAPed counterpart which is probably due to earlier over aging however the secondary peak is higher than ECAPed sample. The loss of hardening effect of aging may be considered as the steeper hardness drop. As can be seen in Figure 5.20-b both samples preserve their hardness values after the second peak for a long time which is probably due to the stabilized structure after secondary peak aging
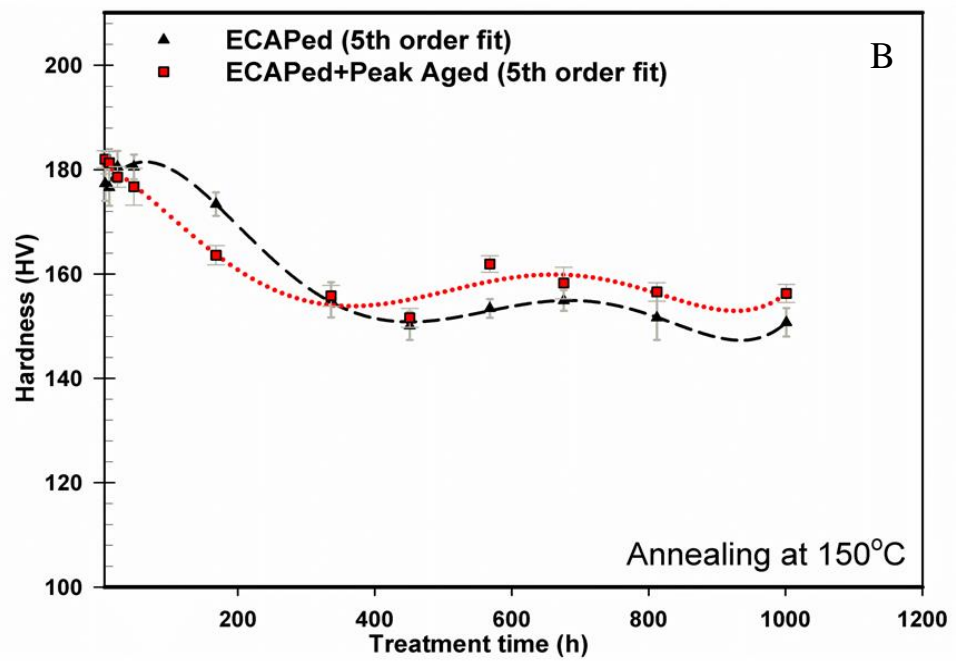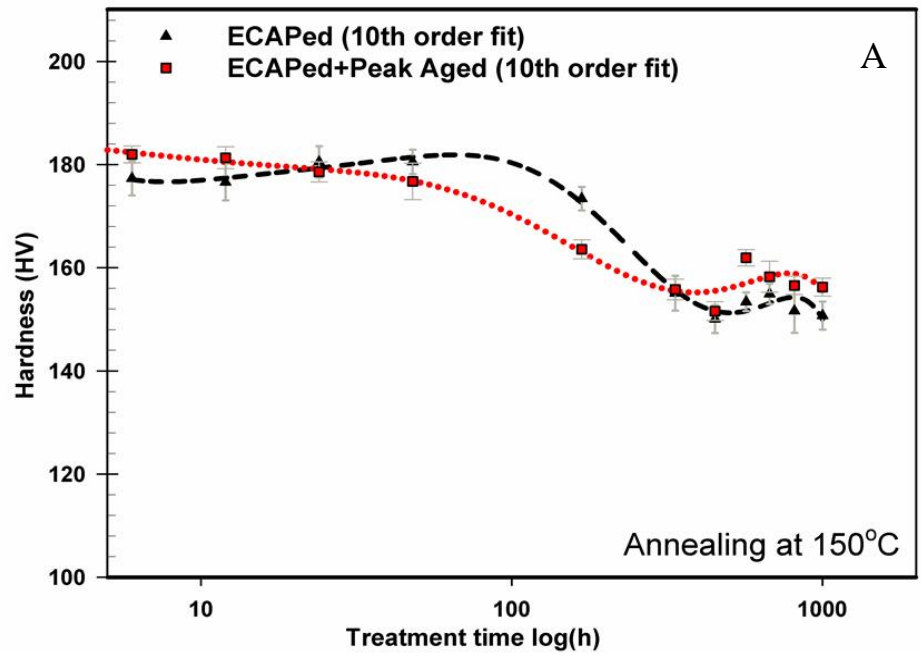
Figure 5.20. 150°C annealing plots in two scales (a) logarithmic scale, (b) linear scale.

Figure 5.21-a and b belong to the post-ECAP aged sample at 190°C after exposure to 150°C for 48 hours. The hardness has just started to drop, the effect of deformation is visible throughout the sample in the form of dislocation bands (Figure 5.21.a). On the other hand cell formation had started as a sign of recovery process. The high precipitate density inside the cells, circled in the Figure 5.21-b, can be regarded as initiation of over-aging in the alloy. Figure 5.21-c and d shows the precipitates more closely. They are not totally visible, meaning that there are strained regions around them. At this stage of precipitation they cannot be considered as incoherent but obviously are large in size above 20 nm which indicates coarsening or heterogeneously nucleating S precipitate formation.

In Figure 5.22, when the post-ECAP aged sample is annealed at 150°C for 568 hours, EBSD image of the recrystallized structure can be noticed. Occasional small grains accompanied with regions of similar colors are observed. Especially in Figure 5.22.a and b, recrystallized grains can be noticed. The red-pink grain denoted as W, shows the formation of pink (113) and red (001) grain. While in the cyan blue (212) grain, denoted as Q; green (101), yellow (112) and dark blue (111) cells are formed. When the dark blue grains, denoted as X, are observed a highly uniform color of dark blue (111) is observed. In Figure 5.22-c, the same behavior is observed at different grains.
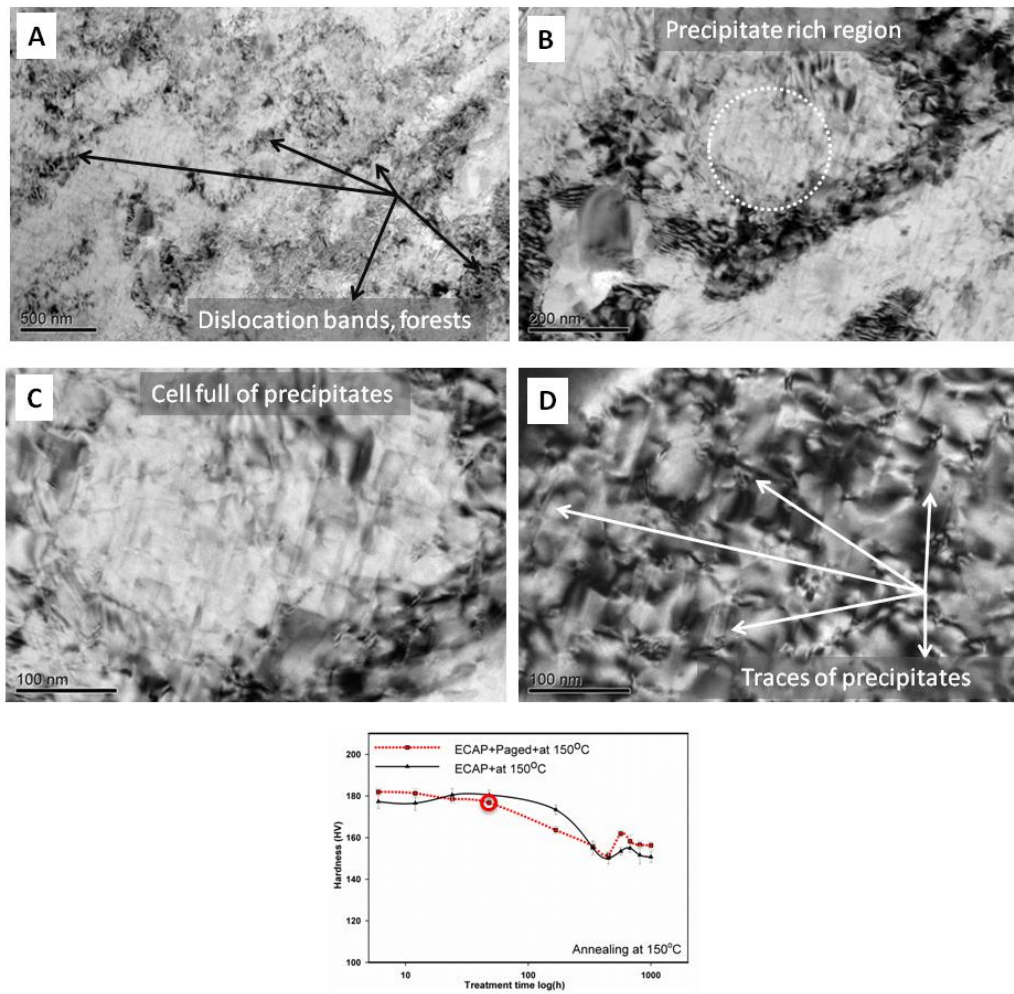
Figure 5.21. ECAPed, peak-aged and heated (150°C / 48h) sample: TEM micrographs accompanied with hardness variation plot (a) deformation bands (b) cells with precipitates, (c) magnified view of b and (d) traces of precipitates.

171
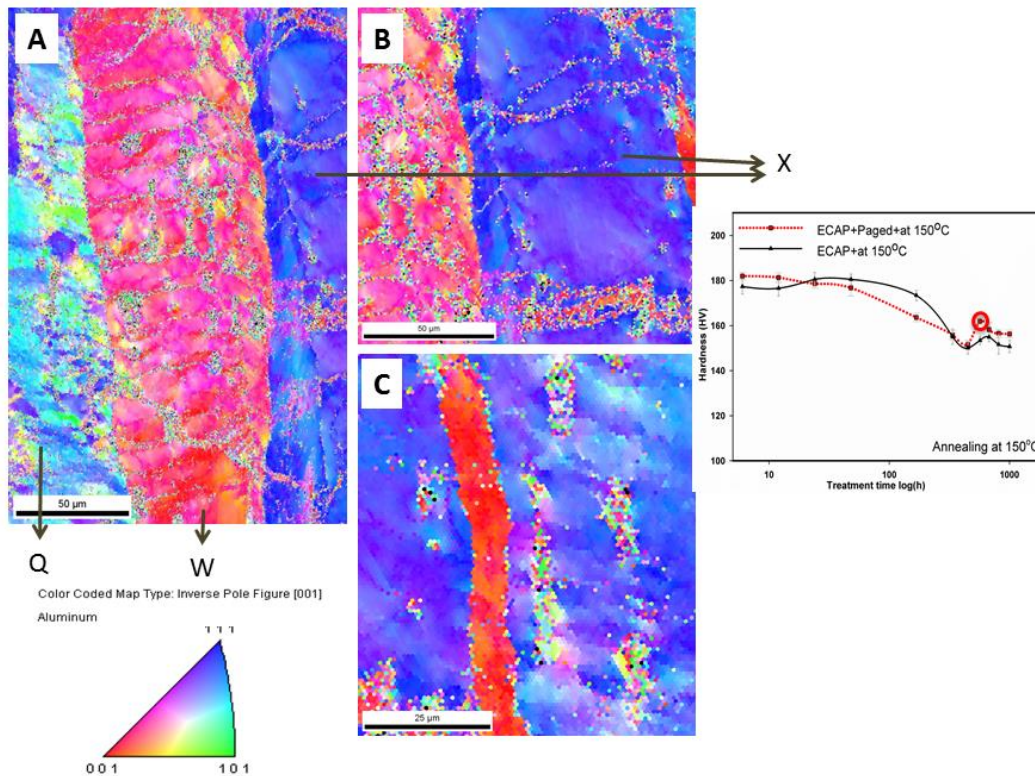
Figure 5.22. ECAPed, peak-aged and heated (150°C / 568h) sample: (a-c) EBSD images of recovered grains accompanied with hardness variation plot.

Figure 5.23.a shows peak aged ECAPed sample after 812 hours. The deformed structure is recovered and the cell boundaries are thinner while subgrains have grown in size. Precipitates were also easily observed. Their sizes are larger than 100 nm and they are mostly interconnected. It is suspected that another precipitate phase (Figure 5.23-b) have grown in the second peak observed in the hardness plot. The stabilization is most probably a result of this new formed precipitate phase, most probably Ω phase, mentioned in a study by Gu et. al. [8].
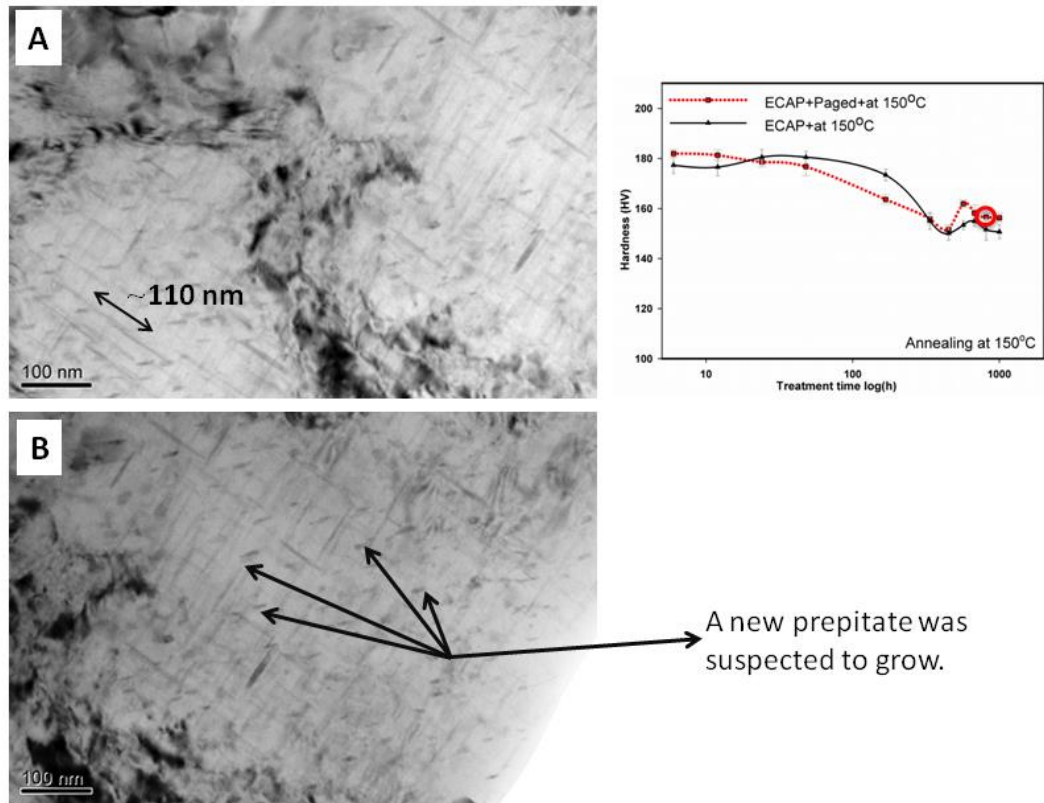
Figure 5.23. ECAPed, peak-aged and heated (150°C / 812h) sample: (a) Precipitates and thin cell boundary, (b) Various types of precipitates accompanied with hardness variation plot.

For the thermal stability of ECAPed Al 2024, 150°C can be regarded as a limit temperature as also stated in literature for standard Al 2024 [1]. Although hardness drops down that of the Al 2024 T8 condition, further drop was not observed even after 1000 hours which is a good sign of thermal stability. A thorough study on the new structure obtained may give more and enough information for other properties of the sample with the above microstructure. Additionally, 2000 hours of annealing experiments may be useful to observe if there will be any further over aging in the structure.

5.4.3. Stability of ECAPed Structure at 190°C and 200°C

It was previously stated that, at 190°C, the kinetics of aging process is nearly 12 times faster than its standard counterpart. As a result, a high over aging and recrystallization rate was expected. The steep decrease in hardness shown in Figure 5.24 proves this expectation. Actually since 190°C is the peak aging temperature it was one of the annealing samples but since both 200°C and 190°C behaved exactly the same (Figure 5.24), the annealing was completed using the samples annealed at 200°C.
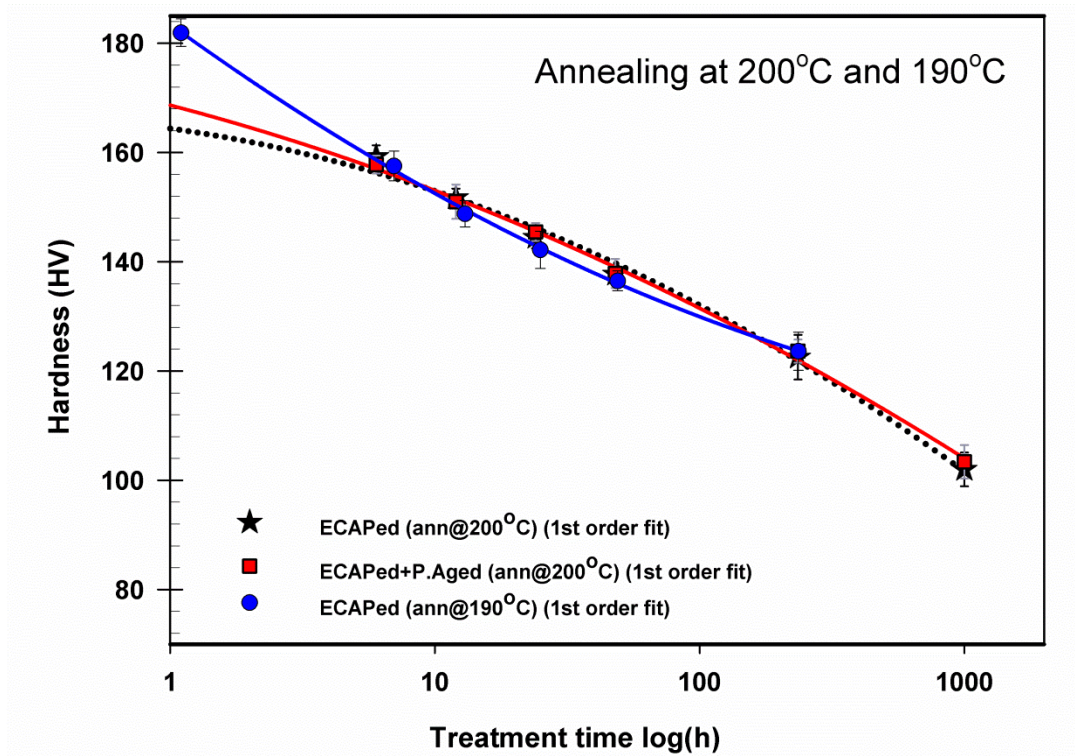
Figure 5.24. Effect of annealing at190-200°C on hardness of the ECAPed samples.

Figure 5.25 shows the structure of ECAPed sample after 6 hours at 190°C. Deformation in the structure is still visible due to the elongated grains however the

grain interiors are transferred into single colors as it is observed in the yellow (103) grain which is becoming green (101) denoted as X. Also there are signs of new grain formations, as seen in the circled region, recrystallization is clearly observed since the grains are clear and bright. The presence of precipitates helps the elongation of grains to survive probably because they have nucleated at the grain boundaries, too. The hardness dropped down to 158 HV in 6 hours.
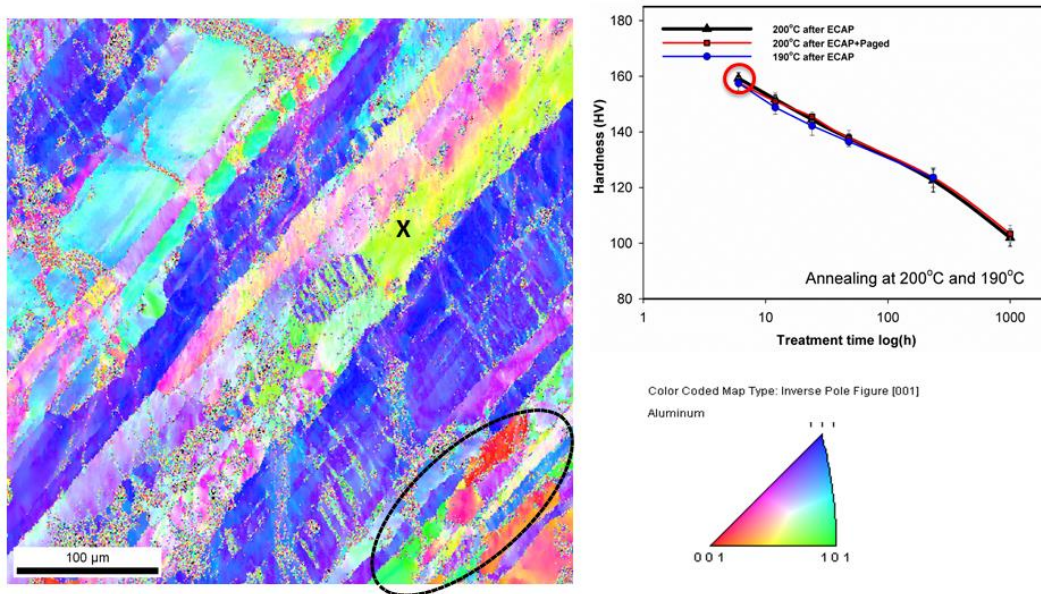
Figure 5.25. EBSD image of ECAPed and heated (190°C / 6h) sample accompanied with hardness variation plot and color coded map.

Figure 5.26-a shows a general view of the ECAPed Al2024 after annealing at 200°C for 48 hours. The sample still preserves some of the deformed structure in the form of dislocation tangles but they are less dense and easier to distinguish from one another. In Figure 5.26-b and c, precipitates are observed to have grown up to nearly 60-80 nm and they are visible. The precipitates are in the form of crosses or long thick plates rather than lines or needles as shown by arrows. The hardness drop is a result of recrystallization of the sample after 48 hours of exposure to 200°C. As a conclusion it would be wise to say, use of ECAPed Al 2024 between 150-200°C is not safe when a few hours of exposure to this temperature range is exceeded.
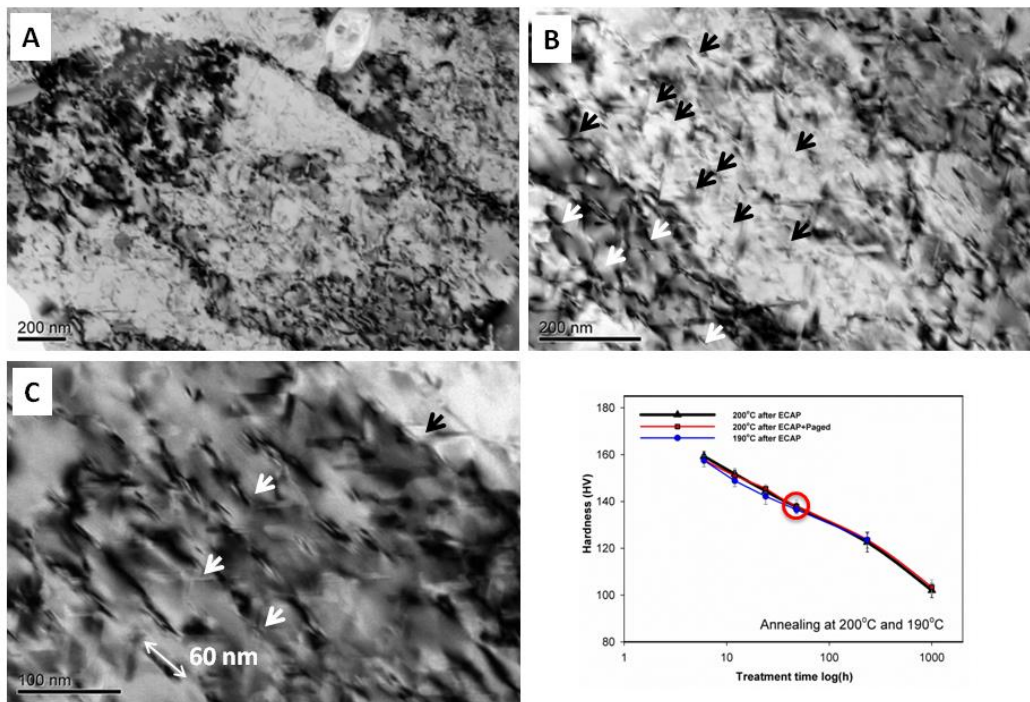
Figure 5.26. TEM image of ECAPed and heated (200°C / 48h) sample accompanied with hardness variation plot.

5.4.4. Stability of ECAPed Structure at 120°C

Figure 5.27 shows the behavior of ECAPed samples in peak aged and as ECAPed condition when exposed to 120°C for 1000 hours. The hardness of both samples have remained either as high as the initial value or improved after 1000 hours. A secondary peak which is similar to the one observed in 150°C with a higher hardening effect was observed. The samples had a hardness value of 198 HV regardless of prior aging. Actually long term-low temperature treatments may be considered as a hardness improvement and stabilization tool in further studies.
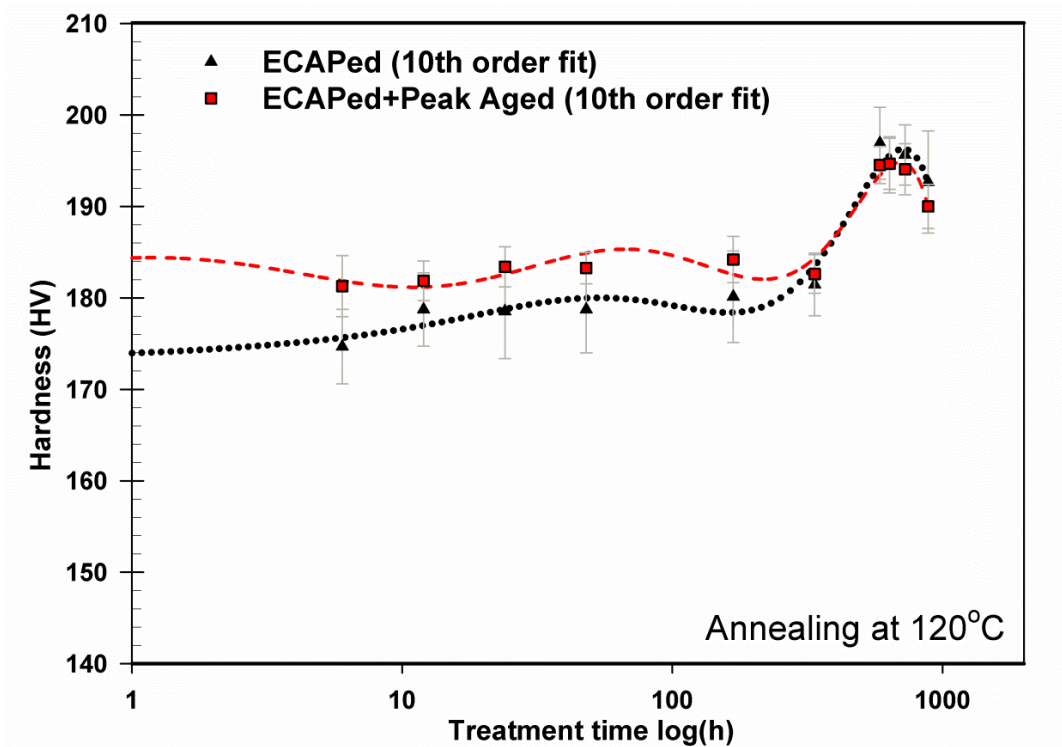
Figure 5.27. Hardness variation plot of ECAPed samples during annealing at 120°C.

The microstructural investigation of 120°C is limited to EBSD after 6 hours. When the stabilized hardness of ECAPed/ECAPed+peak-aged samples at 150°C as a result of the secondary hardening peak is considered, at 120°C, a large drop in hardness is not expected. Yet the predictions on the ECAPed Al 2024 are not straight forward and require further testing for an accurate conclusion. A detailed investigation could be carried out with further annealing up to 2000 hours in further studies..

Figure 5.28 shows the structure of ECAPed sample after 6 hours of exposure to 120°C. There is no sign of annealing as expected and the structure is deformed just before the precipitation of S''/S' phase when the hardness of the sample is considered..
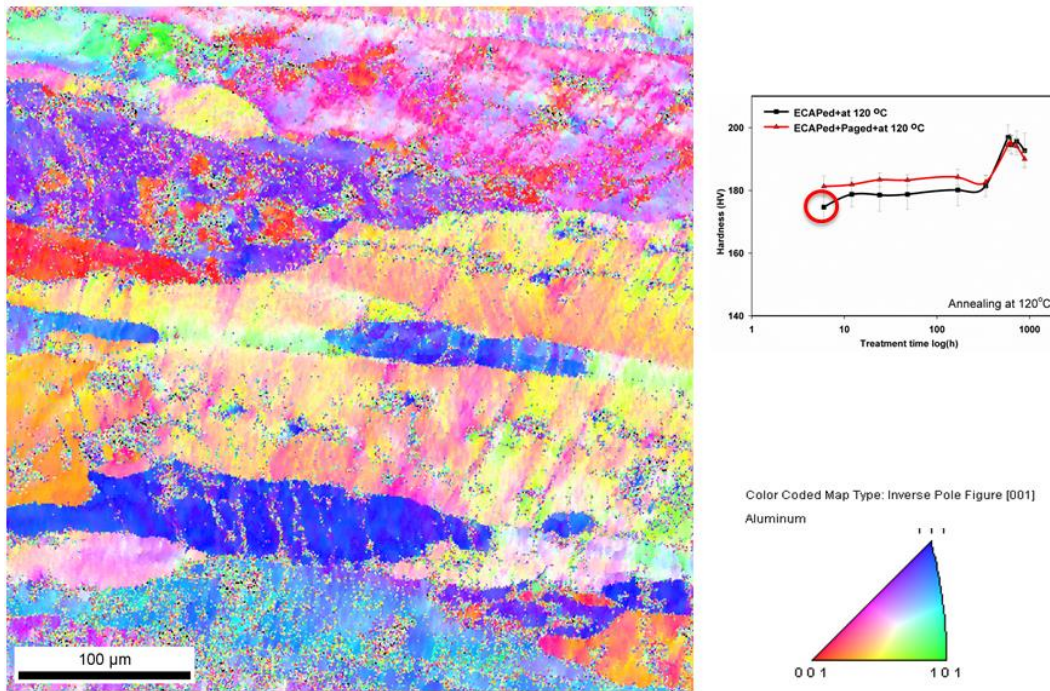
Figure 5.28. EBSD image of ECAPed and heated (120°C / 6h) sample accompanied with hardness variation plot and color coded map.

It was concluded that, the use of ECAPed samples between 120-150°C is safe for long time periods with an improvement in the microstructural and mechanical stability.

5.4.5. Stability of ECAPed Structure at 80°C

When both post-ECAP aged and solely ECAPed samples were annealed at 80°C (Figure 5.29), the hardness of the samples improved compared to 120°C annealing. Actually the upper limit of post-ECAP aged sample could not be observed after 1000 hours. Only one of the samples at this temperature could be investigated which may be regarded as the most important one.
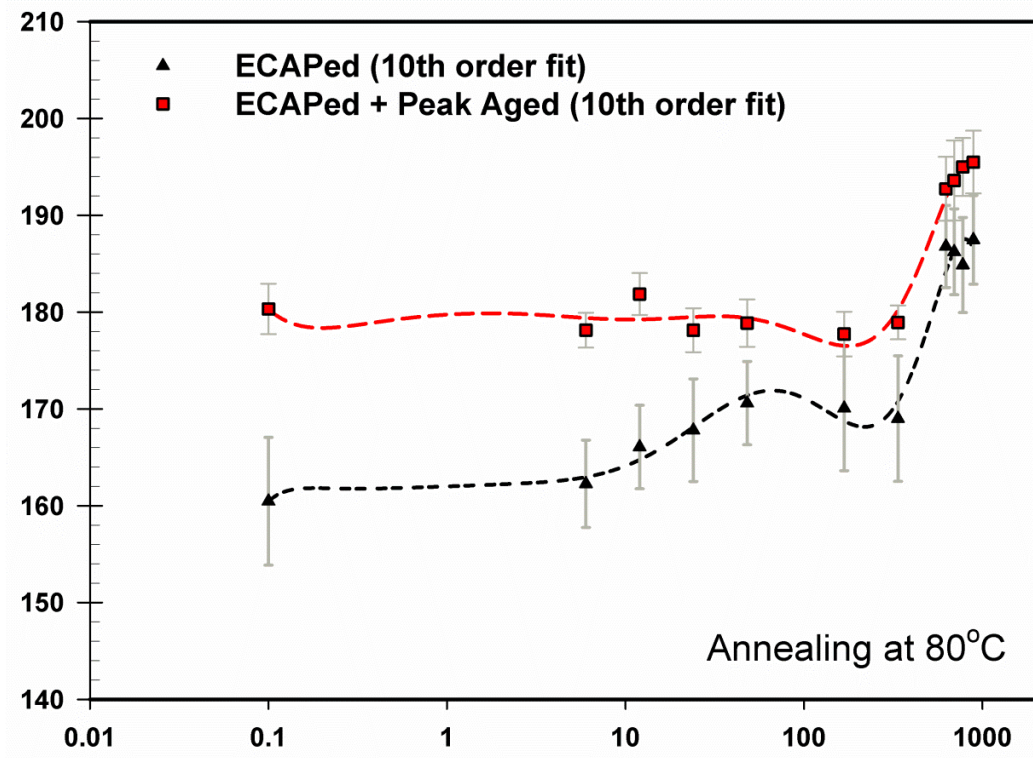
Figure 5.29. Hardness variation plot of ECAPed samples during annealing at 80°C.

In Figure 5.30, ECAPed sample after 694 hours of exposure to 80°C is shown. The cell structure is accompanied with dislocations and precipitates (Figure 5.30-a). In Figure 5.30-c, the precipitates formed in a cell can also be seen. Precipitates in the form of long needles, plates or crossed, interconnected bunches exist (Figure 5.30-d), denoted by arrows. In Figure 5.30-e and f the bunch of precipitates crossing each other at the angles of 80° and 100° are observed. The secondary phase could not be monitored. Further annealing up to 2000 hours accompanied with detailed TEM analysis may be suitable to investigate the underlying cause of the secondary increase in hardness
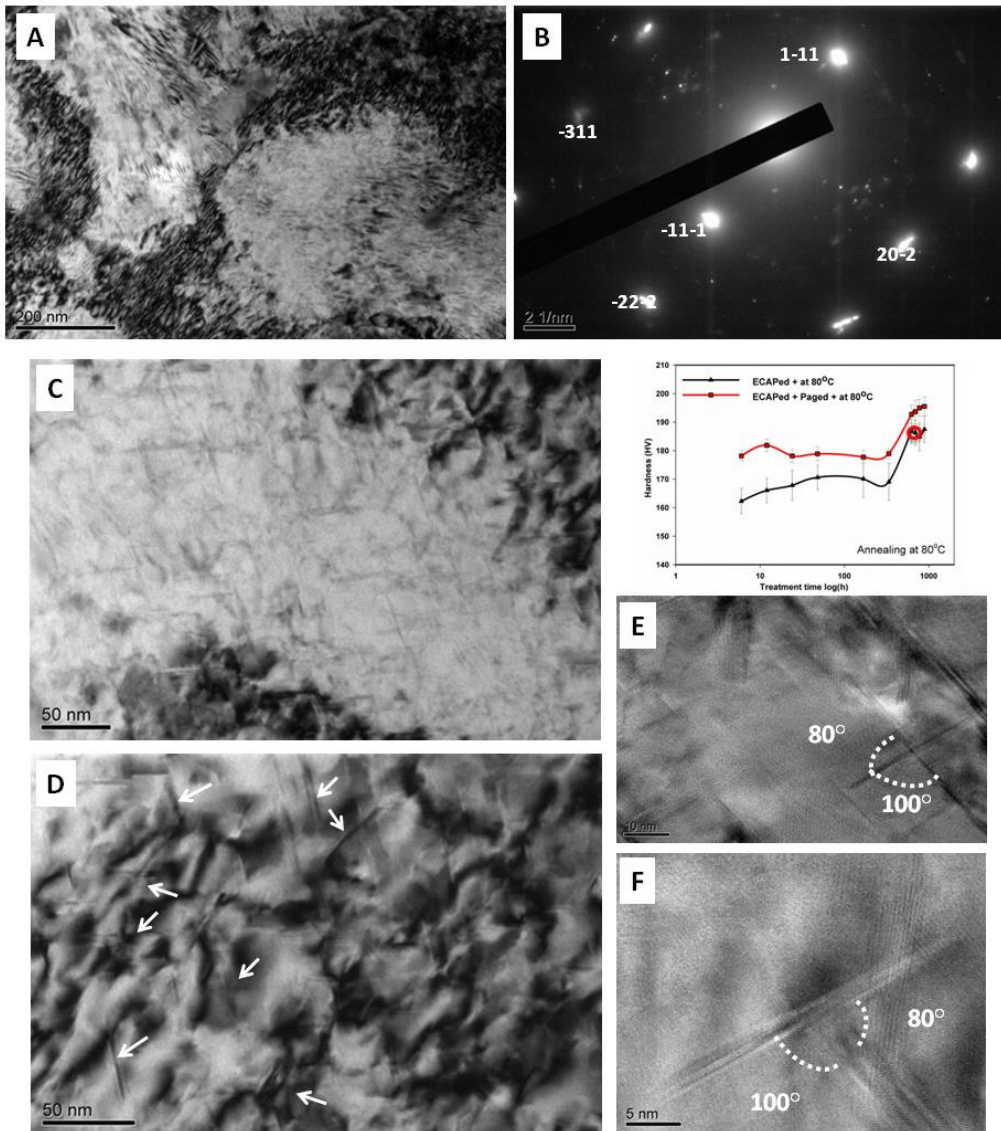
Figure 5.30. TEM images of ECAPed and heated (80°C / 694h) sample: (a) General view, (b) diffraction pattern, (c) precipitates in cells, (d) closer view of precipitates, (e) and (f) High resolution image of precipitates.

The current study showed that the temperature at and below 120°C are totally safe even after 1000 hours, with a further improvement in hardness.

.

CHAPTER 6

CONCLUSIONS

Chapter 3

The preliminary research, involving the aging experiments of standard and ECAPed Al 2024 at 190°C showed that the ECAPed sample has a much higher precipitation rate than the solutionized sample. The ECAPed sample produced precipitates that are finer than those in the solutionized ones, though an accurate measurement could not be taken due to the strain fields around the precipitates. The precipitate distribution was denser in the over-aged standard Al 2024whereas the only detectable difference in the ECAPed one was the absence of a strain field which made it possible to capture HREM images. The hardness drop corresponding to the loss of strain in the specimen as well as TEM image of a recrystallized grain were regarded as possible signs of recrystallization in the presence of nano precipitates. It is not likely for S precipitates to lose the coherency without significant growth of however formation of heterogeneous S precipitates which are already incoherent may be effective on the hardness drop.

ECAPed samples showed inhomogeneity thus an investigation, through a well-planned microhardness study in combination with other characterization techniques like EBSD and TEM, is observed to be necessary. This inhomogeneity factor needs to be taken into account and each step of aging requires careful investigation with this in mind. Using dark field imaging is regarded as a necessity in order to distinguish the precipitates from the strain fields around them to get a clear observation of the precipitate size and distribution.

Chapter 4

The chapter includes the studies on the inhomogeneity among three Al 2024 samples ECAPed through 120° die and the inhomogeneity throughout a particular specimen cut through the shear direction at a 46° angle. Finite element simulations and chemical composition measurements (EDS) were used to analyze inhomogeneity among samples and micro hardness maps, TEM and EBSD analysis were carried out to investigate inhomogeneity of the sample in ECAPed condition and during aging of it at 190°C.

- ✓ The reason of hardness variations in the samples after ECAP was investigated considering back-pressure and Mg content. Simulation of a billet showed that the first loaded sample has the lowest strain (LBP) while the last loaded (HBP) portion has higher strain. In the middle part, a more homogeneous and high strain can be attained. The feeding order and hence back pressure was found to be a possible reason of strain inhomogeneity among different samples.

- ✓ Mg content with 0.2% variation was found to have a small influence on hardness of different samples.

  A combined effect of Mg content and sample order was proposed to have an influence on hardness variation of different samples due to the temperature rise in the ECAP die during deformation leading to rapid hardening, an aging stage.

- ✓ EBSD results of the ECAPed sample showed that at the bottom of the sample, the deformation is less in the shear direction relative to top and bottom indicating the corner gap.

- ✓ After ECAP, the peak aging time of Al 2024 was found to be $1/12^{th}$ of the standard sample with an extra 50% higher hardness.

- ✓ Initial stage of aging, rapid hardening, was not observed in ECAPed samples. Dynamic rapid hardening during aging was proposed to be a possible reason of this. Rapid hardening mechanism, which has not been clearly understood yet, may result from the formation of sessile dislocation

networks due to clusters formed. If it is so, the strengthening mechanisms of ECAP and rapid hardening could be considered as similar and activation of both may not be possible. As a result of this rapid hardening may be absent in ECAPed samples.

✓ The precipitates and GPB zones formed in ECAPed samples were regarded as heterogeneously precipitated at the dislocations.

✓ In ECAPed samples, homogenization through aging was monitored by micro hardness maps and the lowest hardness inhomogeneity index ($\Delta H/H_{avg}$) was observed right after peak aging.

✓ HII of HBP and LBP Samples showed a decrease after peak aging.

✓ The homogenization was regarded to be a result of different kinetics of aging and recrystallization at different regions of the sample due to the present strain inhomogeneity, hence varying driving forces and diffusion rates.

✓ Signs of recrystallization was observed in the TEM images of 50 minutes aged ECAPed Al 2024 Sample (HBP).

✓ S precipitate groups were observed in the standard sample and they could not be recognized in the ECAPed sample after peak aging.

✓ The precipitate size of ECAPed sample was found to be 12 times smaller than the standard sample in good agreement with the 12 times faster aging.

✓ The ease of heterogeneous nucleation was found to be the main cause of 12 times faster aging rather than increased diffusion rates because the precipitate size of peak aged ECAPed sample was measured to be 12 times smaller than the standard sample.

✓ The distribution of precipitate size was found to be more homogeneous in ECAPed and peak aged Al 2024 than the peak aged standard sample.

ECAPed and post ECAP aged Al 2024 samples were annealed at 80°C, 120°C, 150°C and 200°C for 1000 hours to observe thermal stability of the alloy. The results were compared with 2124 cold worked and aged counterpart. Temperature limits for the safe use of the material was aimed to be determined. The annealing characteristics were investigated using TEM and EBSD.

✓ ECAPed and ECAPed+peak aged Al 2024 samples maintained their hardness values at 80°C, 120°C and showed an increase in hardness after 500 hours probably due to secondary precipitate formation. The new hardening peak led to 198 HV (as high as 7075) hardness much higher than ECAPed+peak aged (180 HV) state.

✓ ECAPed and ECAPed+peak aged Al 2024 samples showed drastic decrease in hardness, more than standard sample, when exposed to 200 °C for 1000 hours as a result of recrystallization. Abnormal grain growth was suspected to be the cause of drop. The use of Al 2024 around 200°C can be detrimental. A significant need for long term thermal stability analysis of severely deformed samples was determined.

✓ Temperatures above 150°C were too high for the ECAPed structure to survive but low enough to maintain a hardness slightly higher than peak aged standard Al 2024.

✓ At 150°C, ECAPed Al 2024 experienced peak aging, over-aging and recrystallization followed by a small secondary aging with a final hardness value of 158 HV. The new structure formed after 600 hours was found to be very stable up to 1000 hours of annealing.

✓ Between 120-150°C, the use of ECAPed Al 2024 is safe up to the hardness values of 158 HV and slightly above.

✓ Aging and recrystallization are the key mechanisms during the annealing of ECAPed Al 2024. Recrystallization dominates at and above 150°C while aging dominated below 150°C.

✓ Recrystallization progressed preserving the high angle grain boundaries and elongated grain structure.

✓ Precipitate size remained smaller than or close to 100 nm in all samples.

✓ Precipitation of S phase was faster than standard sample but omega precipitates were slower to form.

REFERENCES

[1]   J. R. Davis, Ed., *ASM Specialty Handbook: Aluminum and Aluminum Alloys*. Materials Park: ASM International, 1993.

[2]   D. S. MacKenzie and G. E. Totten, *Analytical Characterization of Aluminum, Steel and Superalloys*. Boca Raton: CRC Press, 2006.

[3]   G. E. Totten and D. S. MacKenzie, Eds., *Handbook of Aluminum Volume 1 Physical Metallurgy*. Taylor and Francis Group, 2003.

[4]   D. G. Altenpohl, *Aluminum: Technology, Applications, and Environment*, 6th Editio. Washington DC: TMS, 1999.

[5]   S. C. Wang and M. J. Starink, "Precipitates and intermetallic phases in precipitation hardening Al–Cu–Mg–(Li) based alloys," *Int. Mater. Rev.*, vol. 50, no. 4, pp. 193–215, Aug. 2005.

[6]   Z. Q. Feng, Y. Q. Yang, B. Huang, X. Luo, M. H. Li, M. Han, and M. S. Fu, "Variant selection and the strengthening effect of S precipitates at dislocations in Al–Cu–Mg alloy," *Acta Mater.*, vol. 59, no. 6, pp. 2412–2422, Apr. 2011.

[7]   P. I. Gouma, D. J. Lloyd, and M. J. Mills, "Precipitation Processes in Al – Mg – Cu Alloys," *Mater. Sci. Eng. A*, vol. 321, pp. 439–442, 2001.

[8]   Y. Gu, Z. Liu, D. Yu, B. Liu, M. Lin, and S. Zeng, "Growth of Ω Plates and Its Effect on Mechanical Properties in Al-Cu-Mg-Ag Alloy with High Content of Silver," *J. Mater. Eng. Perform.*, vol. 22, no. 6, pp. 1708–1715, Jan. 2013.

[9]   I. N. Khan, M. J. Starink, and J. L. Yan, "A model for precipitation kinetics and strengthening in Al–Cu–Mg alloys," *Mater. Sci. Eng. A*, vol. 472, no. 1–2, pp. 66–74, Jan. 2008.

[10]   H. S. Kim and S. P. Ringer, "On the Crystal Structure of the S-phase Precipitate in Al-Cu-Mg Alloy," *Microsc. Microanal.*, vol. 11, no. S02, pp. 1688–1689, Aug. 2005.

[11]   L. Kovarik, M. K. Miller, S. a. Court, and M. J. Mills, "Origin of the modified orientation relationship for S(S″)-phase in Al–Mg–Cu alloys," *Acta Mater.*, vol. 54, no. 7, pp. 1731–1740, Apr. 2006.

[12]   T. S. Parel, S. C. Wang, and M. J. Starink, "Hardening of an Al–Cu–Mg alloy containing Types I and II S phase precipitates," *Mater. Des.*, vol. 31, pp. S2–S5, Jun. 2010.

[13]   S. P. Ringer, "Origins of Hardening in Aged Al-Cu-Mg- (Ag) Alloys," *Acta Mater.*, vol. 45, no. 9, pp. 3731–3744, 1997.

[14]   R. Cobden, "Aluminium : Physical Properties , Characteristics and Alloys 1501 Aluminium : Physical Properties , Characteristics and Alloys," 1994.

[15]   European Aluminium Association and the M. Project, "Aluselect Mechanical Properties," 2011. [Online]. Available: http://aluminium.matter.org.uk/aluselect/09_mech_browse.asp? [Accessed: 04-Sep-2014].

[16]   S. C. Wang and M. J. Starink, "Two types of S phase precipitates in Al–Cu–Mg alloys," *Acta Mater.*, vol. 55, no. 3, pp. 933–941, Feb. 2007.

[17]   J. G. Kaufman, "Aluminum Alloy Database," *Knovel*, 2006. [Online]. Available: http://app.knovel.com/web/toc.v/cid:kpAAD00001/viewerType:toc/root_slug :aluminum-alloy-database/url_slug:aluminum-alloy-database. [Accessed: 04-Sep-2014].

[18]   The Aluminum Association, "The aluminum association," 2012. [Online]. Available: http://www.aluminum.org/news/aluminum-has-been-go-aerospace-material-more-100-years-and-new-innovations-keep-it-material. [Accessed: 02-Jul-2014].

[19]   A. F. Padilha and R. L. Plaut, *Handbook of Aluminum Volume 2 Alloy Production and Materials Manufacturing*. Taylor and Francis Group, 2003, pp. 193–276.

[20]   I. J. Polmear, "Aluminium Alloys – A Century of Age Hardening," *Mater. Forum*, vol. 28, pp. 1–14, 2004.

[21]   B. Reis, R. França, and J. Spim, "The effects of dendritic arm spacing (as-cast) and aging time (solution heat-treated) of Al–Cu alloy on hardness," *J. Alloy. ...*, vol. 549, pp. 324–335, 2013.

[22]   W. Huang, Z. Liu, L. Xia, P. Xia, and S. Zeng, "Severe plastic deformation-induced dissolution of S" particles in Al-Cu binary alloy and subsequent nature aging behavior," *Mater. Sci. Eng. A*, vol. 556, pp. 801–806, 2012.

[23]   A. Biswas, D. J. Siegel, C. Wolverton, and D. N. Seidman, "Precipitates in Al-Cu alloys revisited: Atom-probe tomographic experiments and first-principles calculations of compositional evolution and interfacial segregation," *Acta Mater.*, vol. 59, no. 15, pp. 6187–6204, 2011.

[24]   J.-H. Jang, D.-G. Nam, Y.-H. Park, and I.-M. Park, "Effect of solution treatment and artificial aging on microstructure and mechanical properties of Al–Cu alloy.pdf," *Trans. Nonferrous Met. Soc. China*, vol. 23, p. 631−635, 2013.

[25]   S. K. Son, M. Takeda, M. Mitome, Y. Bando, and T. Endo, "Precipitation behavior of an Al-Cu alloy during isothermal aging at low temperatures," *Mater. Lett.*, vol. 59, no. 6, pp. 629–632, 2005.

[26]   A. W. Zhu and J. A. Starke, "Stress aging of Al-Cu alloys: Computer modeling," *Acta Mater.*, vol. 49, no. 15, pp. 3063–3069, 2001.

[27]   N. Tsuji, T. Iwata, M. Sato, S. Fujimoto, and Y. Minamino, "Aging behavior of ultrafine grained Al-2 wt%Cu alloy severely deformed by accumulative roll bonding," *Sci. Technol. Adv. Mater.*, vol. 5, no. 1–2, pp. 173–180, 2004.

[28]   J. R. Davis, Ed., *Aluminum and Aluminum Alloys*. Materials Park: ASM International, 1993.

[29]   S. Abis, M. Massazza, P. Mengucci, and G. Riontino, "Early ageing mechanisms in a high-copper AlCuMg alloy," *Scr. Mater.*, vol. 45, no. 6, pp. 685–691, 2001.

[30]   A. Charai, T. Walther, C. Alfonso, A. Zahra, and C. Y. Zahra, "Coexistance oof Clusters, GPB Zones , S"- , S '- and S,Phases in an Al-0.9%Cu-1.4%Mg Alloy," *Acta Metall.*, vol. 48, pp. 2751–2764, 2000.

[31]   N. Gao, M. J. Starink, M. Furukawa, Z. Horita, C. Xu, and T. G. Langdon, "Evolution of Microstructure and Precipitation in Heat-Treatable Aluminium Alloys during ECA Pressing and Subsequent Heat Treatment," *Mater. Sci. Forum*, vol. 503–504, pp. 275–280, 2006.

[32]   X. G. Qiao, M. J. Starink, and N. Gao, "Hardness inhomogeneity and local strengthening mechanisms of an Al1050 aluminium alloy after one pass of equal channel angular pressing," *Mater. Sci. Eng. A*, vol. 513–514, pp. 52–58, Jul. 2009.

[33] V. Radmilovic, R. Kilaas, U. Dahmen, and G. J. Shiflet, "Structure and Morphology of S phase Precipitates," *Acta Metall.*, vol. 47, no. 99, pp. 3987–3997, 1999.

[34] V. Raghavan, "Al-Cu-Mg (Aluminum-Copper-Magnesium)," *J. Phase Equilibria Diffus.*, vol. 28, no. 2, pp. 174–179, May 2007.

[35] P. Ratchev, B. Verlinden, P. D. E. Smet, and P. V. A. N. Houtte, "Precipitation Hardening of an Al-4.2wt% Mg-0.6wt% Cu," *Acta Metall.*, vol. 46, no. 10, pp. 3523–3533, 1998.

[36] H. J. Roven, M. Liu, and J. C. Werenskiold, "Dynamic precipitation during severe plastic deformation of an Al–Mg–Si aluminium alloy," *Mater. Sci. Eng. A*, vol. 483–484, no. 2008, pp. 54–58, Jun. 2008.

[37] H. H. Shih, N. N. Ho, and J. C. Huang, "Precipitation Behaviors in AI-Cu-Mg and 2024 Aluminum Alloys," *Metall. Mater. Trans. A*, vol. 27, no. September, pp. 2479–2494, 1996.

[38] A. Tolley, R. Ferragut, and A. Somoza, "Microstructural characterisation of a commercial Al–Cu–Mg alloy combining transmission electron microscopy and positron annihilation spectroscopy," *Philos. Mag.*, vol. 89, no. 13, pp. 1095–1110, 2009.

[39] V. Vidal, Z. R. Zhang, and B. Verlinden, "Precipitation hardening and grain refinement in an Al–4.2wt%Mg–1.2wt%Cu processed by ECAP," *J. Mater. Sci.*, vol. 43, no. 23–24, pp. 7418–7425, Jul. 2008.

[40] S. C. Wang, M. J. Starink, and N. Gao, "Precipitation hardening in Al–Cu–Mg alloys revisited," *Scr. Mater.*, vol. 54, no. 2, pp. 287–291, Jan. 2006.

[41] M. Tiryakioglu and J. T. Staley, *Handbook of Aluminum: Vol. 1: Physical Metallurgy and Processes*. New York: CRC Press, 2003, pp. 81–209.

[42] Z. R. Liu, J. H. Chen, S. B. Wang, D. W. Yuan, M. J. Yin, and C. L. Wu, "The structure and the properties of S-phase in AlCuMg alloys," *Acta Mater.*, vol. 59, no. 19, pp. 7396–7405, Nov. 2011.

[43] R. Ferragut and A. Somoza, "Positron , Age-Hardening and Precipitation in Predeformed 2024 (Al ± Cu ± Mg) Alloy," *Phys. Status Solidi a*, vol. 175, pp. R1–R2, 1999.

[44] S. P. Ringer and K. Hono, "Aluminium Alloys : Atom Probe Field-Ion Microscopy and Transmission Electron Microscopy Studies M icrostructural Evolution and Age Hardening in," *Mater. Charact.*, vol. 44, pp. 101–131, 2000.

[45] M. J. Starink and S. C. Wang, "The thermodynamics of and strengthening due to co-clusters: General theory and application to the case of Al–Cu–Mg alloys," *Acta Mater.*, vol. 57, no. 8, pp. 2376–2389, May 2009.

[46] S. P. Ringer, S. K. Caraher, and I. J. Polmear, "Response to comments on cluster hardening in an aged Al-Cu-Mg alloy," *Scr. Mater.*, vol. 39, no. 11, pp. 1559–1567, Nov. 1998.

[47] A. T. W. Kempen, E. J. Mittemeijer, and S. van der Zwaag, "Solid State Phase Transformation Kinetics," Max-planck-institut F Ü R Metallforschung, Stuttgart, 2001.

[48] O. Novelo-Peralta, I. a. Figueroa, G. Lara-Rodríguez, and G. González, "New evidence on the nature of the metastable S″-phase on Al–Cu–Mg alloys," *Mater. Chem. Phys.*, vol. 130, no. 1–2, pp. 431–436, Oct. 2011.

[49] C. Wolverton, "Crystal structure and stability of complex precipitate phases in Al–Cu–Mg–(Si) and Al–Zn–Mg alloys," *Acta Mater.*, vol. 49, no. 16, pp. 3129–3142, Sep. 2001.

[50] G. Sha, R. K. W. Marceau, X. Gao, B. C. Muddle, and S. P. Ringer, "Nanostructure of aluminium alloy 2024: Segregation, clustering and precipitation processes," *Acta Mater.*, vol. 59, no. 4, pp. 1659–1670, Feb. 2011.

[51] R. K. W. Marceau, G. Sha, R. Ferragut, a. Dupasquier, and S. P. Ringer, "Solute clustering in Al–Cu–Mg alloys during the early stages of elevated temperature ageing," *Acta Mater.*, vol. 58, no. 15, pp. 4923–4939, Sep. 2010.

[52] T. E. M. Staab, B. Klobes, I. Kohlbach, B. Korff, M. Haaks, E. Dudzik, and K. Maier, "Atomic structure of pre-Guinier-Preston and Guinier-Preston-Bagaryatsky zones in Al-alloys," *J. Phys. Conf. Ser.*, vol. 265, p. 012018, Jan. 2011.

[53] S. P. Ringer, K. Hono, T. Saksai, and I. J. Polmear, "Cluster Hardening in an aged Al-Cu-Mg Alloy," *Scr*, vol. 36, no. 5, pp. 517–521, 1997.

[54] K. Bowman, *Mechanical Behavior of Materials*. John Wiley and Sons Inc., 2004, pp. 152–175.

[55] J. J. Gilman, *Chemistry and Physics of Mechanical Hardness*. Hoboken, NJ, USA: John Wiley & Sons, Inc., 2009.

[56] G. E. Dieter, *Mechanical Metallurgy*, Third edit. New York: McGraw Hill, 1986, pp. 120–220.

[57]   R. W. Hertzberg, *Deformation and Fracture Mechanics of Engineering Materials*, Fourth. Joh Wiley and Sons Inc., 1995.

[58]   J. D. Verhoeven, *Fundamentals of Physical Metallurgy*. John Wiley and Sons Inc., 1975, pp. 513–523.

[59]   J. C. Williams and E. a Starke, "Progress in structural materials for aerospace systems11The Golden Jubilee Issue—Selected topics in Materials Science and Engineering: Past, Present and Future, edited by S. Suresh.," *Acta Mater.*, vol. 51, no. 19, pp. 5775–5799, Nov. 2003.

[60]   S. Muthu Kumaran, "Evaluation of precipitation reaction in 2024 Al–Cu alloy through ultrasonic parameters," *Mater. Sci. Eng. A*, vol. 528, no. 12, pp. 4152–4158, May 2011.

[61]   R. Z. Valiev, R. K. Islamgaliev, and I. V Alexandrov, "Bulk nanostructured materials from severe plastic deformation," *Prog. Mater. Sci.*, vol. 45, pp. 103–189, 2000.

[62]   A. Aronin, "Structure and Properties of Nanocrystalline Solids Prepared by High Pressure Torsion," *Solid State Phys.*, vol. 25, pp. 52–57, 2010.

[63]   K. Bobor and G. Krallics, "CHARACTERIZATION OF SEVERE PLASTIC NON-MONOTONITY," *Rev. Adv. Mater. Sci*, vol. 25, pp. 32–41, 2010.

[64]   K. Nakashima, Z. Horita, M. Nemoto, and T. G. Langdon, "Development of a multi-pass facility for equal-channel angular pressing to high total strains," *Mater. Sci. Eng. A*, vol. 281, no. 1–2, pp. 82–87, Apr. 2000.

[65]   G. I. Raab, A. V Botkin, A. G. Raab, and R. Z. Valiev, "New Schemes of ECAP Processes for Producing Nanostructured Bulk Metallic Materials," *Physics (College. Park. Md).*, pp. 641–646, 2007.

[66]   R. Z. Valiev and T. G. Langdon, "DEVELOPMENTS IN THE USE OF ECAP PROCESSING FOR GRAIN REFINEMENT," *Rev. Adv. Mater. Sci*, vol. 13, pp. 15–26, 2006.

[67]   A. Bachmaier, M. Hafok, R. Schuster, and R. Pippan, "LIMITATIONS IN THE REFINEMENT BY SEVERE PLASTIC DEFORMATION: THE EFFECT OF PROCESSING," *Rev. Adv. Mater. Sci*, vol. 25, pp. 16–22, 2010.

[68]   T. C. Lowe and Y. T. Zhu, "Commercialization of Nanostructured Metals Produced by Severe Plastic Deformation Processing," *Adv. Eng. Mater.*, vol. 5, no. 5, pp. 373–378, May 2003.

[69] M. Furukawa, Y. Iwahashi, and Z. Horita, "The shearing characteristics associated with equal-channel angular pressing," *Mater. Sci. ...*, vol. 257, no. 2, pp. 328–332, Dec. 1998.

[70] A. Vevecka, H. Werner, and M. Göken, "Deformation Behaviour of Nanocrystalline Al Alloy , Processed by Severe Plastic Deformation," *Mater. Sci.*, pp. 151–155, 2009.

[71] V. M. Segal, "Equal channel angular extrusion: from macromechanics to structure formation," *Mater. Sci. Eng. A*, vol. 271, no. 1–2, pp. 322–333, Nov. 1999.

[72] S. Chowdhury, C. Xu, and T. Langdon, "Texture evolution in an aluminum alloy processed by ECAP with concurrent precipitate fragmentation," *Mater. Sci. Eng. A*, vol. 473, no. 1–2, pp. 219–225, Jan. 2008.

[73] A. Gazder, W. Cao, C. Davies, and E. Pereloma, "An EBSD investigation of interstitial-free steel subjected to equal channel angular extrusion," *Mater. Sci. Eng. A*, vol. 497, no. 1–2, pp. 341–352, Dec. 2008.

[74] Y. He, Q. Pan, Y. Qin, X. Liu, W. Li, Y. Chiu, and J. J. J. Chen, "Microstructure and mechanical properties of ZK60 alloy processed by two-step equal channel angular pressing," *J. Alloys Compd.*, vol. 492, no. 1–2, pp. 605–610, Mar. 2010.

[75] K. Xia, J. T. Wang, X. Wu, G. Chen, and M. Gurvan, "Equal channel angular pressing of magnesium alloy AZ31," *Mater. Sci. Eng. A*, vol. 410–411, pp. 324–327, Nov. 2005.

[76] O. Saray, G. Purcek, and I. Karaman, "Principles of Equal Channel Angular Sheet Extrusion (ECASE): Application to IF Steel," *Engineering*, vol. 25, pp. 42–51, 2010.

[77] Z. Horita, T. Fujinami, and T. G. Langdon, "The potential for scaling ECAP : effect of sample size on grain refinement and mechanical properties," *Mater. Sci. Eng. A*, vol. 318, pp. 34–41, 2001.

[78] A. Y. Vinogradov, V. V. Stolyarov, S. Hashimoto, and R. Z. Valiev, "Cyclic behavior of ultrafine-grain titanium produced by severe plastic deformation," *Mater. Sci. Eng. A*, vol. 318, no. 1–2, pp. 163–173, Nov. 2001.

[79] W. Z. Han, Z. F. Zhang, S. D. Wu, and S. X. Li, "Investigation on the geometrical aspect of deformation during equal-channel angular pressing by in-situ physical modeling experiments," *Mater. Sci. Eng. A*, vol. 476, no. 1–2, pp. 224–229, Mar. 2008.

[80] W. Cao, S. Yu, Y. Chun, Y. Yoo, C. Lee, D. Shin, and S. Hwang, "Strain path effects on the microstructure evolution and mechanical properties of Zr702," *Mater. Sci. Eng. A*, vol. 395, no. 1–2, pp. 77–86, Mar. 2005.

[81] Y. J. Chen, Y. J. Li, J. C. Walmsley, S. Dumoulin, P. C. Skaret, and H. J. Roven, "Microstructure evolution of commercial pure titanium during equal channel angular pressing," *Mater. Sci. Eng. A*, vol. 527, no. 3, pp. 789–796, Jan. 2010.

[82] W. J. Kim, C. S. Chung, D. S. Ma, S. I. Hong, and H. K. Kim, "Optimization of strength and ductility of 2024 Al by equal channel angular pressing (ECAP) and post-ECAP aging," *Scr. Mater.*, vol. 49, no. 4, pp. 333–338, Aug. 2003.

[83] W. D. Callister, Jr., *Fundamentals of Materials Science and Engineering*, 5th editio. John Wiley and Sons Inc., 2000.

[84] J. W. Christian, *The Theory of Transformations in Metals and Alloys-PartII*. Oxford: Pergamon Elsevier Science Ltd, 2002.

[85] R. D. Doherty, "DIFFUSIVE PHASE TRANSFORMATIONS IN THE SOLID STATE," in *Physical Metallurgy*, 4th editio., R. W. Cahn and P. Haasen, Eds. New York, Amsterdam: Elsevier, 1996, pp. 1363–1505.

[86] D. A. Porter and K. E. Easterling, *Phase Transformations in Metals and Alloys*, Second. London: Chapman and Hall, 1992, p. 293.

[87] N. E. Bekheet, R. M. Gadelrab, M. F. Salah, and A. N. Abd El-Azim, "The effects of aging on the hardness and fatigue behavior of 2024 Al alloy/SiC composites," *Mater. Des.*, vol. 23, no. 2, pp. 153–159, Apr. 2002.

[88] S. C. Wang and M. J. Starink, "The assessment of GPB2/S″ structures in Al–Cu–Mg alloys," *Mater. Sci. Eng. A*, vol. 386, no. 1–2, pp. 156–163, Nov. 2004.

[89] K. Raviprasad, C. . Hutchinson, T. Sakurai, and S. . Ringer, "Precipitation processes in an Al-2.5Cu-1.5Mg (wt. %) alloy microalloyed with Ag and Si," *Acta Mater.*, vol. 51, no. 17, pp. 5037–5050, Oct. 2003.

[90] H. Lu, P. Kadolkar, K. Nakazawa, T. Ando, and C. a. Blue, "Precipitation Behavior of AA2618," *Metall. Mater. Trans. A*, vol. 38, no. 10, pp. 2379–2388, Aug. 2007.

[91] Z. Huda, N. Taib, and T. Zaharinie, "Characterization of 2024-T3: An aerospace aluminum alloy," *Mater. Chem. Phys.*, vol. 113, no. 2–3, pp. 515–517, Feb. 2009.

[92] M. Wang, Shun Cai Li Chunzhi Yan, "1989 article on TEM of 2024.pdf," *Acta Metall. Sin.*, vol. 3, no. 2, pp. 104–109, 1990.

[93] E. Saraloglu, E. Tan, and C. H. Gür, "Effect of ECAP and Post-aging Processes on 2024 Aluminum Alloy," *Steel Res. inc.*, vol. 79, no. 2, pp. 467–471, 2008.

[94] E. V. Esquivel, "Microstructural Issues Associated with Seere Plastic Deformation: Applications of Transmission Electron Microscopy," 2005.

[95] D. B. . Williams and C. B. Carter, *Transmission Electron microscopy*, 1st Editio. Springer Publishing, 2009.

[96] R. Z. Valiev and T. G. Langdon, "Principles of equal-channel angular pressing as a processing tool for grain refinement," *Prog. Mater. Sci.*, vol. 51, no. 7, pp. 881–981, Sep. 2006.

[97] Z. Horita and T. G. Langdon, "Achieving exceptional superplasticity in a bulk aluminum alloy processed by high-pressure torsion," *Scr. Mater.*, vol. 58, pp. 1029–1032, 2008.

[98] R. Vafaei, M. R. Toroghinejad, and R. Pippan, "Evaluation of mechanical behavior of nano-grained 2024 Al alloy during high pressure torsion (HPT) process at various temperatures," *Mater. Sci. Eng. A*, vol. 536, pp. 73–81, Feb. 2012.

[99] A. V. Nagasekhar and H. S. Kim, "Plastic deformation characteristics of cross-equal channel angular pressing," *Comput. Mater. Sci.*, vol. 43, no. 4, pp. 1069–1073, Oct. 2008.

[100] S. C. Yoon and H. S. Kim, "Finite element analysis of the effect of the inner corner angle in equal channel angular pressing," *Mater. Sci. Eng. A*, vol. 490, no. 1–2, pp. 438–444, Aug. 2008.

[101] M. Prell, C. Xu, and T. G. Langdon, "The evolution of homogeneity on longitudinal sections during processing by ECAP," *Mater. Sci. Eng. A*, vol. 480, no. 1–2, pp. 449–455, May 2008.

[102] F. Djavanroodi, M. Daneshtalab, and M. Ebrahimi, "A novel technique to increase strain distribution homogeneity for ECAPed materials," *Mater. Sci. Eng. A*, vol. 535, pp. 115–121, Feb. 2012.

[103] V. Patil Basavaraj, U. Chakkingal, and T. S. Prasanna Kumar, "Study of channel angle influence on material flow and strain inhomogeneity in equal channel angular pressing using 3D finite element simulation," *J. Mater. Process. Technol.*, vol. 209, no. 1, pp. 89–95, Jan. 2009.

[104] Y. Estrin, L. S. Tóth, a. Molinari, and Y. Bréchet, "A dislocation-based model for all hardening stages in large strain deformation," *Acta Mater.*, vol. 46, no. 15, pp. 5509–5522, Sep. 1998.

[105] Y. W. Ma, J. W. Choi, and K. B. Yoon, "Change of anisotropic tensile strength due to amount of severe plastic deformation in aluminum 2024 alloy," *Mater. Sci. Eng. A*, vol. 529, pp. 1–8, Nov. 2011.

[106] M. Vaseghi, K. A. Taheri, S. I. Hong, and H. S. Kim, "Dynamic ageing and the mechanical response of Al − Mg − Si alloy through equal channel angular pressing," *Mater. Des.*, vol. 31, no. 9, pp. 4076–4082, 2010.

[107] W. Kim and J. Wang, "Microstructure of the post-ECAP aging processed 6061 Al alloys," *Mater. Sci. Eng. A*, vol. 464, no. 1–2, pp. 23–27, Aug. 2007.

[108] H. J. Choi, B. H. Min, J. H. Shin, and D. H. Bae, "Strengthening in nanostructured 2024 aluminum alloy and its composites containing carbon nanotubes," *Compos. Part A Appl. Sci. Manuf.*, vol. 42, no. 10, pp. 1438–1444, Oct. 2011.

[109] C. Genevois, D. Fabrègue, A. Deschamps, and W. J. Poole, "On the coupling between precipitation and plastic deformation in relation with friction stir welding of AA2024 T3 aluminium alloy," *Mater. Sci. Eng. A*, vol. 441, no. 1–2, pp. 39–48, Dec. 2006.

[110] I. Mazurina, T. Sakai, H. Miura, O. Sitdikov, and R. Kaibyshev, "Effect of deformation temperature on microstructure evolution in aluminum alloy 2219 during hot ECAP," *Mater. Sci. Eng. A*, vol. 486, no. 1–2, pp. 662–671, Jul. 2008.

[111] A. L. Ning, Z. Y. Liu, and S. M. Zeng, "Effect of large cold deformation on characteristics of age-strengthening of 2024 aluminum alloys," *Trans. Nonferrous Met. Soc. China*, vol. 16, no. 5, pp. 1121–1128, 2006.

[112] X. Xu, Z. Liu, Y. Li, P. Dang, and S. Zeng, "Evolution of precipitates of Al-Cu alloy during equal-channel angular pressing at room temperature," *Trans. Nonferrous Met. Soc. China*, vol. 18, no. 5, pp. 1047–1052, Oct. 2008.

[113] P. Venkatachalam, S. Ramesh Kumar, B. Ravisankar, V. Thomas Paul, and M. Vijayalakshmi, "Effect of processing routes on microstructure and mechanical properties of 2014 Al alloy processed by equal channel angular pressing," *Trans. Nonferrous Met. Soc. China*, vol. 20, no. 10, pp. 1822–1828, Oct. 2010.

[114] C. Şimşir, P. Karpuz, and C. H. Gür, "Quantitative analysis of the influence of strain hardening on equal channel angular pressing process," *Comput. Mater. Sci.*, vol. 48, no. 3, pp. 633–639, May 2010.

[115] Y. L. Zhao, Z. Q. Yang, Z. Zhang, G. Y. Su, and X. L. Ma, "Double-peak age strengthening of cold-worked 2024 aluminum alloy," *Acta Mater.*, vol. 61, no. 5, pp. 1624–1638, Mar. 2013.

[116] T. G. Langdon, "The Characteristics of Grain refinement in Materials Processed by Severe Plastiic Deformation," *Processing*, vol. 13, pp. 6–14, 2006.

[117] Z. Horita, T. Fujinami, M. Nemoto, and T. G. Langdon, "Equal-Channel Angular Pressing of Commercial Aluminum Alloys : Grain Refinement , Thermal Stability and Tensile Properties," vol. 31, no. March, pp. 691–701, 2000.

[118] M. Cabibbo, E. Evangelista, and V. Latini, "Thermal stability study on two aluminum alloys," vol. 9, pp. 5659–5667, 2004.

[119] H.-W. Chang, P. M. Kelly, Y.-N. Shi, and M.-X. Zhang, "Thermal stability of nanocrystallized surface produced by surface mechanical attrition treatment in aluminum alloys," *Surf. Coatings Technol.*, vol. 206, no. 19–20, pp. 3970–3980, May 2012.

[120] K. Maung, R. K. Mishra, I. Roy, L.-C. Lai, F. a. Mohamed, and J. C. Earthman, "Thermal stability of cryomilled nanocrystalline aluminum containing diamantane nanoparticles," *J. Mater. Sci.*, vol. 46, no. 21, pp. 6932–6940, Jun. 2011.

[121] M. Jafari, M. H. Enayati, M. H. Abbasi, and F. Karimzadeh, "Thermal stability and structural changes during heat treatment of nanostructured Al2024 alloy," *J. Alloys Compd.*, vol. 478, no. 1–2, pp. 260–264, Jun. 2009.

[122] M. Lewandowska and K. J. Kurzydłowski, "Thermal stability of a nanostructured aluminium alloy," *Mater. Charact.*, vol. 55, no. 4–5, pp. 395–401, Nov. 2005.

[123] J. M. Tao, X. K. Zhu, R. O. Scattergood, and C. C. Koch, "The thermal stability of high-energy ball-milled nanostructured Cu," *Mater. Des.*, vol. 50, pp. 22–26, Sep. 2013.

[124] A. Rebhi, T. Makhlouf, Y. Champion, J.-P. Couzinié, and N. Njah, "Microstructure investigation and thermal stability of 99.1% aluminum processed by equal channel angular extrusion," *J. Mater. Sci.*, vol. 46, no. 7, pp. 2185–2193, Nov. 2010.

[125] B. Forbord, H. Hallem, J. Røyset, and K. Marthinsen, "Thermal stability of Al3(Scx,Zr1−x)-dispersoids in extruded aluminium alloys," *Mater. Sci. Eng. A*, vol. 475, no. 1–2, pp. 241–248, Feb. 2008.

[126] M. Fujda, M. Matvija, T. Kvackaj, O. Milkovic, P. Zubko, K. Nagyova, and P. Slama, "Thermal stability of the ultrafine grained EN AW 6082 aluminium alloy," *Kov. Mater. Mater.*, vol. 51, no. 2, pp. 117–122, 2013.

[127] C. H. P. Lupis, *Chemical thermodynamics of materials*. New York : North Holland: Elsevier Science Publishing Co., 1983, pp. 1–100.

[128] F. J. Humphreys and M. Hatherly, *Recrystallization and Related Annealing Phenomena*, 2nd Editio. Elsevier Ltd, 2004.

[129] M. . Jones and F. . Humphreys, "Interaction of recrystallization and precipitation: The effect of Al3Sc on the recrystallization behaviour of deformed aluminium," *Acta Mater.*, vol. 51, no. 8, pp. 2149–2159, May 2003.

[130] G. B. Brook, *Mechanical properties of light metals and alloys*. Union, European Standards, British, 1998.

[131] M. Nikitina, R. Islamgaliev, and A. Kamalov, "Thermal stability of the ultrafine-grained Al-Cu-Mg-Si aluminum alloy," *Rev. Adv. Mater. Sci*, vol. 25, pp. 74–81, 2010.

[132] J. Lipecka, M. Andrzejczuk, M. Lewandowska, J. Janczak-Rusch, and K. J. Kurzydłowski, "Evaluation of thermal stability of ultrafine grained aluminium matrix composites reinforced with carbon nanotubes," *Compos. Sci. Technol.*, vol. 71, no. 16, pp. 1881–1885, Nov. 2011.

[133] R. K. Islamgaliev, M. A. Nikitina, and A. F. Kamalov, "Enhanced Thermal Stability And Mechanical Properties of Ultrafine-Grained Aluminum Alloy," vol. 669, pp. 331–336, 2011.

[134] J. Mao, S. B. Kang, and J. O. Park, "Grain refinement, thermal stability and tensile properties of 2024 aluminum alloy after equal-channel angular pressing," *J. Mater. Process. Technol.*, vol. 159, no. 3, pp. 314–320, Feb. 2005.

[135] N. Hansen, X. Huang, M. G. Møller, and a. Godfrey, "Thermal stability of aluminum cold rolled to large strain," *J. Mater. Sci.*, vol. 43, no. 18, pp. 6254–6259, Aug. 2008.

[136] J. Zrnik, T. Koarik, M. Cieslar, and L. Kraus, "Thermal Stability of Aluminum Ultrafine Grain Structure," 2010.

[137] R. Kužel, Z. Matěj, and M. Janeček, "*In Situ* X-Ray Diffraction Study of Thermal Stability of Cu and Cu-Zr Samples Processed by ECAP," *Mater. Sci. Forum*, vol. 753, pp. 279–284, Mar. 2013.

VITA

GÜHER KOTAN

PERSONAL INFORMATION

Marital Status   : Single

Nationality   : T.C.

Date / Place of Birth   : 18.03.1981 ERZURUM

E- mail   : guherkotan@gmail.com

                      guher@metu.edu.tr

Phone   (GSM)   : 0 533 749 87 78

EDUCATION INFORMATION

PhD   METU, Metallurgical and Materials Enginering Dept., ANKARA

         September 2006 –   *CGPA:* 3.64/4.00

MSc   METU, Metallurgical and Materials Enginering Dept., ANKARA

         September 2003 – September 2006   *CGPA:* 3.79/4.00

BSc   METU, Metallurgical and Materials Enginering Dept., ANKARA

         September 1999 – 29.06.2003   *CGPA:* 3.01/4.00

HighSchool   Atatürk Anadolu Lisesi, ANKARA

         September 1995 – 25.06.1999   *CGPA:* 4.34/5.00

WORK HISTORY

October 2005 – ....   Research Assistant, METU METE

      Department Advertising Committee

      Electron Microscopes Responsible (sample prep, imaging, microanalysis)

      Alumni Committee

      Exam Coordination

      Transmission Electron Microscopy - In Charge Assistant/ 2010-2012

Assisted Courses

      Mechanical Laboratory Assistant (2 semester),

      METE 535 (Transmission Electron Microscopy/Lab. Assistant)

      METE 719 (Structure of Materials)

      MetE 508 (Advanced Optical Techniques/Lab Assistant) (3 semesters)

      MetE 308 (Physical Metallurgy) (2 semesters),

      MetE 403 (Phase Transformatios) (3 semesters),

      MetE 310 (X-Ray Diffraction-Lab Assistant) (2 semesters),

      MetE 206 (X-Ray Diff. And Crystallography/Impact Testing/Heat Treatment) (1 semester),

      MetE 225 (Engineering Materials) (4 semester)

      MetE 401 (Materials Engineering Design- CES laboratory) (1 semester)

October 2012 –March 2013   Researcher, AMES LAB, IOWA STATE UNI, USA

June 2002 – July 2002 ETİ Al A. Ş. Seydişehir/Konya, Summer Intern, Quality Control.

June 2001 – July 2001 ASİLÇELİK/ Summer Intern, Production

EXPERTIES

Physical Metallurgy of phase transformations (Precipitation, precipitation of Al Alloys, heat treatment), Hardening Mechanisms, Dislocations, Severe Plastically Deformed Structures, Al Alloys, Titanium Alloys, Metallic Foams, Microstructural Characterization.

Scanning Electron Microscope (SEM) Operator   till January 2005

Transmission Electron Microscope (TEM) Operator   till April 2009

EBSD attached FEG-SEM Operator   till June 2009

PAPERS IN JOURNALS

	PUBLICATION	Citation	TYPE
2	"*Homogenization of ECAPed Al 2024 alloy through age-hardening*", G. Kotan, E. Tan, Y.E. Kalay, C.H. Gur Mater. Sci. Eng. A, 559 (2013), pp. 601–606	2	ENG
1	"*Production and Characterization of High Porosity Ti-6Al-4V Foam by Space Holder Technique in Powder Metallurgy*", G. Kotan, Ş. Bor, Turkish J. Eng, Env. Sci., 31 (2007), 149-156	19	ENG

CONFERANCE PAPERS /ACTIVITIES

	TITLE	CONF	LANG.
13	Investigation of the Precipitation Mechanism in the Severely Deformed and Aged 2024 Al-Alloy Kotan G, Tan E, Kalay YE, Gur CH	16th Int Metallurgy-Materials Cong. 13-15 Sep 2012 İstanbul	ENG
12	Effect of Post ECAP Aging on the Thermal Stability and Subgrain Structure of 2024 Al-Alloy Kotan G, Tan E, Kalay YE, Gur CH (ORAL)	3rd Int. Symp. Bulk Nanostructured Materials (BNM2011) 22-26 Sep 2009 Ufa-Russia	ENG
11	The Investigation of Inhomogeneity in Single Pass ECAP Through Post-ECAP Aging of Al 2024 Kotan G, Tan E, Kalay YE, Gur CH (POSTER)	3rd Int. Symp. Bulk Nanostructured Materials (BNM2011) 22-26 Sep 2009 Ufa-Russia	ENG